Developing a luminescence chronology for late Quaternary fluvial change in South African floodplain wetlands

Helena Rodnight

Thesis submitted in fulfilment of the requirements for the degree of PhD

University of Wales, Aberystwyth

July 2006

ABSTRACT

Owing to variation in the extent to which sediment grains transported in water are exposed to daylight, problems have been encountered in applying optically stimulated luminescence (OSL) dating to fluvial deposits. This thesis develops the OSL technique so that ages for heterogeneously-bleached fluvial samples can be derived based on the analysis of well-bleached grains. The ages calculated are then used to establish the timing and rates of different channel change processes. For two mixed bedrock-alluvial rivers with extensive floodplain wetlands located in the eastern Free State, South Africa, OSL sample collection was designed to investigate the lateral migration rates, meander cutoff ages, and avulsion frequency on the Klip River, and incision rate on the Schoonspruit.

Heterogeneous bleaching is evident in the majority of the samples and investigation shows that at least 50 equivalent dose (D_e) values are necessary to obtain reproducible dose distributions for these samples. Analysis of samples from palaeochannels of the Klip River demonstrates that the finite mixture model is the most appropriate for calculating the burial dose; replicate samples from the same palaeochannel reach give generally consistent ages, and comparison with radiocarbon ages for overlying organic-rich sediment gives good agreement. Using OSL dating, average lateral migration rates of ~0.05 and ~0.16 m/a over the last ~1.4 ka are obtained for two meander bends on the Klip River, and five avulsions are identified as occurring since ~30 ka. On the Schoonspruit, the average incision rate has been ~2-3 mm/a since ~1.2 ka.

No clear link between these channel change processes and palaeoclimatic records from South Africa is evident. The results from this thesis, therefore, indicate that channel change processes on the Klip River and Schoonspruit result primarily from autogenic controls, rather than allogenic controls such as climate change.

DECLARATION

This work has not previously been accepted in substance for any degree and is not being concurrently submitted in candidature for any degree.

Signed…….. (candidate)
Date……..

STATEMENT 1

This thesis is the result of my own investigations, except where otherwise stated. Where correction services have been used, the extent and nature of correction is clearly marked in a footnote(s).
Other sources are acknowledged by footnotes giving explicit references. A bibliography is appended.

Signed…….. (candidate)
Date……..

STATEMENT 2

I hereby give consent for my thesis, if accepted, to be available for photocopying and for inter-library loan, and for the title and summary to be made available to outside organisations.

Signed…….. (candidate)
Date……..

ACKNOWLEDGEMENTS

This research was funded by a grant from the Institute of Geography and Earth Sciences, University of Wales, Aberystwyth, for which I am extremely grateful. Additional funding for the radiocarbon samples was obtained from the Quaternary Research Association, and conference attendance was made possible by the British Geomorphological Research Group, the International Association of Sedimentologists and the Gooding Fund.

I am deeply indebted to my two supervisors for guiding and encouraging me throughout my PhD - Prof. Geoff Duller and Dr. Stephen Tooth have helped at every step of the way.

I also very much appreciate the help and guidance I have received from Prof. Ann Wintle and Dr. Helen Roberts. Whilst at Aberystwyth Luminescence Laboratory, I have also been aided by Dr. Chris Burbidge, Dr. Zenobia Jacobs, Dr. Mayank Jain, Dr. J-H Choi and Dr. Sumiko Tsukamoto. On field work in 2003 I was assisted by Prof. Spike McCarthy and Dr. Dion Brandt. Prof. James Scourse should also be acknowledged for introducing me to the Quaternary, luminescence dating, and to Geoff.

My fellow IGES postgraduate students and L-floor coffee room companions have kept me going throughout my PhD and in particular, Dr. Angharad Saunders helped keep me sufficiently fed and watered. My friends from outside the university have also done a great deal to keep me sane, reminding me that the real world does still exist with sunshine, beaches and trails. My thanks also to Becky Good for keeping me motivated during the final few months of writing with the thought of our trip to Spain.

Finally, I owe a great deal of thanks and love to all my family for their support and encouragement throughout.

This work is dedicated to the memory of Dr. Gav Winsborrow and Bill Setterfield, whom both inspired and supported me.

CONTENTS

LIST OF FIGURES

CHAPTER 1: INTRODUCTION

Most rivers are highly dynamic systems, with changes in erosion, deposition and channel morphology occurring over various spatial and temporal scales, in response to both autogenic adjustments or to allogenic forcing (e.g. climatic change, tectonic activity). Whilst the broad nature of river changes can be established from identification of morphological or sedimentary features, in order to understand fully the development of river systems, the rates and timescales of channel change processes need to be known. Problems are often encountered in accurately establishing the rates of specific processes of channel change, owing to the lack of sufficient material suitable for dating by traditional methods such as radiocarbon. Recent advances in the technique of optically stimulated luminescence dating, however, have made it suitable for determining rates of geomorphic and sedimentary processes (Duller, 2004). This method combines measurement of the optically stimulated luminescence (OSL) signal from certain mineral grains (e.g. quartz) in a sedimentary deposit with the environmental dose-rate, to derive the age of the last exposure of the sediment to sunlight. Whilst the suitability of this technique has been demonstrated for a range of depositional environments (e.g. Olley *et al.*, 2004b), problems associated with insufficient exposure to sunlight during transport may arise in fluvial settings. Nevertheless, the technique shows great potential for use in accurate determination of the timing of deposition for sediments associated with various channel change processes.

Traditionally, river systems have tended to be studied as two end-members: bedrock rivers (e.g. Tinkler and Wohl, 1998) and alluvial rivers (e.g. Richards, 1982). Mixed bedrock-alluvial rivers, however, occur where dominantly alluvial reaches alternate with dominantly bedrock reaches (Tooth *et al.*, 2004). In the alluvial reaches, the local channel form is primarily controlled by flow and sediment transport processes. The bedrock reaches consist of either a thin veneer of alluvium over bedrock, or bedrock outcrops that form part of the channel bed or banks. In these reaches, the local channel form is dominated primarily by lithological and structural controls. Resistant bedrock outcrops may form local baselevels in the river's long profile and this can influence flow and

sediment transport processes in alluvial reaches upstream and downstream. In mixed bedrock-alluvial rivers, the local geology can thus exert a strong, and sometimes dominant, control on the evolution of the whole river (Tooth *et al.*, 2004). For instance, in many mixed bedrock-alluvial rivers across the subhumid to semi-arid South African interior, intensely meandering channels that are associated with extensive floodplain wetlands often occur in the reaches upstream of bedrock outcrop. These wetlands perform important hydrological and hydrochemical functions and sustain biodiversity, yet they are poorly understood (Tooth *et al.*, 2002). Critical to developing our understanding of the development of these systems are chronologies of river channel change.

The work in this study will focus primarily on the development of OSL dating for fluvial deposits. The results will allow the development of chronologies of channel change for two South African mixed bedrock-alluvial rivers that have extensive floodplain wetlands, thereby enabling our understanding of these types of river system to be improved.

1.1 RESEARCH CONTEXT

In South Africa, mixed bedrock-alluvial rivers are widespread, particularly across the Highveld (Fig. 1.1), where the geology consists largely of Karoo Supergroup sedimentary rocks that have been intruded by dolerite sills and dykes. In this region, post-Gondwana landscape development essentially involved removal of substantial thicknesses (~1-2 km) of volcanic and sedimentary rocks, leading to widespread river superimposition onto the underlying lithologies (McCarthy and Tooth, 2004). The highly resistant dolerite intrusions exert a strong geological control on river behaviour, acting as local baselevels and thus retarding vertical erosion in reaches upstream that are underlain by the more erodible sedimentary rocks (commonly sandstones, siltstones and mudstones). An initial study of the upper Klip River, eastern Free State, attributed the intense meandering and extensive wetlands to baselevel control exerted by a downstream dolerite sill (Tooth *et al.*, 2002). Subsequent work investigated the influence of dolerite intrusions on the longer term (late Cainozoic) development of the Klip River and two neighbouring rivers, the Venterspruit and the Schoonspruit (Tooth *et al.*, 2004). In this later work, a

conceptual model of long-term river and landscape evolution was developed, and it was suggested that channel change occurred by four main mechanisms: 1) lateral migration; 2) cutoff development; 3) avulsion; and 4) incision. Vertical aggradation – a common mechanism of channel change in many river systems – is not important on these river systems because the long-term tendency in this region is for river incision and landscape denudation. Although this conceptual model has been proposed, the timescales associated with the mechanisms of channel change are currently unknown because there are no supporting chronologies for any of the Highveld rivers. In this thesis, therefore, reaches of the upper Klip River and the lower Schoonspruit are the focus of a study using optically stimulated luminescence dating to derive rates of specific channel change processes. At present, the study site on the Klip River is characterised by lateral migration upstream of an intact dolerite sill. Floodplain wetlands are extensive and in a near-pristine condition. By contrast, a dolerite sill on the lower Schoonspruit has been partially breached, which has resulted in knickpoint retreat and deep channel incision in the area studied. The floodplain wetlands have been abandoned and numerous dongas (gullies) have formed.

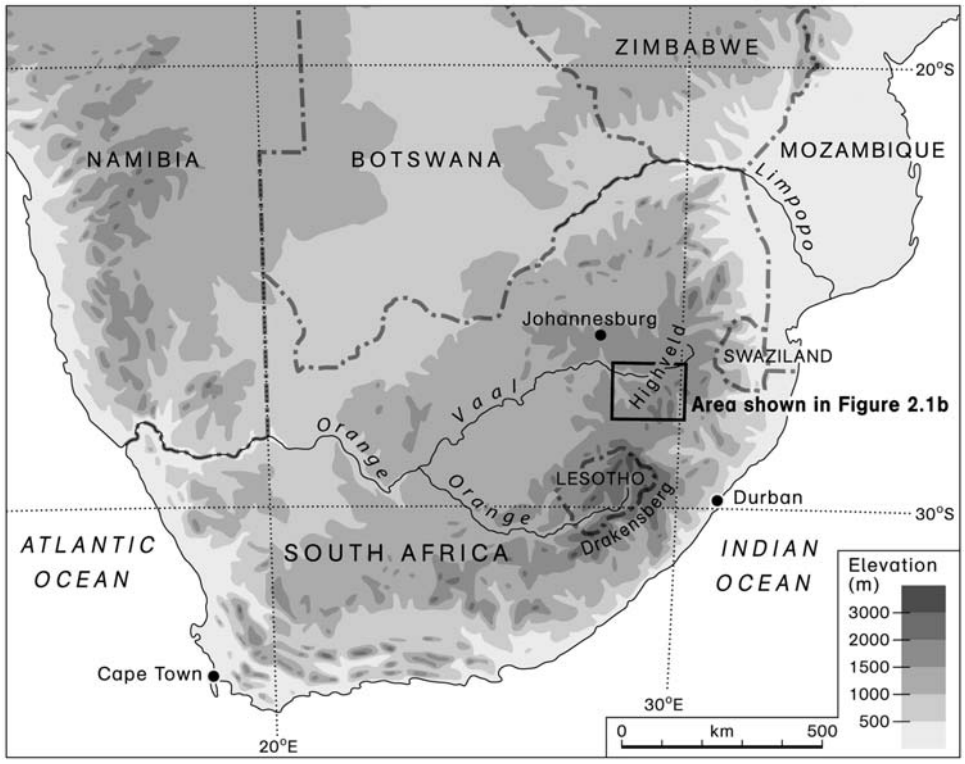

Figure 1.1: Topographical map of South Africa showing the low lying coastal areas and the high interior plateau.

Understanding the development of these river systems has applications in determining empirical and conceptual models, as well as appropriate management strategies for these and numerous similar rivers in South Africa and beyond. Previous research into the development of mixed bedrock-alluvial rivers and floodplain wetlands has been hampered by problems associated with dating of the sedimentary facies. In fluvial settings, the sedimentary deposits often yield insufficient material to enable extensive use of radiocarbon dating to derive rates of channel change. Furthermore, interpretation of radiocarbon ages can be problematic because the ages are commonly derived from organic remains and do not directly date the sediments themselves, therefore they may be subject to errors associated with reworking of older carbon or contamination by younger carbon. The lack of chronologies for such river systems has meant that research in floodplain wetlands has been dominated by hydrologists and ecologists who have tended only to investigate aspects of short-term (less than decades) change, such as flood inundation patterns relevant to flowering/seeding cycles or fish breeding (e.g. Deil, 2005; Capon and Brock, 2006). Hence, it is presently not possible to answer fundamental questions relating to longer-term (centuries to tens of millennia) changes, such as: how old are the wetlands?; how have they developed in response to changes in river activity?; how have past climatic fluctuations affected the wetlands?; how susceptible are the wetlands to human disturbance?

In order to characterise fully past river activity and the implications for wetland development along South African mixed bedrock-alluvial rivers, comprehensive chronologies for fluvial changes have to be established. The technique of OSL dating is able to determine the timing of fluvial deposition. Potentially, therefore, the above questions regarding long-term changes in wetlands can start to be addressed. In this chapter, the technique of OSL dating will be reviewed, particularly with respect to its application to fluvial sediments. The channel change processes of lateral migration, meander cutoff, avulsion, and incision will also be reviewed, particularly with respect to the current understanding of the controls and mechanisms of these processes. These reviews provide the essential basis for the identification of the specific research objectives, which are detailed in Section 1.4.

1.2 OPTICALLY STIMULATED LUMINESCENCE DATING

OSL dating of sediments was first proposed by Huntley *et al*. (1985). The OSL signal acquired during the previous burial period is reset by sunlight during sediment transport prior to deposition (Fig 1.2a). Quartz or feldspar minerals are commonly used for OSL dating of sediments, but where available, quartz is the preferred dosimeter because the physical basis of OSL production is better understood. Additionally, feldspar may be subject to phenomena such as anomalous fading (e.g. Bøtter-Jensen *et al.*, 2003b). For instance, a comparison of the results for quartz and feldspar from fluvial samples by Wallinga *et al*. (2001) found severe underestimation in the feldspar infrared stimulated luminescence (IRSL) ages, which was attributed to changes in the trapping probability of the feldspars during preheating. This led the authors to conclude that quartz is the preferred mineral of choice for dating fluvial deposits.

A simplified model for the production of the luminescence signal is shown in Figure 1.3. Exposure to radiation leads to transfer of negatively charged electrons to the conduction band, leaving positively charged 'holes' in the valence band. In natural quartz grains, impurities present in the crystal lattice may cause defects (L and T on Fig. 1.3i); these defects can trap either electrons or holes. Stimulation by heat or light evicts the electrons from the traps, some of which recombine at luminescence centres (trapped holes), emitting a photon of light in the process (Fig. 1.3iii). The amount of light emitted is proportional to the number of trapped electrons, and hence is related to the total amount of energy received from irradiation. The process of stimulation and eviction of the electrons is termed signal bleaching, with stimulation by heat or light resulting in a thermoluminescence (TL) or OSL signal, respectively. If the grain is stimulated sufficiently to evict all the trapped electrons, it is described as being fully bleached. Whilst the TL glow curve contains contributions from traps of various depths, the main source of the OSL signal is thought to be the traps associated with the readily bleachable 325°C TL trap (Aitken, 1998). Additionally, OSL is generally very much more rapidly reset than TL (Godfrey-Smith *et al.*, 1988), thus making it more suitable for dating sediments where the bleaching occurs by exposure to light.

a)

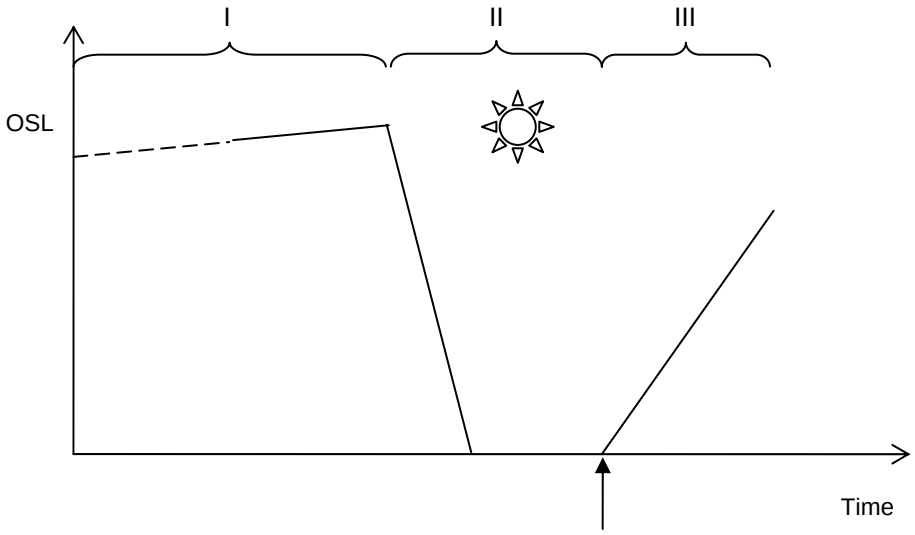

b)

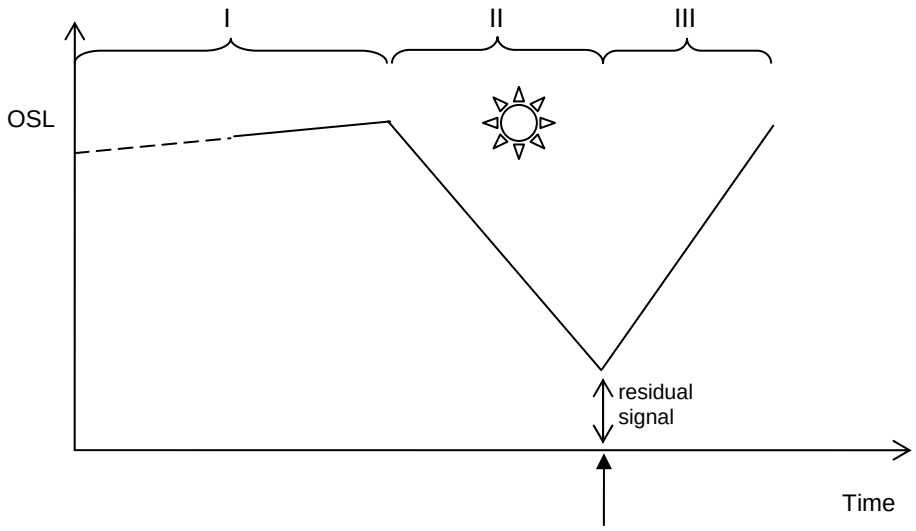

Figure 1.2: a) Schematic diagram showing the OSL signal through time in a sediment grain which is well bleached during transport. The stages shown are: I) geological burial period, where the OSL signal builds up at a rate related to the environmental dose-rate; II) sediment transport, during which the OSL signal is bleached by the sun; III) period of burial, where the OSL signal builds up again at a rate related to the environmental dose-rate. The arrow indicates the depositional event dated. b) Schematic diagram showing the situation where the grain bleaches at a slower rate and is not fully bleached at deposition. A residual signal remains and therefore overestimation of the burial dose value will occur.

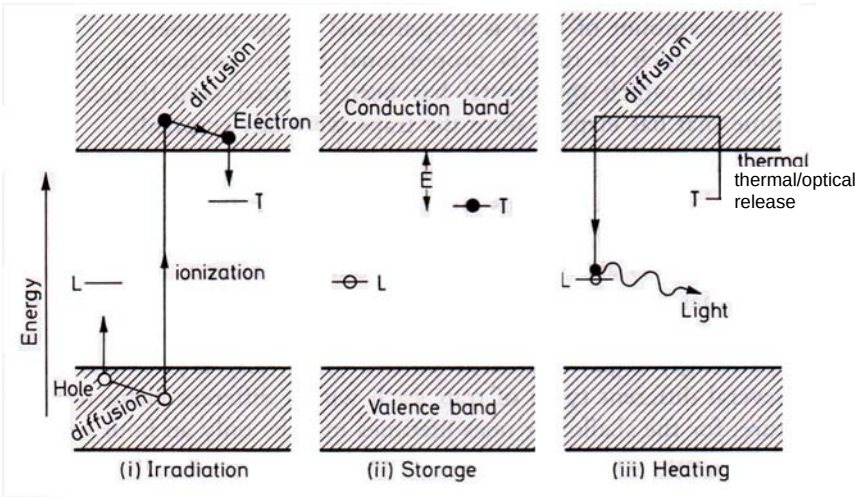

Figure 1.3: Energy level representation of the luminescence signal (adapted from Aitken, 1985). (i) Ionisation from exposure of the crystal to irradiation, with trapping of electrons and holes at defects at *T* and *L*, respectively. (ii) Storage over time. To reduce leakage, the lifetime of the traps needs to be greater than the age span of the sample; the lifetime of the traps is determined by their depth *E*, below the conduction band. For dating purposes, traps greater than ~1.6 eV are used as these are stable for at least several million years. (iii) Stimulation with heat or light of an appropriate wavelength evicts electrons from traps. Some of these reach luminescence centres, and recombination results in the emission of a photon. Alternatively, electrons may recombine at non-luminescence centres, be recaptured by a trap of the same type, or be captured by another type of trap.

The radiation to which a grain is exposed during burial derives from a number of different sources, and consists of alpha and beta particles, and gamma rays. Quartz grains contain very little internal radioactivity, so the majority of the radiation they receive is derived from uranium, thorium, and potassium contained within the surrounding sediment, as well as a small level of cosmic radiation. The radiation flux at a sampling location is termed the environmental dose-rate, and can be obtained either by field or by laboratory measurements. The amount of radiation that a grain has received during burial can be determined by measuring the OSL signal from the natural dose (i.e. that received during burial), and the OSL signals from a series of laboratory irradiations of known dose. The laboratory measurements are used to calibrate the OSL signal derived from the natural dose, and thus determine the laboratory

dose that is equivalent to the dose received by the grains in nature; this is termed the equivalent dose (D_e), with the unit of measurement in Grays (Gy). Since the OSL signal is bleached on exposure to light during sediment transport, the D_e normally represents the amount of radiation received following deposition and burial after the last transport event (Fig. 1.2a). By deriving the burial dose (D_b) of a sample, and the environmental dose-rate at the sampling location, the age of a sample can be found using the equation:

$$\text{Age (ka)} = \frac{\text{Burial dose (Gy)}}{\text{Environmental dose-rate (Gy/ka)}}$$

Initial studies of the application of OSL dating to sediments concentrated on depositional environments where the transport process ensured that sufficient exposure to sunlight to bleach the material had occurred, such as aeolian deposits (e.g. Huntley *et al.*, 1985; Stokes, 1992; Ollerhead *et al.*, 1994). In some other depositional settings (e.g. fluvial or colluvial), not every grain receives light exposure of a sufficient strength and/or duration to bleach fully the dose from the previous burial period (Fig 1.2b). If a residual trapped charge remains in the grains, the sediment is regarded as partially or incompletely bleached. Where partial bleaching is present, careful assessment of the distribution of D_e values is necessary to obtain the correct D_b. Simply taking some measure of the average from the D_e values for a partially bleached sample is not appropriate because the grains with residual trapped charge will cause overestimation of the age.

1.2.1 OSL dating of fluvial deposits

Murray *et al*. (1995) were the first to publish results from OSL dating of fluvial sediments. They found that whilst modern overbank deposits were well bleached, channel deposits contained partially bleached grains. These partially bleached grains caused overestimation in the D_e values, thereby preventing an accurate assessment of the D_b value for the well bleached component of the sample. Subsequently, measurement procedures and the equipment used for analysis have advanced to an extent that it is now feasible to automate the rapid collection of multiple D_e values for a sample. In particular, development of the single-aliquot regenerative-dose protocol (Murray and Roberts, 1998;

Murray and Wintle, 2000; Wintle and Murray, 2006) corrects for sensitivity change that may occur in quartz during OSL analysis, and the measurement equipment available can include laser systems that are capable of stimulating individual grains on a disc if necessary (e.g. Duller *et al.*, 1999a; 1999b). The ability to obtain a D_e value based on just one, or a few grains, enables the variation in bleaching of grains from a sample to be investigated, thus allowing a D_b value based on only the well bleached portion of the sample to be derived.

In recent years, a considerable amount of research has been undertaken to investigate the presence of partial bleaching in fluvial sediments. Duller (1994) identified two types of partial bleaching in sediments: 'type A' where the sediment is homogeneously bleached (i.e. all the grains are partially bleached to the same extent); and 'type B' where the sediment is heterogeneously bleached (i.e. each grain has been exposed to sunlight of differing strength and/or duration, causing varying amounts of residual trapped change to remain in the grains). Owing to the mechanisms of river transport, whereby each grain will follow a different path during transport, it is likely that grains in fluvial deposits will usually be heterogeneously bleached, thus causing scatter in the D_e values. Hence, careful analysis of the D_e distribution is necessary to obtain an appropriate D_b value.

The procedures developed to detect heterogeneous bleaching of samples (type B) can be divided into two groups of methods: distribution methods and signal analysis methods (Bailey, 2003a). The former group uses the shape and form of D_e distributions to classify a sample as heterogeneously bleached. It includes various statistical techniques that aim to calculate an appropriate D_b value from a heterogeneously bleached sediment (e.g. Olley *et al.*, 1998; Galbraith *et al.*, 1999; Lepper *et al.*, 2000; Fuchs and Lang, 2001; Thomsen *et al.*, 2003). The latter group relies on differential bleaching of the components that form the OSL signal to detect partial bleaching of the grains (e.g. Huntley *et al.*, 1985; Bailey *et al.*, 1997; Bailey, 2000; Bailey *et al.*, 2003; Singarayer *et al.*, 2005). At present, no consensus on which type of method is most suitable for detecting heterogeneous bleaching, or on how to calculate the appropriate D_b value, has been reached. The majority of published research into dating of fluvial sediments either uses the shape of the D_e distribution to detect

heterogeneous bleaching (e.g. Thomas *et al.*, 2005), or uses a comparison with an independent age to detect partial bleaching (e.g. Eitel *et al.*, 2006).

Although fluvial deposits might be expected to be heterogeneously bleached, a number of workers have reported evidence of well-bleached samples from fluvial environments. Murray and Olley (2002) presented a review where they collated results from various studies on fluvial samples which showed good correspondence between the OSL ages and those obtained from independent age control using methods such as radiocarbon, ^{210}Pb, tephra, and ^{230}Th/^{234}U flowstone dating (Fig. 1.4). A more specific review of fluvial samples by Jain *et al.* (2004) concluded that whilst heterogeneous bleaching of modern and young (<1 ka) samples may lead to errors in the estimate of D_b if not considered in analysis, the impact of heterogeneous bleaching is negligible for samples older than 1 ka. Consistent with the results from Jain *et al.* (2004), well-bleached deposits have been identified for fluvial samples over a large age range and include recent flood deposits on the Murrumbidgee River, Australia (Murray, 1996), and modern bedload samples from the Loire River, France (Stokes *et al.*, 2001). OSL dating of slackwater flood and overbank deposits from various

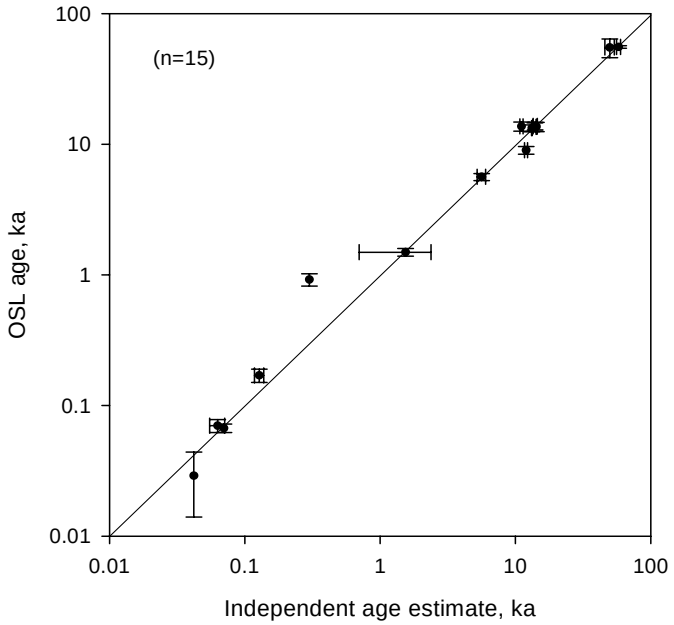

Figure 1.4: Age comparisons between the ages derived from OSL dating, and those derived from independent methods, for samples from fluvial deposits. From data in Murray and Olley (2002).

sites on the Luni River in the Thar Desert, India, resulted in ages that were in broad agreement with independent records of monsoonal rainfall over the last ~80 ka, leading the authors to conclude that the samples were well bleached (Kale *et al.*, 2000; Kar *et al.*, 2001). Extensive work on late Pleistocene deposits from the Mississippi and other braided rivers on the Atlantic Coastal Plain, USA, derived D_e distributions that were generally Gaussian in shape and tightly clustered, and thus appeared to be well bleached (Rittenour *et al.*, 2003; Leigh *et al.*, 2004; Rittenour *et al.*, 2005).

However, whilst well-bleached fluvial samples have been described, there is also evidence for heterogeneously-bleached samples, especially for younger deposits (< 1ka). Jain *et al.* (2004) recommend that all fluvial samples younger than 1 ka should be checked for heterogeneous bleaching. In the literature, heterogeneously-bleached, young fluvial samples have been identified in studies looking at various different depositional environments. Young glaciofluvial samples (<0.2 ka) from the Bhagirathi River, India, were found to be very poorly bleached by Rhodes and Pownall (1994). Murray (1996) identified well-bleached samples from the Murrumbidgee River, Australia, but Olley *et al.* (1998) found age overestimation occurred when a modern point bar and a young flood deposit were analysed owing to incomplete bleaching. Evidence of poor bleaching was also found on a scroll-bar deposit from the Colorado River, Texas, where a residual age between 0.1-0.3 ka was obtained for the modern deposit (Stokes *et al.*, 2001). More recently, incomplete bleaching was identified in young oxbow samples (<1 ka) from three lowland river systems in Papua New Guinea and the USA (Rowland *et al.*, 2005).

Contrary to the suggestion of Jain *et al.* (2004), heterogeneous bleaching has also been found in older fluvial deposits (>1 ka). The OSL ages for fluvial samples from a palaeochannel of the River Seine, France, were found to be 40% greater than the age of 13 ka derived from ^{14}C dating (Folz *et al.*, 2001). Partial bleaching was suggested as the cause for the discrepancy between the two dating methods, despite the D_e distributions being tightly clustered and therefore suggesting that the samples were well bleached. Comparison between results from single-grain and small aliquot OSL dating of fluvial deposits from southern India identified thirteen out of nineteen samples (age

range <0.1-3 ka) as being poorly bleached (Thomas *et al.*, 2005). Partial bleaching has also been found in early Holocene and late Pleistocene Namibian fluvial samples, including the Homeb silt sands, deposited between ~6 and 20 ka (Brook *et al.*, 2006; Srivastava *et al.*, 2006), and fluvial sands from the Hoanib catchment (Eitel *et al.*, 2006).

Thus the picture that emerges from previous studies is that heterogeneous bleaching may be present in fluvial samples from various depositional settings, and in both relatively young (Holocene) and old (Pleistocene) samples. Therefore, fluvial deposits should be assessed for heterogeneous bleaching on a sample-by-sample basis.

1.3 PROCESSES OF CHANNEL CHANGE ON THE KLIP RIVER AND THE SCHOONSPRUIT

Some changes in channel form (e.g. lateral migration, meander cutoff, and avulsion) can either occur as a process inherent to the river activity (i.e. autogenically controlled), or as a response to externally-driven changes (i.e. allogenically controlled) such as modifications of discharge and sediment supply resulting from climate change, tectonics, or human activities (Tooth and Nanson, 2004). Other processes (e.g. incision) tend to occur only in response to allogenic controls. Schumm (2005) identified the variables leading to different types of channel change; those related to the processes of channel change relevant to this study are detailed in Table 1.1. The column headed "time" represents autogenic change in the river system, "+" indicates an increase and "–" indicates a decrease in the variable concerned.

Table 1.1: Variables affecting processes of channel change. Adapted from Schumm (2005).

		Variables					
		Discharge		Sediment load		Baselevel	
Channel response	Time	+	-	+	-	rise	fall
Incision		✓			✓		✓
Lateral migration	✓	✓					
Meander cutoff	✓	✓		✓		✓	✓
Avulsion	✓	✓		✓		✓	

1.3.1 Lateral migration

Lateral migration is the movement of a river across the floodplain. Along meandering rivers, lateral migration results from the erosion of the concave (outer) bank and concomitant deposition on the convex (inner) bank (Hickin and Nanson, 1984). Aerial photographs of the Klip River show the presence of arcuate (curved) bands on the inside of many of the currently active and former meanders. These suggest that the floodplain topography is characterised by swales and ridges (scroll bars) formed during lateral migration.

1.3.1.1 Controls and processes of lateral migration

Lateral meander migration can involve various styles of bend deformation (e.g. translation, expansion; Fig. 1.5) and is associated with various morphological and sedimentary features. In their genetic classification of floodplains, Nanson and Croke (1992) associated meandering rivers with medium-energy, non-cohesive floodplains; lateral migration of the meandering rivers results in either non-scrolled floodplains, or scrolled floodplains with a topography characterised by swales and ridges (scroll bars). In the latter case, Nanson and Croke (1992) identified three mechanisms of scroll bar formation. First, migration of dunes or bars out of the main river channel and onto point bars, which are subsequently

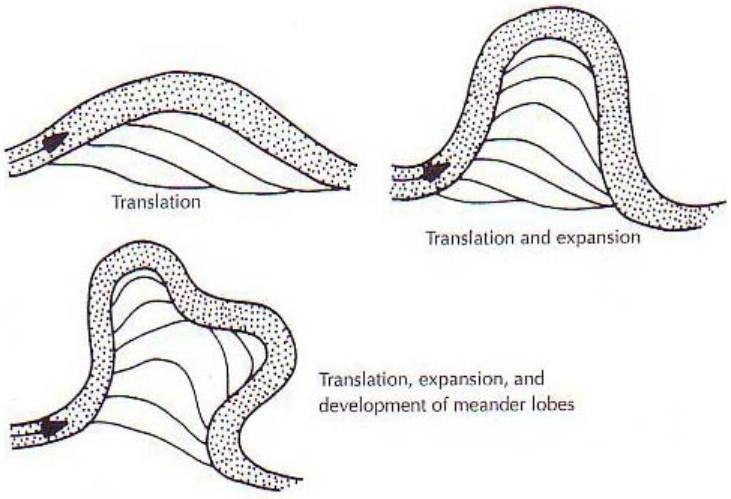

Figure 1.5: Different styles of meander migration, the lines on the inner bends represent scroll bars that provide evidence of the nature of meander migration, and can be dated using OSL. From Bridge (2003).

topped with overbank deposits (Sundborg, 1956; Nilsson and Martvall, 1972; Jackson II, 1976). Second, deposition of suspended sediment within zones of flow separation over point bars (Nanson, 1980) or around stranded debris (Nanson, 1981), initiates scroll bars that subsequently grow in both upstream and downstream directions. Third, where coarse grained point bars are present, a chute channel can form between the convex bank and adjacent point bar (McGowan and Garder, 1970) and as the meander migrates, the ridge and swale topography is formed by sequential development of these chute channels. An additional method of scroll-bar formation was suggested by Hickin (1974). He proposed that weakly consolidated material from the concave bank is eroded during low frequency, high flows, and transported into a zone of low shear stress and low velocity at the convex bank where it is deposited as a bar. When the river level falls, this bar remains exposed as a ridge which is colonised by vegetation and forms a river bank. In situations where the hydrological regime consists of seasonal low and high flows, this method of formation results in annual scroll bars. It is not known which formation mechanism is the most widespread, but the formation of scroll-bar sequences is generally attributed to discontinuous erosion and deposition, whether owing to annual fluctuations in the water level (e.g. Hickin, 1974) or otherwise (e.g. Nanson and Hickin, 1983; Bridge, 2003). Irrespective of the formation mechanism, scroll bars provide evidence of lateral migration and by dating the associated sediment, they can be used to estimate the average rate of lateral migration.

Brooks (2003) modified a theory proposed by Hickin and Nanson (1984), and stated that the rate of channel migration (M) is likely to vary according to the following relationship:

$$M = f(\omega, b, G, h, Y_b)$$

where ω is the stream power per unit bed area, b is an expression of the planform geometry (described by r/w, where r is the radius of the meander curvature and w is the channel width), G is the rate of sediment supply, h is the bank height, and Y_b is the erosional resistance of the outer bank material. Stated another way, for meander bends of simple geometry, and assuming that

factors such as slope, channel width, sediment supply, bank height, bank vegetation and boundary material remain roughly constant over time, discharge and planform geometry (r/w ratio) are the primary controls on lateral migration rate (Hickin and Nanson, 1975; 1984). Discharge is a surrogate for the intensity of boundary shear stress and flow velocity and a key control on ω, whilst the r/w ratio influences flow resistance and therefore erosive potential. A higher discharge rate results in an increased lateral migration rate, whilst r/w exerts a more complex control. For instance, from studies on meander bends on the Beatton River, Canada, Hickin and Nanson (1975) found that during the initial development of a channel bend (high r/w ratio) the rate of lateral migration is slow, but as the bend develops and r/w approaches a value between 2.0 and 3.0, the migration rate increases to a maximum before rapidly decreasing as the bend tightens and r/w decreases further (Fig. 1.6). Measurements on 189 bends from 21 different rivers in Western Canada by Hickin and Nanson (1984) found considerable scatter in the migration rates, although the trend still showed a peak in the migration rates at r/w ~3. Analysis of 18 of these rivers suggested

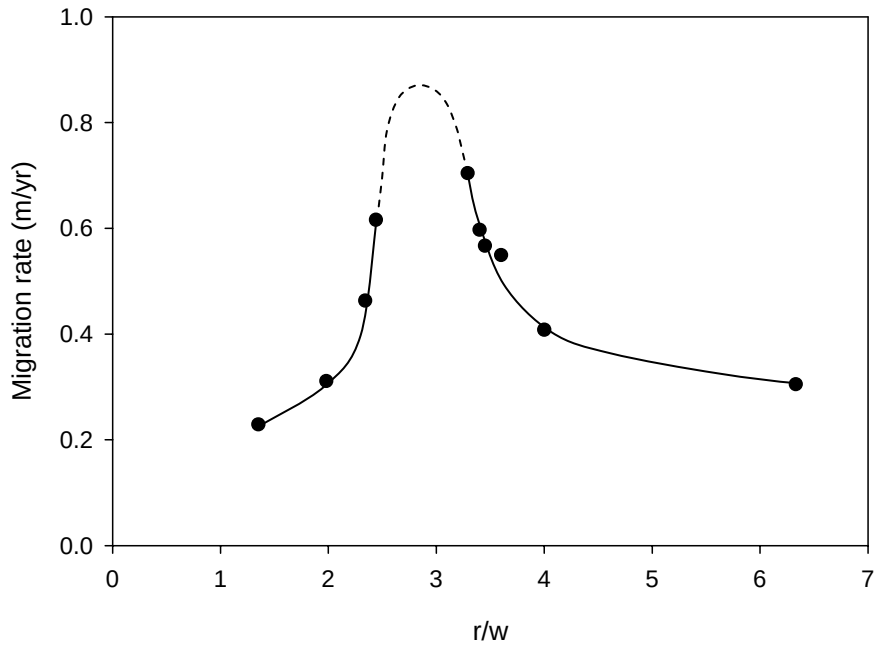

Figure 1.6: The relation of the average lateral migration rate to the ratio of radius of curvature (r) to the channel width (w), for 10 survey sites on the Beatton River, based on data from Hickin and Nanson (1975). The absence of data points with 2.5 < r/w < 3.2 was attributed to the influence of rapid migration in altering the pattern of the bend to a tighter or more open curvature.

that almost 70% of the scatter could be explained by the differences in the river scale, particularly with respect to the discharge, channel width, and coarseness of the sediment at the base of the outer bank (Nanson and Hickin, 1986). By contrast, peak lateral migration rates along meanders on the River Dane, England (Hooke, 1987) and the lower Mississippi River (Hudson and Kesel, 2000) occurred when r/w was ~1.0 and ~1.5, respectively. In both studies, at least 100 meander bends were examined. The lower r/w ratio associated with the maximum lateral migration rates was attributed to the complex suite of floodplain deposits present in these river valleys. Instead of the relatively homogeneous floodplain sediments typical of the Canadian rivers studied by Hickin and Nanson (1975; 1984), the lower Mississippi floodplain has older geomorphic units and clay plugs of varying resistance present which influence channel migration and adjustment. These results led Hudson and Kesel (2000) to propose that the relationship between r/w and the lateral migration rate may exhibit two patterns: one typical of homogeneous floodplains, and another typical of floodplains that contain varying deposits. In addition, other aspects of bend geometry have also been proposed as affecting the migration rate; for instance, Furbish (1988; 1991) showed that as well as meander curvature, the bend length influenced the rate of migration.

1.3.1.2 Rates of lateral migration

Central to the discussion on the controls of lateral migration rates is an ability to establish absolute values for these rates. Lateral migration rates can often only be established indirectly, either through comparison of sequential maps or aerial photography, or by using dendrochronology (examples detailed in Table 1.2). Direct dating of lateral meander migration is more difficult as sediments from scroll bars or other floodplain deposits often yield insufficient material for extensive dating by radiocarbon, but there have been a few instances where sufficient material has been found enabling investigations into lateral migration rates. From radiocarbon dating of floodplain and bank samples, Brakenridge (1985) calculated rates of lateral migration through bedrock for the Duck River, Tennessee, of 0.06-0.19 m/a since 6.4 ka BP. Similarly, Brooks (2003) performed a comprehensive radiocarbon dating study on the Red River,

Manitoba. 24 samples were taken for radiocarbon dating from two meander bends, and the results gave an average lateral migration rate of 0.04 m/a.

From the results for the studies using both indirect and direct methods of establishing lateral migration rates, one can see that the rate of meander bend migration varies considerably between different rivers. In general, larger rivers and those located in the tropics, have higher rates of channel migration (up to hundreds of metres in a year) than smaller rivers in temperate regions which often migrate only a few metres per year (Knighton, 1998). Even within a single river system, lateral migration rates on different meander bends can vary considerably. For instance, Hudson and Kesel (2000) noted that meander migration rates on the lower Mississippi are highly variable (range 1-123 m/a), with some bends that experienced very high migration rates located adjacent to other bends with very low migration rates. They attributed this variability to the strong influence of local controls on the rates of migration.

Table 1.2: Details of studies where indirect methods have been used to obtain rates of lateral migration.

Study	Location	Method	Rate of lateral migration (m/a)
Crickmay (1960)	Pembina River, Canada	Aerial photographs and maps	0.3
Hickin and Nanson (1975)	Beatton River, Canada	Dendrochronology	0.48
Jackson II (1976)	lower Wabash River, Illinois	Maps	0-10
Dietrich *et al.* (1999)	Fly River, Papua New Guinea	Aerial photographs and maps	~5
Hudson and Kesel (2000)	Mississippi River	Maps	<123
Gilvear *et al.* (2000)	Luangwa River, Zambia	Aerial photographs and field-based studies	<33
Tooth and McCarthy (2004)	Okavango River, Panhandle region of the Okavango delta, Botswana	Aerial photographs	<0.5

1.3.2 Meander cutoff

A cutoff occurs when the river breaks through the neck of a meander, shortening the active channel and leaving the abandoned meander as an oxbow. Numerous meander cutoffs can be identified on both maps and aerial photographs of the Klip River and the Schoonspruit. The cutoffs are generally well preserved in form, and their association with either the modern channel or a palaeochannel reach can be determined.

1.3.2.1 Controls and processes of meander cutoff

Although the importance of cutoffs has long been recognised, views on the controls and processes of cutoff formation still differ (Hooke, 1997). Cutoffs are generally thought to be a response to excessive sinuosity where the channel gradient is too low to transport the sediment load (Knighton, 1998), because cutoffs increase the gradient of the river and thereby allow it to transport more sediment locally. For instance, four cutoffs on the rivers Bollin and Dane increased the gradient by an average of 2.7 times (Hooke, 1995) and artificial cutoffs have also been used on the lower Mississippi to increase the gradient and reduce flood heights, resulting in an average increase in gradient of 12 % but with local increases as much as 2000 % (Winkley, 1982). Other explanations for the cause of cutoffs have also been proposed, such as inhomogeneities in bank material (Friedkin, 1945), and continuous evolution and inherent instability associated with nonlinear meander behaviour (Stolum, 1996).

Two basic styles of cutoff can be identified: chute cutoffs and neck cutoffs (Fig. 1.7). For instance, Lewis and Lewin (1983) studied alluvial cutoffs along Welsh rivers. Following Tower (1904), they found that neck cutoffs and multi-loop cutoffs (the latter referred to as avulsions in this work, see below) occur more commonly on low gradient reaches, and chute cutoffs occur more commonly on high gradient reaches.

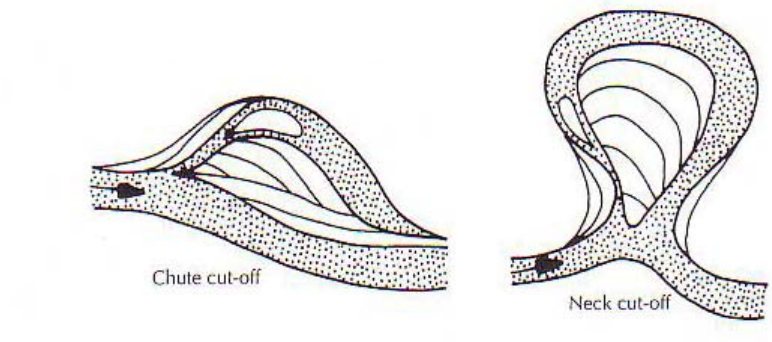

Figure 1.7: Different styles of meander cutoff. From Bridge (2003).

1.3.2.2 Ages of cutoffs

Various dating methods have been used to obtain the ages of oxbows. For recently abandoned meanders, dendrochronology has been used to date oxbow lakes along the Gulf Coast region of the southern USA (Shankman, 1991). To derive the timing of oxbow formation, radiocarbon dating has been applied to wood and organic material from oxbows on North Fish Creek, Wisconsin, USA (Fitzpatrick *et al.*, 1999) and wood fragments in cores from an oxbow lake in Mississippi, USA (Davidson *et al.*, 2004). OSL dating has also been used successfully to establish the timing of oxbow formation on the lower Mississippi River, Birch Creek, Alaska, and the Middle Fly River, Papua New Guinea (Rowland *et al.*, 2005). The results for five out of the six samples from the Lower Mississippi River gave OSL ages <1 ka, that were consistent with the expected ages estimated from historical documentation, indicating that it is a suitable method for dating the formation of oxbows along this river.

1.3.3 Avulsion

Avulsion is defined as a channel belt shifting abruptly from one location on the floodplain to another in order to follow a steeper gradient (Bridge, 2003) (Fig 1.8). Aerial photographs from the Klip River show evidence of a number of palaeochannels over a short (~5 km) reach. The palaeochannels are clearly defined, continuous, and run subparallel to the modern river, indicating that the river has undergone several avulsions in the past.

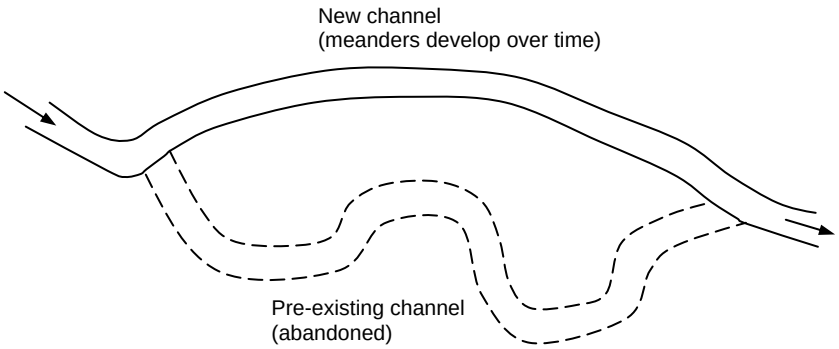

Figure 1.8: Schematic of avulsion, showing abandonment of a section of channel.

1.3.3.1 Controls and processes of avulsion

Avulsions can occur both autogenically (e.g. in response to development of excessive channel sinuosity) and in response to allogenic variations such as increases in discharge, sediment load, and baselevel rise. The scale of avulsions varies considerably, both spatially and temporally. Avulsions can affect varying lengths of channel, from a few tens of metres such as on the Rio Grande, Colorado (Jones and Harper, 1998), to many kilometres such as on the lower Mississippi (Fisk, 1944). They can also cause the river to shift over varying distances from only a few tens or hundreds of metres to many kilometres; for instance, the Po River in Italy has moved 50 km northwards in the past 3000 years (Nelson, 1970), and the Yellow River, China, has shifted 800 km in a series of avulsions over the last 4200 years (Mackey and Bridge, 1995). The time for completion of an avulsion – from initiation of a new channel reach to complete abandonment of the old channel reach – is also highly variable. For instance, the Yellow River has cut new channels in one day (Qian, 1990), whereas avulsions on the Rhine-Meuse delta, the Netherlands, have taken up to 1250 years to complete (Stouthamer and Berendsen, 2001).

Although avulsions are thought to be primarily features of aggrading floodplains (Makaske, 2001; Slingerland and Smith, 2004), there is still ongoing debate about the link between the aggradation rate and parameters of avulsion such as the avulsion frequency, interavulsion period and avulsion rate (Törnqvist, 1994; Tooth *et al.*, submitted). Following initial alluvial architecture models which

decoupled avulsion frequency from aggradation rate (e.g. Allen, 1978; Leeder, 1978; Bridge and Leeder, 1979), later flume experiments, theoretical studies and revised alluvial architecture models suggest a positive relationship between the frequency of avulsions and aggradation rate (e.g. Bryant *et al.*, 1995; Mackey and Bridge, 1995; Slingerland and Smith, 1998; Törnqvist and Bridge, 2002). Field studies from moderately to rapidly aggrading settings (aggradation rates >1 mm/a) tend to support this proposed positive relationship (e.g. Törnqvist, 1994; Ethridge *et al.*, 1999; Stouthamer and Berendsen, 2001), but it has also been found that infrequent avulsions can occur on river systems in very slowly or non-aggrading settings (e.g. Nanson and Knighton, 1996; Gibling *et al*., 1998).

Schumm (2005; following Jones and Schumm, 1999) placed the processes and events that can lead to avulsions into four groups. The first two groups involve an increase in the S_a/S_e ratio, where S_a is the slope of the potential avulsion course and S_e is the slope of the existing channel. Group 1 covers processes that are caused by a decrease in S_e, and thus a decrease in the capacity of the channel to transport sediment and discharge. These include changes such as sinuosity increase, baselevel rise or tectonic uplift (reduced gradient), and delta growth (channel lengthening). Group 2 covers processes which increase S_a with no change in the capacity of the existing channel to transport sediment and discharge. These include changes such as levee or alluvial ridge growth, alluvial fan and delta growth, and lateral tilting from tectonism. Group 3 covers processes which involve no change in the S_a/S_e ratio, but the capacity of the channel to transport sediment and discharge is still reduced. This can occur through changes such as variation in flood peak discharge, increased sediment load, vegetation encroachment, and log or ice jams. Group 4 covers avulsions which are not caused by a change in the S_a/S_e ratio, or the capacity of the channel to transport sediment and discharge. This group includes processes such as the formation of animal trails or river capture that results in diversion of flow into adjacent channels.

1.3.3.2 Timing and frequency of avulsion

River systems can be influenced by many factors and thus the cause of avulsions on a particular river is likely to be complex and variable through time. To understand fully the controls of avulsions, chronologies of avulsion events are needed to determine the possible influence of allogenic controls, such as variations in climate or baselevel. Most studies that have investigated the timing and frequency of avulsions during the Holocene have been based on radiocarbon dating, but historical records and aerial photographs have been used to constrain the timing of more recent avulsions.

The most recent work on the numerous avulsions of the Rhine-Meuse delta by Stouthamer and Berendsen (2001) used radiocarbon dates to determine the frequency of avulsions and identify the main controlling processes. They found that the avulsion frequency varied between 0.85 and 2.43 avulsions per 0.1 cal a during the last 8.0 cal ka. The maximum avulsion frequency of 2.43 per 0.1 cal ka occurred during a period of rapid sea-level rise between 8.0 and 7.3 cal ka. Subsequent slowing of the rate of sea-level rise lowered the avulsion frequency to 0.85 avulsions per 0.1 cal ka, prior to an increase in discharge and/or an increase in channel sedimentation at 3200 cal a that resulted in 1.89 avulsions per 0.1 cal ka. In addition to the different avulsion frequencies, the duration of avulsion events (avulsion rate) varied between <0.20 to 1.25 cal ka.

Radiocarbon dating on the anastomosing upper Columbia River in Canada revealed nine avulsions over the past 3.0 cal ka (average of 3 avulsions per 1 cal ka) (Makaske *et al.*, 2002). The length of activity of any given channel (channel lifetime) ranged between 0.8 and 3.0 cal ka, variability which was attributed to randomly occurring log jams being the primary cause of avulsion on this system. On the Saskatchewan River, radiocarbon dating identified nine principal avulsions that occurred since 5.4 ka BP (Morozova and Smith, 1999). Some major channel belts were active for up to 2.4 ka, indicating that at times, multiple channel belts coexisted.

On a more recent timescale, dam construction on the Niobrara River, Nebraska, in the early 1950s caused three avulsions between 1988 and 1995 (Ethridge *et*

al., 1999). These avulsions were attributed to a baselevel rise of 2.9 m, which led to aggradation and superelevation of the channel belt, with the final trigger for the avulsions being provided by ice jam events during spring break-up, and bank erosion.

Whilst not a study of avulsion *sensu stricto*, Banerjee *et al.* (2002) used OSL dating to derive ages for palaeochannel sands from the Riverine Plain, southeastern Australia, thereby demonstrating the applicability of OSL dating to palaeochannel deposits.

1.3.4 Incision

Incision (or degradation) is the lowering of the channel bed by erosion. In stark contrast to the Klip River, where lateral migration, cutoff formation and avulsion are the dominant channel change mechanisms, aerial photographs and field investigations of the Schoonspruit indicate that it is currently undergoing incision. The river has incised into bedrock along its formerly meandering course, and in some locations dongas have formed along the channel banks.

1.3.4.1 Controls and processes of incision

During incision, the channel width to depth ratio often decreases, owing to preferential erosion of the bed, but bank erosion and widening of the channel may occur concurrently (Fig 1.9a-c). Schumm (2005) grouped the causes of incision into six categories: 1) geologic (e.g. uplift, subsidence); 2) geomorphic (e.g. stream capture, baselevel lowering, meander cutoffs); 3) climatic (e.g. changes in vegetation cover from increased/decreased rainfall); 4) hydrologic (e.g. increased discharge, increased peak discharge); 5) animals (e.g. overgrazing causing reduction in vegetation cover, tracking leading to decreases in infiltration rates and therefore increasing runoff); and 6) human activity (e.g. dam construction, sediment diversion). Incision associated with the processes in groups 1 to 4 generally occurs over long time scales (up to thousands of years), whereas those processes in groups 5 and 6 can cause more rapid incision on relatively short timescales (tens of years). Once incision along a channel has commenced, it commonly progresses through several stages until stabilisation occurs (Fig. 1.9). The style and magnitude of incision

is generally controlled by the type of sediment in the alluvial valley; whilst channels incising into sandy sediments tend to widen preferentially and deepen less, those incising into cohesive sediments such as clay and silts tend to deepen preferentially (Schumm, 2005).

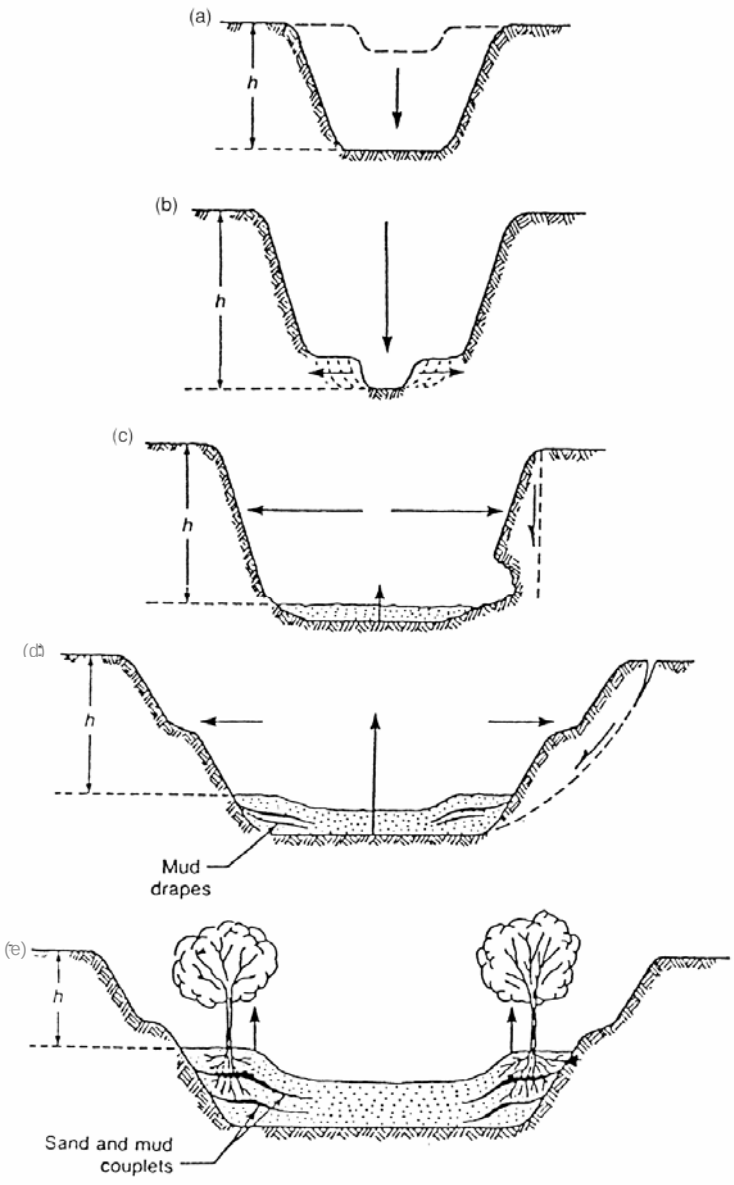

Figure 1.9: Evolution of an incised channel. Stages include initial incision (a and b), widening (c and d), and eventual stability (e). The dashed cross-section in a) represents the initial channel. From Schumm (2005).

1.3.4.2 Rates of incision

Incision can be caused by a wide range of processes, and thus the rate of incision varies considerably between different rivers. Dating techniques such as radiocarbon and optically stimulated luminescence have been used to derive rates of incision that ranged from <1 mm/a up to ~10 mm/a.

Brooks (2003) used radiocarbon dating to determine Holocene rates of incision for the Red River, Canada. The average channel incision since 8.1 cal ka BP has been <1 mm/a. OSL dating of scroll-bar plains on the Sabarmati River, India, demonstrated that ~30 m of incision had occurred in the period between 12 ka and 4.5 ka, giving an average incision rate of >4 mm/a (Srivastava ***et al.***, 2001). Srivastava ***et al.*** (2003) also used OSL dating to constrain the formation of terraces on the River Ganga, India, with the results indicating that ~20 m of incision occurred between <6 ka and 4 ka; which equates to an average incision rate of ~10 mm/a.

1.4 RESEARCH OBJECTIVES

The overall aim of this thesis is to derive chronologies of late Quaternary channel change on the Klip River and the Schoonspruit. This will be achieved by pursuing six specific objectives. Objectives 1-4 are concerned with developing the application of OSL dating to fluvial samples to overcome problems with partial bleaching. Objectives 5-6 relate to using the OSL ages to establish the chronology and controls of channel change. The objectives are:

1) To assess whether fluvial samples along these systems are partially bleached, and if so, to determine the degree of partial bleaching;

2) To determine the number of accurate D_e values that is required to ensure a reproducible D_e distribution for each sample, and to determine which statistical model is the most appropriate to calculate the D_b value;

3) To assess the reproducibility of OSL dating on sediments from the same depositional units over a range of spatial scales;

4) To assess the accuracy of OSL dating on fluvial sediments by comparison with independent age control;

5) To derive the rates and absolute timing of channel change processes (lateral migration, meander cutoff, avulsion and incision) on the Klip River and Schoonspruit;

6) To identify the controlling factors of channel change (e.g. autogenic and/or allogenic), particularly the degree of correspondence with episodes of climatic change.

1.5 STRUCTURE OF THESIS

In line with the objectives specified above, the main body of this work will be concerned with developing the successful application of OSL dating to fluvial samples. In Chapter 2, background information relevant to the study, such as South African physiography and climate change since ~50 ka, are reviewed. The Klip River and Schoonspruit field sites, and the sampling methods, are also be detailed. Chapter 3 covers the derivation of the environmental dose-rate for each sample, giving one half of the OSL age equation. The following two chapters (4 and 5) detail investigations into the OSL signal, and the use of the OSL signal in obtaining a D_e value for each aliquot. Chapter 6 details investigations into the presence of partial bleaching in the samples, looking at both how to detect heterogeneous bleaching and how to obtain an appropriate D_b value for a heterogeneously-bleached sample, thus giving the second half of the OSL age equation. The calculation of the OSL ages and the rates of the channel change processes are covered in Chapter 7. This chapter also includes an interpretation of the rates obtained, particularly with respect to whether they indicate that the controlling factors of channel change are autogenic or allogenic. Chapter 8 summarises the main findings and considers future research priorities.

CHAPTER 2: FIELD SITES AND SAMPLE DETAILS, AND A REVIEW OF SOUTH AFRICAN RECORDS OF LATE QUATERNARY CLIMATE CHANGE

2.1 INTRODUCTION

In this study, samples were taken for OSL dating from two river systems in South Africa. The majority were taken from the Klip River, where the sampling strategy was designed to determine the rates of lateral migration, cutoff formation and avulsion. Further samples were taken from the Schoonspruit to attempt to obtain rates of incision. On the Klip River, sediment was also collected for radiocarbon dating at some of the sampling sites to provide independent age control. In this chapter, the regional setting of the rivers is discussed, and sampling details covered.

The present-day climate of South Africa is outlined in this chapter and evidence for the palaeoclimates of South Africa through the late Quaternary is described. Long-term, high resolution records of palaeoclimate are rare in the Southern Hemisphere and particularly in South Africa, but an outline is given of the general picture of climatic change over the last ~50 ka in the region where the sample sites are located.

2.2 SOUTH AFRICAN PHYSIOGRAPHY

The Republic of South Africa is located on the southernmost part of the African continent, bordered by the Atlantic Ocean in the west and the Indian Ocean on the east (Fig. 1.1). Its physiography is dominated by three main regions (Fig. 1.1): an extensive high, interior plateau (with peaks above 3000 m altitude in the south-east and declining westwards to <1000 m); an escarpment following the coast at a variable distance (<120 km) inland, of which the Drakensberg forms a major part; and lower lying piedmont and coastal areas. Both the varied topography and the proximity to two major oceans cause the climate of South Africa to vary regionally and to be strongly seasonal.

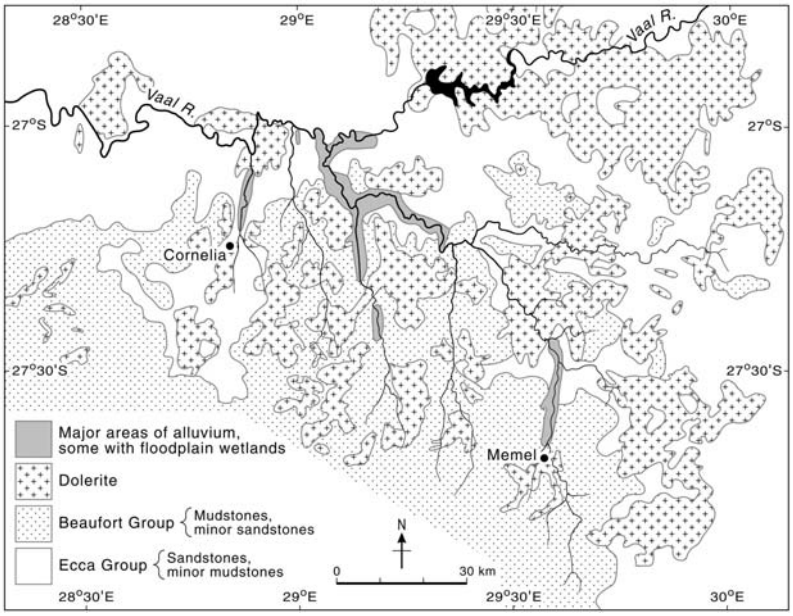

Figure 2.1: Geology of the study region, showing how wide valleys and extensive alluvium with floodplain wetlands occur where the Karoo Supergroup sedimentary rocks crop out, and narrow valleys and limited alluvium occurs where dolerite sills and dykes crop out. From Tooth *et al.* (2004).

South Africa forms part of the southern African subcontinent, which has behaved as a single tectonic entity since the break-up of Gondwana in the Cretaceous (McCarthy and Hancox, 2000). Following the separation of Africa from India and South America (Press and Siever, 1998), epeirogenic uplift of the subcontinent occurred, and although the timings and mechanisms of this process are still under debate (e.g. Partridge and Maud, 1987; Gilchrist and Summerfield, 1990; Burke, 1996; de Wit, 1999), it has been argued that the south-eastern part of the subcontinent was subjected to greater uplift than the western part (Partridge and Maud, 1987). The high interior plateau of southern Africa, known in the eastern and central parts as the Highveld, is underlain predominantly by late Carboniferous and mid-Jurassic Karoo Supergroup sedimentary rocks (Smith *et al.*, 1993) that have been extensively intruded by dolerite sills and dykes. Since the late Mesozoic, therefore, the rivers on the subcontinent have been downcutting through an elevated region underlain by lithologies of variable resistance to erosion (Tooth *et al.*, 2002). Rock commonly crops out in river channel beds and banks, although alluvial veneers are widespread.

2.2.1 Geological control on rivers

The variable geology of the Highveld, with its extensive dolerite intrusions in essentially flat-lying or gently dipping sedimentary rocks (Fig. 2.1), has a strong influence on the rivers in the region (Tooth *et al.*, 2002; 2004; Marren *et al.*, in press). Where the river beds are grounded on the weakly-cemented sedimentary rocks (e.g. sandstones, shales), incision can occur with relative ease. In contrast, the dolerite intrusions (sills and dykes) are much more resistant, with the river courses being guided along joints and fractures. These hard dolerite sills and dykes form local baselevels for the rivers, retarding vertical erosion in the upstream reaches underlain by the less resistant sedimentary rocks. Eventually, however, the dolerite barrier will be breached by erosion, which lowers the baselevel of the river and allows a knickpoint to retreat upstream.

In schematic terms, therefore, the geomorphic evolution of the rivers on the Highveld can be divided into three main phases of development (Tooth *et al.*, 2004), as shown in Figure 2.2:

A) Initially, where low sinuosity rivers flow over a gently sloping sedimentary surface, igneous intrusions are not present in the uppermost levels of the sedimentary layers.

B) Over time, the sedimentary layers are removed by erosion and the dolerite sills and dykes are exposed. These form local baselevels that retard vertical erosion in the reaches upstream. In these latter reaches, the river undergoes extensive lateral migration and forms meanders (Stage 1, Figure 2.2b). The increased sinuosity helps to dissipate the excess erosional energy (Tooth *et al.*, 2002). Lateral migration results in wide river valleys with low gradients both parallel and perpendicular to the channel with numerous cutoff events creating oxbow lakes, and periodic avulsions leading to channel abandonment. In some areas, extensive floodplain wetlands form in association with these processes.

C) Eventually the dolerite barriers are breached (partially or wholly) by the river, and knickpoint retreat leads to channel incision in the upstream reach (Stages 2 and 3, Figure 2.2c). When the river starts to incise, overbank flooding becomes

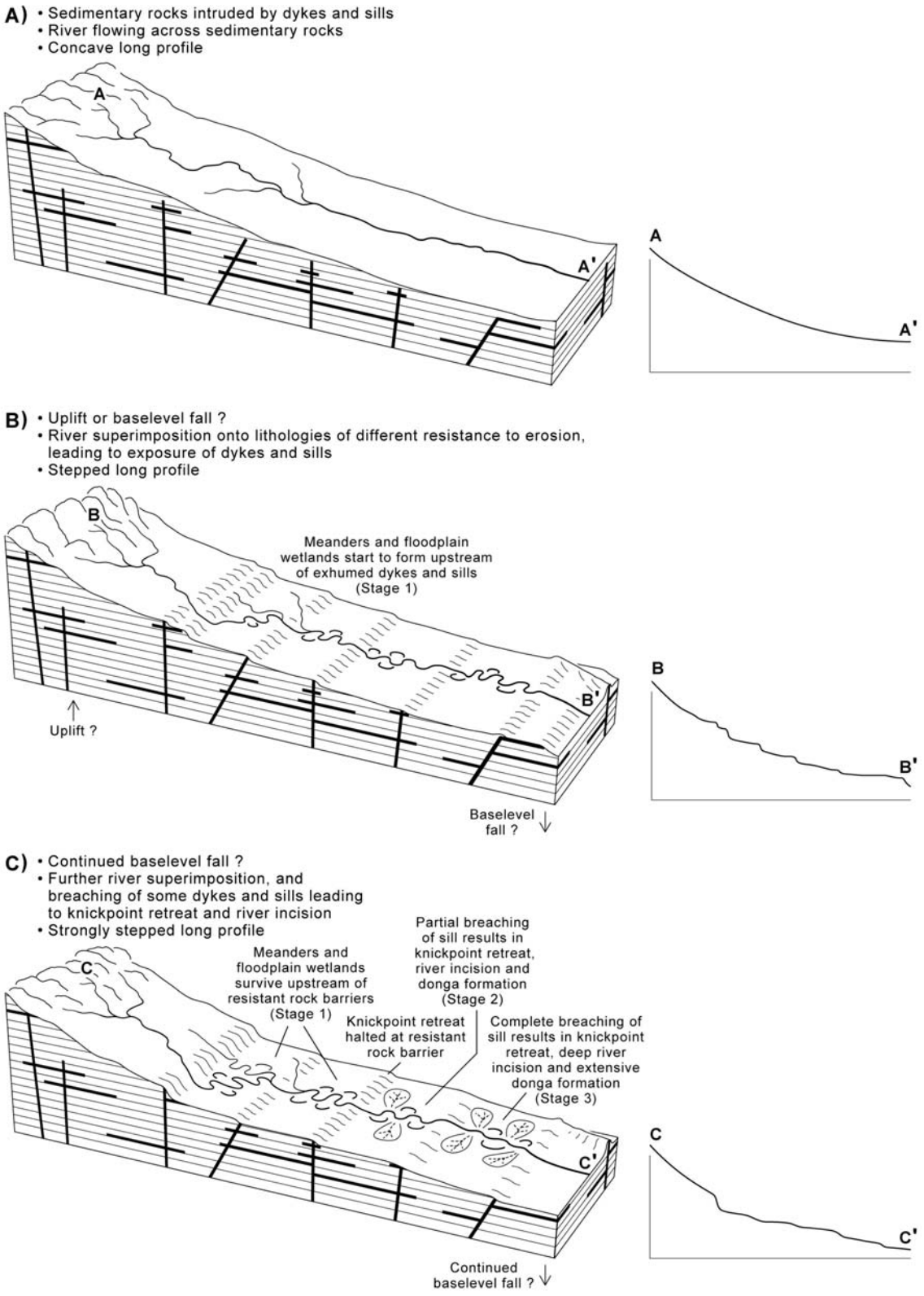

Figure 2.2: Phases A – C showing the long-term evolution of a Highveld River, and stages 1 – 3 of the rivers development following superimposition onto exhumed dolerite sills and dykes. From Tooth *et al.* (2004).

less frequent, and any associated wetlands start to desiccate and become abandoned. Dongas (gullies) also start to form in alluvial fills, forming high density dendritic networks of small channels which merge downslope to form larger, flat-floored channels (Tooth *et al.*, 2004). The river incises along the path it was following prior to breaching of the dolerite, until another dolerite intrusion, or a more resistant part of the same intrusion, is encountered lower in the crust, at which point the baselevel will stabilise again.

2.3 THE KLIP RIVER

The Klip River is typical of many rivers on the Highveld, with extensive floodplain wetlands in some reaches upstream of dolerite intrusions. It arises at an elevation of ~1950 m in the eastern Free State and drains a total catchment area of 5129 km^2 (Tooth *et al.*, 2002; 2004) before joining the Vaal River (Fig. 2.3). The study reach is located near the town of Memel (Fig. 2.3). Mean annual precipitation is ~1200 mm in the headwaters and decreases to ~700 mm in the study reach, with the majority falling during the summer months (Tooth *et al.*, 2002). The bedload of the Klip River is predominantly sand and minor gravel, with suspended sediment concentrations <1.5 g/l during high summer flows (Tooth *et al.*, 2002).

The present form of the river with intense meandering, associated wetlands, and numerous oxbow lakes (Fig. 2.4) places the river in Stage 1 of the sequence of river development (Fig. 2.2c). Where the river has been superimposed upon dolerite sills or dykes, the incised valleys are narrow (<200 m) and channel sinuosity is low (<1.35), but where the river is grounded on sandstone/shale, valleys are wide (up to 1500 m) and the channel highly sinuous (>1.64) (Tooth *et al.*, 2002). The marked difference in river character in the transition between the different lithologies can be seen in Figures 2.5 and 2.6a. Within the sandstone/shale valleys, extensive floodplain wetlands are commonly present, with the largest expanse (>30 km^2) developed in the study reach. Many of the wetlands are within the Seekoeivlei Nature Reserve, which is a designated Ramsar site protected under international agreement. During the wet summer months, flooding is extensive in the reach (Fig. 2.4a), but

during the dry winter season only the modern channel contains flow, with standing water present in some of the palaeochannels and oxbows (Fig. 2.4b). At the ~5 km long Seekoeivlei site, palaeochannels and oxbows could be located in aerial photographs (Fig. 2.7a, b), and on the ground where they appear as distinct depressions (Fig. 2.7c). The depressions formed by the palaeochannels and oxbows have been infilled to differing degrees; this allowed a relative age order based on the extent of infilling to be obtained for the palaeochannels. The extent of infilling varied considerably between parallel reaches, suggesting that they were not active concurrently, and indicating that in the past this reach of the Klip River has been an avulsive system rather than a braided river.

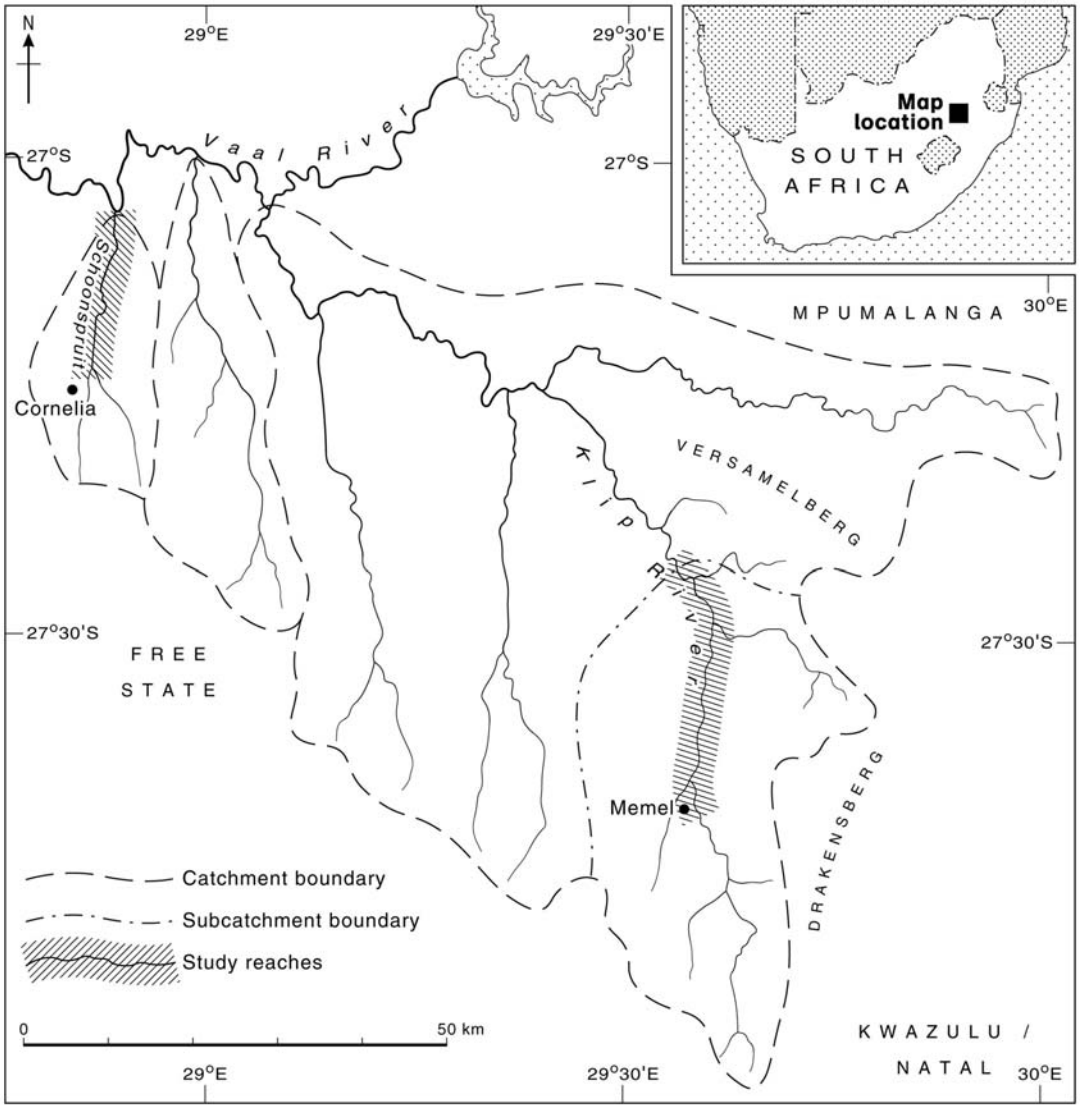

Figure 2.3: Catchment areas of the Klip River and Schoonspruit. Inset shows the location of the study region in South Africa. Adapted from Tooth *et al.* (2004).

a)

b)

Figure 2.4: The Klip River during a) the wet summer season (flow direction to the top) (photo: S. Tooth) and b) the dry winter (flow direction to the upper right) (photo: T.S. McCarthy). In b) the modern channel is indicated in addition to two palaeochannels which have been placed in relative age order based on the extent of infilling.

Figure 2.5 Aerial photograph of the Klip River looking downstream (flow is towards the upper left). The transition in the lithology from sandstone/shale to dolerite, and the corresponding change in river character from a highly sinuous form, to being constrained in narrow valleys along joints and fractures in the dolerite, can be clearly seen (photo: S. Tooth).

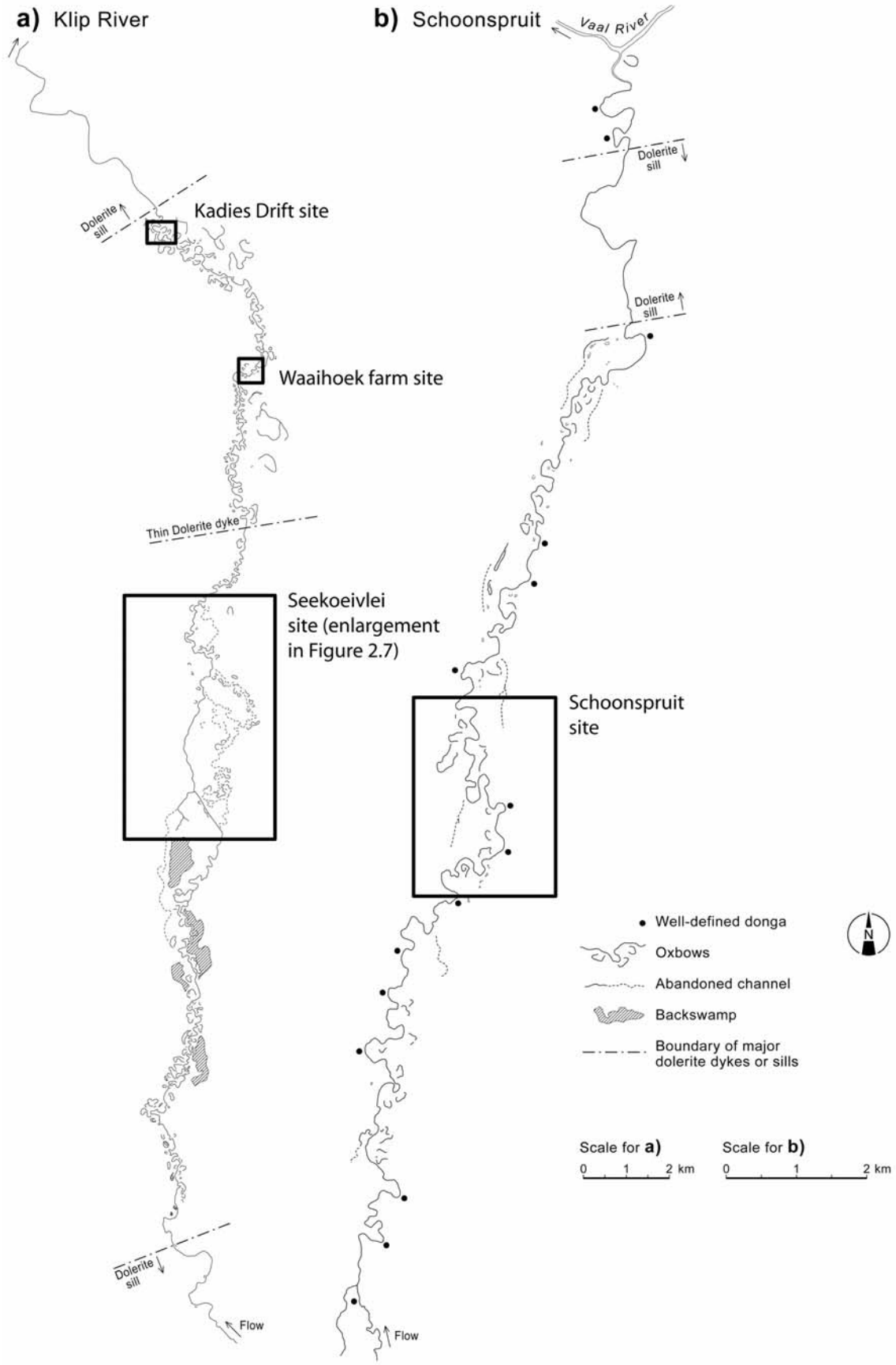

Figure 2.6: Planforms of a) the Klip River and b) Schoonspruit with study sites marked. Note the difference in scales. Adapted from Tooth *et al.* (2004).

a)

b)

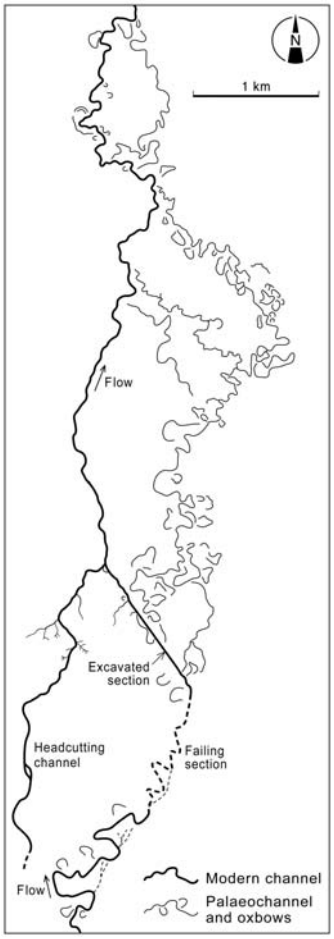

c)

Figure 2.7: a) Aerial photographs of the Seekoeivlei Nature Reserve; b) map of the palaeochannels and oxbows identified from the aerial photographs; and c) bend of a palaeochannel (largely infilled) identified on the ground.

2.4 THE SCHOONSPRUIT

The Schoonspruit arises at ~1680 m a.s.l. and drains a catchment area of 325 km^2 (Tooth *et al.*, 2004), before joining the Vaal River ~20 km to the west of the Klip River (Fig. 2.3). The Schoonspruit also flows mainly across sandstone/shale lithologies but locally has been superimposed across dolerite sills and dykes. North of the town of Cornelia, a dolerite sill has been partially breached (Fig. 2.8a) which has generated a knickpoint that has migrated upstream. Although the river retains its highly sinuous form (sinuosity ~1.99) and wide floodplain (>1000 m) (Tooth *et al.*, 2004), in places it has incised up to ~3 m through the shale bedrock (Fig. 2.8b) and is currently in Stage 2 of development (Fig. 2.2c). Knickpoint retreat has also occurred up tributaries (Tooth *et al.*, 2004) and donga erosion has initiated on some of the channel banks. On the elevated floodplain surface associated with the former river level, oxbow lakes can be seen (Fig. 2.8b). An inset floodplain associated with the modern river channel has formed at a lower level within the incision slot (Fig. 2.9), suggesting a decrease or cessation of incision.

2.5 SAMPLING STRATEGY AND COLLECTION

Along the Klip River, samples were collected for OSL dating in order to look at the timescales associated with lateral migration, channel cutoff and avulsion events. Samples for radiocarbon dating were taken from abandoned channels, primarily to provide an independent check on the accuracy of the OSL ages, but also to give some indication of the timescales associated with post-abandonment channel infilling. Along the Schoonspruit, samples for OSL dating were collected to investigate the rate of incision.

A complete list of all the samples collected and relevant details such as the depositional environment, location, and sampling depth are shown in Table 2.1.

a)

b)

Figure 2.8: The Schoonspruit a) deeply incised (~3-4 m) through a dolerite sill (photo: S. Tooth) and b) incising through shale bedrock. An extensive donga (gully) system can also be seen (photo: T.S. McCarthy).

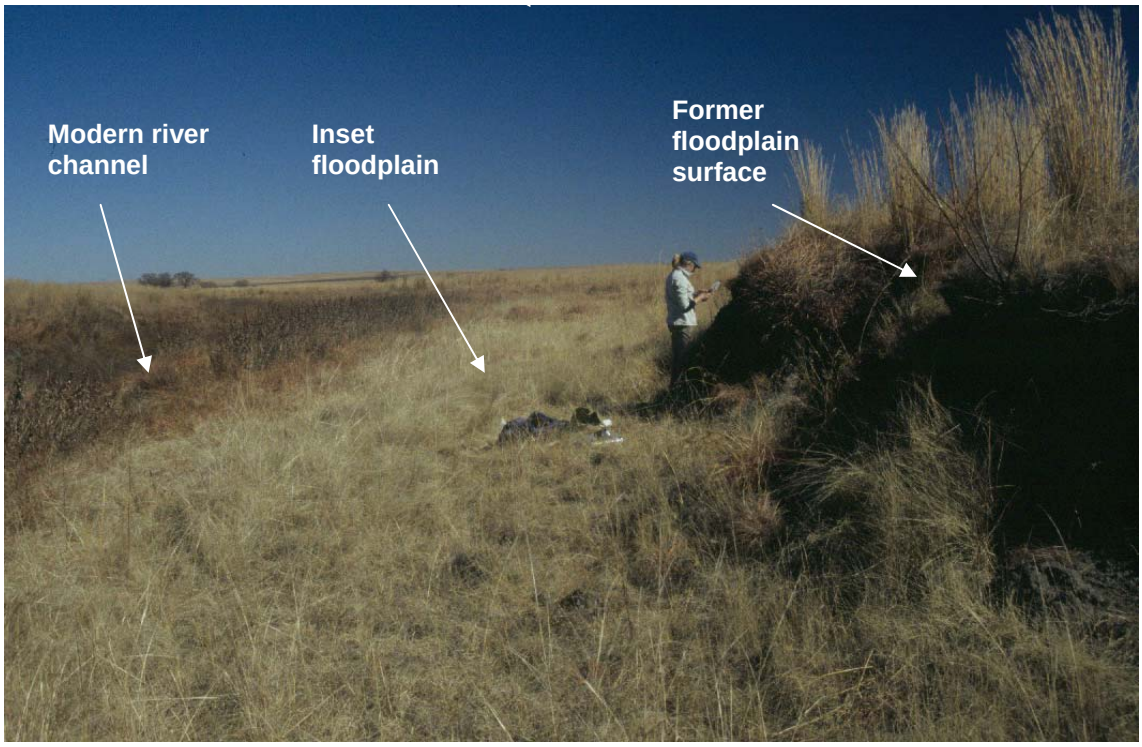

Figure 2.9: Inset and former floodplains of the Schoonspruit (photo: S. Tooth).

Table 2.1: Details of samples collected for OSL and ^{14}C dating from the Klip River and the Schoonspruit.

Sample	Location		Environment	Depth	Latitude	Longitude
OSL SAMPLES						
70KLA1	Seekoeivlei	Reach B	Channel fill	0.85-0.95	S 27° 33’ 56”	E 29° 35’ 01”
70KLA2	Seekoeivlei	Reach C	Channel fill	0.70-0.90	S 27° 33’ 50”	E 29° 35’ 29”
70KLA3	Seekoeivlei	Reach D	Channel fill	1.55-1.65	S 27° 33’ 50”	E 29° 35’ 22”
70KLA4	Seekoeivlei	Reach E	Channel fill	0.65-0.85	S 27° 35’ 28”	E 29° 35’ 30”
70KLA5	Seekoeivlei	Reach F	Channel fill	1.10-1.20	S 27° 35 56”	E 29° 35’ 19”
70KLA6	Seekoeivlei	Reach G	Channel fill	1.70-1.80	S 27° 35’ 18”	E 29° 35’ 28”
75KL0301	Seekoeivlei	Failing channel	Channel fill	0.50-0.72	S 27° 35’ 41”	E 29° 35’ 31”
75KL0302	Seekoeivlei	Trench		1.50	S 27° 34’ 10”	E 29° 35’ 00”
75KL0303	Seekoeivlei	Trench		1.50	S 27° 34’ 10”	E 29° 35’ 00”
75KL0304	Seekoeivlei	Trench		1.50	S 27° 34’ 10”	E 29° 35’ 00”
75KL0305	Seekoeivlei	Trench		0.50	S 27° 34’ 10”	E 29° 35’ 00”
75KL0306	Seekoeivlei	Trench		Surface	S 27° 34’ 10”	E 29° 35’ 00”
75KL0307	Seekoeivlei	Modern river	Point bar	Surface	S 27° 34’ 10”	E 29° 35’ 02”
75KL0308	Seekoeivlei	Reach B	Channel fill	0.80-1.00	S 27° 33’ 47”	E 29° 35’ 56”
75KL0309*	Seekoeivlei	Reach B	Channel fill	0.80-1.00	S 27° 33’ 47”	E 29° 35’ 56”
75KL0310	Seekoeivlei	Reach A	Channel fill	1.20-1.45	S 27° 32’ 45”	E 29° 35’ 29”
75KL0311†	Seekoeivlei	Reach A	Channel fill	1.70-1.80	S 27° 32’ 45”	E 29° 35’ 29”
75KL0312	Seekoeivlei	Reach A	Channel fill	1.20-1.35	S 27° 32 36”	E 29° 35’ 29”
75KL0313	Seekoeivlei	Sandstone outcrop		Surface	S 27° 32’ 12”	E 29° 35’ 26”
75KL0314	Seekoeivlei	Reach B	Oxbow	1.20-1.40	S 27° 32’ 50”	E 29° 35’ 05”
75KL0315	Seekoeivlei	Reach B	Oxbow	1.45-1.60	S 27° 32’ 44”	E 29° 36’ 01”

75KL0316	Kadies Drift		Oxbow	0.15-0.35	S 27° 27’ 22”	E 29° 34’ 49”
75KL0317	Kadies Drift		Scroll bar	1.20-1.40	only one GPS reading taken at this site	
75KL0318	Kadies Drift		Scroll bar	0.40-0.60		
75KL0319	Kadies Drift		Scroll bar	0.50-0.70		
75KL0320	Kadies Drift		Scroll bar	0.30-0.50		
75KL0321	Kadies Drift		Scroll bar	1.05-1.25		
75KL0322	Waaihoek		Scroll bar	1.45-1.65	S 27° 29’ 08”	E 29° 36’ 07”
75KL0323	Waaihoek		Scroll bar	0.65-.85	only one GPS reading taken at this site	
75KL0324	Waaihoek		Scroll bar	0.80-1.00		
75KL0325	Waaihoek		Scroll bar	0.45-0.65		
75KL0326	Waaihoek		Point bar	0.00-0.20		
75KL0327	Waaihoek		River bank	0.00-0.00		
75KL0328	Seekoeivlei	Reach B	Oxbow	1.05-1.25	S 27° 34’ 02”	E 29° 36’ 06”
75KL0329	Seekoeivlei	Reach B	Channel fill	1.50-1.70	S 27° 34’ 09”	E 29° 35’ 53”
75KL0330	Seekoeivlei	Reach C	Channel fill	1.25-1.45	S 27° 33’ 44”	E 29° 35’ 22”
75KL0331	Seekoeivlei	Reach C	Channel fill	1.00-1.10	S 27° 33’ 55”	E 29° 35’ 36”
75KL0332	Seekoeivlei	Reach E	Channel fill	0.90-1.10	S 27° 34’ 07”	E 29° 35’ 44”
75KL0333	Seekoeivlei	Reach E	Channel fill	0.80-0.90	S 27° 34’ 23”	E 29° 35’ 39”
75KL0334	Seekoeivlei	Reach E	Oxbow	0.75-1.00	S 27° 34’ 16”	E 29° 35’ 34”
75KL0335	Seekoeivlei	Reach E	Oxbow	2.00-2.20	S 27° 34’ 18”	E 29° 35’ 37”
75KL0336	Seekoeivlei	Reach G	Channel fill	0.90-1.05	S 27° 35’ 17”	E 29° 35’ 30”
75KL0337	Seekoeivlei	Reach G	Channel fill	1.70-1.80	S 27° 35’ 07”	E 29° 35’ 37”
75KL0338‡	Seekoeivlei	Reach G	Channel fill	2.50-2.60	S 27° 35’ 07”	E 29° 35’ 37”
75KL0339	Seekoeivlei	Reach E	Channel fill	1.10-1.30	S 27° 34’ 59”	E 29° 35’ 30”
75KL0340	Seekoeivlei	Reach E	Oxbow	1.45-1.65	S 27° 35’ 05”	E 29° 35’ 28”
75KL0341	Seekoeivlei	Reach F	Oxbow	1.25-1.45	S 27° 34’ 57”	E 29° 35’ 16”

75KL0342	Seekoeivlei	Reach E	Channel fill	2.10-2.25	S 27° 34’ 49”	E 29° 35’ 33”
92KL0401	Kadies Drift		Scroll bar	0.90-1.20	S 27° 27’ 27”	E 29° 34’ 45”
91SC0401	Schoonspruit	Upper floodplain	Oxbow	1.15-1.30	S 27° 09’ 41”	E 28° 51’ 07”
91SC0402[Δ]	Schoonspruit	Upper floodplain	Oxbow	1.30-1.50	S 27° 09’ 41”	E 28° 51’ 07”
91SC0403	Schoonspruit	Upper floodplain		0.90	S 27° 09’ 44”	E 28° 52’ 29”
91SC0404	Schoonspruit	Upper floodplain		1.75	S 27° 09’ 41”	E 28° 52’ 37”
91SC0405	Schoonspruit	Upper floodplain		1.40	S 27° 09’ 41”	E 28° 52’ 37”
91SC0406	Schoonspruit	Upper floodplain		0.50	S 27° 09’ 33”	E 28° 52’ 35”
91SC0407	Schoonspruit	Inset floodplain		0.80	S 27° 09’ 33”	E 28° 52’ 36”
91SC0408	Schoonspruit	Inset floodplain		0.40	S 27° 09’ 41”	E 28° 52’ 37”
91SC0409	Schoonspruit	Inset floodplain		1.15	S 27° 09’ 45”	E 28° 52’ 30”
91SC0410	Schoonspruit	Upper floodplain	Oxbow	2.50-2.60	S 27° 09’ 50”	E 28° 52’ 20”
^{14}C SAMPLES						
14CKL0308	Seekoeivlei	Reach B	Post-abandonment infill	0.70-0.80	S 27° 33’ 47”	E 29° 35’ 56”
14CKL0310	Seekoeivlei	Reach A	Post-abandonment infill	1.10-1.20	S 27° 32’ 45”	E 29° 35’ 29”
14CKL0342	Seekoeivlei	Reach E	Post-abandonment infill	2.00-2.10	S 27° 34’ 49”	E 29° 35’ 33”

*Taken 30 cm horizontally from 75KL0308

[†]Sampled from the same auger hole as 75KL0310

[‡] Sampled from the same auger hole as 75KL0337

[Δ] Sampled from the same auger hole as 91SC0401

2.5.1 OSL sample collection

OSL samples from the scroll bars, oxbow lakes and channel fill deposits on the Klip River and Schoonspruit were collected by augering vertically through fine floodplain alluvium (mud and fine sand) until continuous medium-coarse sand was encountered. The equipment used is shown in Figure 2.10. The change in texture could be detected by the sound the auger created as it moved through the sediment, and confirmed by visual inspection of the sediment retained in the auger barrel. The sand was then sampled by attaching an ~0.3 m long tube of 0.1 m diameter drainpipe to the auger, pushing the drainpipe down the auger hole, and rotating until it was filled with sediment. When retrieved, the tube retained the sample for OSL analysis without exposing it to sunlight. This sampling strategy ensured that the bedload sand associated with either the top

Figure 2.10: Equipment used for auguring samples, showing sample tubes on the left and the various augering equipment used.

of the scroll bar, or the final flow in the channel, was sampled as opposed to overbank deposits associated with later floods.

Floodplain exposures on the Schoonspruit were sampled using lengths of metal drainpipe which were hammered horizontally into the face, using a mallet (Fig. 2.11). When filled with sediment, they were carefully extracted; any unfilled space in the tube was packed with black plastic to ensure that no mixing of the sediment occurred and that the end that was exposed to light, as the tube was extracted, did not contaminate the sample. Section 2.6 provides further details regarding the sampling strategy employed to investigate the various processes of channel change.

Figure 2.11: Sampling tube *in-situ* in river bank on the Schoonspruit (black plastic inserted into end of tube is to prevent light entering).

2.5.2 Radiocarbon sample collection

A small number of samples were collected for radiocarbon (^{14}C) dating from the palaeochannels. ^{14}C samples were collected from the organic-rich mud lying directly above the sampled bedload sand. The ^{14}C ages provide minimum ages for the initiation of infilling following channel abandonment, and hence should be younger than the OSL ages of the sand associated with the final bedload transport events in the channels.

2.6 OSL SAMPLING STRATEGY

2.6.1 Lateral migration

To determine rates of lateral migration on the Klip River, samples were taken at two meander bends located at Waaihoek farm and Kadies Drift, ~22 and 27 km downstream of Memel, respectively (Fig. 2.6a). Both sites showed clear evidence of meander bend migration with well-defined scroll-bar sequences represented by a ridge-and-swale topography on inner bends. Transects perpendicular to the apex of the meander bend and across the associated sample locations were surveyed using a staff and level.

At the Waaihoek site (Fig. 2.12a), four scroll-bar ridges could be identified (Fig. 2.12b) and each of these was sampled. Samples were also taken from the point bar and channel bank of the modern river channel to examine residual ages. The transect across the Waaihoek scroll-bar sequence, and the sample locations are shown in Figure 2.12c.

Following page:

Figure 2.12: a) Waaihoek site, indicating the location of the scroll bar sequence investigated (photo: S. Tooth), b) looking across the meander loop in the direction indicated by the arrow in the photograph above. The scroll bar ridges are marked by black lines and are associated with subtle changes in the grassy vegetation cover. c) Transect across the Waaihoek site, with the sample locations marked (VE = 20).

a)

b)

c)

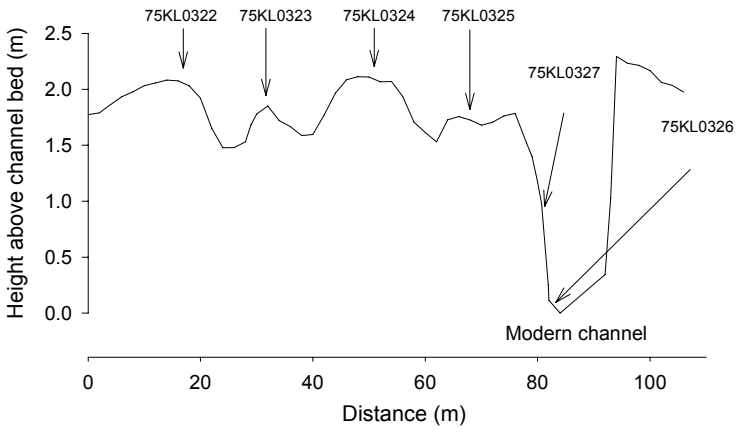
75KL0322
75KL0323
75KL0324
75KL0325
75KL0327
75KL0326
Modern channel
Height above channel bed (m)
2.5
2.0
1.5
1.0
0.5
0.0
0
20
40
60
80
100
Distance (m)

At the Kadies Drift site, the meander loop associated with the scroll-bar sequence has been cutoff, forming an oxbow. Aerial photographs from 1954 show the meander as part of the main river channel (Fig. 2.13a), but by 1979 cutoff had occurred and the oxbow lake had formed (Fig. 2.13b), placing the date of final bedload transport in this section of channel between 1954 and 1979. The scroll-bar ridges could be readily distinguished on the ground (Fig. 2.14a), and six samples from the scroll-bar ridges were taken (five in 2003 and a sixth in 2004). During fieldwork in 2003, the oxbow lake was dry (Fig. 2.14b), so a sample for OSL dating was also collected from the channel. The transect across the Kadies Drift scroll-bar sequence, and the sample locations are shown in Figure 2.14c.

a)

b)

Figure 2.13: Kadies drift meander loop in a) 1954 and b) 1979.

Following page:

Figure 2.14. Kadies drift scroll-bar sequence, a) looking south-west across the sequence, the scroll-bar ridges are marked by black lines; and b) the abandoned oxbow lake. c) Transect across the Waaihoek site, with the sample locations marked (VE = 15).

a)

b)

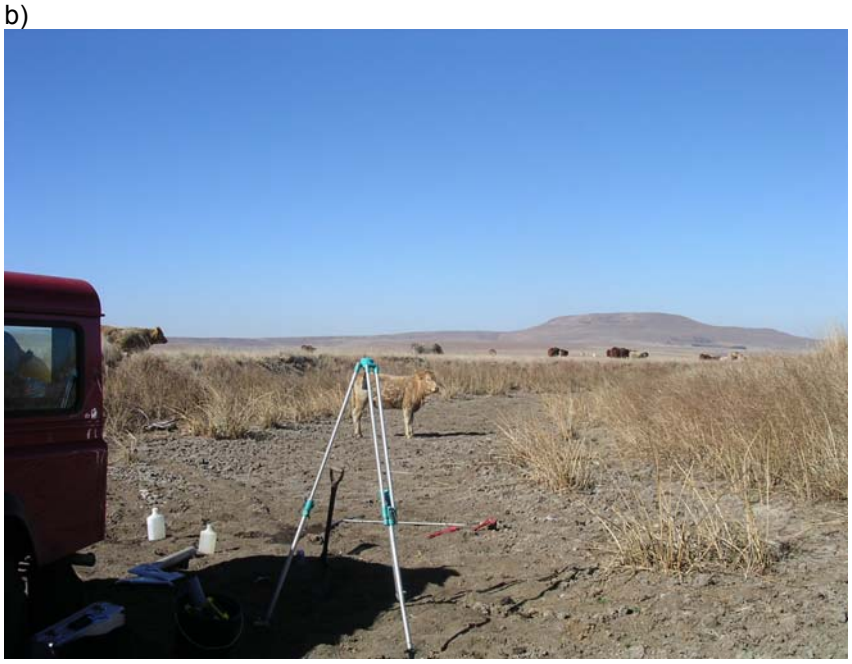

c)

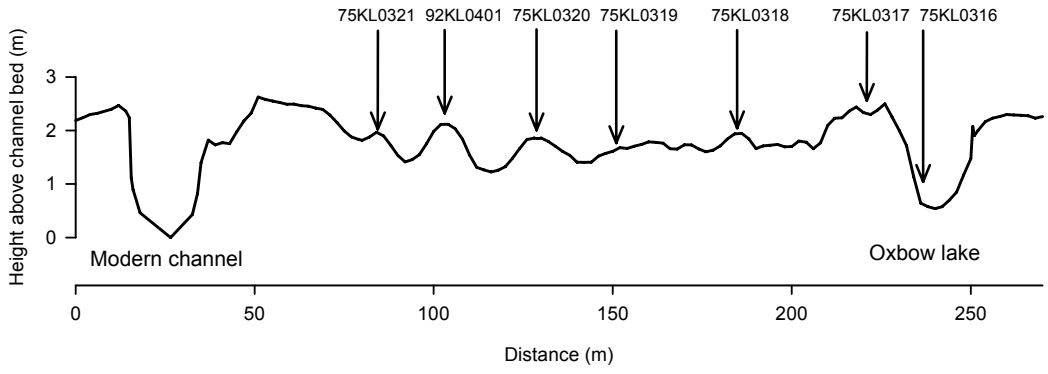
75KL0321
92KL0401
75KL0320
75KL0319
75KL0318
75KL0317
75KL0316
Height above channel bed (m)
3
2
1
0
Modern channel
Oxbow lake
0
50
100
150
200
250
Distance (m)

2.6.2 Avulsion

To derive a chronology of Klip River avulsions, samples were taken from generations of palaeochannels that could be identified on the basis of aerial photography at the Seekoeivlei site. Sampling the uppermost bedload sand from within the palaeochannel reaches allows determination of the timing of the final bedload transport and thus the maximum age of abandonment of the channel. Along some reaches, multiple samples were collected to allow the reproducibility of the results to be investigated. The sample locations are marked in Figure 2.15, and the discrete reaches of palaeochannel are indicated and identified by letters.

2.6.3 Meander cutoff

Dating of meander cutoff events (leading to formation of oxbows) allows the longevity of a channel belt to be investigated. Samples from oxbows establish when the last bedload transport occurred in that section of former channel and thus provide a maximum age for the cutoff event itself. Ages for the oxbows will allow the longevity of the reaches of palaeochannel to be investigated; although the samples will not allow the formation of the entire channel reach to be determined, the oldest oxbow will give a minimum age for initiation of flow along that reach. Samples from oxbows associated with palaeochannels at the Seekoeivlei site (Fig. 2.6b) were collected for OSL analysis. The samples were taken from the centre of the oxbows, at the apex of the bends. Sample locations are marked on Figure 2.15 (15, 28, 34, 35, 40, 41).

2.6.4 Incision

The Schoonspruit is different from the Klip River in that is has undergone a period of incision (Fig. 2.8). To investigate the timing of incision along the Schoonspruit, samples were collected from bank exposures along the lower, inset floodplain and the former, elevated floodplain, and by augering through the oxbows on the former floodplain (Fig. 2.16). Samples 91SC0403-09 were collected from the inset floodplain and the former floodplain at three locations (Transects 1-3 on Figure 2.16) in order to determine the ages of both levels, and thus constrain the timing of incision; surveys were taken

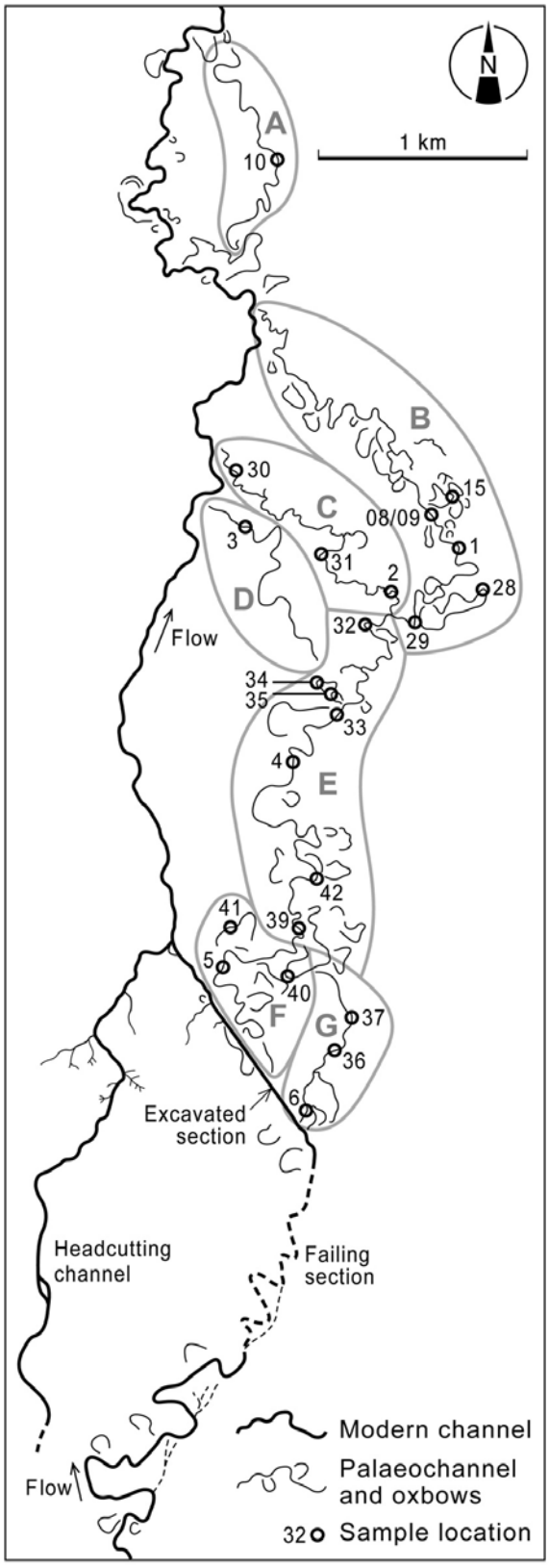

Figure 2.15: Map of the Seekoeivlei site, with sample locations (prefixed 70KLA- for samples 1 to 6, and 75KL03- for all other samples) from abandoned channels and oxbows marked. The different section of palaeochannel have been grouped into reaches and lettered A -G. Note that samples 11 and 38 were taken at the same locations as samples 10 and 37 respectively.

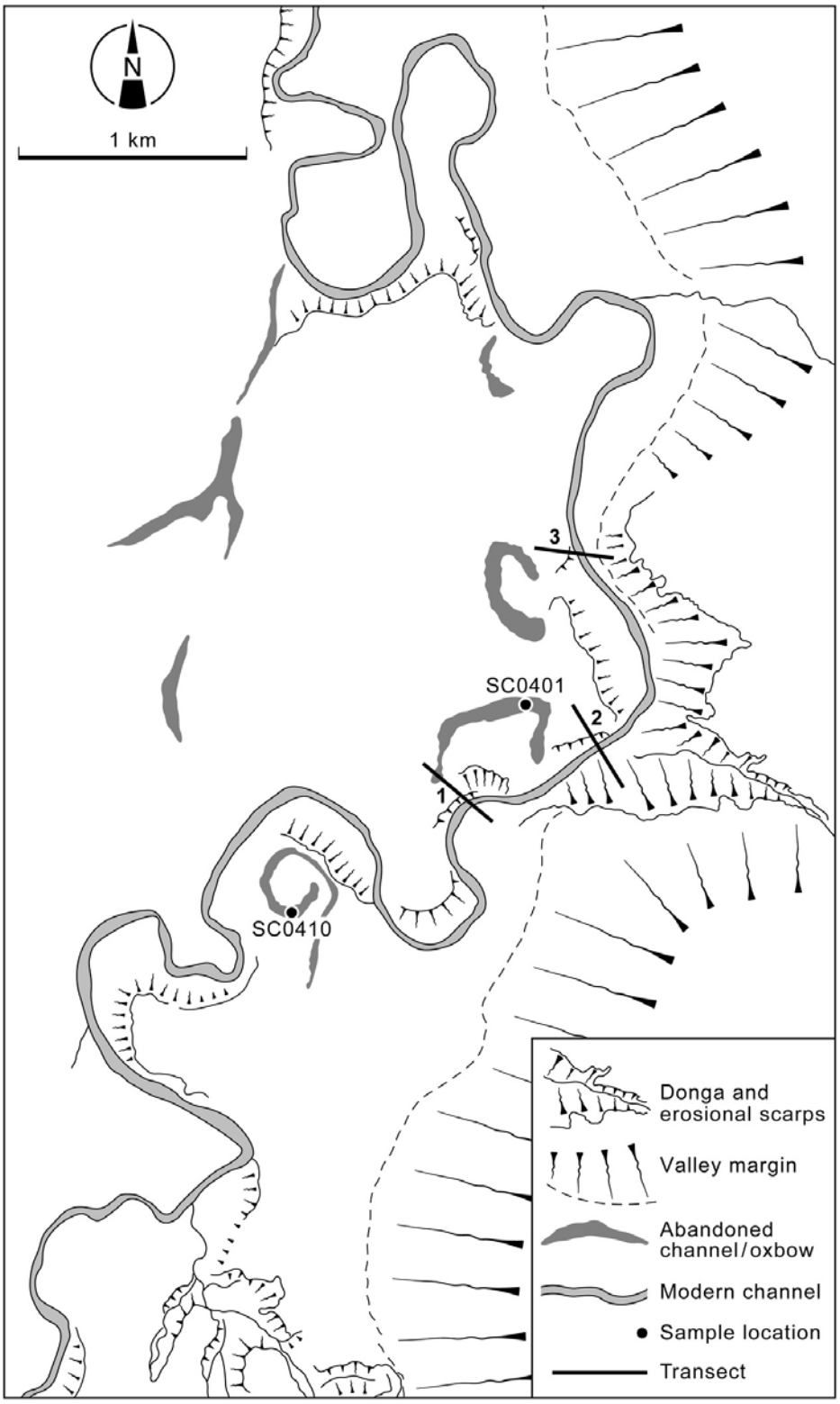

Figure 2.16: Map of the Schoonspruit with the location of samples from oxbows marked (samples codes are prefixed 91-), and transects along which further samples were taken are also marked. Samples 91SC0403 and 91SC0409 were taken from Transect 1; 91SC0404, 91SC0405 and 91SC0408 were taken from Transect 2; and 91SC0406 and 91SC0407 were taken from Transect 3. Note that sample 91SC0402 was taken from the same location as 91SC0401.

perpendicular to the river at these sites. The oxbows samples (91SC0401 and 91SC0410 on Figure 2.16, and additional sample 91SC402 taken from the same auger hole as 91SC0401) indicate when the river was active at the higher level, and thus provide a maximum age for the initiation of incision.

2.7 SOUTH AFRICAN CLIMATE

2.7.1 Modern prevailing weather systems

Since the uplift of the southern African subcontinent during the Cretaceous, the climate of southern Africa has been influenced by the mean circulation of the atmosphere over the subcontinent, and by deviations from this mean (Tyson and Preston-Whyte, 2000). The mean atmospheric circulation over southern Africa is dominated by Walker circulation. This climatic pattern occurs when seasonal lows form over a continent because the air mass above the land heating up more than the adjacent air over the oceans. The continental land mass forms a topographical barrier to zonal flows, forcing a series of cells to be formed. In the case of Africa, the main Walker circulation is caused by the easterly trade winds over the Atlantic Ocean, with westerlies at higher altitudes. The wind stress caused by this, in conjunction with the Eckman force, lead to upwelling of cool water off the west coast of southern Africa. This upwelling increases the sea surface temperature gradient, which in turn enhances the atmospheric temperature gradient. In the Indian Ocean the atmospheric circulation is in the opposite direction, with westerlies near the sea surface and easterlies aloft (Tyson, 1987). Temperate disturbances originating in the circumpolar westerlies, and the interaction between temperate and tropical disturbances are major factors affecting the rainfall over southern Africa (Tyson and Preston-Whyte, 2000). Rainfall is highly seasonal over southern Africa; Figure 2.17 shows the rainfall maxima in South Africa. Eastern and north-eastern South Africa (covering the study region) has a strong summer rainfall season with more than 80% of the annual total rain occurring between November and March. Along the south-western coast, the majority of the rain falls in the winter months (May to September).

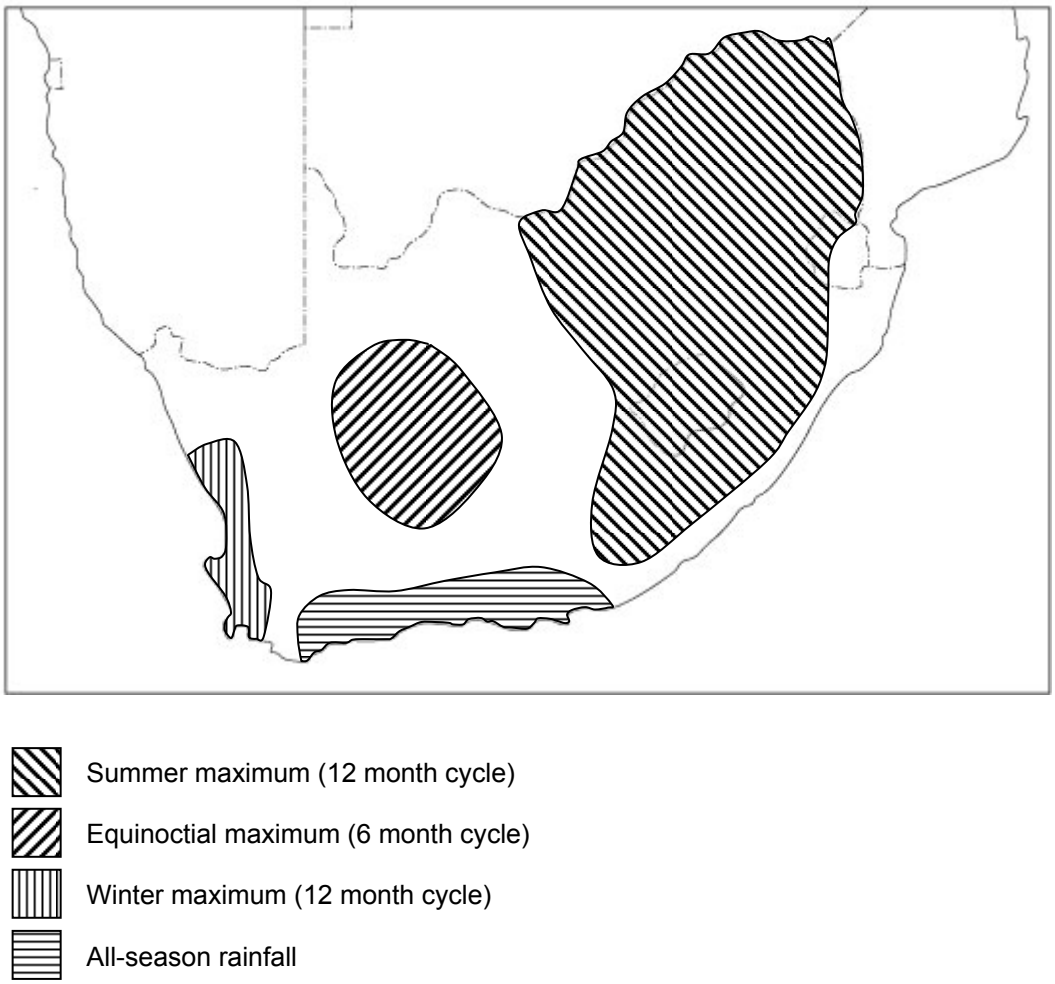

Figure 2.17: Map showing the rainfall regimes in South Africa. Adapted from Hall (1976).

Evidence of quasi-decadal wet-and-dry cycles have been recorded in southern Africa, both as proxy records in tree-ring series (Tyson, 1987) and as measured rainfall oscillations (e.g. Tyson *et al.* (1975) showed evidence of wet-and-dry cycles lasting 18 years using data from 157 stations located in the east of South Africa over a 62-year period). Principal component analysis showed that an ~18 year cycle is dominant over the entire summer rainfall region of southern Africa, with a higher frequency 10-12 year oscillation prevailing in the southern Cape all-season rainfall zone. Tyson (1987) suggested that the wet spells may be caused by strengthening of the tropically induced circulation disturbances which are formed by the easterly trade winds. This leads to increased cloud cover and rainfall, which in turn causes lower maximum temperatures compared to those experienced during the dry spells. During the dry spells, expansion of the circumpolar vortex increases the occurrence of westerly disturbances which

in turn, decrease the relative amount of cloud cover during the summer. In the summer rainfall zone this causes the summers to become drier and the winters wetter, but with an overall decrease in the net rainfall.

2.7.2 Evidence of palaeoclimates through the late Quaternary

The modern weather systems have not always prevailed in southern Africa, with the climate being considerably warmer and cooler than at present at different times in the past (Tyson, 1987). Many reviews have been written on the palaeoclimates of southern Africa covering a range of timescales; from the Cainozoic (e.g. Partridge, 1997), to reviews focussing on late Quaternary environmental change (e.g. Deacon and Lancaster, 1988; Tyson, 1999; Thomas and Shaw, 2002).

Globally, climatic variations are driven by orbital cycles of different periodicity; eccentricity has ~100 ka cycles, tilt has ~41 ka cycles, and precession has ~23 ka cycles. During the Quaternary, these orbital cycles are thought to have been the cause of glacial and interglacial cycles that are seen in the $\delta^{18}O$ records of benthic marine foraminifera and in the δD records of ice cores from Vostok, Antartica (Fig. 2.18); the last glacial maximum occurred at ~21 ka when the continental ice sheets were at their greatest extent. During the late Pleistocene and Holocene in southern Africa, it has been suggested that climatic change has been dominated by the ~23 ka precessional cycle (Tyson *et al.*, 2001). The precession of the Earth influences the distribution of solar irradiation received. Currently it is the austral summer when the perihelion (when the Earth is closest to the sun) occurs, thus the Southern Hemisphere receives an increased amount of solar radiation during the summer, and a corresponding decrease during winter at the aphelion (when the Earth is furthest from the sun). This leads to more extreme seasons in the Southern Hemisphere, with a milder climate in the Northern Hemisphere at the present day. The situation was reversed at 11.5 ka, with relatively mild winters and summers in the southern hemisphere (Tyson, 1999). Evidence for the influence of the precessional cycle on rainfall comes from work on the Pretoria Saltpan (Tswaing Crater) (Partridge *et al.*, 1997). Using ^{14}C ages obtained from upper layers of the core, and a fission track age at the base, the resulting precipitation record (Fig. 2.19)

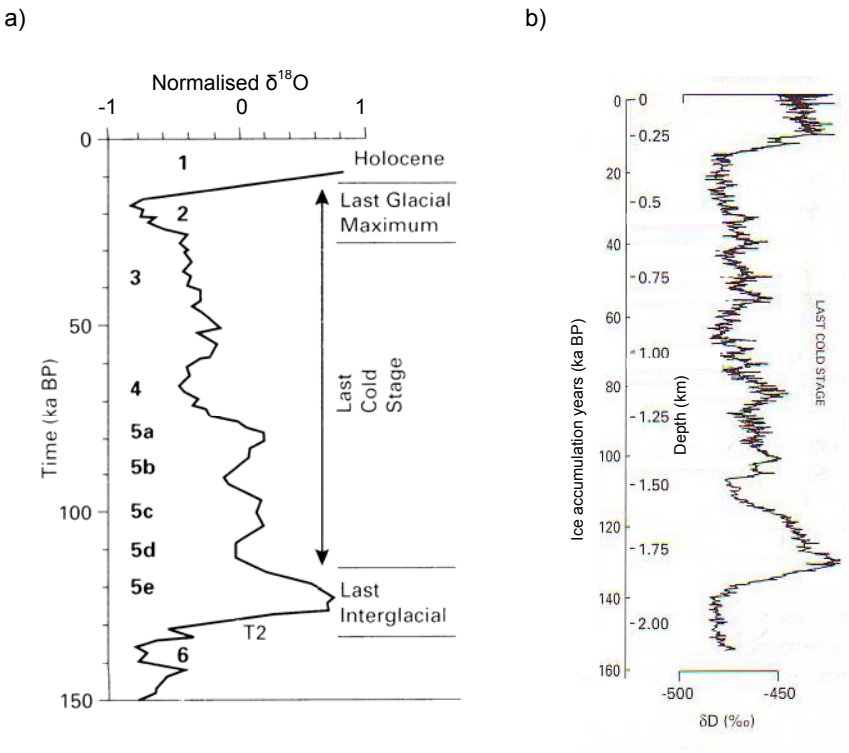

Figure 2.18: a) Stacked marine oxygen isotope record for the past 150 ka (after Martinson *et al.*, 1987). b) Deuterium ratios in the Vostok core from Antarctica. From Lowe and Walker (1997).

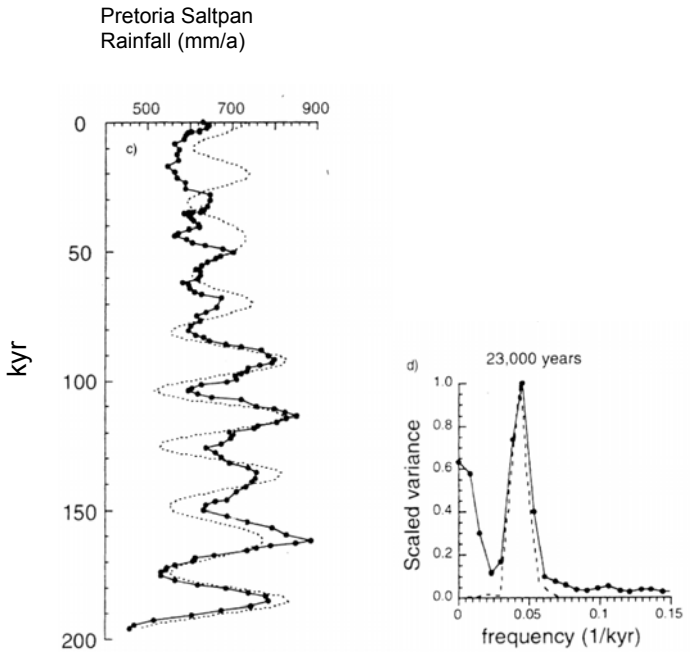

Figure 2.19: Tswaing crater rainfall (mm/a) derived from soil texture and precipitation relationship. The raw, corrected and calibrated radiocarbon ages have been used for the age model. The precessional variability dominates in the power spectrum, accounting for 44% of the total variability. From Partridge *et al.* (1997).

demonstrated evidence of a 23 ka periodicity, and the precessional signal was found to account for 44% of the total rainfall variance. Despite the generally good agreement between the rainfall and the precessional cycle, over the period of the core which has been well dated (the last 43 ka BP) a poor relationship is evident.

Only Holocene and late Pleistocene palaeoclimates are of relevance to the work in this thesis, so the following sections concentrate on this period of time. As yet the understanding of the synchronicity of events over large spatial scales is not sufficient for records obtained on the west coast of South Africa to be confidently related to events occurring on the eastern side. Nevertheless, a number of high resolution records from locations in southern Africa have recently been published and these are detailed in the sections below. Records in the vicinity of the Klip River and Schoonspruit tend to be of short duration and/or poor resolution but the details of these are also included below. The locations of the sites mentioned are shown in Figure 2.20. In the following section, the ages and dates are reported in the format used in the original work to reflect the accuracy of the quoted values. For ^{14}C ages, "BP" is used to indicate that the age reflects the time pre-1950, and "cal" indicates that those ages have been calibrated to correct for temporal variations of atmospheric ^{14}C.

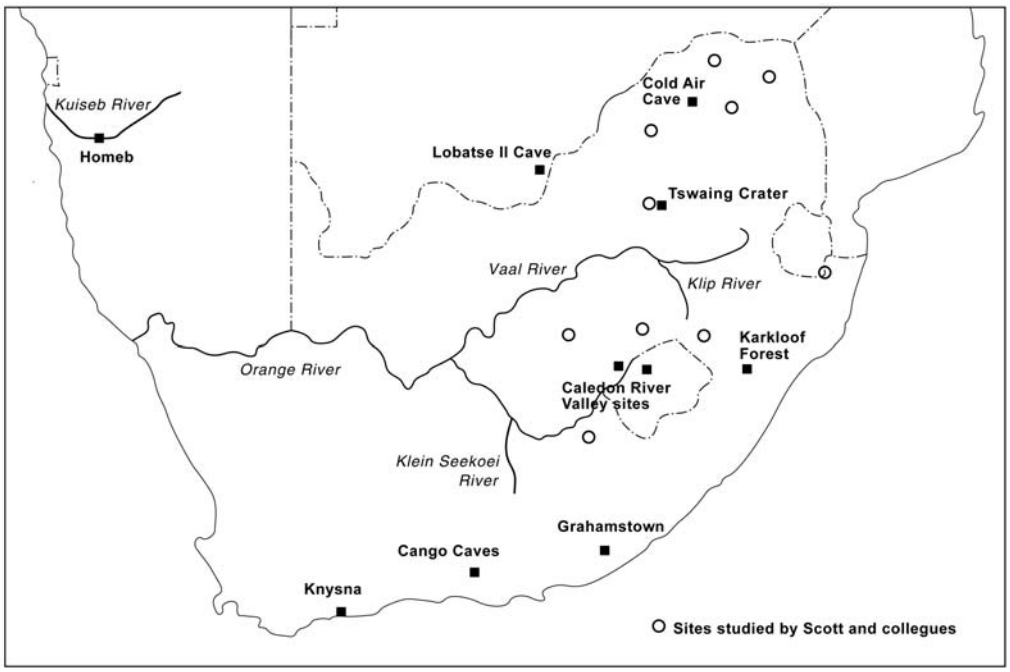

Figure 2.20: Map of South Africa showing location of sites mentioned in Section 2.7.2.

2.7.2.1 Speleothem records

The majority of the near-continuous, high precision records of southern African palaeoclimates come from well-dated stalagmites. The first significant work was performed on a stalagmite in Cango Caves, located near the southern margin of the summer rainfall zone of the Cape Province. This was dated using ^{14}C and showed that the stalagmite contained a near-continuous record for the last 30 ka BP (Talma and Vogel, 1992), but with a hiatus in deposition between 13.8 to 5 ka BP. Analysis of the $\delta^{18}O$ data from the stalagmite (Fig. 2.21) indicates that during the period 30 ka BP to 13.8 ka BP the average temperature was about 4-7°C lower than today's mean, with the coldest conditions occurring ~18 ka BP. Between 5 ka BP and the present, the temperature has been relatively stable, averaging ~17°C. During this period two cool periods were identified as occurring between 4.7 and 4.2 ka BP, and 3.2 to 2.5 ka BP.

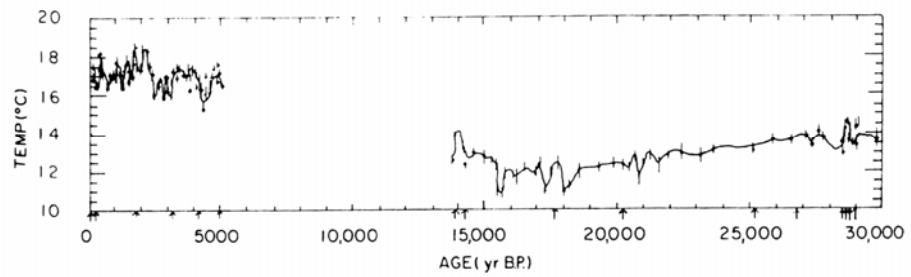

Figure 2.21: Depositional temperatures of the stalagmite from the Cango Caves back to 30 ka BP. The solid line is a calculated spline curve, and the arrows on the x-axis indicate the ages of samples taken for dating; a hiatus in deposition occurred between 13.8 and 5 ka BP. From Talma and Vogel (1992).

Holmgren *et al.* (1995) studied a stalagmite located in the Lobatse II cave on the western margins on the summer rainfall zone in southern Botswana. ^{14}C and U-series dating led to identification of two periods of growth between 51-43 ka and 27-21 ka. The authors interpreted the stable isotope records of the speleothem (Fig. 2.22) as indicating that the earlier growth period was wetter and ~2°C warmer than the later period.

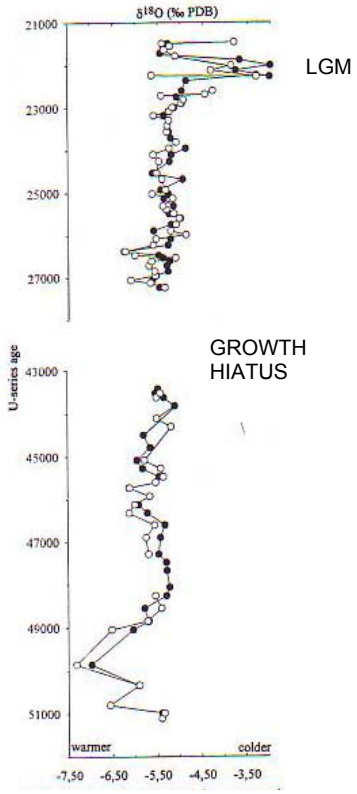

Figure 2.22: Oxygen isotope analysis of the stalagmite from Lobatse II cave. The solid circles represent the LII4 series samples, and the open circles represent a second set of samples (KH). These series were sampled from different depths in the speleothem. From Holmgren *et al.* (1995). The high $\delta^{18}O$ values that occurred during the Last Glacial Maximum are indicated.

Three stalagmites from the Cold Air Cave (Makapansgat Valley), located in the summer rainfall zone of the Northern Province, have been studied in detail: T5 (Repinski *et al.*, 1999); T7 (Holmgren *et al.*, 1999; Stevenson *et al.*, 1999; Tyson *et al.*, 2000; Lee-Thorpe *et al.*, 2001); and T8 (Holmgren *et al.*, 2003). U-series dating showed that the stalagmites cover the last ~25 ka. The different stalagmites grew over different times: the T5 stalagmite grew during the periods 4.4-4.0 ka and 0.8 ka to the present; T7 covers the last 6.6 ka continuously; and T8 covers the last 24.4 ka in high resolution but with a growth hiatus between 12.7-10.2 ka. During the overlapping periods of growth, good correlation generally was found between the stable isotope records (Holmgren *et al.*, 2003); Figure 2.23 shows the $\delta^{18}O$ and $\delta^{13}C$ values for stalagmites T7 and T8 over the last 6.6 ka.

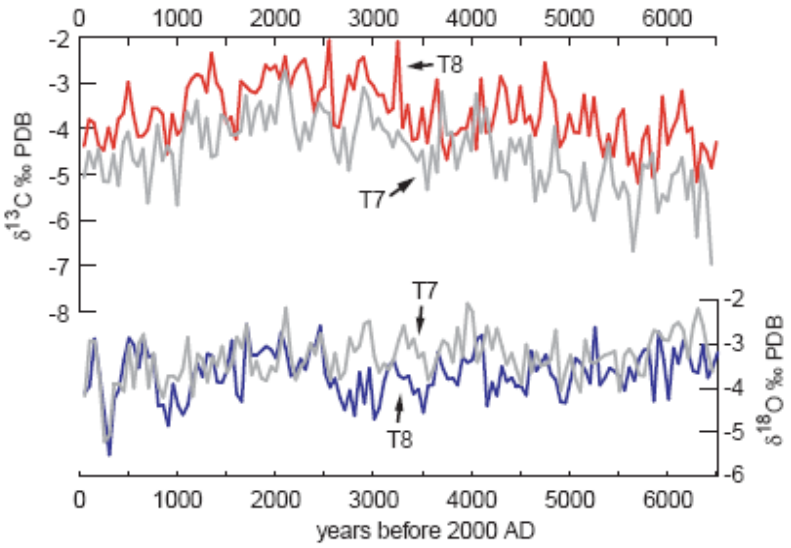

Figure 2.23: Comparison over 6.6 ka between the T7 and T8 Makapansgat speleothems $\delta^{13}C$ and $\delta^{18}O$ values. From Holmgren *et al.* (2003).

Using the Makapansgat Valley stalagmites, drier conditions, with cooler temperatures than at present, were identified during the periods 23-21 ka, 19.5-17.5 ka and 15-13 ka, with the most rapid warming occurring after 17.5 ka (Fig. 2.24). Work on the T7 stalagmite by Lee-Thorpe *et al.* (2001) showed that warm and humid conditions prevailed between 6.5 ka and 5.2 ka, before changing to a variable but generally moist period between 4.3 ka and 3.2 ka (Fig. 2.23). This was followed by a cooling cycle with arid conditions that ended in AD 1750. In contrast, the T8 stalagmite record was interpreted as indicating a cooler period over 6.0-2.5 ka, with high variability occurring after 5.2 ka.

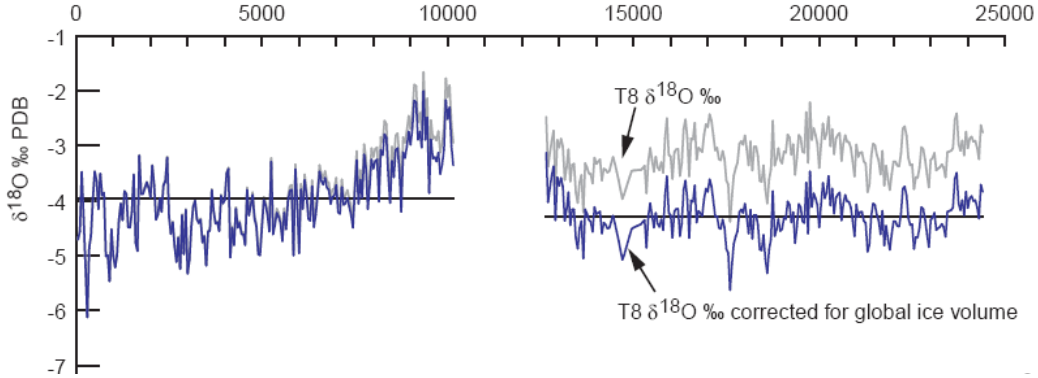

Figure 2.24: T8 Makapansgat speleothem $\delta^{18}O$ record for the last 24.4 ka, resolved at 50 year intervals. From Holmgren *et al.* (2003).

Unlike speleothem records from other sites, the dominant feature of these records is depleted isotopic values during the period between AD 1300 to 1800 and, more specifically, AD 1500 to 1800 for the T8 record (Fig. 2.23). These low values are indicative of cooling, and correlate with northern hemispheric evidence of the Little Ice Age (LIA). Holmgren *et al.* (1999, 2003) provide a comprehensive summary of other South African studies which show palaeoclimatic evidence in agreement with conclusions drawn from the T7 (Fig. 2.25) and T8 $\delta^{18}O$ records respectively.

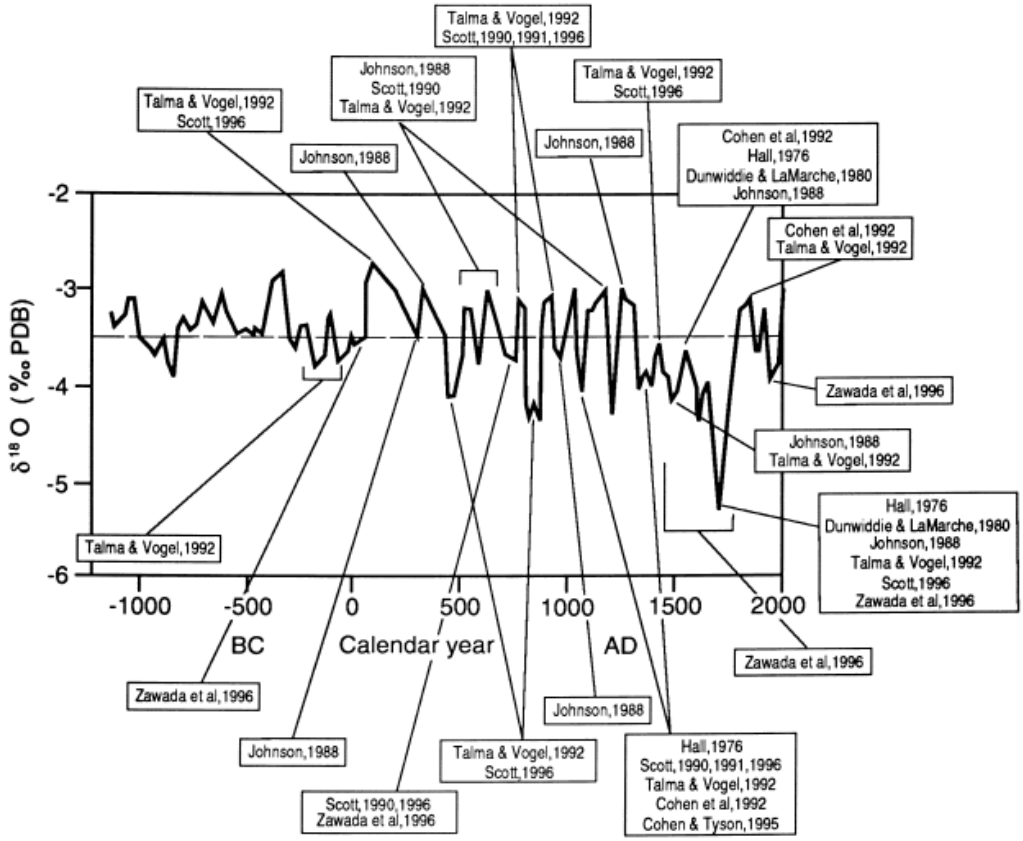

Figure 2.25: Corroboration of major events recorded in $\delta^{18}0$ record from the T7 Makapansgat speleothem by other South African records. From Holmgren *et al.* (1999.

The speleothem records discussed in the previous section derive from localities spread over southern Africa, but despite this there are a number of consistent palaeoclimatic signals. Combining the records allows one to create a general picture of climate change since 51 ka. The Lobatse II Cave record suggests that throughout the period 51-43 ka conditions were wetter and ~2ºC warmer than at present. The Cango Cave speleothem shows that this was followed by a generally cool period from 30 ka with temperatures between 4ºC and 7ºC lower than at present. During this interval, the Makapansgat Valley stalagmites indicate that there were three pronounced cold spells centred on 22 ka, 18 ka and 14 ka, followed by temperatures increasing during the Antarctic Cold Reversal at ~13.5 ka before gradually cooling until ~6.5 ka. The Cango Cave speleothem showed a generally warm and humid period from 6.5 ka, with cool periods evident at 4.7-4.2 ka and 3.2-2.5 ka; the timing of these cool periods broadly coincides with the Makapansgat T7 stalagmite record. Evidence of the LIA from speleothems was found only in the Makapansgat records, with maximum cooling occurring at AD 1750.

2.7.2.2 Pollen profiles

A large body of work using pollen profiles from various sites located in the old Transvaal region (now consisting of the Gauteng, North West, Limpopo and Mpumalanga Provinces) has been published by Scott and colleagues (Scott, 1982; Scott and Vogel, 1983; Scott, 1989; 1993; Nyakale and Scott, 2002; Scott and Nyakale, 2002). For much of the work, problems with obtaining suitable material for radiocarbon dating led to anomalous results in the chronologies (Scott, 1982; 1989; Scott and Vogel, 1983); the anomalous results were thought to be as a result of deep root penetration, so in later work rootlets were removed from the ^{14}C samples (Nyakale and Scott, 2002; Scott and Nyakale, 2002). Despite the problems with the chronology, broad palaeoenvironmental changes can be identified and the palaeoclimatic implications have been established. The palynological evidence suggests that at ~35 ka the climate in the Transvaal was cool and moist, before becoming drier until 25 ka (Scott, 1982). This was followed by cooler conditions, with temperatures 5-6°C colder than at present, with dry summers until ~11ka (Scott, 1982, 1989). The northern Transvaal had a cool, subhumid period between 12 and 10 ka (Scott,

1982), whilst evidence from sites near Lesotho suggested that at ~11 ka temperature was relatively warm (Scott, 1989). At ~6.5 ka the temperature increased to a maximum (Scott and Vogel, 1983; Scott, 1993). The humidity increased over the whole region until ~5 ka, with temperatures decreasing after ~4 ka (Scott and Vogel, 1983; Scott, 1993). The period from ~2.5 ka until the present day has been characterised by more variable conditions (Scott, 1982; Scott and Vogel, 1983; Scott and Nyakele, 2002). Although this work provides some useful palaeoenvironmental and palaeoclimatic information about southern Africa, the problems with the ^{14}C dating mean that exact dates must be treated with caution.

2.7.2.3 Ungulate enamel

$\delta^{13}C$ analysis on ungulate grazers' tooth enamel from four sites located in the Caledon River Valley near the Lesotho-South Africa border was used to determine the proportions of C_3 and C_4 grasses and hence infer palaeoclimatic shifts (Smith *et al.*, 2002). Remains from four archaeological sites were investigated and a good correlation was found between results from these sites. The results indicated that arid periods with cooler temperatures (i.e. dominated by C_3 grasses) occurred during the periods 16-14 cal ka BP, 10.2-9.6 cal ka BP and 8.4-8.0 ka cal BP.

2.7.2.4 Palaeoflood analysis

Studies investigating evidence of palaeofloods or river behaviour in the past, with absolute chronologies, are limited in South Africa. Smith (1992) identified two recent periods of high flood activity during AD 1874-1896 and AD 1650-1720 and one prior to 2.4 ka on the Orange River. From analysis of a larger global dataset, it was concluded that increased flooding generally represents cooler, wetter conditions. Work by Zawada (2000) on the lower Orange River found four palaeoflood periods, each having a different threshold discharge which was not exceeded during the flood period. Period 1 (threshold discharge of 12800 m^3/s) comprises of five palaeoflood events dated using IRSL as occurring between 1.8 ka and 5.4 ka; period 2 (threshold discharge of 14700 m^3/s) comprises of four palaeoflood events found to occur from AD 961 to AD

1332 using ^{14}C dating; period 3 (threshold discharge of 27000 m^3/s) represents a catastrophic flood, ^{14}C and IRSL dating of the underlying non-palaeoflood surface indicates that it occurred sometime between AD 1453 and AD 1785; and period 4 which occurred from AD 1785 to the modern day (threshold discharge of 9500 m^3/s). The authors suggest that the flood periods can be associated with wetter and warmer periods during the Holocene.

Holmes *et al.* (2003) investigated sedimentary sequences in the catchment of the upper Klein Seekoei River, a tributary of the Orange River. Stratigraphic analysis led to the identification of three major depositional cycles. A coarse boulder deposit was interpreted as the remains of a large fan from debris flow during, or prior to the last interglacial; the deposits would have been emplaced under high energy conditions, subsequent to a long period of weathering during cold conditions. The second depositional sequence of clastic sediments capped by organic rich sediment was associated with Holocene aggradation. This was followed by more recent mobilisation of fine silts and sands from the valley slopes.

Lewis and Illgner (1998) identified and dated river terraces of the Palmiet River (near Grahamstown). Evidence of continuous fine floodplain sediment accumulation was interpreted as reflecting an environmentally stable period between 9.6 ka BP and 4.4 ka BP.

As well as these studies on fluvial sequences from South Africa, work has also been undertaken on the west coast of Namibia. Sediment accumulation on the Hoanib river, in the Kaokoland Namib Desert, between AD 1640 and the 19th century was attributed to an arid climate in the hinterland associated with the Little Ice Age (LIA) by Vogel and Rust (1990). Using further ^{14}C dates, Rust (1999) reduced the length of the proposed arid period to between AD 1640 and AD 1720. Heine (2004) however, suggests that the silt accumulations do not indicate arid periods in the upper reaches of the catchment; instead they are indicative of extraordinary discharge events. Initial work by Heine and Heine (2002) found that the Homeb silts on the Kuiseb River in the Namib Desert were slack water deposits from flash floods. The main sediment accumulation of these silts was dated as occurring between 23 and 19 ka BP using ^{14}C,

indicating increased rainfall or increased high magnitude precipitation events in the Kuiseb catchment during this period. Further investigations into slack water deposits in various valleys in the Namib Desert by Heine (2004) found a young accumulation phase during the LIA, associated with extremely heavy rainfall in the catchments.

2.7.2.5 Tree ring studies

Hall (1976) published one of the first dendroclimatological studies in South Africa, measuring the ring size (i.e. growth increment) of a section of *Podocarpus falcatus* originating from the Karfkloof Forest in Natal. Changes in the ring size of this tree are thought to originate primarily from variation in the rainfall of the region. An ~18 year cycle, of various intensity, was identified in the growth structures and although the record was not interpreted in detail, increasing wetness was noted during the second half of the 18th century.

Two studies were also undertaken on a second trunk of *P. falcatus* (Thackeray, 1996; Thackeray and Potze, 2000). Unfortunately, although the tree is known to been have been felled in either 1932 or 1937, its origin is unknown. However, it is thought to possibly originate from the high rainfall region of Knysna on the southern Cape coast. Over 500 rings have been counted on the trunk section, developing a proxy for rainfall back to ~ AD 1350. When the tree-ring width was assessed, a 17.4 year cycle was evident, similar to the 18 year wet-and-dry cycle found by Tyson (1987) discussed previously.

2.7.3 Palaeoclimates since ~50 ka

The studies covered above have been summarised in a number of reviews by Tyson and his colleagues (Tyson, 1987; Tyson and Lindesay, 1992; Tyson, 1999; Tyson *et al.*, 2000; Tyson *et al.*, 2001). These works allow one to derive a general picture of climate change over the ~50 ka, as outlined below.

Over the period 51-43 ka, conditions were generally wet and relatively warm in southern Botswana (Holmgren *et al.*, 1995). From ~35 ka, the temperature became cooler in the interior (Scott, 1982) with temperatures in the summer rainfall zone over the period 30-13.8 ka on average 4-7°C cooler than the

modern climate (Talma and Vogel, 1992). The Makapansgat record (Holmgren *et al.*, 1999) shows evidence of more pronounced cooling into the last glacial maximum (LGM) during the period 23-21 ka. During the LGM, the temperatures over the southern African subcontinent were 5-6 °C lower than the modern day, with rainfall generally less than at present; at the site of the Tswaing crater, rainfall during LGM was estimated to have been 25% lower than the present day (Partridge, 1997). Evidence of cold conditions continuing after the LGM until 17.5 ka is found in the speleothem records from Cango Caves (Talma and Vogel, 1992) and Makapansgat (Holmgren *et al.*, 1999).

Cool conditions are also evident over the period covering ~16-13 ka in some records (Holmgren *et al.*, 1999; Smith *et al.*, 2002), but Tyson (1999) suggests that rapid warming occurred after 16 ka BP. A pronounced cold spell was centred on 14 ka, prior to warming during the Antarctic Cold Reversal at ~13.5 ka (Holmgren *et al.*, 2003). This was followed by further cooling (Scott, 1982; 1989; Holmgren *et al.*, 2003) with dry summers. During the Holocene altithermal (~7 ka) rainfall is thought to have decreased over eastern South Africa, whilst the interior and western areas were wetter than today (Fig. 2.26, Tyson, 1999). During the mid to late Holocene, speleothem records suggest that the warming ended ~5.5 ka, with decreasing temperatures also evident from pollen profiles (Scott, 1982; Scott and Vogel, 1983). A cool period occurred from 4.7-2.5 ka (Talma and Vogel, 1992), interrupted by a variable and moist climate during the period 4.3-3.2 ka (Talma and Vogel, 1992; Lee-Thorpe *et al.*, 2001).

Over the last 2 ka, temperatures have also been variable with a cooling period between AD 100-200 followed by warming between AD 240-600, and another cooling episode from AD 600-900 (Tyson *et al.*, 2001). Following this latter cooling episode, evidence of the Medieval Warm epoch can be found for the period AD 900-1300 (Tyson and Lindesay, 1992); during this time flooding increased on the lower Orange River (Zawada, 2000). The Little Ice Age (LIA) (AD 1300-1800) which followed, appears to have been evident at various localities in southern Africa characterised by colder and generally drier conditions, but with periods of increased storminess (Tyson and Lindesay, 1992; Tyson *et al.*, 2000). The lowest temperatures occurred around AD 1700,

following a short warm episode AD 1500-1675 (Tyson *et al.*, 2000). During the LIA, the summer rainfall region is thought to have become drier whilst the winter rainfall zone became wetter (Tyson and Lindesay, 1992). High magnitude flood events on the Orange River and in the Namib Desert during the LIA (Vogel and Rust, 1990; Rust, 1999; Zawada, 2000; Heine, 2004) have been attributed to warmer, wetter periods within the LIA (Zawada, 2000; Heine, 2004).

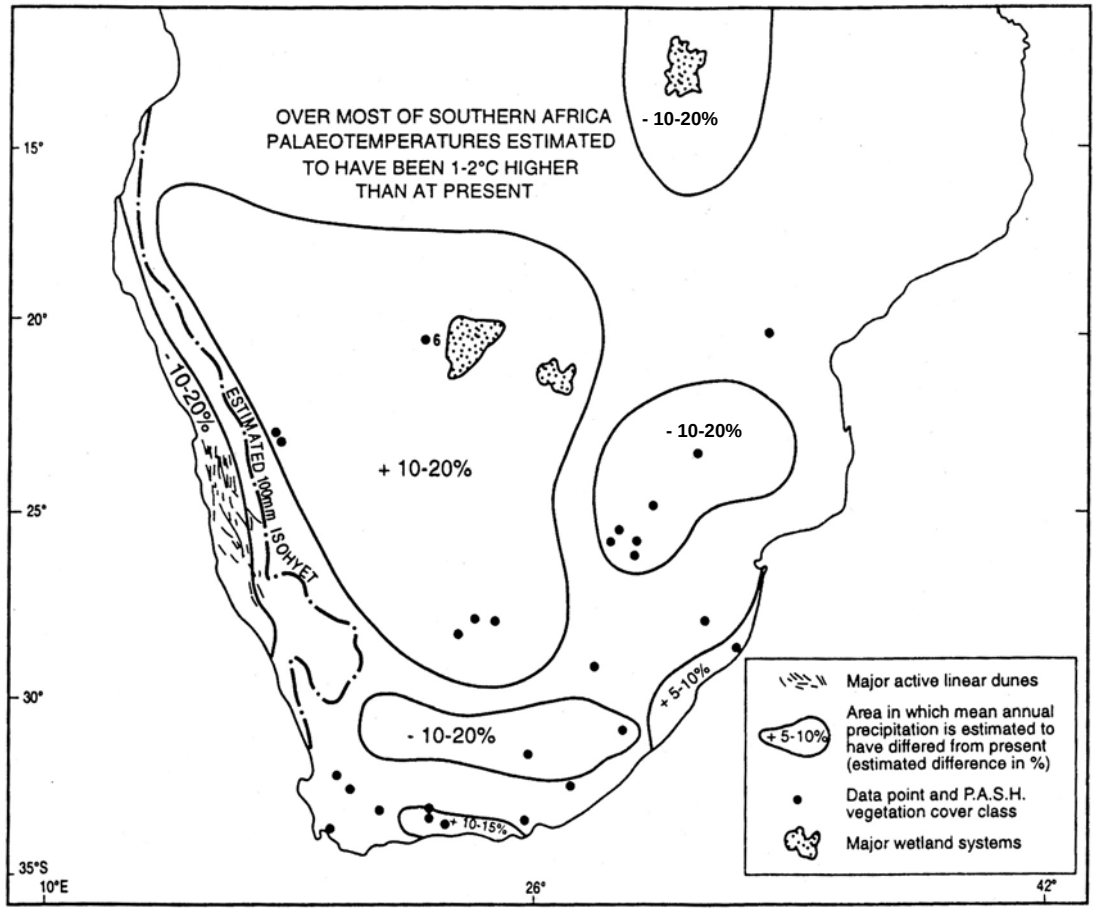

Figure 2.26: A palaeoclimatic reconstruction of rainfall conditions at the time of the Holocene Altithermal ~7ka BP. From Tyson (1999).

CHAPTER 3: DOSIMETRY

3.1 INTRODUCTION

The environmental dose-rate forms one half of the equation that forms the basis for OSL dating, thus its accurate assessment for each sample is important. For each grain, the total environmental dose-rate is a sum of two sources: 1) internal (i.e. radioisotopes present within the grain itself); and 2) external (i.e. potassium-40 (^{40}K), rubidium-87 (^{87}Rb), uranium (U) and thorium (Th) in the surrounding sediment, and cosmic radiation). The parent of the thorium decay series is ^{232}Th, and two series are present for natural uranium, ^{238}U and ^{235}U; the latter chain is a minor component and only accounts for 0.72 % of the atoms in natural uranium (Aitken, 1985). The external sources of radiation consist of alpha (α) particles from the decay chains of U and Th, beta (β) particles from the U, Th, K and Rb decay series, and gamma (γ) rays from U, Th, K, as well as a small contribution from cosmic radiation. Figure 3.1 shows the decay chains for ^{235}U, ^{238}U, and ^{232}Th.

The half-lives of the U and Th parent isotopes, and of ^{40}K, are of the order of 10^9 years. Thus the natural abundance of these remains nearly constant over the period of time that OSL dating is feasible (up to 10^5 – 10^6 years). By assessing the current radioactive flux, the dose-rate during the entire burial period can be calculated. The present-day dose-rate was determined in this thesis by emission counting methods which measure the α, β and/or γ emissions. This allows the concentration of the parent radionuclides to be calculated, and thus the total environmental dose-rate to be found.

Disequilibrium of the decay chain occurs when an isotope is added to or removed from a system without its parent or a daughter isotope (Osmond and Cowart, 1982). If an isotope is in disequilibrium with the rest of the decay chain, the concentration of daughter products will change through time and thus the environmental dose-rate cannot be calculated from the concentrations of the parent isotopes alone. Weathering processes in surficial environments can cause disequilibria by two main processes: solution and precipitation reactions;

a)

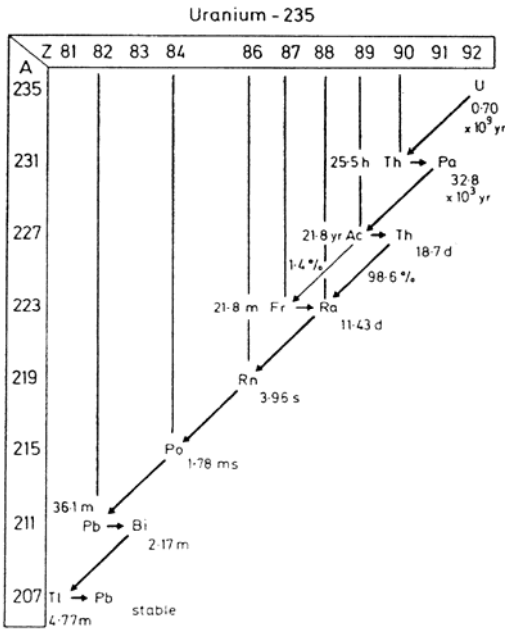

b)

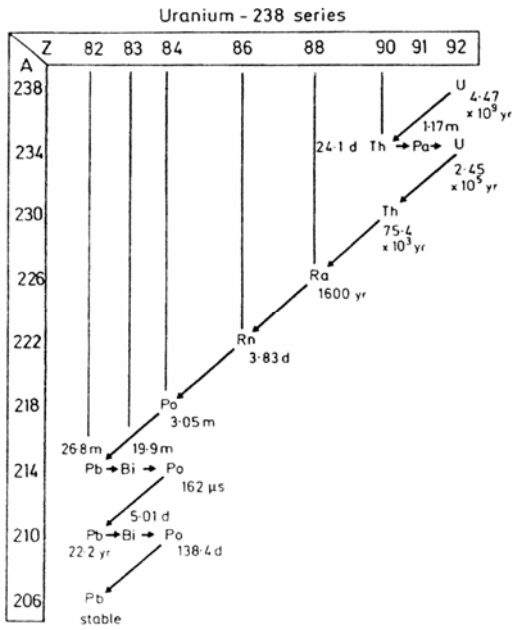

c)

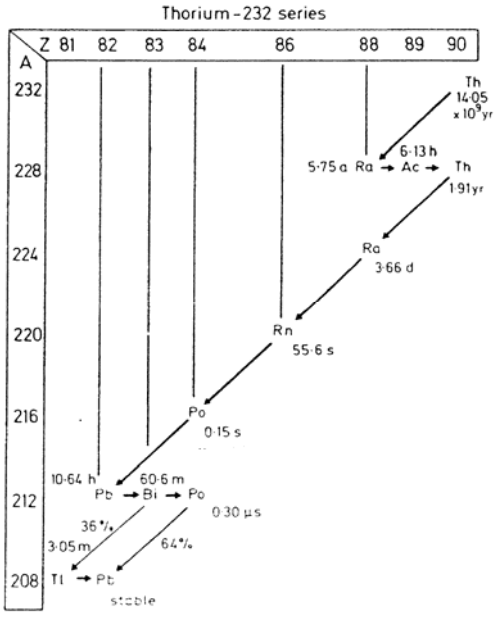

Figure 3.1: Decay series for a) ^{235}U; b) ^{238}U; and c) ^{232}Th. A long arrow indicates alpha decay and a short one beta decay. The half-lives of the isotopes are indicated. From Aitken (1985).

and emanation of radon isotopes (Olley *et al.*, 1996). These processes are more likely to occur in waterlain sediments, and thus for a fluvial environment it is important to assess if a decay chain is in secular equilibrium. Disequilibrium cannot be detected by all of the emission counting techniques, because some of these methods only allow the parent concentrations to be derived. Studies investigating sediments with disequilibrium have been performed using high-resolution gamma spectrometry (Olley *et al.*, 1996) or a combination of alpha-particle and gamma spectrometry (Krbetschek *et al.*, 1994; Olley *et al.*, 1997); these techniques determine the radioactivity of various nuclides in the decay chains. In this thesis, high-resolution gamma spectrometry is performed on some samples to assess equilibria of the decay chain.

Krbetschek *et al.* (1994) investigated the uranium fractionation (because of the weaker binding of ^{234}U to the crystal lattice of minerals than ^{238}U) of samples from various depositional environments. Their results (Fig. 3.2) suggested that $^{234}U/^{238}U$ disequilibrium predominantly occurs in limnic sediments, and this was attributed to leaching of water enriched in ^{234}U. A slight deficit of ^{234}U was evident in fluvial sediments, although this was only significant in one out of four samples. Olley *et al.* (1996) investigated 209 young (<50 years) fluvial samples for disequilibria in the both the U and Th decay chains. Their results showed significant disequilibrium for various parent-daughter ratios of the ^{238}U decay chain, although this rarely exceeded 50 %. The ^{232}Th decay chain was generally at or near secular equilibrium. In a number of samples, however, an excess of ^{228}Ra was present; this was attributed to rapid, significant, radium redistribution. Because of the short half-lives in the Th decay chain (the longest lived daughter product is ^{228}Ra with a half-life of 5.75 years), disequilibrium in the ^{232}Th decay chain is unlikely to be important in sediments that have been buried more than ~20 years (Olley *et al.*, 1996), and thus the ^{228}Ra excess should not be a problem in dose-rate calculation. The findings from these studies indicate that it is important to assess if disequilibrium, particularly in the U decay series, is present in the samples studied in this thesis.

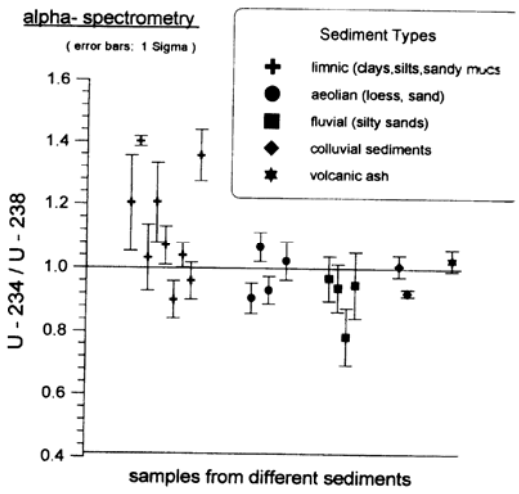

Figure 3.2: Comparison of the $^{234}U/^{238}U$ activity ratios for samples from different sediment types. From Krbetschek *et al.* (1994).

3.2 INTERNAL DOSE-RATE

The D_b values in this work are obtained from measurements on quartz grains. If K was present in significant quantities in the grains the Rb contribution to the internal dose-rate should be taken into account (Mejdahl, 1987). Quartz, however, contains very low levels of U, Th and K, and hence whilst the grains may have some slight alpha activity, one is able to assume that the internal dose-rate of the grains is negligible (Aitken, 1998).

The internal dose-rate of the quartz can be determined experimentally through alpha counting of a mineral separate. Feathers and Migliorini (2001) found values between 0.01 Gy/ka and 0.05 Gy/ka for the attenuated internal alpha dose-rate for quartz from East Africa, and Jacobs (2004) measured a similar value of 0.029 ± 0.002 Gy/ka for a sample from South Africa. Unfortunately, owing to the small amount of quartz obtained from samples in this study, the internal dose-rate could not be assessed. Because there is nothing to suggest that a significant internal dose-rate would be expected from the Klip River and Schoonspruit quartz, and because the values found by previous studies would contribute such a minor component of the total environmental dose-rate (<3 %), following the suggestion of Aitken (1985), the internal dose-rate of quartz was not taken into account in the total dose-rate for samples in this study.

3.3 EXTERNAL DOSE-RATE

Whilst the cosmic contribution to the environmental dose-rate can be calculated from the geographic location and overburden of a sample, the radiation emitted by U, Th and K within a sediment needs to be determined by measurement. For the work in this thesis, methods which measure the α and β particles and γ ray emissions over a given time were used. These "emission counting methods", such as thick source alpha counting (TSAC), G-M beta counting and gamma spectrometry, allow the concentrations of U, Th and K to be derived. From these values, the external alpha, beta and gamma dose-rates can be calculated. The external beta and gamma dose-rates, and the cosmic dose-rate, are used to derive the environmental dose-rate for the sample. The external alpha dose-rate does not need to be taken into consideration because alpha particles only penetrate the outer rind of a quartz grain; the alpha particles are attenuated before reaching the inner core and the HF acid treatment used in sample preparation (Section 4.2.5) etches away the alpha irradiated skin (the outer 10 μm of the quartz grain).

3.3.1 Cosmic ray contribution

The contribution of cosmic rays to the environmental dose-rate is generally small, but should be included in estimates of the external dose-rate (Aitken, 1985). Cosmic radiation consists of two types of components: the 'soft' component (electrons and photons) which is absorbed by the top 150 g/cm^3 (~0.6 m) of overburden; and the 'hard' component, which is mostly composed of muons (Aitken, 1998). This 'hard' component is less readily absorbed and thus penetrates to a much greater density than the 'soft' component. In this thesis, calculation of the cosmic ray contribution to the total dose-rate was undertaken using the software package COSMIC written by Robert Clark, University of Durham. The equation for the density dependence of the dose-rate, at densities less than 150 g/cm^3, is estimated by a fourth order polynomial, fitted to the data in Prescott and Hutton (1988):

$$D_C = 3.20\times10^{-2}x^4 - 1.35\times10^{-1}x^3 + 2.21\times10^{-1}x^2 - 2.07\times10^{-1}x + 0.295$$

where x is the density in 100 g/cm^3 and D_C is in Gy/ka. The equation used for derivation of the dose-rate from muons, at densities greater than 150 g/cm^3, is given in Prescott and Hutton (1994, after Barbouti and Rastin, 1983):

$$D_C = \frac{6072}{((x+11.6)^{1.68}+75)(x+212)} \exp(-5.50\times10^{-4}x)$$

where x is the density in 100 g/cm^3 and D_C is in Gy/ka. The dose-rate from cosmic rays has to be corrected for the altitude and geomagnetic latitude (λ) of the sample site. The geomagnetic latitude (λ) can be calculated using:

$$\sin\lambda = 0.203 \cos\theta \cos(\phi\text{-}291) + 0.979 \sin\theta$$

where θ is the geographic latitude and ϕ is the geographic longitude (with positive indicating north and east). The dose-rate can then be calculated using:

$$D = D_C\left[F + J\exp\left(\frac{h}{H}\right)\right]$$

where D is the corrected dose-rate, h is the altitude in km, and F, J, and H are obtained from the graph in Figure 3.3. The error on the cosmic dose-rate was generally taken to be 10 % of the cosmic dose-rate value.

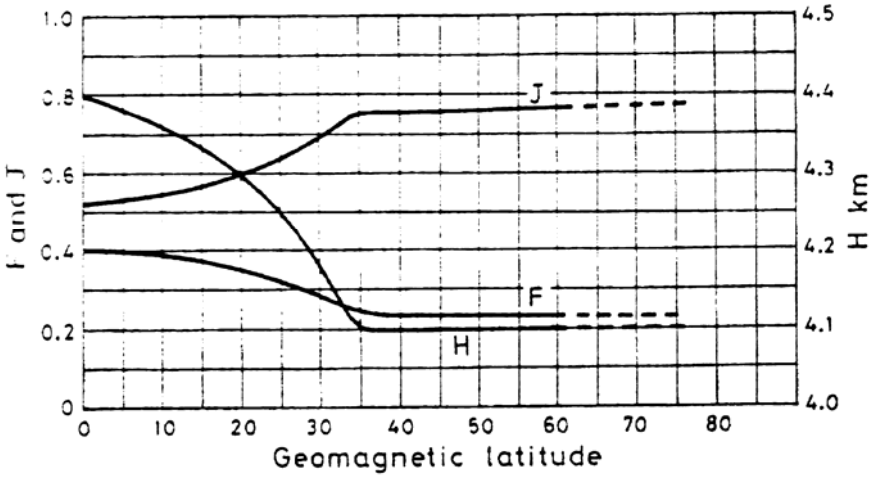

Figure 3.3: Parameters for calculation of cosmic dose-rate as a function of altitude and geomagnetic latitude. From Prescott and Hutton (1994).

From the Schoonspruit, a number of samples (91SC0403-09) were collected from the face of a section. In these instances the error was increased to 20 % to reflect the uncertainty on the timing of the cutting event. Because of the small solid angle of the horizon, the increase in cosmic dose-rate would be expected to be a second-order effect. In similar sampling circumstances, Burbidge (2003) found that the contribution to the gamma dose-rate from the cosmic dose-rate, at a distance of 12 cm into the face, was less than 1.8 %. For all the samples from the Klip River and Schoonspruit, it is likely that the overlying sediment would have accumulated rapidly following deposition, making a correction for changing overburden thickness unnecessary. The cosmic dose-rate for each sample is detailed in Table 3.1.

3.3.2 Water content

The water content of each sample was measured in the laboratory. The sampling tubes were completely sealed with plastic bags at the time of sampling, so the laboratory measured water content is a good representation of the field value. The water content measured in the laboratory is calculated as the mass of water divided by the mass of the dry sediment (after drying to a constant mass for at least 24 h at 50°C), multiplied by 100. The measured water content for each sample is shown in Table 3.1. For some samples, the saturation water content was calculated by weighing ~50 g of sediment into a nylon stocking, which was then placed in a beaker of water for 2 hours. The stocking and sediment were removed from the water, and after dripping had ceased, it was weighed. This was then dried in an oven (for at least 24 h at 50°C), before being weighed again. A good estimate of the water content is necessary for calculation of the appropriate environmental dose-rate because water absorbs a significant amount of radiation that would otherwise reach the mineral grains; a change of 10 % in the water content leads to a difference of ~10 % in the environmental dose-rate.

Table 3.1: Details of values and measurements used in calculating the environmental dose-rate. Including the sample code; sampling location and environment; depth of sample; depth of bedrock (BR); measured water content (WC); cosmic dose-rate; concentrations of potassium, uranium and thorium; sealed/unsealed (S/US) ratio from alpha counting; the infinite beta dose-rate; the gamma dose-rate; and the environmental dose-rate used in calculation of age.

Sample	Location*	Environ-ment	Depth (m)	BR (m)	WC (%)	Cosmic (Gy/ka)	Potassium (%)	Uranium (ppm)	Thorium (ppm)	S/US ratio	Infinite beta dose rate (Gy/ka)	Gamma dose-rate (Gy/ka)	Environmental dose-rate (Gy/ka)
70KLA1	Reach B	Channel	0.9 -1.0		25.6	0.239 ± 0.024	1.137 ± 0.110	3.256 ± 0.400	9.998 ± 1.327	1.026 ± 0.029	1.638 ± 0.052	1.120 ± 0.082	1.84 ± 0.11
70KLA2	Reach C	Channel	0.5 - 0.6		26.8	0.242 ± 0.024	1.086 ± 0.110	3.467 ± 0.394	9.385 ± 1.303	1.017 ± 0.026	1.612 ± 0.053	1.102 ± 0.081	1.82 ± 0.11
70KLA3	Reach D	Channel	1.5 - 1.6		15.2	0.220 ± 0.022	1.592 ± 0.133	4.161 ± 0.445	11.980 ± 1.476	1.047 ± 0.024	2.179 ± 0.071	1.427 ± 0.092	2.31 ± 0.13
70KLA4	Reach E	Channel	0.8 - 1.0		48.0	0.243 ± 0.024	1.298 ± 0.121	4.063 ± 0.427	11.237 ± 1.413	1.071 ± 0.024	1.915 ± 0.060	1.309 ± 0.088	2.11 ± 0.12
70KLA5	Reach F	Channel	1.1 - 1.2		18.1	0.231 ± 0.023	1.029 ± 0.082	2.448 ± 0.261	7.273 ± 0.864	1.031 ± 0.027	1.361 ± 0.046	0.873 ± 0.054	1.51 ± 0.08
70KLA6	Reach G	Channel	1.7 - 1.8		24.4	0.213 ± 0.021	1.345 ± 0.124	3.789 ± 0.431	11.038 ± 1.428	1.051 ± 0.036	1.906 ± 0.062	1.280 ± 0.089	2.06 ± 0.12
75KL0308	Reach B	Channel	0.8 - 1.0		80.4	0.370 ± 0.037	1.393 ± 0.124	3.994 ± 0.425	10.317 ± 1.406	0.995 ± 0.035	1.954 ± 0.064	1.281 ± 0.088	2.10 ± 0.12
75KL0309	Reach B	Channel	0.8 - 1.0		26.4	0.232 ± 0.023	1.166 ± 0.085	3.325 ± 0.232	7.411 ± 0.764	1.041 ± 0.036	1.600 ± 0.053	1.012 ± 0.049	1.74 ± 0.10
75KL0310	Reach A	Channel	1.2 - 1.5		21.8	0.220 ± 0.022	1.262 ± 0.099	3.763 ± 0.283	10.991 ± 0.938	0.996 ± 0.032	1.837 ± 0.060	1.255 ± 0.060	2.01 ± 0.11
75KL0311	Reach A	Channel	1.7 - 1.8		11.4	0.213 ± 0.021	1.297 ± 0.088	2.475 ± 0.262	7.063 ± 0.865	1.044 ± 0.032	1.568 ± 0.052	0.931 ± 0.055	1.65 ± 0.09
75KL0314	Reach B	Oxbow	1.2 - 1.4		13.0	0.220 ± 0.022	0.855 ± 0.121	5.152 ± 0.454	11.233 ± 1.499	1.063 ± 0.023	1.727 ± 0.054	1.324 ± 0.093	2.00 ± 0.12
75KL0315	Reach B	Oxbow	1.5 -1.6		49.5	0.214 ± 0.021	1.385 ± 0.113	2.431 ± 0.383	12.796 ± 1.278	1.064 ± 0.026	1.787 ± 0.059	1.220 ± 0.080	1.96 ± 0.11
75KL0316	Kadies Drift	Oxbow	0.2 - 0.4	0.7	7.9	0.299 ± 0.030	0.807 ± 0.043	1.017 ± 0.115	3.046 ± 0.376	0.963 ± 0.035	0.862 ± 0.030	0.456 ± 0.025	1.32 ± 0.09
75KL0317	Kadies Drift	Scroll bar	1.2 - 1.4		15.8	0.226 ± 0.023	1.285 ± 0.080	1.898 ± 0.236	7.523 ± 0.782	0.978 ± 0.034	1.488 ± 0.048	0.885 ± 0.050	2.08 ± 0.15
75KL0318	Kadies Drift	Scroll bar	0.4 - 0.6		12.7	0.266 ± 0.027	1.434 ± 0.106	2.421 ± 0.337	12.103 ± 1.125	0.951 ± 0.033	1.805 ± 0.059	1.198 ± 0.071	2.63 ± 0.19
75KL0319	Kadies Drift	Scroll bar	0.5 - 0.7		9.6	0.256 ± 0.026	1.246 ± 0.098	2.687 ± 0.323	8.731 ± 1.069	0.996 ± 0.036	1.605 ± 0.053	1.022 ± 0.067	2.30 ± 0.17
75KL0320	Kadies Drift	Scroll bar	0.3 - 0.5		8.7	0.277 ± 0.028	1.130 ± 0.118	3.354 ± 0.429	11.758 ± 1.424	1.015 ± 0.034	1.695 ± 0.056	1.213 ± 0.088	2.57 ± 0.19
75KL0321	Kadies Drift	Scroll bar	1.1 - 1.3		25.7	0.231 ± 0.023	1.398 ± 0.116	3.634 ± 0.382	10.958 ± 1.265	0.991 ± 0.026	1.923 ± 0.063	1.272 ± 0.079	2.74 ± 0.20
75KL0322	Waaihoek	Scroll bar	1.5 - 1.7		12.7	0.212 ± 0.021	1.467 ± 0.102	2.642 ± 0.306	11.260 ± 1.019	1.075 ± 0.032	1.840 ± 0.060	1.191 ± 0.065	2.49 ± 0.17
75KL0323	Waaihoek	Scroll bar	0.7 - 0.9		5.7	0.236 ± 0.024	1.535 ± 0.109	2.668 ± 0.328	12.928 ± 1.093	1.024 ± 0.030	1.943 ± 0.064	1.290 ± 0.069	3.03 ± 0.24
75KL0324	Waaihoek	Scroll bar	0.8 - 1.0		3.0	0.232 ± 0.023	1.525 ± 0.100	2.923 ± 0.286	8.196 ± 0.945	1.079 ± 0.035	1.843 ± 0.060	1.091 ± 0.060	2.76 ± 0.22
75KL0325	Waaihoek	Scroll bar	0.5 - 0.7		2.4	0.253 ± 0.025	0.985 ± 0.082	2.306 ± 0.270	7.412 ± 0.894	1.021 ± 0.033	1.310 ± 0.044	0.853 ± 0.056	2.12 ± 0.17
75KL0326	Waaihoek	Point bar	0.0 - 0.2		20.2	0.328 ± 0.033	0.859 ± 0.065	1.569 ± 0.203	6.371 ± 0.671	1.006 ± 0.035	1.074 ± 0.037	0.689 ± 0.042	1.64 ± 0.11
75KL0327	Waaihoek	River Bank	0.0 - 0.2		3.4	0.328 ± 0.033	0.288 ± 0.102	4.386 ± 0.397	11.763 ± 1.314	0.997 ± 0.030	1.186 ± 0.041	1.125 ± 0.081	2.40 ± 0.19
75KL0328	Reach B	Oxbow	1.1 - 1.3		18.1	0.226 ± 0.023	0.974 ± 0.103	2.462 ± 0.383	12.796 ± 1.278	1.126 ± 0.027	1.470 ± 0.047	1.124 ± 0.079	1.74 ± 0.10
75KL0329	Reach B	Channel	1.5 - 1.7		39.8	0.211 ± 0.021	1.567 ± 0.114	3.689 ± 0.366	10.073 ± 1.209	1.006 ± 0.035	2.039 ± 0.063	1.277 ± 0.076	2.13 ± 0.12

75KL0330	Reach C	Channel	1.3 - 1.5		16.3	0.225 ± 0.023	1.531 ± 0.100	3.192 ± 0.283	7.803 ± 0.932	1.060 ± 0.023	1.876 ± 0.061	1.104 ± 0.060	1.94 ± 0.11
75KL0331	Reach C	Channel	1.0 - 1.1		22.5	0.232 ± 0.023	1.483 ± 0.100	4.105 ± 0.276	8.768 ± 0.909	1.047 ± 0.034	1.998 ± 0.062	1.242 ± 0.059	2.10 ± 0.12
75KL0332	Reach E	Channel	0.9 - 1.1		34.8	0.203 ± 0.020	1.485 ± 0.117	3.668 ± 0.373	11.494 ± 1.238	1.136 ± 0.036	2.010 ± 0.065	1.322 ± 0.078	2.13 ± 0.12
75KL0333	Reach E	Channel	0.8 - 0.9	1.8	70.4	0.207 ± 0.021	1.585 ± 0.125	3.438 ± 0.431	11.402 ± 1.432	0.968 ± 0.034	2.052 ± 0.064	1.316 ± 0.089	2.16 ± 0.13
75KL0334	Reach E	Oxbow	0.8 - 1.0		20.7	0.211 ± 0.021	1.144 ± 0.078	2.271 ± 0.222	7.320 ± 0.734	1.117 ± 0.032	1.426 ± 0.048	0.883 ± 0.047	1.53 ± 0.08
75KL0335	Reach E	Oxbow	2.0 - 2.2	2.5	24.8	0.179 ± 0.018	0.654 ± 0.074	2.677 ± 0.252	7.947 ± 0.832	1.128 ± 0.038	1.119 ± 0.039	0.840 ± 0.052	1.32 ± 0.07
75KL0336	Reach G	Channel	1.9 - 2.1	3.0	16.5	0.181 ± 0.018	1.459 ± 0.148	2.541 ± 0.554	18.165 ± 1.855	1.094 ± 0.025	2.008 ± 0.066	1.506 ± 0.114	2.23 ± 0.14
78KL0337	Reach G	Channel	1.7 - 1.8		20.0	0.188 ± 0.019	1.422 ± 0.146	3.783 ± 0.527	16.875 ± 1.760	1.016 ± 0.031	2.125 ± 0.069	1.576 ± 0.109	2.34 ± 0.14
75KL0338	Reach G	Channel	2.5 - 2.6		10.2	0.169 ± 0.017	1.343 ± 0.098	2.653 ± 0.296	11.150 ± 0.986	1.020 ± 0.033	1.742 ± 0.057	1.157 ± 0.062	1.85 ± 0.11
75KL0339	Reach E	Channel	1.1 - 1.3	1.6	71.0	0.223 ± 0.022	1.480 ± 0.094	3.509 ± 0.238	6.709 ± 0.780	1.017 ± 0.018	1.853 ± 0.061	1.076 ± 0.051	1.91 ± 0.11
75KL0340	Reach E	Oxbow	1.5 - 1.7		64.2	0.193 ± 0.019	1.537 ± 0.118	4.042 ± 0.356	11.893 ± 1.182	1.083 ± 0.033	2.117 ± 0.069	1.396 ± 0.075	2.23 ± 0.13
75KL0341	Reach E	Oxbow	1.3 - 1.5		29.4	0.186 ± 0.019	1.409 ± 0.131	3.953 ± 0.459	12.068 ± 1.522	1.130 ± 0.360	2.009 ± 0.065	1.364 ± 0.095	2.14 ± 0.13
75KL0342	Reach E	Channel	2.1 - 2.3		57.0	0.196 ± 0.020	1.444 ± 0.105	3.375 ± 0.327	7.819 ± 1.077	1.075 ± 0.022	1.836 ± 0.060	1.105 ± 0.068	1.89 ± 0.07
92KL0401	Kadies Drift	Scroll bar	0.9 - 1.1		20.6	0.299 ± 0.030	1.517 ± 0.095	2.539 ± 0.263	8.916 ± 0.875	1.063 ± 0.02	1.744 ± 0.058	1.060 ± 0.056	2.45 ± 0.18
91SC0401	Upper FP**	Oxbow	1.2 - 1.3		14.7	0.233 ± 0.044	1.452 ± 0.100	3.067 ± 0.295	8.722 ± 0.976	1.080 ± 0.029	1.600 ± 0.053	1.115 ± 0.062	2.52 ± 0.19
91SC0403	Upper FP**		0.9		7.6	0.232 ± 0.046	1.490 ± 0.099	3.480 ± 0.282	6.386 ± 0.924	0.990 ± 0.026	1.623 ± 0.054	1.159 ± 0.059	2.68 ± 0.21
91SC0404	Upper FP**		1.8		9.3	0.236 ± 0.047	1.630 ± 0.105	1.970 ± 0.324	9.527 ± 1.079	1.059 ± 0.029	1.601 ± 0.053	1.072 ± 0.068	2.65 ± 0.21
91SC0405	Upper FP**		1.4		9.8	0.217 ± 0.044	1.542 ± 0.099	2.666 ± 0.287	8.943 ± 0.949	1.087 ± 0.031	1.616 ± 0.053	1.102 ± 0.061	2.64 ± 0.21
91SC0406	Upper FP**		0.5		4.5	0.258 ± 0.052	1.722 ± 0.104	2.356 ± 0.293	9.529 ± 0.971	1.027 ± 0.031	1.714 ± 0.057	1.138 ± 0.062	2.95 ± 0.24
91SC0407	Inset FP**		0.8		6.8	0.235 ± 0.048	1.671 ± 0.102	2.490 ± 0.315	8.415 ± 1.042	1.083 ± 0.033	1.669 ± 0.052	1.088 ± 0.066	2.78 ± 0.23
91SC0408	Inset FP**		0.4		10.0	0.269 ± 0.054	1.528 ± 0.084	1.371 ± 0.224	8.048 ± 0.748	1.095 ± 0.028	1.418 ± 0.048	0.909 ± 0.048	2.35 ± 0.18
91SC0409	Inset FP**		1.2		14.1	0.224 ± 0.044	1.589 ± 0.099	2.826 ± 0.277	8.117 ± 0.914	1.025 ± 0.024	1.649 ± 0.055	1.092 ± 0.059	2.57 ± 0.19
91SC0410	Upper FP**	Oxbow	2.5 - 2.6		9.2	0.189 ± 0.038	1.656 ± 0.105	2.326 ± 0.308	10.471 ± 1.025	1.061 ± 0.024	1.687 ± 0.056	1.164 ± 0.065	2.76 ± 0.22

* All the samples located in a "Reach A-G" are from the Seekoeivlei floodplain

** “FP” represents “floodplain”

The water content value used to calculate ages for the samples from the Klip River was selected on the basis of the depositional environment. The scroll-bar sequences on the Klip River are located downstream of the Seekoeivlei floodplain wetlands and are thus are only inundated for short periods of time following major flood events. For the scroll bars at these two sites, Waaihoek (samples 75KL0322-25) and Kadies Drift (samples 75KL0317-21 and 92KL0401), the average water content measured from the field samples was used in the dose-rate calculation (6 % and 15 %, respectively). For the oxbow lakes and modern samples from the scroll-bar sites, the measured water content was used.

For the samples from the Seekoeivlei site, the average measured water contents for the palaeochannels and the oxbow lakes were 32 % and 28 %, respectively. The history of variation in the water content is likely to be similar for all the samples from the Klip River floodplains because the topographic variations are so minor, so that when flooding occurs, the majority of the depressions such as palaeochannels and oxbows are inundated or saturated. For ten samples from the Seekoeivlei site (70KLA1-6, 75KL0314-15, 75KL0329-30) the saturation water content was calculated, and the values ranged from ~50 % to ~80 %, with an average value of 71 %. The field water content values were measured on samples from the Seekoeivlei site collected in the austral winter, whilst the saturation value is representative of the state of the sediment during the summer, when flooding occurs. Since an assessment of the two end states has been made, a value halfway between these end states was considered appropriate for age calculation of these samples, and therefore a water content value of 50 % was used. For all the samples, an error of 10 % on the water content value was included to reflect the uncertainty in assessment.

The Schoonspruit has cut through a downstream dolerite barrier leading to incision through the sandstone/shale bedrock. Thus floodplain inundation in the upstream reach of the Schoonspruit, where the samples were collected from, only occurs very infrequently. This means that for the samples from the Schoonspruit, the measured field water content (~5-15 %) should be a good representation of the average water content since deposition, so they were

used in the dosimetry calculation. An error of 10 % on the water content values was incorporated to account for the uncertainty of the level in saturation over time.

3.4 THICK SOURCE ALPHA COUNTING (TSAC)

Thick source alpha counting (TSAC) measures the combined, total alpha-particles emitted from the decay of the U and Th decay chains. In this study, TSAC was undertaken at the Aberystwyth Luminescence Laboratory using Daybreak 582 and 583 alpha-counters. A sample for alpha counting is dried, and then milled in a ball mill to homogenise the sediment. For measurement, a zinc sulphide (ZnS) screen is held in a Perspex holder and the milled sample is spread over the screen to a depth greater than the range of alpha particles in the material (~1 mm). The retaining ring in the holder allows the counting area to be well defined. Interaction between ionising radiation emitted by the sample with the ZnS screen causes the screen to scintillate; when the holder is placed onto the detection window of a photomultiplier tube, the photons produced by the scintillations are detected as a current pulse across the photocathode.

All the samples in this study were measured in holders with counting areas of 15.45 cm^2. The background counts for couplets of ZnS screens were counted, with a glass screen inserted, for at least 24 h prior to the screen being used with a sample. Once the sample was loaded, wooden spacers were inserted between the holder and the lid to allow the 'unsealed' alpha counts to be measured until a minimum of 3000 counts had been registered. Following this, the holder was sealed tight and the 'sealed' alpha count was continued until at least 1000 counts were registered.

3.4.1 Calculation of U and Th concentrations

In the ^{232}Th decay chain, the successive alpha decays of ^{220}Rn to ^{216}Po (half-life = 0.145 s) emit alpha particles within quick succession. These are counted using a gate set to 0.21 s as a pairs count (Aitken, 1990). Since about 3 % of the counts in the Th decay chain are emitted as such a pair, the pairs count can be used as a measure of the Th activity in a sample. The number of pairs counted, compared to the total alpha particles detected, can be used to

calculate the U and Th concentrations in the sample (Aitken, 1985). The calculations used to derive the U and Th concentrations are detailed in Appendix A. The U and Th concentrations of each sample calculated from TSAC are shown in Table 3.1.

3.4.2 Detection of radon escape

Measuring both the sealed and unsealed alpha counts allows any radon (Rn) escape to be detected (Aitken, 1985). Rn gas is a daughter product in the decay series from ^{232}Th, ^{238}U and ^{235}U. A different isotope of Rn is produced in each decay series, with different half-lives (shown in brackets): ^{220}Rn (55.6 s), ^{222}Rn (3.83 d); and ^{219}Rn (3.96 s). If the radon gas escapes through the pores of the sediment, disequilibrium in the decay chain can result; if this is not detected, the environmental dose-rate for a sample will be incorrectly calculated. If no Rn escape has occurred, the sealed/unsealed ratio should be close to unity and not in excess of 1.10. The sealed/unsealed ratios for the Klip River and Schoonspruit samples are shown in Table 3.1, and averaged 1.041 ± 0.007 and 1.056 ± 0.012, respectively, demonstrating that radon escape is not a problem.

3.5 GM-BETA COUNTING

Beta counting at the Aberystwyth Luminescence Laboratory was performed using the Risø GM-25-5 beta counter (Bøtter-Jensen and Mejdahl, 1988). This measures the combined beta dose-rate (D_β) from U, Th and K in the sample holder. A sample for beta counting is dried, and then milled in a ball mill to homogenise the sediment. To measure a sample, a Perspex pot (internal measurements of 21 mm diameter and 7 mm depth) is packed with this homogenous sediment and the top is levelled to form a flat surface. This top surface is covered with a layer of cling-film to prevent contamination of the counter.

The GM-25-5 beta counter consists of five gas flow (99 % argon, 1 % isobutane) Geiger-Muller counter elements, and a common guard counter (Fig. 3.4). The cosmic ray background is reduced by the guard counter, which uses an anticoincidence technique to reject coincidence counts from the guard and

detectors (Bøtter-Jensen and Mejdahl, 1988). In addition, the instrument is placed inside a 100 mm thick lead shield to reduce the ambient background radiation. A sample slide with places for five sample pots is used to ensure that the position of the samples under the GM counters is reproducible. Three replicates of each sample were counted at the same time as two standards of known radioactivity: milled Shap granite ($D_{\beta\text{-Shap}}$ = 5.99 Gy/ka) and magnesium oxide (MgO) powder ($D_{\beta\text{-Mgo}}$ = 0.00 Gy/ka). Each measurement run was made for at least 24 h. The raw counts at each position were corrected for minor variations in the detection efficiency of the GM counters, using the values calculated by Helen Roberts (University of Wales, Aberystwyth) following analyses of a ^{36}Cl standard, to yield the corrected counts (CC).

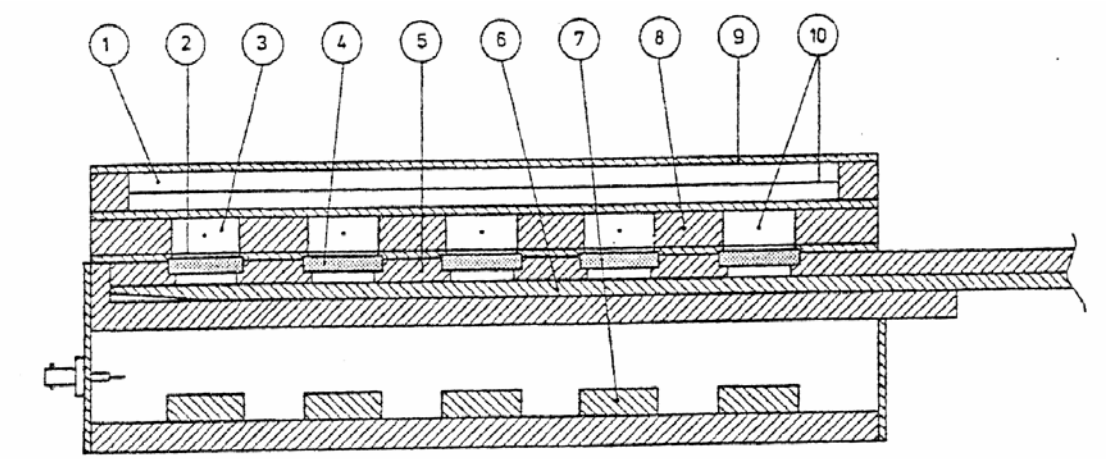

Figure 3.4: The schematic diagram of the GM-25-5 beta counter showing (1) guard counter, (2) aluminised Mylar window, (3) sample counter, (4) sample, (5) sample slide, (6) lift slide, (7) pre-amplifier, (8) acrylic frame, (9) Cu plate, and (10) anode cores.

3.5.1 Calculation of beta dose-rate and K concentration

The dose-rate of each sample ($D_{\beta\text{-sample}}$) was determined by interpolation of the corrected counts from the average of measurements on three pots of the sample, between the two standards with known dose-rates using the following equation (errors from counting statistics were propagated through):

$$D_{\beta\text{-sample}} = D_{\beta\text{-Shap}} [(CC_{sample} – CC_{Mgo})/ (CC_{Shap} – CC_{Mgo})]$$

where D_β is the beta dose-rate and CC are the position corrected counts. The beta dose-rate expected from the concentrations of U and Th derived from TSAC can be calculated using the conversion factors from Adamiec and Aitken (1998). Subtracting this value from the measured beta dose-rate for the sample allows the beta dose-rate from K to be found, and thus the K concentration to be derived. The calculations for the K concentration for each sample are shown in Appendix A, and the K concentration of each sample is detailed in Table 3.1.

3.5.2 Reproducibility of the beta dose-rate measurements

The reproducibility of the measurements of beta dose-rate for the three pots of each sample was investigated using the Klip River and Schoonspruit samples. For one sample, 75KL0309, the beta dose-rate was measured a number of times. Initially, a set of three pots was counted five times giving 15 beta dose-rates in total; the location of the pots, including the Shap and MgO standards, were changed after each measurement. The average beta-dose rate of the 15 position corrected values was 1.92 ± 0.01 Gy/ka, with a relative standard deviation of 2.8 %. The pots were then repacked four times from the bulk sample, allowing the beta dose-rate to be measured from 12 different pots. The average beta-dose rate of these values was 1.89 ± 0.03 Gy/ka, with a relative standard deviation of 4.8 %.

For all the samples counted using the GM-beta counter (n = 63, some samples were measured more than once), the position corrected beta dose-rate was calculated for each pot, and the standard deviation of the mean of the three beta dose-rates was found for each sample. The results (Fig. 3.5) showed a range in the percentage standard deviation of between 0.4 % and 6.1 %, with an average value of 2.3 %. Based on measurements both of different samples, and recounting of sample 75KL0309, a value of 3 % was selected to represent a systematic error on the beta dose-rate of the sample. This value was added in quadrature to the error from the interpolation of the sample counts to calculate the total error on the beta dose-rate.

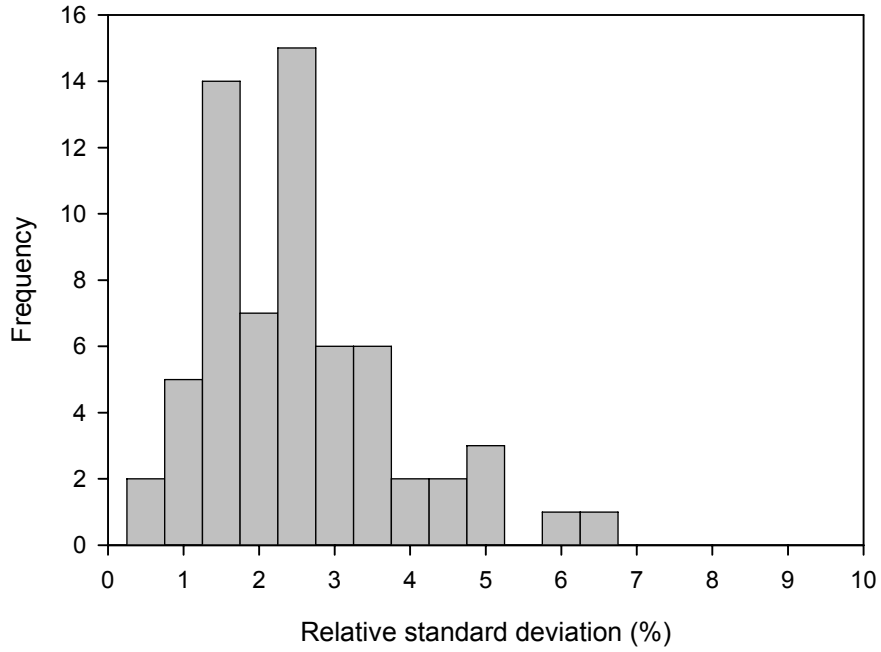

Figure 3.5: Relative standard deviations (%) on the position corrected beta dose-rates found for the three pots of each sample from the Klip River and Schoonspruit.

3.6 FIELD GAMMA SPECTROMETRY (FGS)

Measurements of the gamma dose-rate in the field were made for six samples from the Klip River, using the Aberystwyth portable field gamma spectrometer (FGS). The spectrometer used at Aberystwyth is an EG&G Micronomad gamma spectrometer with a two inch sodium iodide (NaI) crystal. In a similar manner to alpha counting, gamma rays produce scintillations in the crystal which a photomultiplier converts to a pulse of electricity (Aitken, 1985). Peaks in the gamma spectrum can be associated with discrete nuclides from the decay chains; integration of these peaks allows the U, Th and K concentrations, and the cosmic dose-rate to be calculated. For uranium, the 1.76 MeV peak from ^{214}Bi is integrated over the range 1.69 - 1.84 MeV. For thorium, the 2.61 MeV peak from ^{208}Tl is integrated between 2.46 - 2.76 MeV. For potassium, the 1.46 MeV ^{40}K peak is integrated between 1.38 and 1.53 MeV. All pulses above 3 MeV are recorded as cosmic dose. The spectrum measured for sample 75KL0311 is shown in Figure 3.6. The photopeak associated with each nuclide

has a tail to lower energies, which is termed the Compton continuum (Aitken, 1985). This tail arises from the interaction of some of the gamma photons with the NaI crystal, such that these photons initially only deposit some of their energy in the crystal, with the rest continuing as a lower energy photon. In order to correct for the interference of peaks used for derivation of U and K by higher energy nuclides, spectrum stripping is performed.

The FGS has been calibrated using four blocks of doped concrete, based at the Research Laboratory for Archaeology and the History of Art, University of Oxford; an undoped block was used for background measurement, and the remaining three were doped with either U, Th or K. The concentrations of the radionuclides in the blocks are known, allowing the peak height of the spectrum to be directly correlated to the concentration of the radionuclide. For the measurements of the field gamma spectra made in this study, the spectrometer was placed directly into the sampling hole, and the measurement was made for between 30 and 60 minutes.

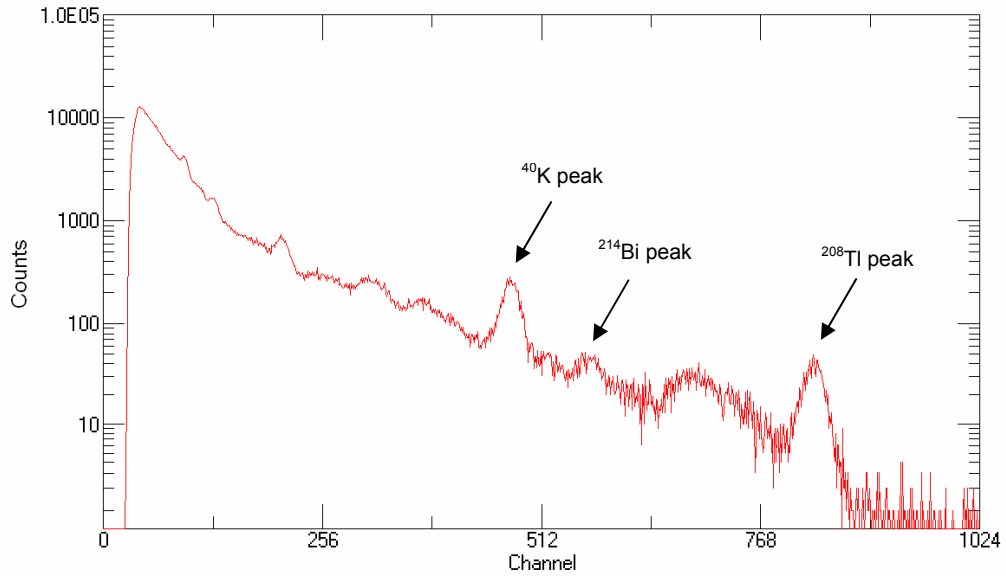

Figure 3.6: Gamma spectrum measured using a field gamma spectrometer for 40 minutes for sample 75KL0311. The peaks indicated are integrated to obtain U (^{214}Bi), Th (^{208}Tl), and K (^{40}K) concentrations.

3.6.1 Water content correction

Whilst the laboratory methods of determining the environmental dose-rate are made on dried sample, the FGS measurements are made *in situ* and thus the effect of the water content in the sediment is included in the results. In order to allow a comparison of the values obtained from the FGS with the laboratory derived values, a water content correction needs to be applied to the data from the field gamma spectrometer (Jacobs, 2004; p228, Fig 7.12). These data were corrected using the equation in Aitken and Xie (1990), following one proposed by Zimmerman (1971). The gamma dose-rate for a dry soil was calculated from:

$$\gamma_d = \gamma_w(1 + 1.14WF)$$

where γ_d is the dry dose-rate, γ_w is the dose-rate in a wet soil with a saturation water content (W) for F, the average level of saturation in the sample over the burial period (expressed as a fraction of the saturation water content). The value of 1.14 was suggested by Zimmerman (1971) on the basis that for gamma rays of ~1 MeV, this is the ratio of the absorption coefficients for water and aluminium (which has similar absorption properties to soil).

When the measurements from the Klip River were corrected for the water content, the measured field water content (divided by 100) was substituted for the WF term, and an error on the water content percentage of 5 % (i.e. 0.05) was included in the calculation.

3.7 HIGH-RESOLUTION GAMMA SPECTROMETRY (HRGS)

High-resolution gamma spectrometry (HRGS) gives information on the concentrations of some of the parent and daughter nuclides in the U, Th and K decay chains. This method was used to investigate whether the decay series were in equilibrium or not, in addition to using the sealed/unsealed ratio from TSAC to detect radon escape. The high resolution gamma spectrometer at Aberystwyth is an EG&G ORTEC High Purity Germanium gamma-ray detector with a coaxial photon detector system. The entire detector is housed in 100 mm thick lead shielding, which is lined with a lower atomic number liner to attenuate

^{10}Pb contamination and lead X-rays generated in the shield (Ivanovich and Murray, 1992).

Liquid nitrogen is used to maintain the germanium semiconductor diode at -196°C, as this minimises detector leakage current and gives the best resolution possible. The use of a semiconductor diode allows the electrons ejected from atoms by gamma rays to be measured directly without the use of a photomultiplier, thus improving the resolution (Aitken, 1985). The improvement in resolution allows isotopes with similar energies to be detected individually, whereas the resolution obtained with FGS is not sufficient to do this.

Samples for HRGS are ashed at 450°C to remove any organic matter, and then milled in a tema mill to homogenise the sample. A known mass of the milled sample (~220 g) is mixed with an epoxy resin to form a Marinelli geometry cast with a volume of ~200 cm^3. After the cast has been made, it is left for at least 28 days prior to measurement to allow the levels of ^{222}Rn (Murray, 1981) and the short-lived daughters of ^{228}Th to equilibrate. Casts of six samples from the Klip River were measured for 400 ks (~4.75 days) each. The peak areas associated with the energies of the different isotopes are determined from a calibration obtained from a number of low- and high-activity standards by Helen Roberts (University of Wales, Aberystwyth).

3.7.1 Calculation of activities

Using HRGS, the activity of some radionuclides can be measured directly from peaks in the gamma ray spectrum (Fig. 3.7), whilst some have to be derived from the activities of other radionuclides in the decay series. ^{238}U cannot be measured directly but can be derived from the ^{234}Th activity (~63 keV and ~92 keV) as the two radionuclides generally exist in secular equilibrium (Murray *et al.* 1987). The weak emission of ^{234}U (~53 keV) cannot be measured because of interference from ^{214}Pb, and a weak emission from ^{230}Th at ~68 keV is not sufficient to allow direct measurement of this radionuclide in these samples. To derive the concentration of these radionuclides, secular equilibrium was assumed and the activities of ^{234}U and ^{230}Th were calculated as the mean of the estimates of ^{238}U and ^{226}Ra. The activity of ^{226}Ra was derived from its emission

at ~186 keV, taking into account the contribution from ^{235}U emission at this level. ^{210}Pb was measured directly using the ~46 keV gamma line.

^{232}Th has no direct emission, but was calculated as the average of ^{212}Pb (~239 keV), ^{208}Tl (~583 keV) and ^{228}Ra, where ^{228}Ra is derived assuming secular equilibrium from the short-lived daughter ^{228}Ac (~338, 911 and 969 keV) (Ivanovich and Murray, 1992). ^{220}Rn was also calculated as the average of these radionuclides (^{228}Ra, ^{212}Pb and ^{208}Tl), whilst ^{228}Th was calculated as the average of ^{224}Ra, ^{212}Pb and ^{208}Tl (^{224}Ra at ~241 keV) . The activity of K in the sample can be derived directly from the peak associated with ^{40}K at ~1461 keV.

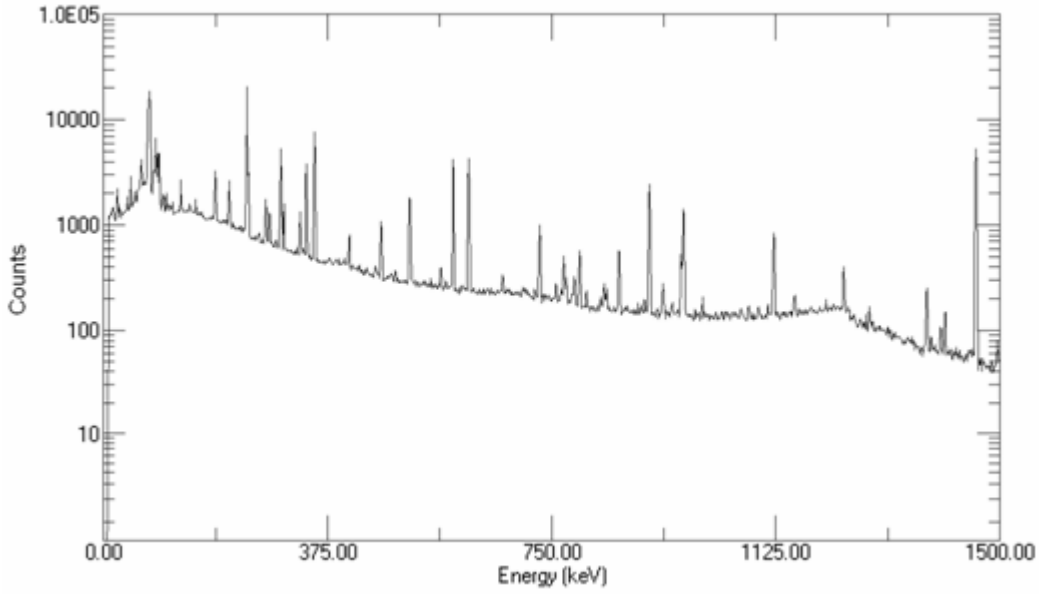

Figure 3.7: Gamma spectrum measured using a high resolution gamma spectrometer for 400 000 s for sample 75KL0311.

3.7.2 Investigation into disequilibrium

Disequilibrium in the ^{238}U decay chain can be a problem in estimating the environmental dose-rate for fluvial sediments (Olley *et al.*, 1996). Disequilibrium in the ^{238}U series is generally assessed by finding the activity ratios for ^{238}U, ^{234}U, ^{230}Th and ^{226}Ra (Ivanovich and Harmon, 1992). When using HRGS, however, the values for ^{234}U and ^{230}Th are based on the activities of ^{238}U and ^{226}Ra, so only ^{238}U and ^{226}Ra should be compared. ^{210}Pb, a late member in the ^{238}U series, can also be measured directly; using this

radionuclide allows one to investigate the state of equilibrium at the latter end of the decay chain. The calculated radionuclide concentrations for the Klip River samples analysed are detailed in Table 3.2. Figures 3.8a and b show the levels of the daughter products ^{226}Ra and ^{210}Pb, plotted as a function of the parent isotope (^{238}U). The results show that there is a slight excess of ^{226}Ra in all the samples studied, but this is generally within 20 % of equilibrium (Fig. 3.8a); the average ^{226}Ra/^{238}U activity ratio is 1.18 ± 0.08. This level of disequilibrium is similar to what was found in modern fluvial sediments by Olley *et al.* (1996). The ^{210}Pb values are closer to equilibrium with ^{238}U (Fig. 3.8b); the average ^{210}Pb/^{238}U activity ratio is 1.10 ± 0.09, consistent with unity within two sigma errors.

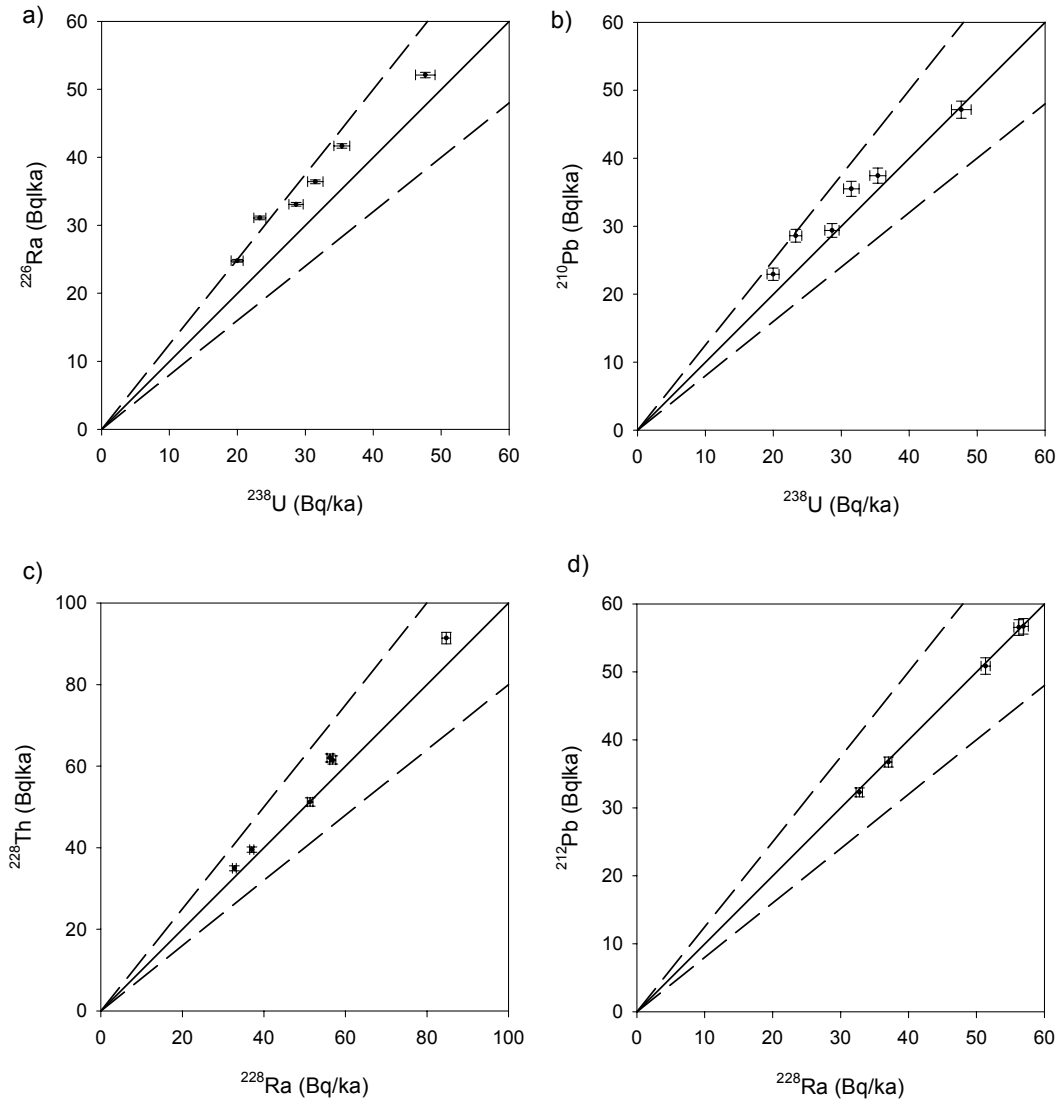

Figure 3.8: Equilibrium plots for HRGS results from six Klip River samples, showing: a) ^{226}Ra/^{238}U; b) ^{210}Pb/^{238}U; c) ^{228}Th/^{228}Ra; and d) ^{212}Pb/^{228}Ra. The solid line represents secular equilibrium and the dashed lines indicate the range of values that are within 20 % of equilibrium.

Table 3.2: Radionuclide activities (Bq/kg) for samples from the Klip River.

Sample	^{238}U	^{226}Ra	^{210}Pb	^{228}Th	^{228}Ra	^{212}Pb	^{40}K
75KL0311	28.6 ± 1.1	33.1 ± 0.3	29.4 ± 1.0	51.2 ± 1.0	51.3 ± 0.7	50.9 ± 1.2	464 ± 7
75KL0315	47.7 ± 1.4	52.1 ± 0.4	47.1 ± 1.3	91.4 ± 1.4	84.7 ± 1.0	84.7 ± 1.7	423 ± 7
75KL0331	31.5 ± 1.1	36.4 ± 0.3	35.5 ± 1.1	61.5 ± 1.0	56.9 ± 0.7	56.7 ± 1.2	489 ± 8
75KL0333	20.0 ± 0.9	24.8 ± 0.2	22.9 ± 0.9	39.5 ± 0.7	37.0 ± 0.5	36.7 ± 0.8	404 ± 6
75KL0336	35.4 ± 1.2	41.7 ± 0.3	37.4 ± 1.1	62.0 ± 1.0	56.2 ± 0.7	56.5 ± 1.2	464 ± 7
75KL0340	23.3 ± 0.9	31.1 ± 0.3	28.6 ± 0.9	35.0 ± 0.6	32.8 ± 0.5	32.3 ± 0.7	397 ± 6

The slight excess of ^{226}Ra found in the samples is likely to be caused by the mobility of this radionuclide in environments with fluctuating ground-water levels. Olley *et al.* (1996) modelled the effect of a 50 % excess of ^{226}Ra on the dose-rate with time (Fig. 3.9); if the dose-rate is derived from values of the parent isotopes only, and the decay chain is assumed to have always been in equilibrium, the maximum deviation from the true dose-rate is 4 %. The ^{226}Ra excess in the sediments from the Klip River is generally less than 20 %, so one would expect that the maximum deviation in the calculated dose-rate (assumed from parent isotopes only) from the true dose-rate (i.e. taking into account the ^{226}Ra excess), would be less than 2 %. Because the U decay series contributes only ~30 % of the beta and gamma radiation for the Klip River samples, the deviation in the true dose-rate owing to the excess ^{226}Ra is negligible, and thus does not need to be taken into account.

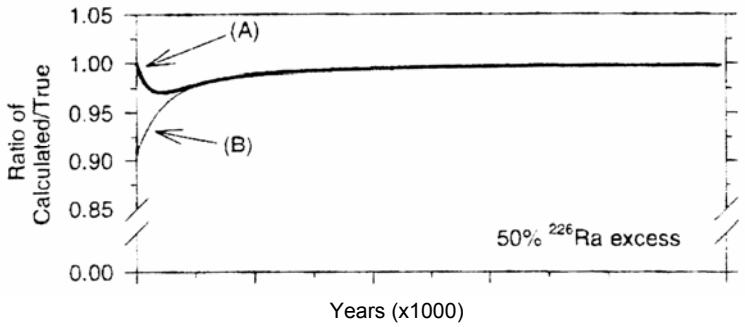

Figure 3.9: Graph showing the effect of a 50 % excess of ^{226}Ra on the calculated/true dose-rates as a function of time. (A) assuming that the dose-rate measured at the time of sample collection (not necessarily assuming secular equilibrium) has prevailed; and (B) assuming that the decay chains have always been in equilibrium and deriving the dose-rate from measurements of the parent isotope only. From Olley *et al*. (1996).

Thorium is generally thought to be immobile in most sediments, and disequilibrium of the decay chain is unimportant in sediments that have been buried for longer than 20 years (Olley *et al.*, 1996). Nevertheless, ensuring that the Th decay chain is in equilibrium is important, as it allows one to make a confident estimate of the dose-rate arising from ^{232}Th and its daughters. ^{232}Th cannot be measured directly from HRGS, so the concentration of its daughter product ^{228}Ra is used for comparison instead. For this study, the concentration of ^{228}Ra is compared to the ^{228}Th and ^{212}Pb, which is located near the end of the decay chain. A slight excess of ^{228}Th is found in the Klip River samples (Fig. 3.8c); however, the ^{228}Th/^{228}Ra activity ratio has an average of 1.07 ± 0.04, demonstrating equilibrium within two sigma. When looking at ^{212}Pb, which occurs near the bottom of the Th decay chain, the values of ^{212}Pb and ^{228}Ra are consistent with equilibrium (Fig. 3.8d); the average ^{212}Pb/^{228}Ra activity ratio is 0.99 ± 0.01. These results indicate that disequilibrium is insignificant in the Th decay chain.

3.8 COMPARISON BETWEEN THE DIFFERENT METHODS OF DOSE-RATE DETERMINATION

The environmental dose-rate can be determined from the three methods of analysis used in this thesis: thick source alpha counting and GM-beta counting (TSAC & GM-beta); field gamma spectrometry (FGS); and high resolution gamma spectrometry (HRGS). Because the latter two gamma spectrometry methods derive the values of U, Th and K from measurement of the gamma spectrum, it is appropriate to compare the gamma dose-rate for a dry sediment (water content = 0 %) calculated by the different methods. Measurements for TSAC & GM-beta and HRGS are made on a dried, milled sample so no correction for water content is necessary, and the FGS results were corrected as described in Section 3.6.1.

Table 3.3 shows the dry gamma dose-rates for samples which were analysed using more than one method. The ratios of the results from either FGS or HRGS, to those obtained from TSAC & GM-beta, are also detailed. Although the ratios of the gamma dose-rates obtained using different analytical methods are not always consistent with unity, the average ratios for the spectrometry

methods compared to TSAC & GM-beta are consistent with unity. Thus, these results indicate that there is no systematic deviation in the gamma dose-rate calculation when using any of the method of analysis. As no method shows evidence of either over- or under-estimating the gamma dose-rate, all are equally suitable for sample analysis in order to calculate the environmental dose-rate. Ideally, all the samples in a study should have the environmental dose-rate found from the same method of analysis, so TSAC and GM-beta counting was used for every sample.

Table 3.3: Dry gamma dose-rates derived using field gamma spectrometry (FGS), thick source alpha counting and GM-beta counting (TSAC & GM-beta) and high-resolution gamma spectrometry (HRGS), for samples where at least two methods were used. The ratios of FGS and HRGS, to TSAC & GM-beta are also shown.

	Dry gamma dose-rate (Gy/ka)			Ratios	
Sample	**FGS**	**TSAC & GM-beta**	**HRGS**	**FGS/TSAC& GM-beta**	**HRGS/TSAC& GM-beta**
75KL0310	1.31 ± 0.07	1.26 ± 0.06		1.05 ± 0.07	
75KL0311	1.07 ± 0.06	0.93 ± 0.06	1.23 ± 0.02	1.15 ± 0.09	1.32 ± 0.08
75KL0314	1.08 ± 0.06	1.32 ± 0.09		0.82 ± 0.07	
75KL0315		1.22 ± 0.08	1.77 ± 0.02		1.45 ± 0.10
75KL0317	0.99 ± 0.05	0.89 ± 0.05		1.12 ± 0.09	
75KL0318	0.90 ± 0.05	1.20 ± 0.07		0.75 ± 0.06	
75KL0319	1.09 ± 0.06	1.02 ± 0.07		1.06 ± 0.09	
75KL0331		1.24 ± 0.06	1.34 ± 0.01		1.08 ± 0.05
75KL0333		1.32 ± 0.09	0.93 ± 0.01		0.71 ± 0.05
75KL0336		1.51 ± 0.11	1.38 ± 0.02		0.92 ± 0.07
75KL0340		1.40 ± 0.08	0.91 ± 0.02		0.65 ± 0.04
Average ratios				**0.99 ± 0.07**	**1.02 ± 0.13**

3.9 GAMMA DOSE-RATE HOMOGENEITY

Aitken (1985) states that samples for luminescence dating should be taken from a location where the surrounding sediment is uniform in every direction for 0.3 m. When trying to date the last river flow in a palaeochannel or oxbow, ideally the uppermost bedload sand should be sampled (Section 2.5.1). This sampling procedure, however, means that the OSL sample itself is thus derived from sediment <10 cm below a change in the sedimentary type. Directly above the final bedload sand in the abandoned channels of the Klip River the sediment

generally consisted of an organic-rich fine sandy clay. From two locations, this overlying post-abandonment infill was sampled in order to allow assessment of the gamma dose-rate; these samples were given the same sample code as the luminescence sample, with a suffix 'B'. Additionally, at a surficial exposure of sandstone bedrock, a sample (75KL0313) was taken for assessment of the gamma dose-rate. Although the modern Klip River flows directly on its sandstone/shale bedrock, older fluvial deposits underlie the samples taken for OSL dating. At a number of locations, augering was continued after the OSL sample was collected to determine the depth of bedrock (Table 3.1); at all of these locations the bedrock was at least 0.3 m below the OSL sample.

The gamma dose-rates for the samples, calculated from the concentrations of U, Th and K derived from TSAC and GM-beta counting on the dried milled sample, are shown schematically in Figure 3.10 and detailed in Table 3.4. The results indicate that the bedrock has a much lower gamma dose-rate than the sediment associated with the palaeochannels. This should not be a problem, however, for assessment of the correct dose-rate for the OSL samples because these were collected from at least 0.3 m above the bedrock base of the valley. The gamma dose-rates of the two samples of organic-rich sandy clay are dissimilar, but because only two samples were collected, this may not be representative of the system as a whole.

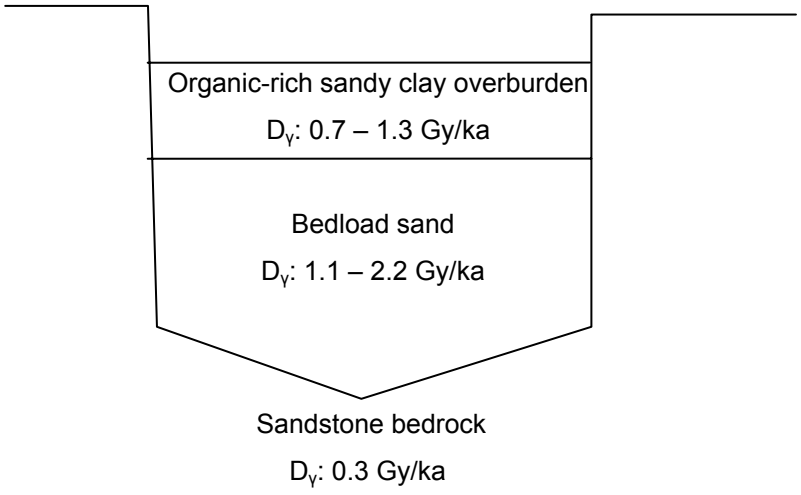

Figure 3.10: Range in gamma dose-rates found for samples from the different sedimentary units.

Table 3.4: Gamma dose-rates calculated for: sandstone bedrock (75KL0313); organic-rich fine sandy clay overlying samples taken for OSL dating (75KL0314B, 75KL0315B); and the comparative OSL bedload sand samples (75KL0314, 75KL0315).

Sample	Gamma dose-rate (Gy/ka)	Comparative OSL Sample	Gamma dose-rate (Gy/ka)
75KL0313	0.324 ± 0.015		
75KL0314B	0.657 ± 0.042	75KL0314	1.324 ± 0.093
75KL0315B	1.320 ± 0.077	75KL0315	1.200 ± 0.080

Nevertheless, whilst the gamma dose-rates for sample 75KL0315 and its organic-rich sandy clay overburden (75KL0315B) are consistent within errors, those associated with sample 75KL0314 vary considerably. Calculations by Løvborg (Aitken, 1985) allow one to assess the effect of adjacent sediments with different radioactivities on one another. Using the gamma dose-rates for samples 75KL0314 and 75KL0314B to represent the worst-case scenario, the total gamma dose-rate in the sediment either side of the boundary between the organic-rich sandy clay and the final bedload sand has been calculated. The results are shown in Figure 3.11; the solid line shows the gamma dose-rate in the sediment at any given vertical distance from the horizontal boundary, whilst the dashed and dotted lines indicate the gamma dose-rate from the organic-rich sandy clay overburden and the bedload sand, respectively. At a depth of 10 cm into the bedload sand, the total gamma dose-rate is 1.224 ± 0.054 Gy/ka, which leads to a total environmental dose-rate of 1.946 ± 0.243 Gy/ka. Using the gamma dose-rate calculated from TSAC and G-M beta counting of the bedload sand (1.324 ± 0.093 Gy/ka), the total environmental dose is 1.997 ± 0.248 Gy/ka. Therefore the effect of the lower gamma dose-rate from the organic-rich sandy clay overburden leads to a 2 % decrease in the total environmental dose-rate at 10 cm into the bedload sand. However, given the ~10 % error in the total dose-rate calculation, and because this calculation was based on the most extreme discrepancy between the gamma dose-rates, the difference in the gamma dose-rate from the organic-rich sandy clay overburden is thought to be negligible.

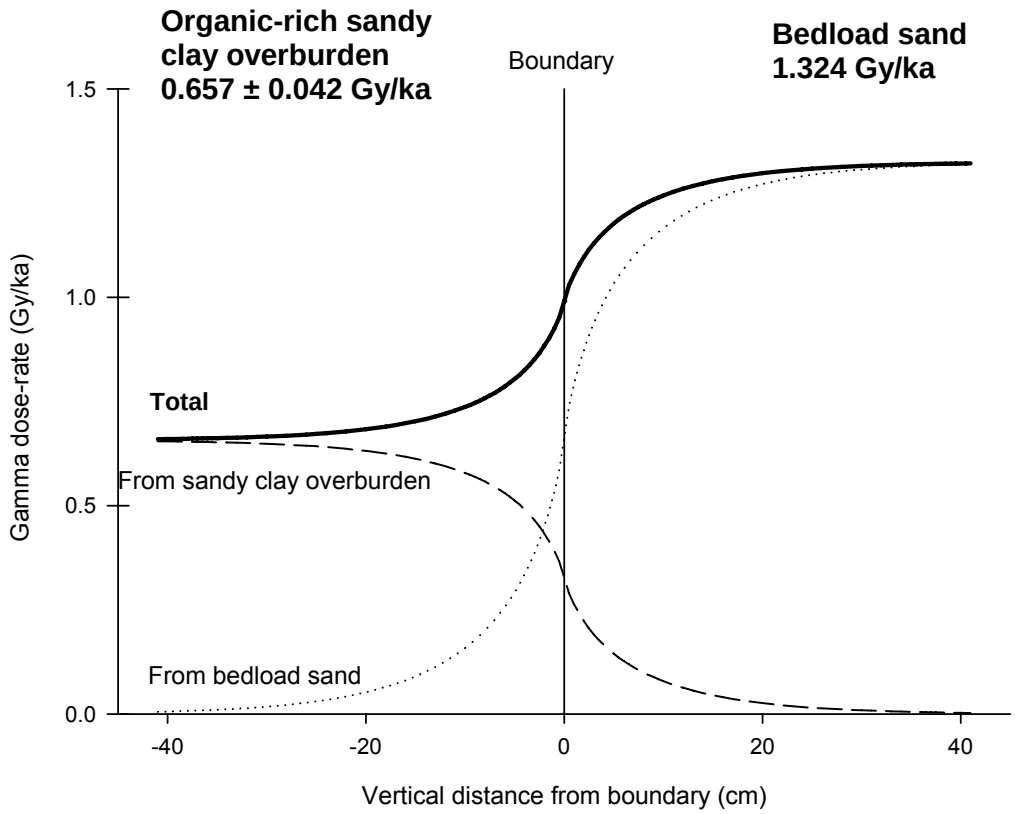

Figure 3.11: The predicted gamma dose-rate around the boundary between the organic-rich sandy clay overburden and the bedload sand for the location of sample 75KL0314. The dotted line shows the gamma dose-rate from the bedload sand, the dashed line shows that from the post-abandonment organic-rich sandy clay overburden, and the solid line shows the total gamma dose-rate at any vertical distance from the sedimentological boundary.

3.10 DERIVATION OF THE ENVIRONMENTAL DOSE-RATE

The concentrations of the radioelements (in ppm for U and Th, and % for K) derived from TSAC and GM-beta counting were converted to dose-rates (in Gy/ka) in the software package LDB2005, written by Geoff Duller, by using the conversion factors in Adamiec and Aitken (1998). The emission values (from nuclear data tables) for the three radioactive decay series were converted to dose-rate by assuming an infinite matrix where the rate of energy emission is equal to the rate of energy absorption in a volume with dimensions greater than the ranges of the radiation. An example of the conversion from radioelement concentration to the alpha, beta and gamma dose-rate is shown in Appendix A; and this is automated in LDB2005. As mentioned in Section 3.3, the alpha

dose-rate does not need to be taken into account in calculation of the environmental dose-rate. The unattenuated beta and gamma dose-rates, and the total environmental dose-rates are detailed in Table 3.1.

3.10.1 Attenuation of the beta dose-rate

The beta dose-rate needs to be corrected both for attenuation within the grains and for attenuation from the water content of the sediment (Bell, 1979; Mejdahl, 1979). The degree of attenuation within the grain is dependent on the energy of the emission, and thus varies according to whether the emission is from U, Th or K. Mejdahl (1979) provided tabulated figures for the absorbed beta-dose in quartz grains over a range of diameters (5-10 000 μm); from these, the appropriate values for the grain size of quartz used for OSL analysis can be selected to calculate the attenuation.

The HF etching performed on the quartz grains will have a disproportionate effect on the beta dose-rate. This is because the exterior of the grain will have a higher absorbed fraction than the centre of the grain (Mejdahl, 1979). In the program LDB2005, the values used for the effect of etching are taken from Bell (1979), who calculated the effect of etching on each of the beta emissions from the U, Th and K chains, and thus the attenuation factors take into account the distribution of dose within the grain arising from the different energies of the emissions.

The values used to account for the attenuation of the beta-dose (Mejdahl, 1979) and the effect of HF etching (Bell, 1979) are shown in Table 3.5. These values are for grains in the 180 – 212 μm size fraction, with the outer 10 μm removed from HF etching.

Table 3.5: Beta dose-rate correction factors to account for attenuation within the grain and the effect of HF etching for 180 – 212 μm grains

Nuclide	Correction factor
U	0.800 ± 0.07
Th	0.733 ± 0.08
K	0.931 ± 0.06
Average	0.879 ± 0.04

3.10.2 Correcting for water content

Water within the pore space of sediments absorbs beta and gamma radiation that would otherwise reach the grains. The water content correction for the gamma dose-rate has already been covered in Section 3.6.1, but it is included again here for completeness. Using the equations in Aitken and Xie (1990), following those proposed by Zimmerman (1971), the correction for the water content for the beta and gamma dose-rates can be calculated using:

$\beta_w = \beta_d/(1 + 1.25WF)$

$\gamma_w = \gamma_d/(1 + 1.14WF)$

where β_w and γ_w are the beta and gamma wet dose-rates in a soil with a saturation water content (W) for F, the average level of saturation in the sample over the burial period (expressed as a fraction of the saturation water content), and β_d and γ_d are the beta and gamma dry dose rate. For the purposes of correcting the beta and gamma dose-rates in this thesis, the water content value chosen to be suitable for the depositional environment (discussed in Section 3.3.2) was substituted for WF. The final environmental dose-rates for all the samples from the Klip River and the Schoonspruit are given in Table 3.1, and these ranged from ~1.3-2.9 Gy/ka.

3.11 CONCLUSIONS

In this chapter, the various methods used to calculate the U, Th, and K concentrations from the Klip River and Schoonspruit samples have been outlined. Both laboratory and field-based methods were used, and conversion of the radionuclide concentrations from the three methods to gamma dose-rates allowed a comparison between the different techniques. The results indicated that there was no systematic deviation between the methods. Previously, disequilibrium in the U and Th decay chains has been found in fluvial sediments. HRGS showed a slight ^{226}Ra excess in the U decay chain of the Klip River samples, but the effect of this on the total environmental dose-rate is minor. Combined with a Th decay chain in equilibrium, disequilibrium was deemed not to be a problem for the Klip River samples. As significant

disequilibrium is not evident, using the parent radioelements to derive the environmental dose-rate is sufficient, thus for standard analyses, thick source alpha counting and GM-beta counting on dried milled samples was performed.

Investigation of gamma dose-rate heterogeneity between the different sediment types present at the palaeochannel and oxbow sample sites showed that the post-abandonment organic-rich sandy clay overburden has a slightly lower gamma dose-rate than the bedload sand, whilst the underlying bedrock has a much lower gamma dose-rate than either of the overlying units. The difference in the dose-rate between the post-abandonment infill and that of the bedload sand was shown to cause a 2 % decrease in the environmental dose-rate when the worst example of heterogeneity in the gamma dose-rate was used. This difference in the environmental dose-rate is insignificant when compared to other errors on the environmental dose-rate, which arise primarily from doubt in the water content estimate. Furthermore, because the OSL samples were taken from at least 30 cm above the bedrock, the difference in the gamma dose-rates of the bedload sand and the bedrock does not need to be taken into account.

Assessment of the correct environmental dose-rate is vital to allow the correct age to be calculated for a sample using optically stimulated luminescence dating as it forms one half of the age equation. Assessing the value used in the other half of the equation, D_b, forms the subject of the following chapters.

CHAPTER 4: MEASUREMENT AND CHARACTERISATION OF THE OPTICALLY STIMULATED LUMINESCENCE SIGNAL

4.1 INTRODUCTION

When measuring an optically stimulated luminescence (OSL) signal for dating a deposit, it is desirable that the signal is derived from a single type of mineral grain. OSL dating of coarse mineral grains is generally performed on either quartz or potassium feldspar mineral separates. Quartz grains are the most commonly used in recent research. One of the primary reasons why quartz has increasingly been used in preference to feldspar is that the latter may be subject to anomalous fading (Lamothe and Auclair, 1999). To ensure that the OSL signal from a multiple-grain aliquot is produced by only one type of mineral, careful preparation of the samples needs to be undertaken in the laboratory. Details of the preparation techniques used for the samples in this thesis will be outlined in this chapter.

In addition, the OSL signal from quartz grains is known to consist of a number of discrete components (e.g. Bailey *et al.*, 1997). So, if quartz is being analysed, assessing what components are present in the OSL signal from a sample is important for determining which procedures are appropriate for obtaining equivalent dose values. This chapter reports the results of investigations into the components found in the OSL signal from quartz obtained from the Klip River and Schoonspruit, and describes the equipment used for measurement.

4.2 SAMPLE PREPARATION

After collection in the field, the samples for OSL dating were wrapped tightly in thick black plastic bags to ensure that they were not exposed to light until opened in the laboratory. The sampling techniques used (detailed in Section 2.5.1) should mean that the sediment was not exposed to any sunlight during collection. However, to ensure that the sample used for dating was completely unexposed, the sediment at both ends of the tube was removed to a depth of 3 cm. This removed portion was retained for dosimetry measurements. All

sample pre-treatment stages were undertaken in subdued red-light conditions so that the OSL signal of the quartz was not affected.

At least 600 g of sediment from each sample was removed from the unexposed part of the sampling tube and placed in a labelled beaker for treatment following standard techniques used at the Aberystwyth laboratory. Preparation of the initial sample suite (70KLA1-6) took an unusually long time (up to three months), and on drying at 60°C the samples formed solid brick-like clumps. These problems were thought to arise because the samples had a high proportion of clay and silt-sized particles. A number of procedures to remove these fine grains and speed up the processing of samples in the laboratory were used as detailed below (Section 4.2.1). Following the removal of the fine grains the samples were dried for a least 24 h at 60°C, before undergoing subsequent stages of preparation (Section 4.2.2-4.2.5).

4.2.1 Removal of fine grains

Three methods were used to remove fine grains (<90 μm) from the sediment sample before subsequent treatment stages were performed. The details of these three methods are outlined below.

Method 1: Sodium Oxalate ($Na_2C_2O_4$)

Sodium Oxalate acts as a deflocculating agent allowing each particle to settle individually. A 0.01 Normal solution of Sodium Oxalate was made up by mixing 6.7 g of Sodium Oxalate with 10 litres of distilled water. Following “Stokes' Law” the settling times for different grain sizes were calculated; over a depth of 30 cm it takes 20 minutes for particles <11 μm to settle, and 40 minutes for particles <4 μm to settle. For the samples from the Klip River, approximately 100 g of sediment was put in a 1 litre measuring cylinder, which was filled with the Sodium Oxalate solution to a depth of 30 cm. The measuring cylinder was put in a sonic bath for 10 minutes followed by 1 minute of vigorous manual shaking. It was then placed in the fume cupboard and allowed to settle for 20 minutes to remove all particles greater than 11μm. The material still in suspension (i.e. <11 μm) was decanted into a beaker. This procedure was performed on each 100 g

of sediment at least three times. The remaining sediment was washed three times with distilled water to remove the Sodium Oxalate.

Method 2: Sodium Pyrophosphate decahydrate ($Na_4O_7P_2.10\ H_2O$)

Sodium Pyrophosphate decahydrate also acts as a deflocculating agent and disperses the clays particles. A beaker containing the sample was filled with a 5 % solution of Sodium Pyrophosphate decahydrate and stirred vigorously. This was allowed to settle for 20 minutes, and then the liquid and material in suspension were decanted. The 5 % Sodium Pyrophosphate decahydrate solution was added to the sample in the beaker until the liquid appeared clear after settling for 20 minutes.

Method 3: Wet-sieving at 90 μm

To remove all particles <90 μm in diameter, the sediment samples were wet-sieved through a 90 μm sieve. In order to do this, small amounts of the sample (~30 g) were placed in a 10 cm diameter sieve with a 90 μm mesh. The sieve was washed through with tap water to allow particles <90 μm to go through the mesh, until the water running through the sieve was clear.

Prior to using method 3, either method 1 or 2 was employed in order to deflocculate the clays and thus allow the sample to be wet sieved with ease. For the initial sample suite, consisting of samples 70KLA1-6, method 1 was used. This method however, is very time-consuming because of the number of times it has to be performed for each sample. Method 2 is a lot more efficient because the entire sample can be treated at once, and multiple samples can be treated simultaneously. Thus, all samples subsequent to the initial sample suite (i.e. those prefixed with 75KL03-; 91SC04-; and 92KL04-) had the grains <11 μm removed using method 2, prior to being wet-sieved.

4.2.2 Sieving

Each sample was dry sieved through a set of six sieves (90, 125, 150, 180, 212, 250 μm mesh size) using an automatic sieve shaker for 45 minutes. The grains

retained in the size fractions 180-212 μm and 212-250 μm were used in the subsequent steps.

4.2.3 Removal of carbonates

The sample was covered in 10 % v.v. hydrochloric acid (HCl) and stirred periodically to enable chemical reactions to occur and remove any carbonates in the sediment. Cessation of any reaction took less than 24 hours for the samples from the Klip River and the Schoonspruit, and in many instances no reaction occurred at all. The sample was then rinsed three times in distilled water.

4.2.4 Removal of organics

The sample was placed in 20 volumes hydrogen peroxide (H_2O_2) to digest any organic matter. The sample was stirred periodically, and additional H_2O_2 added until any reaction had finished. The length of time taken by this stage of treatment varied between one and three months. The sample material had a low organic content (<2 %) so the reaction was not vigorous, however it persisted for a relatively long time. Once the reaction ceased, distilled water was used to rinse the sediment three times.

4.2.5 Isolating quartz

Isolating quartz from the multi-mineral sample was performed in two stages, and the size fractions 180-212 μm and 212-250 μm were processed separately. In the first stage, the sample was split according to density using sodium polytungstate (SPT) solutions with densities of 2.62 g/cm^3 and 2.70 g/cm^3. These were used to remove feldspars ($\rho < 2.62$ g/cm^3) and heavy minerals ($\rho > 2.70$ g/cm^3), respectively. The remaining grains (2.62 g/cm^3 < ρ < 2.70 g/cm^3) were retained for the second stage.

In the second stage, to ensure that the quartz extract obtained from SPT separation was completely free of feldspar contamination and to etch the alpha-irradiated 'skin' of the quartz grains, the grains were placed in 40 % hydrofluoric acid (HF) for 45 minutes. This was followed by treatment for 45 minutes in concentrated hydrochloric acid to remove any fluoride precipitates, and three

distilled water washes. This treatment was undertaken by Lorraine Morrison. The HF-etched material was re-sieved, and grains retained in the original size fraction (either 180-212 μm of 212-250 μm) were then used for OSL analysis. During routine measurements, the purity of the quartz was checked using an infra-red stimulation to detect the presence of any contaminant feldspar (Section 5.3.4).

4.2.6 Disc preparation

The etched quartz of a single-size fraction (either 180-212 μm or 212-250 μm) was used for OSL analysis. In this work both multiple-grain and single-grain aliquots were used. To make up a multiple-grain aliquot, the grains need to be held on a 9.7 mm diameter aluminium disc. This is done by placing a mask over the disc and spraying the exposed area of disc with 'Silkospray' silicone spray. The disc is then placed upside down onto a pile of the quartz extract to enable the grains to adhere to the disc. The disc was then tapped lightly to remove any loose grains and the grains retained formed a monolayer for analysis. Three mask sizes with hole diameters of 2, 5 and 8 mm were used, and were termed small, medium and large aliquots respectively (Fig. 4.1a-c). The number of grains retained on a disc when the small mask size was used (i.e. a "small aliquot") was counted for 96 discs and the average number of grains on each aliquot was ~30.

A single-grain aliquot uses a 1 mm thick, 9.7 mm diameter aluminium disc containing 100 holes in a ten by ten array. Each of the holes is 300 μm deep and 300 μm in diameter. To place a single grain into each hole the disc is placed on a sheet of weighing paper and grains (180-212 μm diameter) are carefully poured onto its surface. Using grains of this size ensured that only one grain is retained in each hole. A fine brush is then swept over the surface of the disc to remove any grains not retained in holes (Fig. 4.1d).

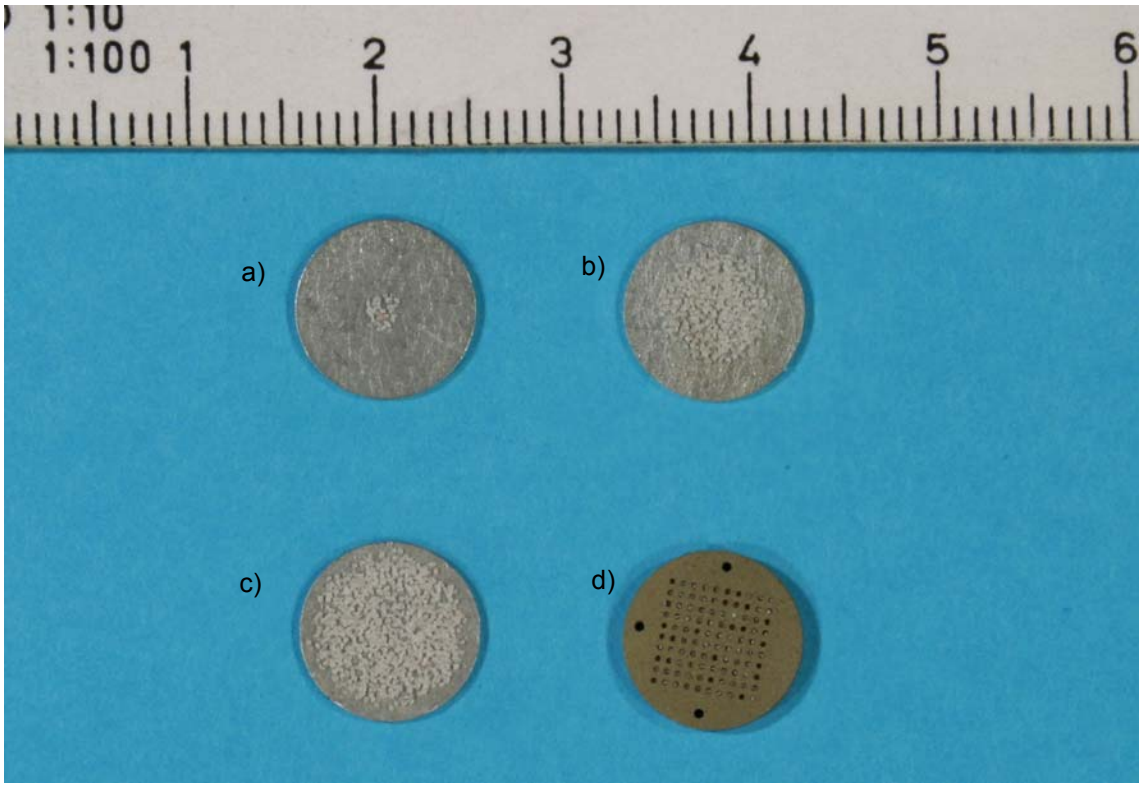

Figure 4.1: Examples of aliquots used in this study: a) small multiple-grain; b) medium multiple-grain; and c) large multiple-grain aliquots; and d) single-grain aliquot. In this photograph ~30 % of the single grain holes are empty because of movement during photography. In routine analysis, >95 % of the holes were filled.

4.3 BETA IRRADIATION AND LUMINESCENCE MEASUREMENT

All the luminescence measurements made in this study were performed on one of three Risø TL/OSL readers at Aberystwyth Luminescence Laboratory. Measurements on multiple-grain aliquots were performed on Risø 2 or 3 and single-grain measurements were made on Risø 4. All the readers are controlled by a "Mini-Sys" computer (Markey *et al.*, 1997) which allows automation of the irradiation, heating, stimulation and measurement of samples. Recent developments and modifications to the Risø readers have been covered by Bøtter-Jensen (1997) and Bøtter-Jensen *et al.* (2000; 2002; 2003a; 2003b). A general schematic of the stimulation and measurement system in the Risø readers is shown in Figure 4.2. Development of the single-grain laser system is

covered by Duller *et al.* (1999a; 1999b) and Bøtter-Jensen *et al.* (2000; 2003a). Details of the three readers used in this thesis are contained in Table 4.1 and some aspects are discussed below to allow comparison of the equipment with that used in other studies.

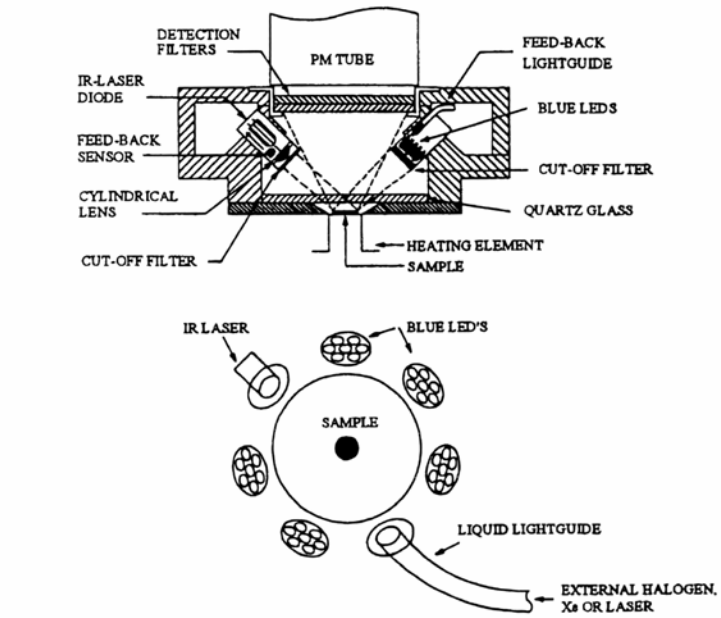

Figure 4.2: Schematic diagram showing stimulation and measurement system in a Risø reader, with the combined blue LED cluster and IR laser diode OSL unit. From Bøtter-Jensen *et al*. (2000).

4.3.1 Beta irradiation

All laboratory irradiations were administered under "Mini-Sys" control from Risø mounted beta sources. The different readers have two types of systems for irradiation. Risø 2 has the older system of a shutter between the source and sample aliquot so when the shutter is withdrawn irradiation occurs. Risø 3 and 4 have a rotating source as described in Markey *et al.* (1997); this source irradiates when it is positioned immediately above the sample, and stops immediately when it is rotated 180° and points upwards. Tests to determine how precisely the different type of sources can deliver short irradiations (<5 s) were performed by Markey *et al.* (1997) and constant offset values of 0.04 s and 0.11 s were found for the shutter and rotating sources, respectively. For

Table 4.1: Risø reader specifications

	Risø 2	Risø 3	Risø 4
System type	TL-DA-12	TL-DA-15	TL-DA-15
Positions on carousel	24	48	48
Beta source type	40mCi $^{90}Sr/^{90}Y$	40mCi $^{90}Sr/^{90}Y$	40mCi $^{90}Sr/^{90}Y$
Irradiation mechanism	Shutter	Rotating source	Rotating source
Source to sample distance (mm)	13	7	5
Dose rate on 01.04.05 (Gy/min)	1.08 ± 0.08	5.49 ± 0.18	2.60 ± 0.09
Multiple-grain aliquot measurement			
Blue LED type	NISHIA (type NSPB-500S)	NISHIA (type NSPB-500S)	NISHIA (type NSPB-500S)
Number of diodes	35	21	28
Emission wavelength (nm)	470 Δ 20	470 Δ 20	470 Δ 20
Stimulation power at 90 % power (mW/cm^2) [a]	20.2	8.0	30.6
Stimulation light breakthrough (counts/s) [b]	32	75	-
Single-grain measurements			
Laser type			$Nd:YVO_4$
Emission wavelength (nm)			532
Stimulation power (mW)			10
Infrared stimulation by laser diode			
Emission wavelength (nm)	830 Δ 10	830 Δ 10	830 Δ 10
Stimulation power (mW)	400	400	150
PMT type	9635Q	9635Q	9635Q
PMT dark count (counts/s) [b]	33	75	42
Detection efficiency (relative to Risø 3) (%) [a,c]	16	100	79
OSL filters	3 x 2.5 mm Hoya U340	3 x 2.5 mm Hoya U340	3 x 2.5 mm Hoya U340

[a] Derived from experimental work and based on technical details of Risø 4. Details are shown in Section 4.3.2.1.

[b] Average of 10 values.

[c] Derived using method i (Section 4.3.2.1).

long irradiation times the difference in the offset values is negligible, but for short irradiation times it becomes more significant. Thus, for OSL analysis of very young samples the shutter system of Risø 2 is more appropriate because it allows accurate short irradiations. The relatively low dose rate (Table 4.1) of this reader also makes it more suitable for young samples. The calibration of the beta sources is covered in Section 5.4.3.

4.3.2 Optical stimulation sources

Huntley *et al.* (1985) first performed OSL measurement of quartz grains using a 514 nm argon ion laser. Since then a range of stimulation sources have been employed, including 565 nm green LEDs (Galloway, 1993; 1994; Galloway *et al.*, 1997) and filtered halogen and xenon lights (Bøtter-Jensen and Duller, 1992; Bøtter-Jensen *et al.*, 1993). Bøtter-Jensen *et al.* (1999) discussed the use of blue LEDs (peak emission 470 nm) for measurement of OSL from quartz. These diodes have a number of advantages over previously available methods of stimulation. Blue LEDs are cheap and compact, they have minimal heat dissipation, the switch-on and -off times are rapid, and the power output can be controlled easily by adjusting the current flowing through them.

4.3.2.1 Multiple-grain stimulation

In Risø 2 and 3, blue diodes are grouped in clusters of seven, with a maximum of seven clusters (Bøtter-Jensen *et al.*, 2000). The clusters are arranged in a ring and located between the photomultiplier tube and sample heater plate. At one location, a cluster of blue LEDs is replaced by a solid state infrared laser diode emitting at 830 nm (Bøtter-Jensen *et al.*, 2000) whilst other clusters may be replaced by facilities for single-grain measurements. The infrared laser diode was used in this work for assessing the purity of quartz (see Section 5.3.4). The stimulation power delivered by the blue LEDs to samples on the different readers, and the detection efficiency of the readers has been assessed experimentally.

Repeat measurements on a single aliquot of quartz were performed to calculate the power of the blue LEDs and characterise the detection efficiencies of the

Risø readers at Aberystwyth. Although not all the readers at Aberystwyth were used for work in this thesis, they are included here for completeness. A single large aliquot of "calibration quartz" (provided by Dr A.S. Murray, NDLL) which had previously been sensitised by thermal annealing was used to obtain CW-OSL decay curves from each reader. The sequence of steps used to obtain the optical stimulation power of the readers is detailed in Table 4.2. The aliquot was given either a 4.7 Gy or a 1.9 Gy irradiation and a 220ºC preheat (held for 10 s) on Risø 3. The aliquot was either then kept in Risø 3 or transferred to a different reader, and stimulated at 90 % diode power. The decay curves from both 4.7 Gy and 1.9 Gy doses were measured repeatedly throughout the experiment on Risø 3; the results demonstrated that no change in the brightness of the sample occurred (Fig. 4.3). Each reader was used to measure both a 4.7 Gy and a 1.9 Gy dose; the decay curves from both doses were compared for each reader to ensure that the results were reproducible, and that the level of dose had no effect on the results. The OSL curve was measured for either 100 s (Risø 1 and 2) or 40 s (Risø 2-5). In each instance the data was collected in 250 bins; each bin contained data from 0.4 s in the former case, and 0.16 s in the latter.

Table 4.2: Steps followed for investigation into optical stimulation power and detection efficiency of the Risø readers at Aberystwyth.

Step	Treatment	
1	Give 4.7 Gy or 1.9 Gy dose	Risø 3
2	Preheat to 220°C for 10 s	Risø 3
3	OSL stimulation at 125°C for 40 s	Risø 3
4	Give 4.7 Gy or 1.9 Gy dose	Risø 3
5	Preheat to 220°C for 10 s	Risø 3
6	OSL stimulation at 125°C for 40 s or 100 s	Risø 1,2,4,5
7	Repeat steps 1-6 with different dose and/or a different reader	

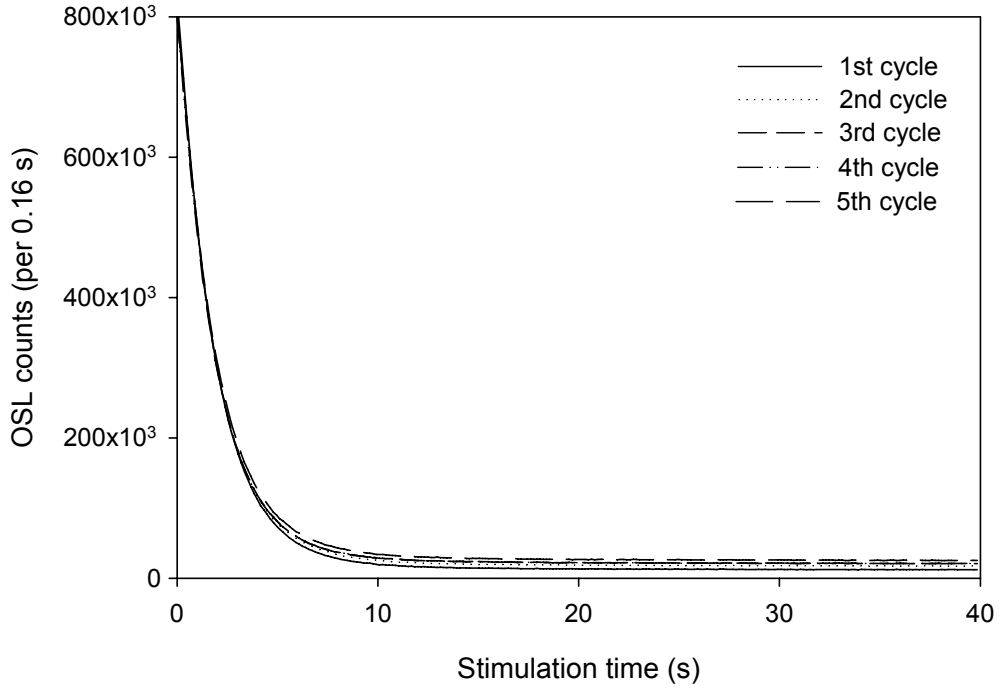

Figure 4.3: OSL decay curves measured on Risø 3 following a 4.7 Gy dose during Step 3 in Table 4.2. The brightness of the signal remains constant during the different cycles, indicating that no sensitivity change occurred during the experiment.

Optical stimulation power

The time taken for optical stimulation to reduce the OSL intensity by a factor of two allows the intensity of the diodes at the disc location to be calculated. The method described by Armitage (2003) was used to derive the decay "half-time". This method assumes that the initial part of the OSL signal is dominated by the fast component and thus has a simple exponential decay, the OSL of the calibration quartz used in this experiment is known to be dominated by the fast component. The initial part of the OSL decay was plotted as the natural logarithm of the intensity (I) divided by the initial intensity (I_0), as a function of stimulation time; an example of this can be seen in Figure 4.4. The straight line describing the initial decay of the OSL signal was used to calculate the half-life using the following logic:

if the equation of the best-fit line is	$y = mx$
when the signal intensity is half the original value	$y = \ln(I/I_0) = \ln(0.5) = -0.693$
the half-life can be calculated from	$x = -0.693/m$

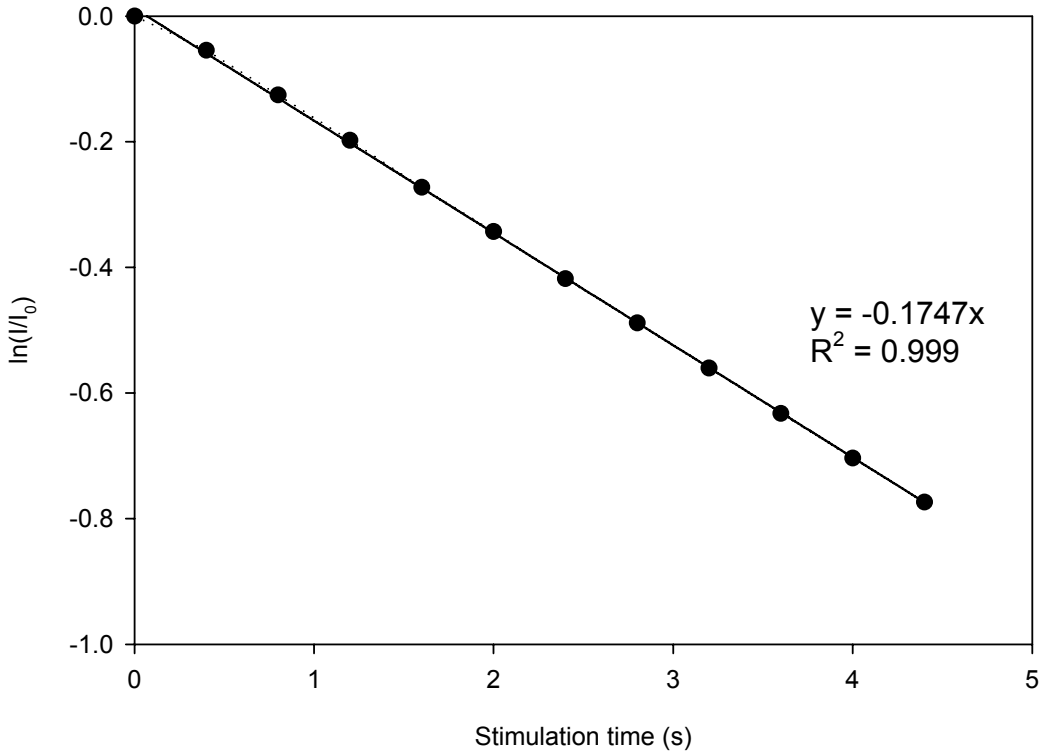

Figure 4.4: OSL decay on Risø 1 following a 4.7 Gy dose. A straight line has been fitted through the data, and the equation is indicated in the plot.

Using this method, the half-times calculated from both the 4.7 Gy and the 1.9 Gy doses are shown in Table 4.3.

Technical notes supplied by the manufacturer with Risø 4 state that the stimulation power is 34 mW/cm^2 at 100 % power, corresponding to 30.6 mW/cm^2 at 90 % power. Using the calculated values of half-times (Table 4.3), the stimulation powers for all five readers can be derived using the known value from Risø 4, the results are shown in Table 4.3. The stimulation power varies considerably between the different readers; e.g. Risø 4 has 10 times the optical power of Risø 1. The optical stimulation power affects the rate at which the electrons are evicted from the traps, thus a higher stimulation power will cause the OSL signal to decay more rapidly than a lower power.

Table 4.3: Values of optical half-times derived from the OSL signal decay and stimulation powers of the LEDs at 90 % power (based on optical half-times following a 4.7 Gy dose).

Reader	Optical half-time (s) following an 4.7 Gy dose	Optical half-time (s) following an 1.9 Gy dose	Stimulation power at 90 % (mW/cm^2)
Risø 1	3.967	4.087	2.83
Risø 2	0.555	0.536	20.2
Risø 3	1.407	1.429	7.98
Risø 4	0.367	0.361	**30.6***
Risø 5	0.472	0.444	23.8

* obtained from manufacturers technical notes.

Luminescence detection efficiency

All the OSL measurements were performed on the same aliquot after exposure to identical amounts of irradiation, thus meaning that the luminescence emitted over the entire optically stimulated decay should be constant regardless of which reader the OSL signal is measured on. Any variation in the total counts detected on each reader can therefore be related to differences in the detection efficiency of the reader. The relative detection efficiency was calculated by two methods:

i) After subtraction of the background (obtained by averaging over the last 10 channels of the OSL decay curve), the sum of the total counts over the entire OSL decay curve was calculated.

ii) The total number of counts (background subtracted) emitted was calculated up to where the total stimulation energy reached 10 mJ, calculated from the diode power calculated in Table 4.3. Where the time needed to deposit this amount of energy was not equal to an integer number of bins, fractions of a bin were used.

The total number of OSL counts calculated using both methods are shown in Table 4.4. These values allow the relative detection efficiencies to be derived,

and they are normalised to the value for Risø 3 in Table 4.4. The results calculated using the two different methods are broadly similar, although there are some subtle differences. These differences may arise because method ii looks at the initial part of the signal (dominated by the fast component), whereas method i looks at the entire OSL signal (composed of multiple components). This effect is likely to also cause the difference in the results for the two optical stimulation times on Risø 2. Nevertheless, the results are similar and both methods place the readers in the same relative order for detection efficiency, with a considerable difference in the detection efficiencies of the readers apparent. From these results, Risø 2 was shown to have a poor detection efficiency, e.g. Risø 5 is five times more efficient than Risø 2. This poor detection efficiency was identified as a problem because the low dose-rate of this reader makes it the most suitable for dating young samples (Section 4.3.1). Young samples, however, are likely to have dim OSL signals and thus it is desirable to have a high detection efficiency. A new photomultiplier tube with a greater sensitivity was installed in Risø 2 in August 2004 to improve the detection efficiency and make it more suitable for analysis of young samples. Whilst analysis of the majority of the samples in this thesis was performed on Risø 3 to provide consistency in the results, the youngest samples, those from the scroll-bar sequences, were analysed on Risø 2 because of the short irradiation periods necessary. For these samples, those from Kadies Drift were analysed on the old photomultiplier tube, and those from Waaihoek were analysed on the new photomultiplier tube.

Table 4.4: Detection efficiencies of the Risø readers, for different stimulation times. The OSL counts (x 10^6) used for the analysis, and the detection efficiencies, normalised to Risø 3 are shown.

Stimulation time (s)	Method i				Method ii			
	100 s		40 s		100 s		40 s	
Reader	*Counts*	Efficiency	*Counts*	Efficiency	*Counts*	Efficiency	*Counts*	Efficiency
Risø 1	*7.89*	0.75			*4.05*	0.74		
Risø 2	*2.39*	0.23	*1.69*	0.16	*0.79*	0.14	*0.97*	0.18
Risø 3			*10.48*	1.00			*5.48*	1.00
Risø 4			*8.24*	0.79			*4.17*	0.76
Risø 5			*13.24*	1.26			*7.23*	1.32

4.3.2.2 Single-grain stimulation

For single-grain measurements on Risø 4, stimulation is performed by a 10 mW Nd:YVO_4 solid state diode-pumped laser, which emits in the green at 532 nm. This means that there is a large difference in the stimulation wavelength for the single-grain OSL on Risø 4 and the multiple-grain aliquot OSL on Risø 2 and 3. Duller and Bøtter-Jensen (1996) performed an experiment investigating the OSL signal from an aliquot of quartz when stimulated at different wavelengths. Their results showed that for stimulation wavelengths in the range 425-575 nm, the OSL signal behaves in a similar way (Fig. 4.5). Therefore, the blue diodes and single-grain laser systems of the Risø readers should stimulate the same traps in the quartz.

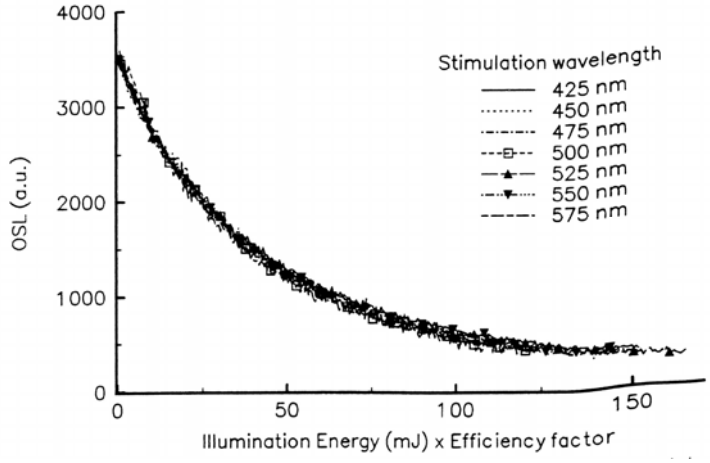

Figure 4.5: OSL decay curves obtained using narrow stimulation bands (25 nm) following a 10.8 Gy dose. Note that the x-axis is the product of the illumination energy and an efficiency factor, to account the stimulation efficiency of the different wavelengths. From Duller and Bøtter-Jensen (1996).

4.3.2.3 Optical filters

It is crucial that no scattered light from the optical stimulation source reaches the photomultiplier tube. To prevent this happening a combination of filters is used (Fig. 4.6). Detection of luminescence is through three 2.5 mm thick Hoya U-340 filters (peak transmission at 340 nm) fitted in front of the PM tube (Bøtter-

Jensen *et al.*, 1999). One of the U-340 filters has a metal oxide coating to reduce transmission in the red region.

To ensure that there is no leakage from the optical stimulation source, two further precautions are taken. First, a Schott GG-420 green long-pass filter is fitted in front of each LED cluster to reduce the intensity of the highest energy electrons (Bøtter-Jensen *et al.*, 1999) and thus diminish the likelihood of any directly scattered light reaching the photocathode. Second, a Schott RG-115 long-pass filter is fitted in front of the IR laser diode to reduce the background caused by a weak blue emission from the IR laser (Bøtter-Jensen *et al.*, 2000).

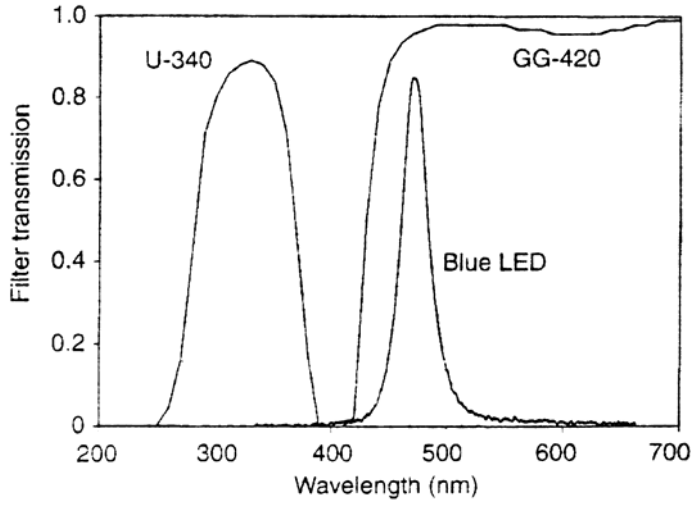

Figure 4.6: Emission spectrum of blue LEDs overlain with the transmission curves for the U-340 detection filter, and the GG-420 green long-pass filter. From Bøtter-Jensen *et al.* (1999).

4.4 OSL SIGNAL COMPONENTS

Smith and Rhodes (1994) first identified that when stimulated at 514 nm, the OSL emission at a constant stimulation power (continuous-wave or CW- OSL) from Chaperon Rouge quartz could be fitted by the sum of three exponential components (Fig. 4.7). Based on the relative rate of decay, the components were termed the fast, medium and slow components. At temperatures above 150°C the difference in the mean lifetime of the fast and medium components

was a factor of four. Further work by Bailey *et al*. (1997) showed that the proportion of each component in the OSL signal varies on a sample to sample basis, and they also calculated the half lives of the three components.

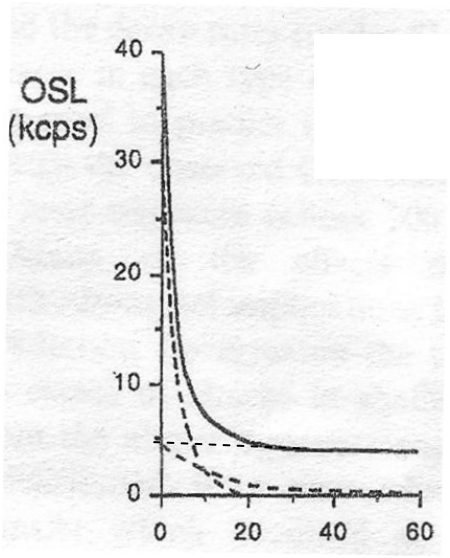

Figure 4.7: OSL signal (in thousands of counts per second) from Chaperon Rouge quartz when held at 220°C, and stimulated with a 7 mW/cm^2 beam from a 514.5 nm Ar ion laser. The dashed lines indicate the three exponential components identified. Adapted from Smith and Rhodes (1994).

Bulur (1996) first suggested measuring the OSL signal using a linearly increasing light power for optical stimulation. The linearly-modulated (LM-) OSL signal appeared as a series of peaks each corresponding to a signal component. This type of LM-OSL measurement allowed the peaks to be resolved easily. By ramping the stimulation intensity, the easy-to-bleach traps are emptied quicker than the hard-to-bleach traps, and thus a plot of the OSL emitted as a function of stimulation time, or power, distinguishes between the different components more effectively than a decay curve from a constant power optical source (Fig. 4.8). This stimulation method was first applied to quartz by Bøtter-Jensen *et al.* (1999), and initial LM-OSL studies on sedimentary quartz at room temperature (Kuhns *et al.*, 2000) and after heating to 280°C (Bulur *et al.*, 2000) found three and four first-order components present in the samples, respectively. Bulur *et al.* (2000) found that the slow

component of the sample was not a simple, single trap phenomenon; they showed it to be a combination of two components. The parameters of the components derived from LM-OSL measurements such as the maximum amplitude and peak location can be directly related to physical parameters of the trap, such as the number of trapped electrons and the photoionisation cross-section of the electrons (Bulur *et al.*, 2000).

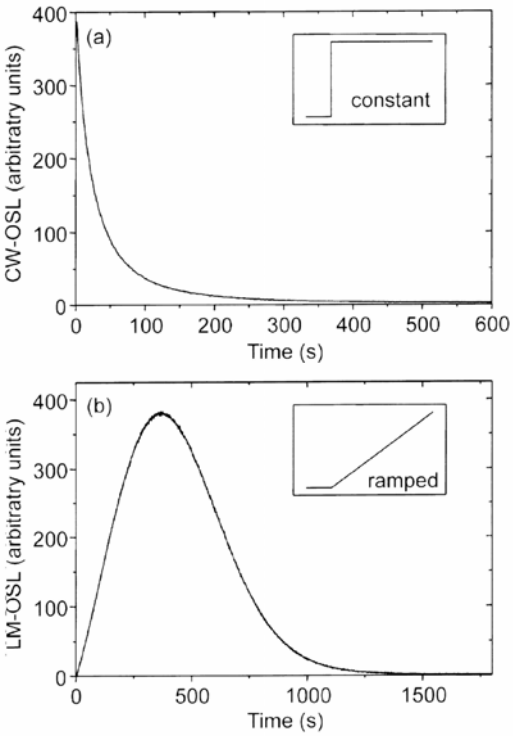

Figure 4.8: Schematic showing a) CW-OSL stimulation and b) LM-OSL stimulation, of a single component decay; the inset diagrams show the stimulation power. From Bøtter-Jensen *et al.* (2003).

Recent LM-OSL studies on sedimentary quartz from various geographical locations (Jain *et al.*, 2003; Singarayer and Bailey, 2003) showed that the OSL signal from the majority of samples consisted of four or five components (Fig. 4.9) that are generally stable up to 10^8 years. In total seven components were identified by Jain *et al.* (2003) (Fig. 4.9a), including a thermally unstable ultra-fast component which had also been identified by Choi *et al.* (2003a). Table 4.5

contains the photoionisation cross-sections calculated for the different components in both studies.

a)

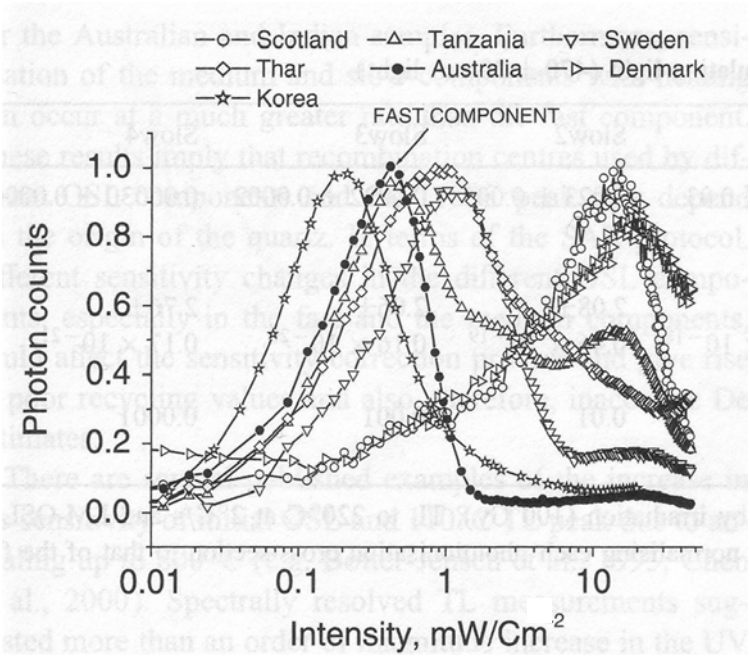

b)

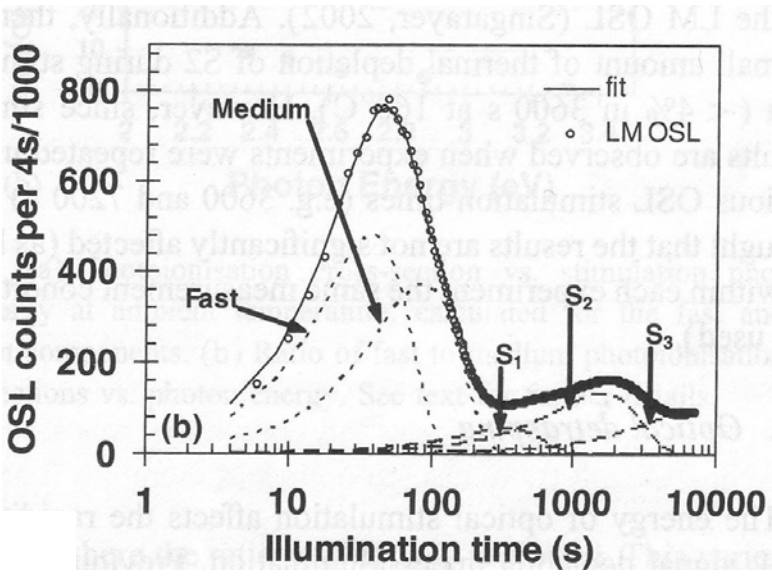

Figure 4.9: a) LM-OSL curves measured from various samples of quartz by Jain *et al.* (2003). The Australian quartz used in this study comes from sample WIDG8. b) LM-OSL curve deconvolved into five components, from Singarayer and Bailey (2003). Stimulation in both studies used 470 nm diodes. Note the logarithmic scales on the x-axes.

Table 4.5: Photoionisation cross-sections calculated for OSL components from LM-OSL analyses on quartz samples using a stimulation wavelength of 470 nm.

	Photoionisation cross-section (cm^2)	
Component	Jain *et al.* (2003)	Singarayer and Bailey (2003)
Ultra-fast	2.9×10^{-16}	
Fast	$2.32 \pm 0.16 \times 10^{-17}$	$2.5 \pm 0.3 \times 10^{-17}$
Medium	$5.59 \pm 0.44 \times 10^{-18}$	$5.9 \pm 2.0 \times 10^{-18}$
Slow 1	$1.33 \pm 0.26 \times 10^{-18}$	
Slow 2	$2.08 \pm 0.46 \times 10^{-19}$	$2.1 \pm 0.5 \times 10^{-19}$
Slow 3	$2.06 \pm 0.16 \times 10^{-20}$	$1.2 \pm 0.2 \times 10^{-20}$
Slow 4	$2.76 \pm 0.17 \times 10^{-21}$	$1.9 \pm 2.8 \times 10^{-21}$

The fast component is the most suitable for luminescence dating. Because it decays quickly under optical stimulation, it should give the lowest residual signal after exposure to sunlight during transport. Furthermore, the single aliquot regenerative dose (SAR) protocol (Murray and Wintle, 2000) (see Section 5.3), was developed on sample WIDG8 which has a dominant fast component (Fig. 4.9a). Although Jain *et al.* (2003) found that the majority of quartz samples have OSL signals which are dominated by the fast component, in some samples this is not the case. Studies of quartz with an OSL signal not dominated by the fast component (e.g. Choi *et al.*, 2003a; Tsukamoto *et al.*, 2003) have shown that in these instances the standard SAR protocol does not work effectively. Thus, it is important to assess whether the samples for OSL dating are dominated by the fast component.

4.4.1 LM-OSL curve deconvolution

Six samples from the Klip River (from six different reaches) and two samples from the Schoonspruit (one from the upper floodplain, and one from an oxbow) were measured using LM-OSL and the resulting data was deconvolved to investigate what components were present. LM-OSL curves from natural doses and regenerated doses of 4.7 Gy were obtained for large aliquots of samples 70KLA1-70KLA6, 91SC0408 and 91SC0410. Prior to each LM-OSL measurement, the aliquot was preheated at 220°C for 10 s to remove charge from lower temperature traps. During measurement the stimulation light

intensity was increased linearly from 0 to 8.9 mW/cm^2 over a period of 5000 s whilst holding the sample at 125°C. The data was collected in 2000 bins (each containing the counts for 2.5 s). The background count (calculated from the average of three blank discs that were measured under the same conditions as the samples; Fig. 4.10) was subtracted from each of the LM-OSL curves.

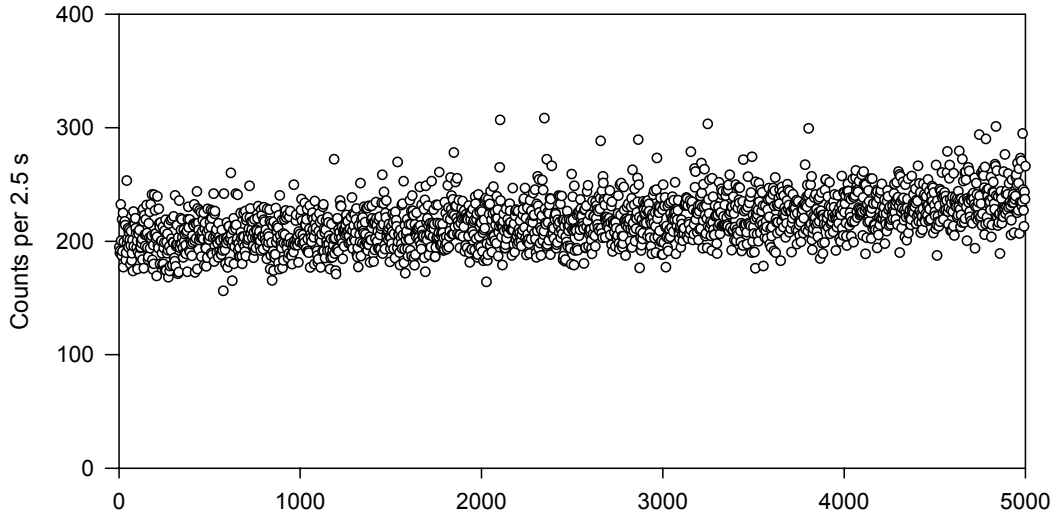

Figure 4.10: Average LM-OSL signal from three blank discs, measured on Risø 3.

Bulur *et al.* (2002) gave the simplest form of a one component LM-OSL curve as:

$$L(t) = n_0 b\,(t/P)\,\exp(-bt^2/2P) \qquad \text{[Eqn. 1]}$$

where $L(t)$ is the luminescence intensity as a function of time (t), n_0 is the number of trapped electrons, P is the total stimulation time, and b is the detrapping probability. The detrapping probability is proportional to the photoionisation cross-section (σ) and the maximum stimulation light intensity (I_0):

$$b = \sigma I_0 \qquad \text{[Eqn. 2]}$$

On the basis of Equation 1, an equation for a multiple component LM-OSL curve can be developed, as follows:

$$x = n_1 b_1 (t/P) \exp(-b_1 t^2/2P) + n_2 b_2 (t/P) \exp(-b_2 t^2/2P) + n_3 b_3 (t/P) \exp(-b_3 t^2/2P) +$$

$$n_4 b_4 (t/P) \exp(-b_4 t^2/2P) + \ldots\ldots\ldots + n_N b_N (t/P) \exp(-b_N t^2/2P) \quad \text{[Eqn. 3]}$$

Using Equation 3, the natural and the regenerated LM-OSL curves were deconvolved in "Sigma Plot 2001", following the procedure outlined in Choi *et al.* (2006). Equations describing between two and five components were fitted to each LM-OSL curve. The R^2 value indicating the goodness of each fit and the n_0 and b values calculated for each component by the software are detailed in Appendix B. From these values the photoionisation cross-sections were calculated, also shown in Appendix B. The best fit number of components for each sample is indicated by the greatest R^2 value. In some instances however, the same R^2 value was obtained for fits of different numbers of components; these instances occurred when a single component was fitted as two components with identical b values. In these cases, the fit with the lesser number of components was selected to be the best fit.

All the samples have a common fast component as evidenced by similar values for the photoionisation cross-sections, and by the location of the peaks in Figures 4.11 and 4.12. The results for the medium and slow components show more scatter, this is likely to have arisen from the poor characterisation of the slower components in the LM-OSL measurement. In general, the photoionisation cross-sections of the other components are consistent to an order of magnitude with those found previously (Table 4.5), but show some scatter.

To investigate whether the initial 0.8 s of the CW-OSL signal (used for D_e calculation) is dominated by the fast component, the deconvolved components from the LM-OSL signal were transformed into a CW-OSL signal. Regenerated signals from samples 70KLA1-70KLA6, 91SC0408 and 91SC0410 were used to ensure that the sample had been fully bleached prior to the dose measured. The components used in the transformations were obtained by deconvolving the LM-OSL signal using b values for the fast and medium components corresponding to the average photoionisation cross-sections obtained from the

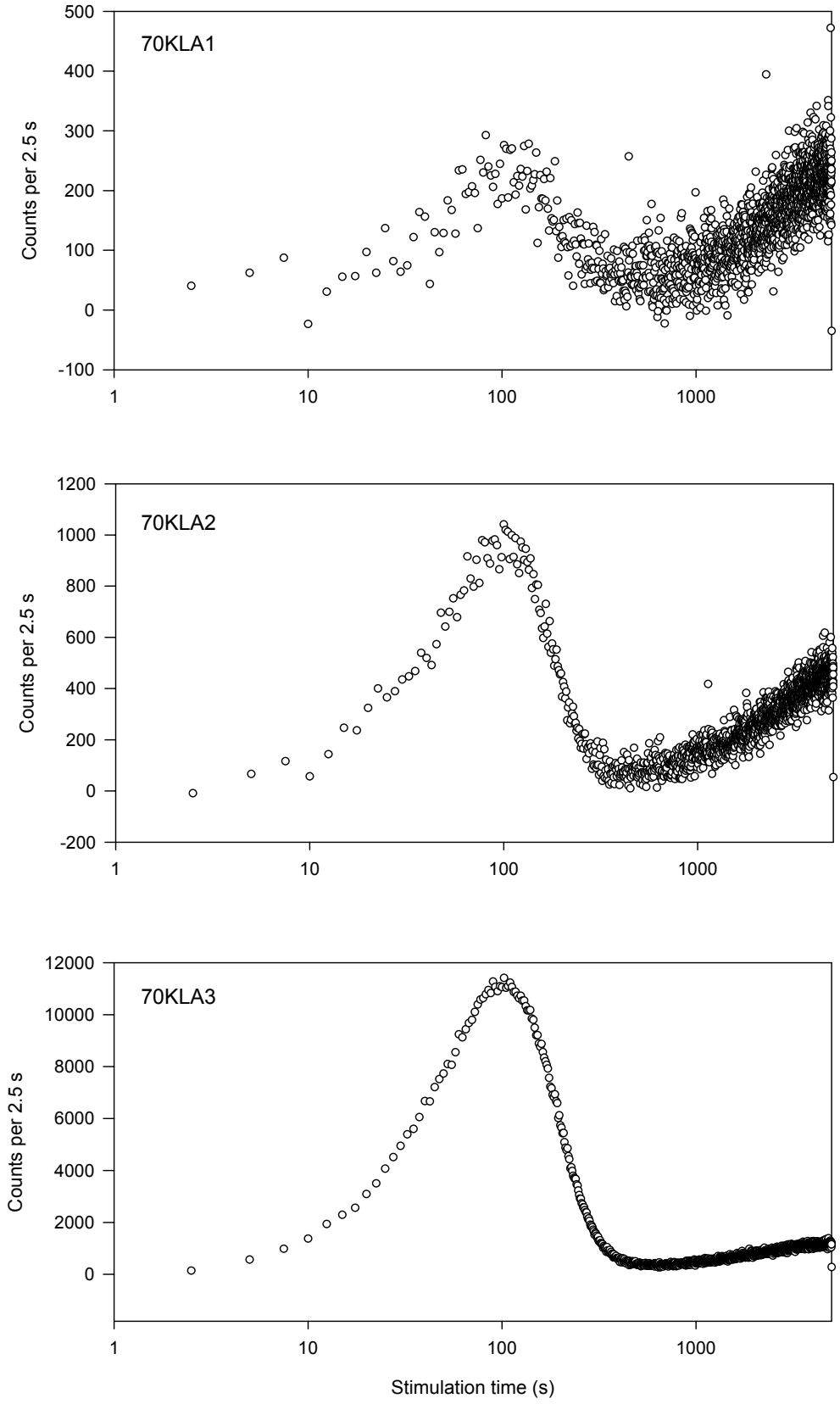

Figure 4.11: LM-OSL curves from the natural signal of samples 70KLA1-70KLA6. Measurements were made at 125°C following a preheat to 220°C.

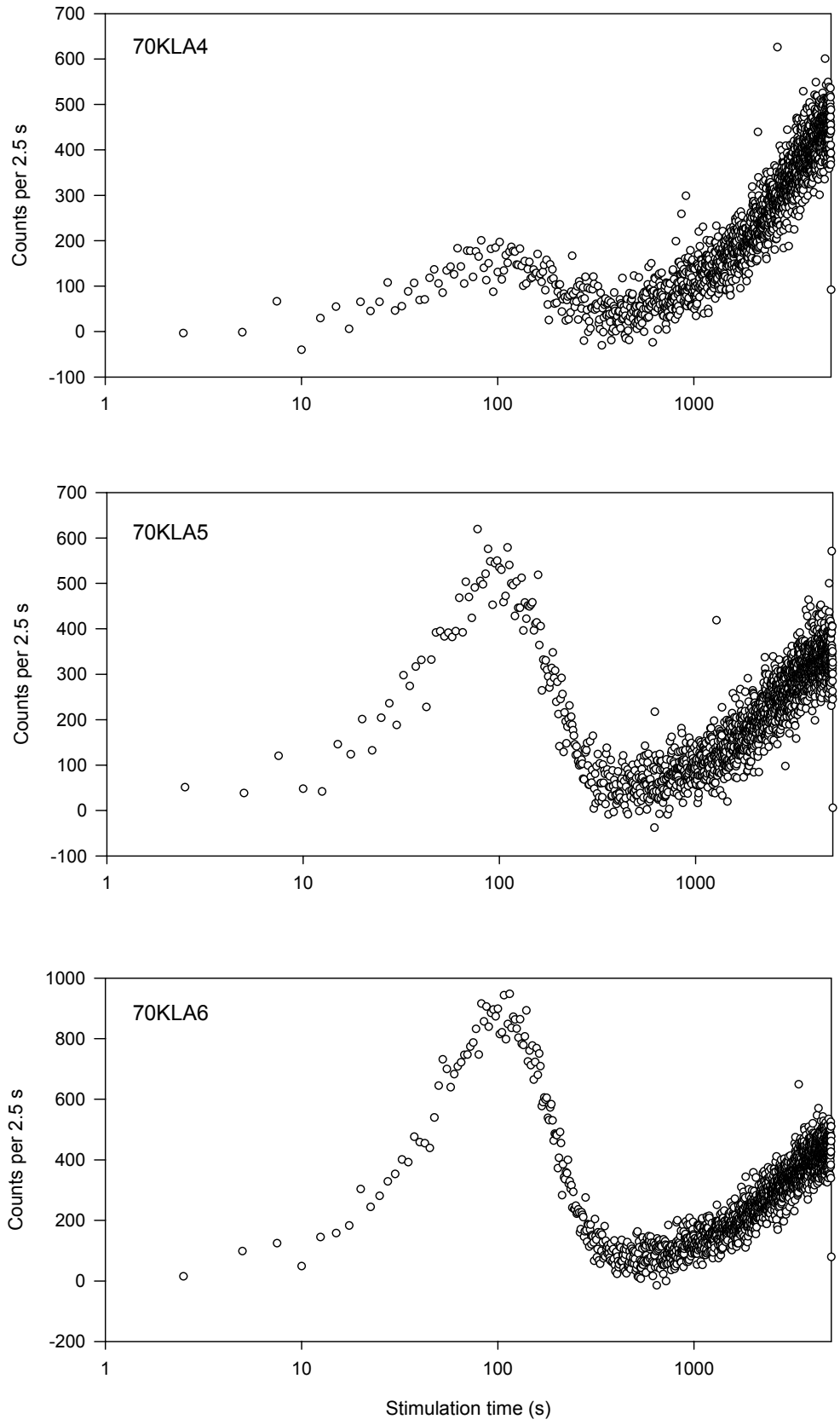

(Figure 4.11 continued)

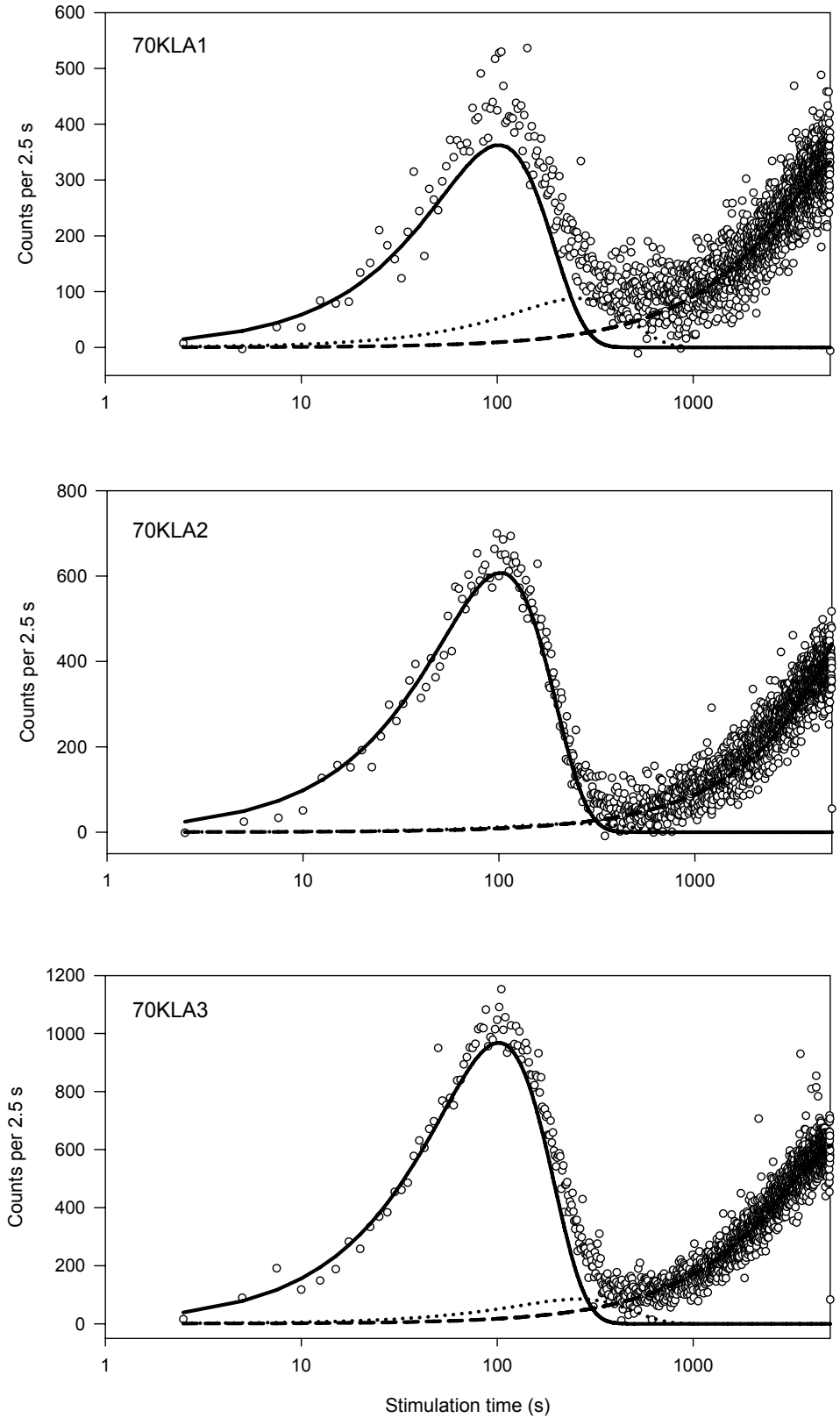

Figure 4.12: LM-OSL curves from a regenerated signal of samples 70KLA1 - 70KLA6, following a 4.7 Gy dose. Measurements were made at 125°C following a preheat to 220°C. The OSL components found by curve fitting are shown.

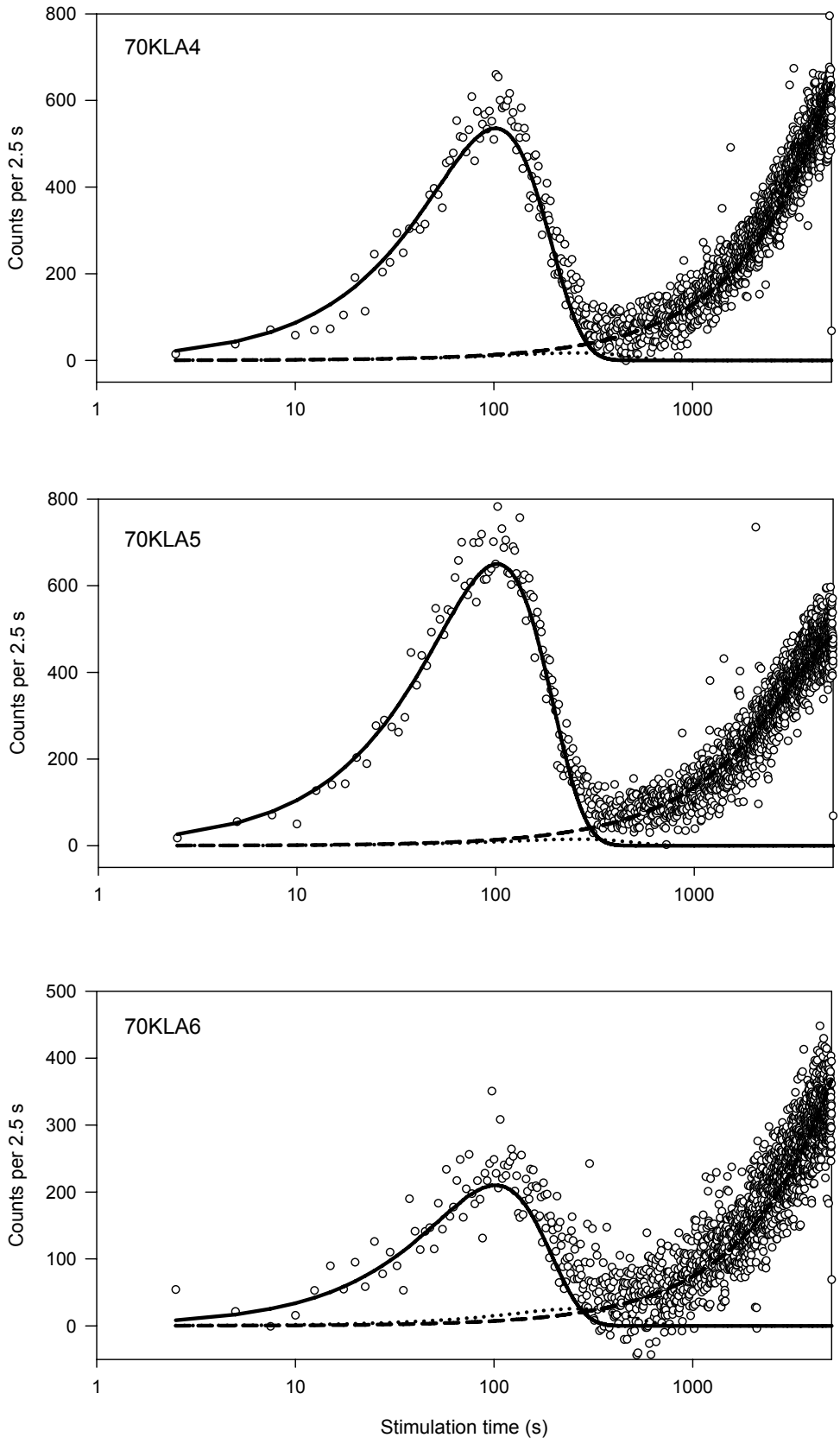

(Figure 4.12 continued)

results shown in Appendix B. These photoionisation cross-sections are 2.30 x 10^{-17} cm^2 for the fast component (b = 4.83 x 10^{-1}) and 3.53 x 10^{-18} cm^2 for the medium component (b = 7.43 x 10^{-2}). The slow components are not of great interest in this study so they were grouped into one component for the analysis; to improve the three component fit, the b value for the slow component was not fixed. Quartz from the different Klip River and Schoonspruit samples is expected to originate from the same source rock because of the small catchment area of the rivers and the relatively uniform regional geology. Thus the components in the quartz would be expected to be similar. The components obtained from the three component curve deconvolution are shown overlying the LM-OSL signals in Figure 4.12; in each instance a good fit was found. Using the transformation method described in Bulur (2000), these separate components were transformed into CW-OSL curves (see Figure 4.13 for an example). Using the transformed data, the proportion of each component in the initial 0.8 s of CW stimulation was calculated. The proportion of the fast, medium and slow components in samples 70KLA1-70KLA6, 91SC408 and 91SC0410 are shown in a ternary diagram in Figure 4.14. These results demonstrate that the part of the CW-OSL signal used for derivation of D_e is dominated (>90 %) by the rapidly bleachable, fast component. Because all the samples in this thesis are expected to have the same geological origin, one would expect them all to have a CW-OSL signal initially dominated by a fast component, and thus the standard SAR protocol should be suitable for D_e analysis.

4.4.2 Thermal stability of the components

The thermal stability of the different components in the OSL signal from quartz has been investigated by Bulur *et al.* (2000), Singarayer and Bailey (2003) and Li and Li (2006). In the former two studies, curve deconvolution of the LM-OSL measurements of irradiated aliquots of quartz was used to separate the components and to calculate the magnitude of these components following different temperature preheats. In the latter study, curve deconvolution of the CW-OSL curves was used to obtain the magnitudes of the fast and medium components. This experiment allowed the trap-dependent retention lifetime of

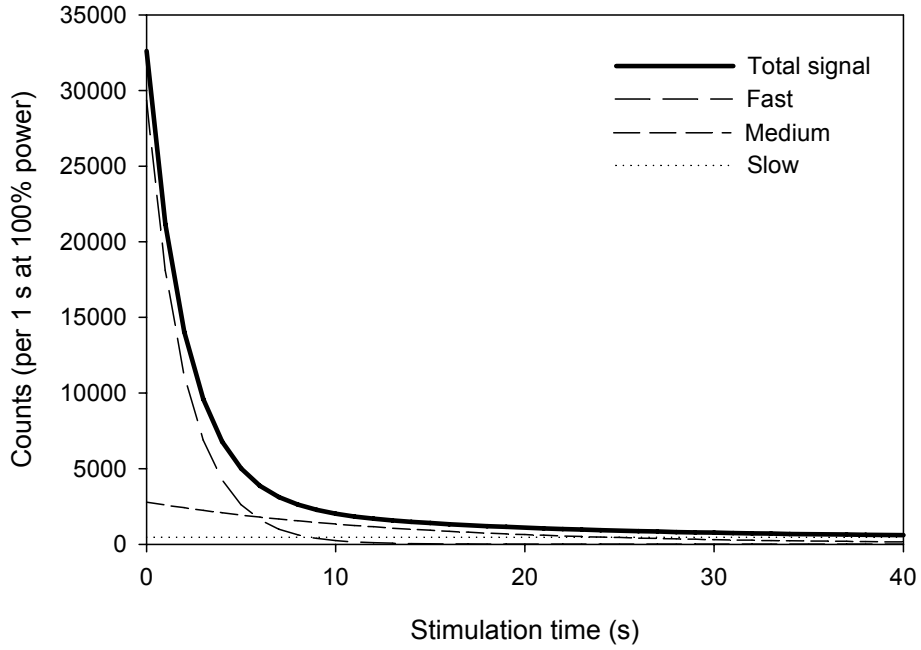

Figure 4.13: CW-OSL curve for 70KLA2 obtained from transformation of the LM-OSL measurement. The thick line represents the total signal, and the dashed lines show the contributions from the fast, medium and slow components.

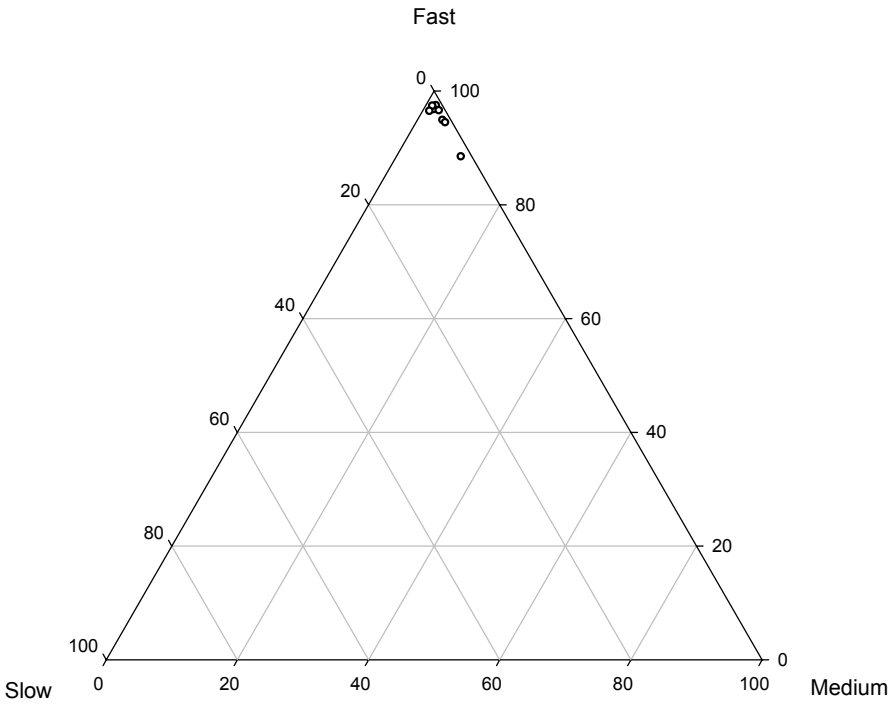

Figure 4.14: Ternary diagram showing the percentage of each OSL component in the initial 0.8 s of CW-OSL measurement for samples 70KLA1-70KLA6, 91SC0408, and 91SC0410.

the traps associated with the OSL components to be assessed (Singarayer and Bailey, 2003). The studies by Bulur *et al.* (2000) and Singarayer and Bailey (2003) show similar results for the thermal stability of the fast, medium and two slow components (Fig. 4.15a, b). The quartz investigated by Li and Li (2006) shows a similar trend for the fast component, however the medium component appears to decrease monotonically at preheat temperatures greater than 240°C (Fig. 4.15c). The fast component (component A of Bulur *et al.*, 2000) is stable up to 300°C and decays sharply at higher preheats. This is consistent with what one would expect because this component derives from the same traps as the 325°C TL peak (Aitken, 1998). The medium component (component B of Bulur *et al.*, 2000) is stable at temperatures up to 300°C in the studies by Bulur *et al.* (2000) and Singarayer and Bailey (2003), but appears to be thermally unstable in the study by Li and Li (2006). Similar decays of the two slow components (components C and D of Bulur *et al.*, 2000) are found in both studies, suggesting that the same slow components are present in the quartz investigated in each study; one slow component (S1 and D) decays at temperatures greater than 200°C, whilst the other (S2 and C) appears stable up to temperatures of 320°C.

For investigation of the thermal stability of components in the Klip River quartz, a single large aliquot of sample 70KLA2 was sensitised by ten irradiation, heating and measurement cycles and annealed to 450°C. Following this stabilisation, for each measurement cycle, the aliquot was given a 3.6 Gy beta dose, a 10 s preheat, and stimulated with the light intensity increasing linearly from 0 mW/cm^2 to 8.9 mW/cm^2 over 1000 s. The data was collected in 1000 bins, with each bin containing the data for 1 s stimulation. The preheat temperature was increased in each cycle in 20°C steps, over the range 140°C to 380°C, giving a total of 13 cycles. Following measurement of the regenerated dose, a 1.8 Gy test dose was administered to the aliquot (cut-heat of 160°C) and the LM-OSL measured. The OSL response to this irradiation was used to monitor sensitivity change (Murray and Wintle, 2000). After measurement of the signal from the test dose, the aliquot was heated to 450°C to remove any signal remaining in the slow components. During the preheat and cut-heat stages, the thermoluminescence (TL) signal was recorded. The

a)

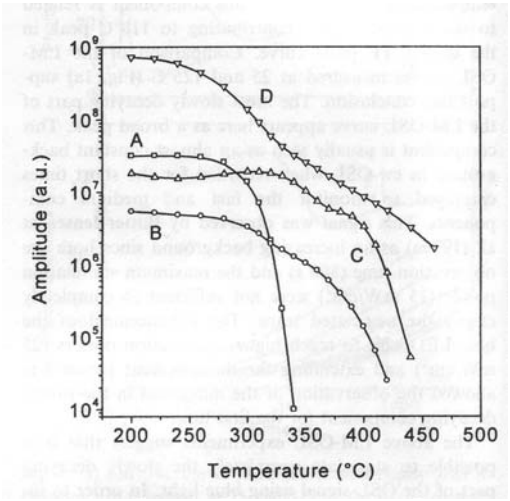

b)

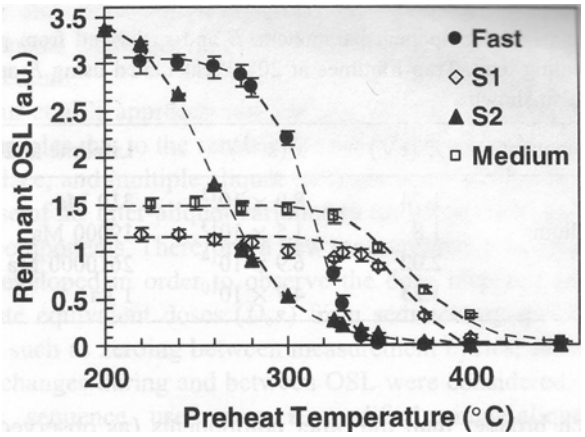

c)

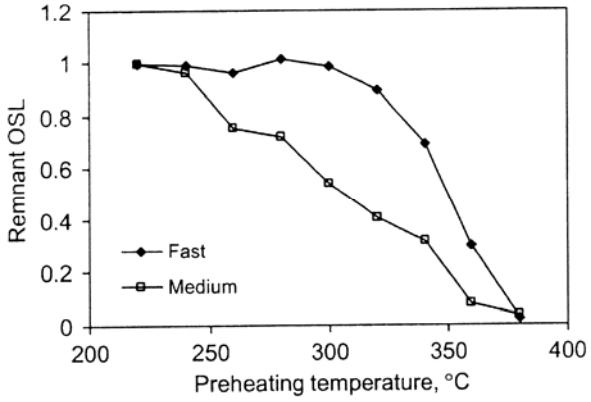

Figure 4.15: Thermal stability of components from a) Bulur *et al.* (2000); b) Singarayer and Bailey (2003); and c) Li and Li (2006). The data was obtained from deconvolution of LM-OSL curves in a) and b), and CW-OSL curves in c).

TL data was collected in the number of bins equal to the maximum temperature, so each bin contained the data for an increase in temperature of 1°C. Chen *et al.* (2000) suggested that the 110°C TL peak can be used to monitor sensitivity changes in the quartz OSL signal, thus measurement of the TL signal during the experiment allowed sensitivity change to be assessed in an additional manner to the test dose OSL.

The regenerated dose signals measured following preheats in the range 140-320°C were deconvolved to separate the components and a three component fit was found to be the most appropriate (average R^2 value = 0.97). For each component the average value of the detrapping probability (*b*) from the 13 measurements was calculated. These average values were 0.4848, 0.0499 and 0.0004 for the fast, medium and slow components respectively. All the LM-OSL measurements were then fitted using these values of *b.* This allowed the magnitude of the components to be compared and enabled fitting of the higher temperature preheat curves where little or no signal remained in some of the components.

The TL signals from the regenerated doses and test doses are shown in Figures 4.16 and 4.17, and the LM-OSL signals from the test doses are shown in Figure 4.18. The inset graphs on Figures 4.16 and 4.17 show the integrated counts between 90°C and 115°C for each curve. This integration should allow one to assess any sensitivity change that has occurred in the OSL components which use the same luminescence centres as the 110°C TL peak. The results show no evidence of systematic sensitivity change during the test dose cycle (Fig. 4.17); but a monotonic decrease can be seen in the 110°C TL peak during preheating in the regenerated dose cycle (Fig. 4.16). Although this decrease is largely systematic, the change over the entire 13 measurements is <2 % of the original level suggesting that it is not significant. Curve deconvolution of the LM-OSL signals from the test doses (Fig. 4.18a) was also used to assess the sensitivity change, and this method allowed changes in the components to be measured individually. The magnitude of each component (n_0) was normalised to the initial test dose measurement value, and in Figure 4.18b the sensitivity change in the three components is shown. The fast and slow components

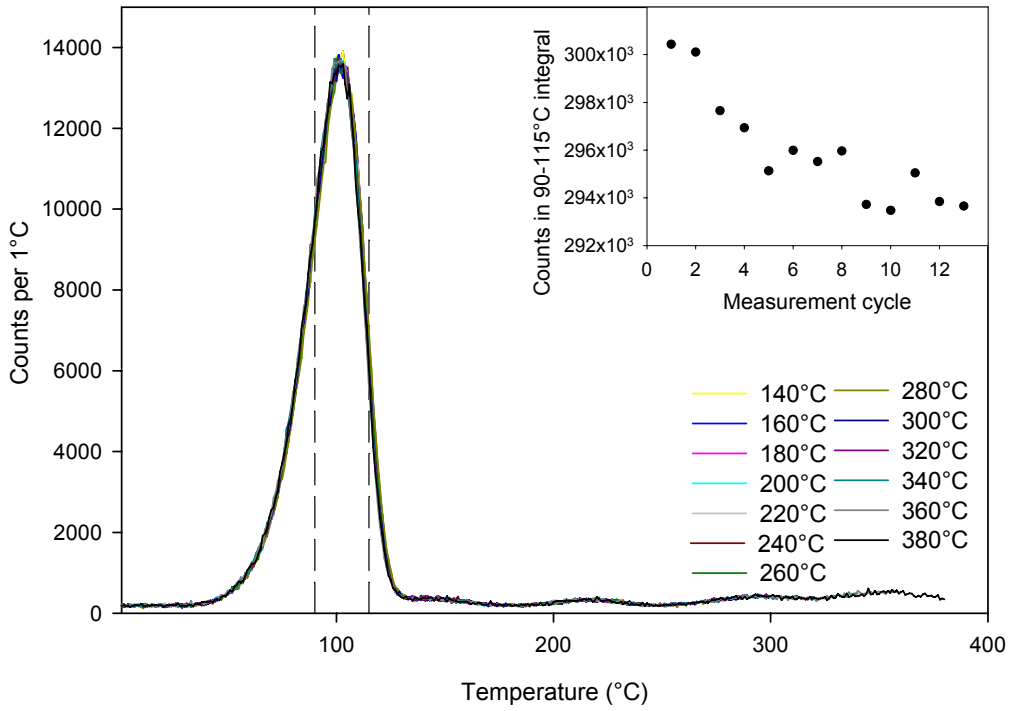

Figure 4.16: Thermoluminescence signal measured during preheats following regeneration doses of 3.6 Gy. The dashed lines indicate 90°C and 115°C. Inset graph shows the sum of the counts in the integral 90 - 115°C.

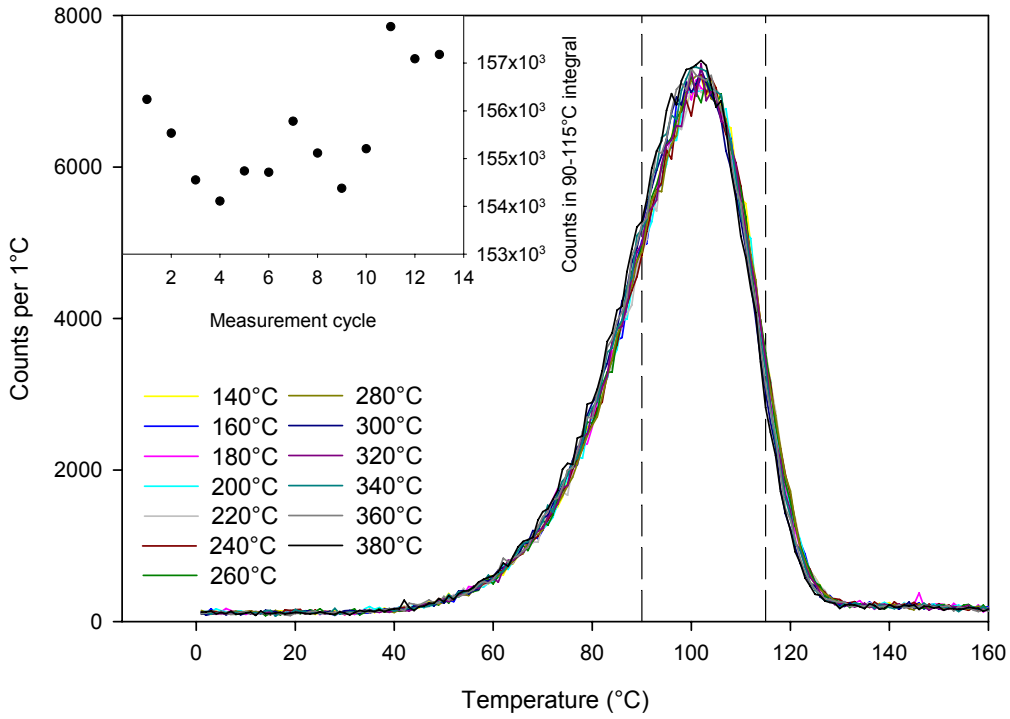

Figure 4.17: Thermoluminescence signal measured during cut-heats following test dose of 1.8 Gy. The dashed lines indicate 90°C and 115°C. Inset graph shows the sum of the counts in the integral 90 - 115°C.

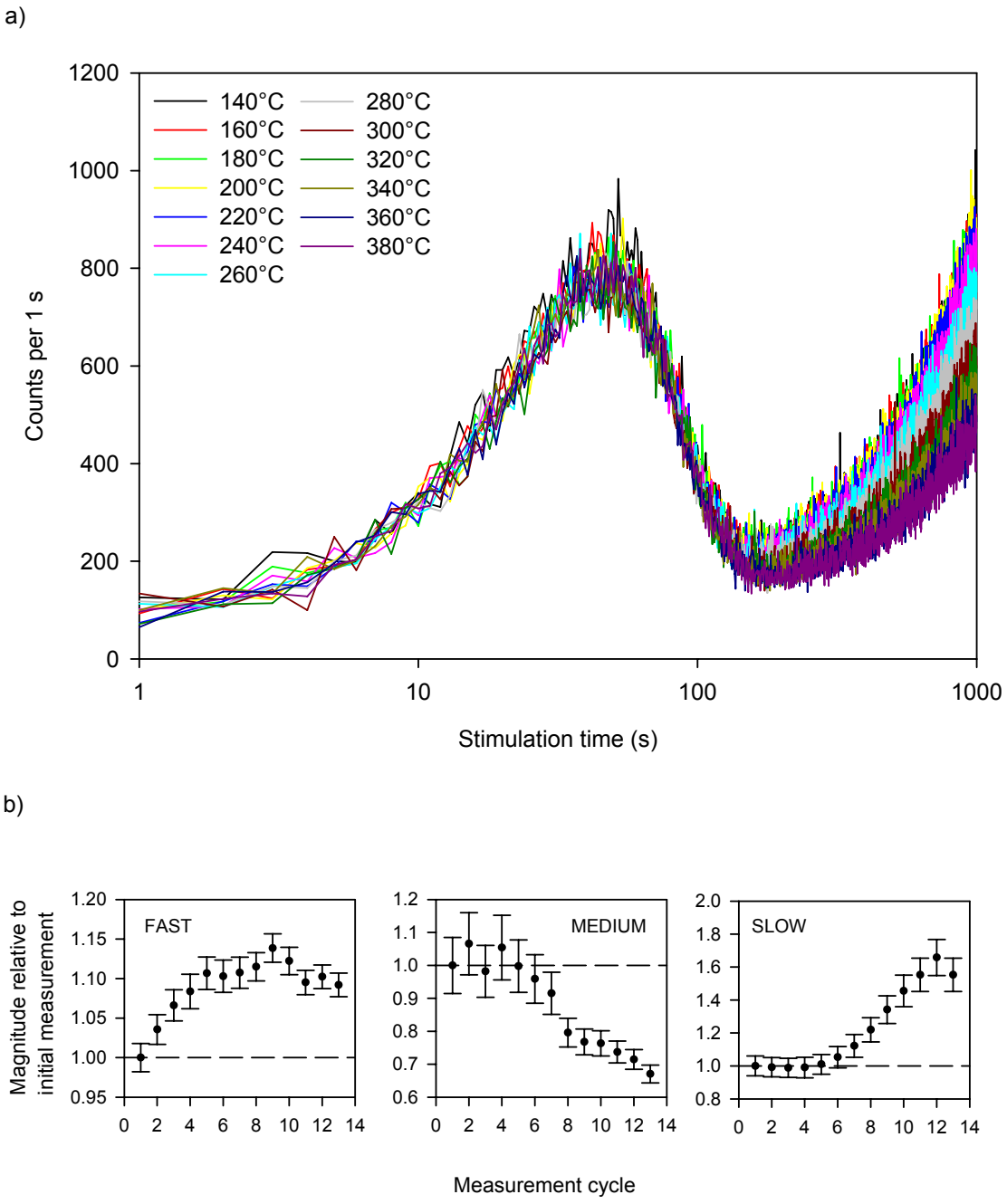

Figure 4.18: a) LM-OSL signals for a single aliquot of quartz following a 1.8 Gy test dose and a cut-heat (for 0 s) at 160°C. The preheat temperature of the previous regenerated dose measurement cycle is indicated. b) Changes in the magnitude of the various components relative to the measurement at 140°C.

sensitise by ~12 % and ~60 % respectively, whilst the medium component desensitises by ~35 % of the initial value. This large amount of sensitivity change evident in the LM-OSL signals is not reflected in the sensitisation of the 110°C TL peak, indicating that the 110°C TL peak is not suitable for assessing sensitivity change in these samples as proposed by Chen *et al.* (2001). Jain *et al.* (2003) also found that the 110°C peak did not reflect sensitivity change in every component found in LM-OSL measurements for samples from India and Denmark.

The LM-OSL signals following 3.6 Gy regeneration doses are shown in Figure 4.19, and a general trend of decreasing signal levels with increasing preheat temperature can be seen. The remnant OSL for each component, normalised by the magnitude of the same component in the subsequent test dose LM-OSL, is shown as a function of preheat temperature in Figure 4.20. The plot shows that the fast component is stable at preheat temperatures less than 280°C. At higher preheats, thermal erosion of the signal occurs and only a negligible amount of the fast component remains after a preheat of 360°C. The slow component shows no systematic reduction until preheat temperatures greater than 260°C. These results for the fast and slow components in the Klip River quartz show similar trends to those found for the fast and D2/slow 1 components in Bulur *et al.* (2002) and Singarayer and Bailey (2003), and the fast component in Li and Li (2006). The medium component reduces monotonically over the range 140-280°C, after which it decreases at a lesser rate, comparable to the thermally unstable medium component identified by Li and Li (2006). This is inconsistent with the results of Bulur *et al.* (2002) and Singarayer and Bailey (2003), where the medium component identified was thermally unstable up to ~300°C. Although this component is thermally unstable in the Klip River quartz, the dominance of the fast component in the initial part of the CW-OSL signal (Fig. 4.14) means that the instability of this component should not affect D_e calculation. The thermal stability of the fast component in the quartz from the Klip River indicates that it is suitable for OSL analysis, and should have a lifetime similar to the value of 310 Ma at 20°C calculated by Singarayer and Bailey (2003).

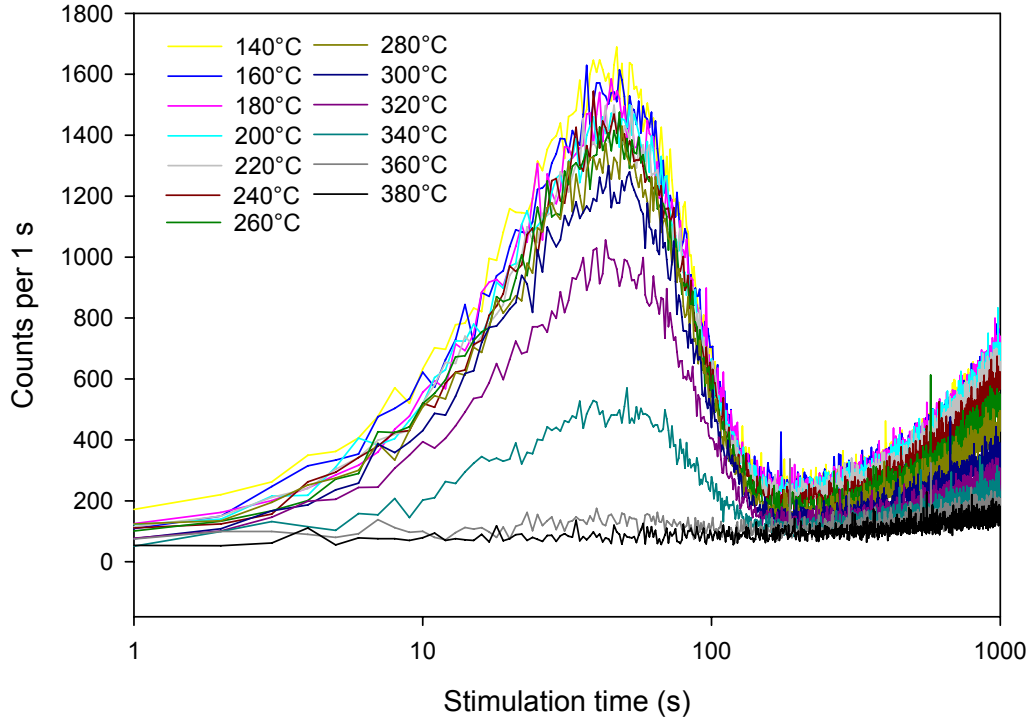

Figure 4.19: LM-OSL signals for a single aliquot of quartz following a 3.6 Gy regeneration dose and a preheat (for 10 s) at the temperature indicated.

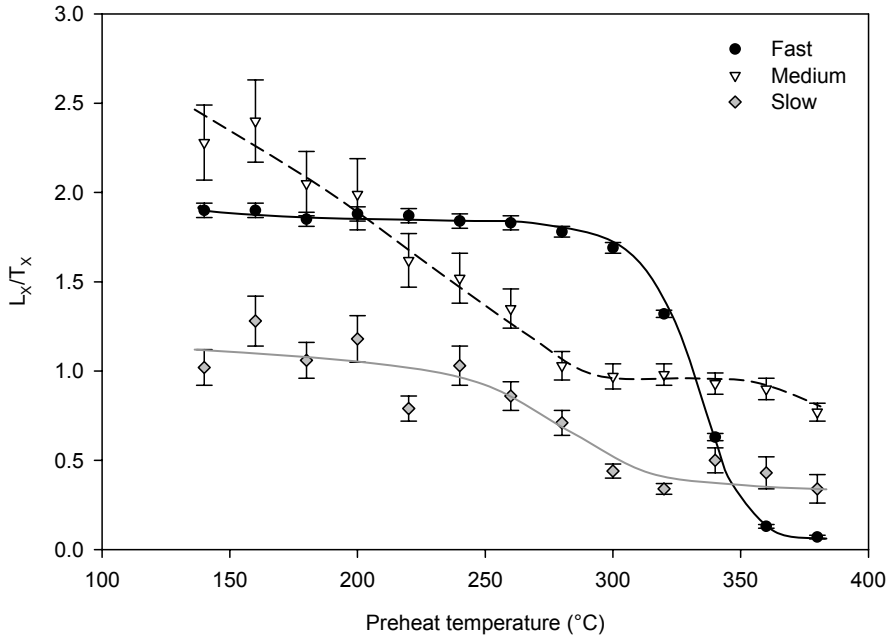

Figure 4.20: Thermal stability of the various components of sample 70KLA2. Showing the normalised luminescence signal, obtained through curve deconvolution of the LM-OSL signals from regeneration and test dose.

4.5 CONCLUSIONS

Different methods of speeding up sample processing by removing the finer grains were investigated because preparation of the initial sample suite from the Klip River took an unusually long time, because of the high proportion of clay and silt-sized particles in the sediment. The most efficient way found to remove these fine particles involved the use of Sodium Pyrophosphate decahydrate as a deflocculating agent. The samples were settled in this liquid to remove grains <11 μm, prior to wet-sieving through a 90 μm mesh. The remaining sediment grains (>90 μm) were then able to be dried without forming hard clumps, thus enabling them to be dry-sieved.

Investigation into the optical stimulation power and luminescence detection efficiency demonstrated that these factors vary considerably between the Risø readers at Aberystwyth. In particular, Risø 2 had a relatively poor detection efficiency. The low dose-rate of this reader makes it the most appropriate to date young and modern samples, so a new photomultiplier tube with greater sensitivity was fitted to this reader thus enhancing the OSL measurements from dim samples.

LM-OSL measurements on multiple-grain aliquots of quartz from the Klip River and the Schoonspruit showed that all the samples have fast, medium and slow components. Transformation to CW-OSL curves demonstrated that the initial part of the OSL signal used for calculation of D_e is dominated by the fast component, thus indicating that standard dating procedures should be suitable for sample analysis. Investigation into the thermal stability of the components established that the fast component is thermally stable, whilst the medium component is unstable at temperatures >140°C. The medium component only forms a small part of the OSL signal, so its thermal instability should not cause problems in routine D_e analysis.

CHAPTER 5: MEASUREMENT OF EQUIVALENT DOSE USING OPTICALLY STIMULATED LUMINESCENCE

5.1 INTRODUCTION

In order to date a sediment using OSL methods it is necessary to derive a value for the equivalent dose (D_e) of the sample, which is defined as the dose that is equivalent to the amount of radiation received during the previous burial period in nature (natural dose). Since there is no absolute relationship between dose and luminescence, a minimum of two OSL measurements are required: the OSL signal from the natural dose, and the OSL signal arising from at least one known radiation dose given in the laboratory to calibrate the material. In the previous chapter, two different methods of measuring the OSL signal (continuous wave, CW-, and linearly modulation, LM-) were described (Section 4.4). The OSL signals of all the samples analysed for dating in this thesis were strongly dominated by the fast component (Fig. 4.14), and therefore CW-OSL measurements are suitable for derivation of the D_e. In this chapter, the various methods of finding D_e from a sample are discussed, including a description of the SAR method used in the thesis (Section 5.2), followed by the initial tests required to confirm the suitability of a sample for dating using the SAR procedure (Section 5.3). Finally, the various ways in which replicate measurements of D_e for a sample can be plotted for analysis are outlined and discussed (Section 5.5).

5.2 METHODS OF EQUIVALENT DOSE DETERMINATION USING OSL MEASUREMENTS ON QUARTZ

For OSL analysis, optical stimulations of quartz are performed at an elevated temperature of 125°C (Murray and Wintle, 1998) to remove the possibility of any trapped charge from the 110°C TL peak affecting the OSL signal of interest. Prior to heating the sample to the stimulation temperature, the aliquots used are subjected to a preheat stage by holding them at a temperature normally within the range of 160-280°C for 10 s (Murray and Wintle, 2000). The purpose of the preheat stage in D_e determination is to remove thermally unstable charge from

optically-sensitive traps e.g. the 110°C and 160°C traps (Godfrey-Smith, 1994; Wintle and Murray, 1999).

5.2.1 Multiple aliquot techniques

The first applications of luminescence dating to sediments used multiple aliquot techniques to calculate the D_e value (Wintle and Huntley, 1982). These methods combine the results from a number of aliquots (often between 20 and 60), following one, or maybe two, measurements on each aliquot of the sample in order to calculate a single value of D_e. A plot of the luminescence signal as a function of the laboratory radiation dose (termed a growth curve) is constructed and the D_e calculated for a sample. These methods were originally developed for thermoluminescence dating before being adapted for OSL measurements. There are three different experimental ways in which a growth curve can be constructed in order to obtain a D_e value: 1) additive dose; 2) regenerative dose; and 3) the partial bleach method (Duller, 1996) (Fig. 5.1).

The first method involves measuring the luminescence signal from both natural aliquots and aliquots that have been exposed to a range of beta doses in addition to the natural dose. The luminescence signal from the aliquots is plotted as a function of the added laboratory dose. A growth curve is fitted through the points and extrapolated to the point at which it intercepts the x-axis (Fig. 5.1a). This gives the value of D_e. A problem with this additive dose technique, however, is the requirement for extrapolation of the growth curve in order to obtain a D_e. It is preferable to use interpolation instead to ensure that the form of the growth curve in the region of interest is correctly defined.

In the regeneration method, a growth curve is constructed using measurements of the luminescence from aliquots that have had the natural signal removed by bleaching, prior to being exposed to laboratory irradiations (Fig. 5.1b). The luminescence from the natural dose is measured from other aliquots, and this value interpolated onto the growth curve in order to obtain the D_e. Early studies, however, found that removal of the luminescence signal prior to the analysis may induce some sensitivity change during this exposure to light, and hence produce errors in the value of D_e (Rendell and Townsend, 1988).

a)

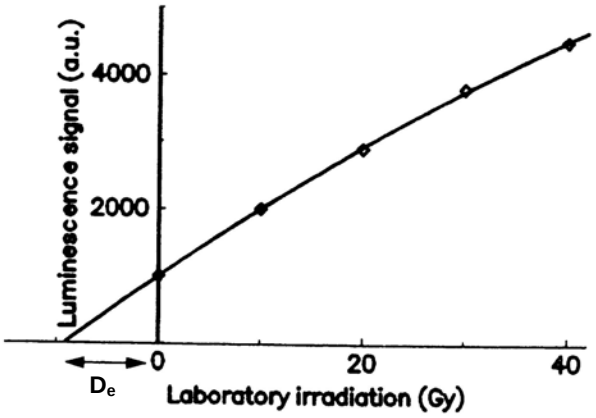

b)

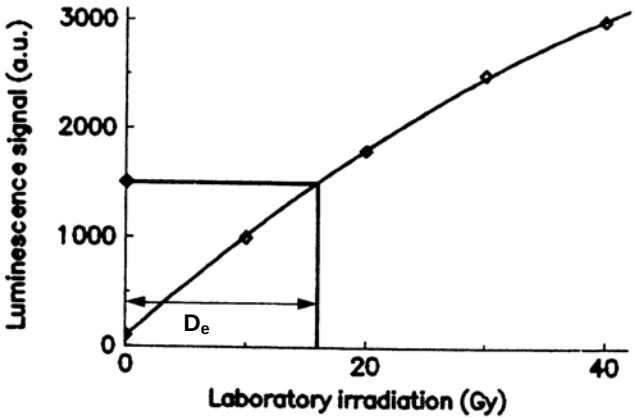

c)

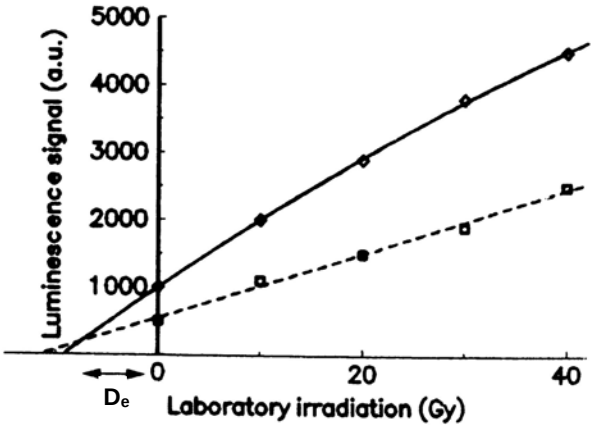

Figure 5.1: Graphs showing the three main methods for determining the D_e using luminescence techniques: a) additive dose; b) regenerative dose; c) partial bleach. From Duller (1996).

The partial bleach method uses the construction of two growth curves to obtain a D_e. The first growth curve is constructed in the manner described above for the additive dose method. A second set of aliquots are then given the same beta doses as those in the first set, then exposed to light for a short period of time (a partial bleach), followed by measurement of the luminescence signal; the partial bleach removes a fixed proportion of the light sensitive luminescence signal. A growth curve is constructed from this second set of aliquots and the intersection point between the two growth curves gives the sample D_e (Fig. 5.1c). This technique was primarily developed in order to circumvent the problems of dating sediments whose TL signal had been homogeneously partially bleached. By using the intersection of the two growth curves, rather than the intercept with the x-axis, the appropriate D_e can be obtained. The exposure of the second set of aliquots to a bleaching of short time duration is expected to empty a fixed proportion of the traps that are easily stimulated by light. Like the additive dose method, however, this technique relies on extrapolation and, if it is used to look at samples close to saturation, the extrapolation required may be extensive.

One of the main problems with multiple aliquot techniques is the assumption that the natural D_e of every aliquot of a sample is the same. This is only a valid assumption in samples that are truly homogeneous, i.e. each grain has been bleached to the same extent during transport and is exposed to an identical dose-rate during burial. This situation may not occur in nature where sediments consist of grains from a variety of geological sources that have been subject to different sedimentation histories. In many cases, multiple aliquot techniques derived a single D_e value for each sample (e.g. Hütt and Jungner, 1992; Stokes, 1992; Lian and Brooks, 2004). However, a single D_e value does not enable one to investigate the variation of D_e values within a sample, and is therefore not suitable for detecting heterogeneous bleaching in samples.

5.2.2 Single aliquot techniques

The concept of obtaining D_e values from each aliquot was first proposed by Huntley *et al.* (1985), but it was Duller (1991) who first described a practical method. His measurements were on potassium feldspar grains using infrared

stimulation, but the methods he described were subsequently adapted for dating of quartz grains (Mejdahl and Bøtter-Jensen, 1994; Murray *et al.*, 1995; Murray *et al.*, 1997). Single aliquot methods are an improvement on multiple aliquot techniques for two reasons (Duller, 1996; 2004). First, single aliquot methods make the measurement of multiple D_e values for a sample feasible, allowing variation of D_e values within a sample to be assessed. For analysis of fluvial sediments this is essential for detection of heterogeneous bleaching. Second, the precision of D_e values is improved, because no normalisation is required between measurements on a single aliquot. Recent technological advances in the equipment used for luminescence dating allows the measurement process to be automated, making it efficient and simple to operate, and thus enabling the measurement of large numbers of aliquots in a relatively short time.

5.2.2.1 Single Aliquot Additive Dose (SAAD)

Duller (1991) initially suggested that the addition of increasing doses to a single aliquot of feldspar grains could be used to build up a growth curve; in order to minimise the depletion of trapped charge, optical stimulation times are kept short (0.1 s). A correction factor to account for the signal depletion over the measurement procedure is then incorporated using a second aliquot of the sample. This procedure was adapted for application to quartz as a true single-aliquot technique by Murray *et al*. (1997); other workers had previously used the technique described by Duller (1991), but the use of a second aliquot for the signal correction was still necessary (Galloway, 1996; Stokes, 1994; Liritzis *et al.*, 1997). Following the method described by Murray *et al.* (1997), the natural OSL signal of the aliquot is measured using a 0.1 s stimulation. This is followed by repeated dosing, preheating and subsequent stimulation of the aliquot (Fig. 5.2, doses 1-4). The same aliquot is then preheated and stimulated a number of times, with no additional dosing (Fig. 5.2), and an exponential function can be fitted through these points, allowing a correction factor to be derived (see Fig. 5.3).

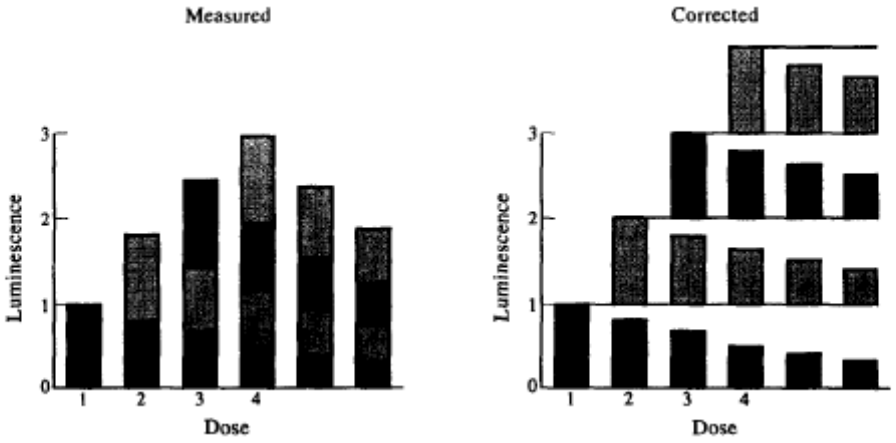

Figure 5.2: Schematic representation of the single aliquot additive dose technique; the proportion of each dose remaining after optical stimulation is depicted. The measurements to the right of dose 4 involve no further addition of dose, and should be equal after correction. From Galloway (1996).

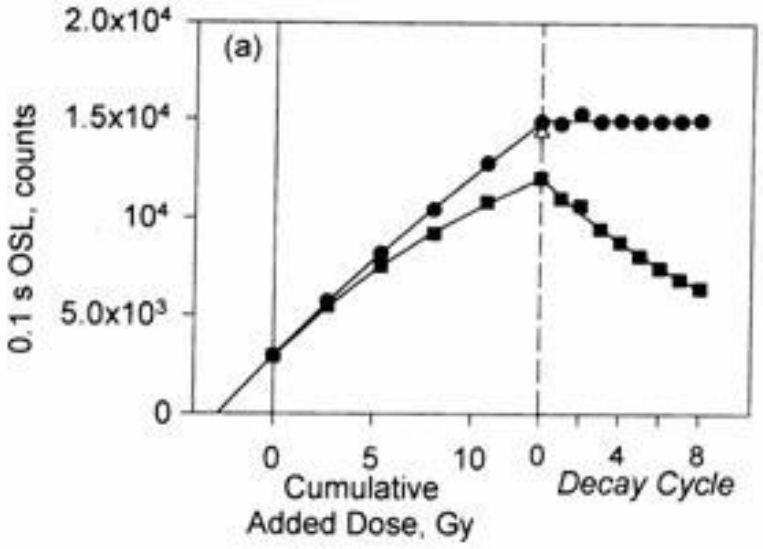

Figure 5.3: Measurements made using the single aliquot additive dose procedure. Points denoted by squares show the measured luminescence following added dose. The last eight points received no dose between subsequent preheats and stimulations, allowing a correction factor for the loss of signal to be found. The circular data points show the data corrected for signal loss. From Murray *et al.* (1997).

Murray *et al.* (1997) applied the SAAD protocol to eleven samples that had previously been analysed using the multiple-aliquot additive-dose procedure, and despite different calibrations and preheat temperatures used for the analysis, the results were generally in good agreement (Fig. 5.4). Although the SAAD protocol appeared to be suitable for the samples analysed by Murray *et al.* (1997), the Oxford Luminescence Research Group found that a large proportion of their samples were not suitable for analysis using this method (Stokes *et al.*, 2000). They identified the two main assumptions of the SAAD protocol as being: 1) that the sensitivity of an aliquot does not alter during the procedure; 2) that the amount of OSL signal depletion during each preheat and stimulation cycle remains constant and is not dependant on the given dose. Investigation into the characteristics of 62 samples by Stokes *et al.* (2000) found that for 65 % of the samples, at least one of these assumptions did not hold true and hence led to invalid results using the SAAD procedure. A high proportion of the sensitivity change in quartz is induced by the preheating of the sample; this repeated thermal treatment is necessary in single-aliquot techniques and recognition of this problem led to the development of a single-aliquot procedure that corrects for any sensitivity change.

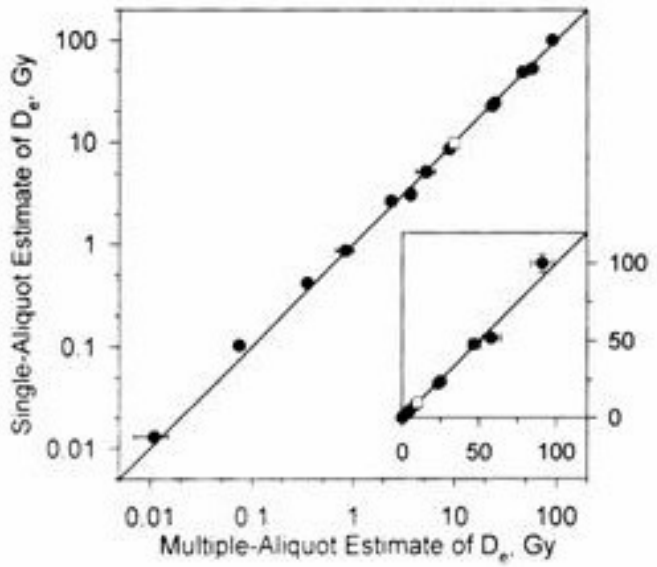

Figure 5.4: Plot comparing D_e values obtained for the same sample using both multiple aliquot and single aliquot additive dose techniques. Axes are logarithmic to best show the low doses; inset shows the same data on a linear scale. From Murray *et al.* (1997).

5.2.3 Single Aliquot Regenerative Dose (SAR)

A regeneration dose procedure was initially developed for feldspar by Duller (1991) but was found to have severe limitations because of sensitivity changes. The single aliquot regenerative dose (SAR) procedure for quartz was described by Murray and Roberts (1998) and further developed by Murray and Wintle (2000). The most important modification of the later work was the inclusion of a fixed test dose following measurement of the natural and regeneration doses, allowing sensitivity change to be monitored throughout the procedure and corrected for. Prior to measurement of the test-dose, a thermal treatment termed the 'cut-heat' is applied, instead of a preheat. This step has the same purpose as the preheat, but in order to minimise sensitivity change between measurement of the natural or regenerated signal and the test dose signal, the heating step applied during the cut-heat is less severe than the preheat. The cut-heat is different to the preheat in two fundamental ways: first, the sample is cooled immediately once the desired temperature has been reached, as opposed to being held at this temperature for 10 s; and second, where possible the cut-heat temperature is kept at 160°C.

The basic outline of the SAR sequence is given in Table 5.1. After preheating and subsequent measurement of the natural OSL signal (L_N) (Steps 1-2) the aliquot is given a small beta irradiation, termed the test dose (Step 3). It was suggested by Murray and Wintle (2000) that this should be around 10-20 % of the natural dose. Following a cut-heat, the OSL signal from this test dose (T_N) (Step 4) is measured (Step 5) and used to normalise the natural signal (L_N/T_N). The same aliquot is then given a range of regeneration doses (D_X), followed by a preheat step, for which the resulting OSL decay curves (L_X) are recorded (Steps 6-8). Each regeneration dose is followed by a test dose, cut-heat, and measurement of the subsequent OSL signal (T_X), allowing L_X/T_X to be found for each regeneration point (Steps 9-11). Thus, the test dose response corrects for any sensitivity change that occurs during the SAR procedure. To confirm that the sensitivity correction is working suitably, the final regeneration dose (D_5), termed the recycling point, is the same as the initial dose (D_1). The ratio of L_1/T_1 to L_5/T_5 should be consistent with unity if the sensitivity correction is satisfactory. A growth curve (Fig. 5.5) is constructed by plotting the L_X/T_X

values as a function of the regeneration dose for each aliquot. Projection of the L_N/T_N value onto the growth curve allows the D_e value to be derived. Following publication of the SAR procedure (Murray and Roberts, 1998; Murray and Wintle, 2000), it was widely used for samples covering a range of depositional environments including aeolian, lacustrine, marine, and fluvial. Murray and Olley (2002) provided a comprehensive review comparing OSL ages found using the SAR protocol with independent age control, for samples from a range of environments. They found that the majority of OSL ages were consistent with the independent ages, and no systematic deviation with increasing age could be found.

Table 5.1: Standard SAR protocol as described by Murray and Wintle (2000).

Step	Treatment	
1	Preheat (160 -300°C) for 10s	
2	OSL stimulation at 125°C for 40s	L_N
3	Test dose beta irradiation	
4	Cut-heat to 160°C for 0s	
5	OSL stimulation at 125°C for 40s	T_N
6	Beta irradiation of regeneration dose (D_{1-5})	
7	Preheat (160 -300°C) for 10s	
8	OSL stimulation at 125°C for 40s	L_X
9	Test dose beta irradiation	
10	Cut-heat to 160°C for 0s	
11	OSL stimulation at 125°C for 40s	T_X
12	Repeat steps 6 - 11 with further regeneration doses	

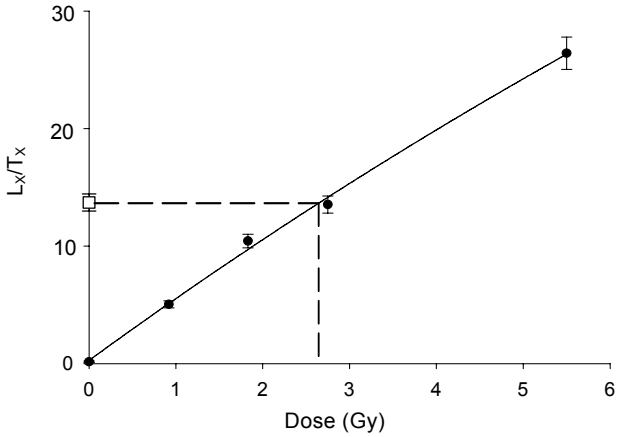

Figure 5.5: Growth curve constructed using the SAR procedure for one aliquot of sample 70KLA1. The equivalent dose for this aliquot is 2.6 ± 0.2 Gy, and the recycling ratio is 1.00 ± 0.04.

5.2.3.1 Potential problems

The application of the SAR protocol by many researchers in the last six years has shown that the procedure recommended by Murray and Wintle (2000) may not be suitable for every quartz sample. Stokes *et al.* (2000) found that 16 % of 112 samples were not suitable for analysis using this procedure. Continued use of the SAR protocol with samples from a range of depositional environments and geographical localities has found that use of the standard procedure can be problematic in three different situations:

1) Where the OSL signal is dominated by medium and/or slow components as opposed to the fast component. Tsukamoto *et al*. (2003) found that the D_e decreased with stimulation time for samples of Japanese loess and volcanic quartz leading to significant underestimation of the OSL age compared to independent age control. They suggested that the change in D_e value occurred because of increasing recuperation of the medium and slow components with stimulation time. In order to obtain a D_e value not affected by recuperation, they found both the D_e and percentage recuperation for different time intervals. The D_e was then plotted as a function of the percentage recuperation and an exponential curve was fitted to the points; the intercept of this curve with the y-axis allowed the 'true' D_e to be found. In a more recent study, however, Li and Li (2006) found that recuperation did not cause the D_e underestimation; instead they attributed the variation in D_e with stimulation time to the thermal instability of the medium component. In order to construct a growth curve based on a single component, curve deconvolution of LM-OSL signals to isolate either a small fast component or the medium component has been suggested as a method for obtaining D_e values from samples that are not dominated by the fast component (Singarayer and Bailey, 2003).

2) Where the OSL signal includes a component with a higher detrapping probability than the fast component. Choi *et al.* (2003a,b) found evidence of an ultra-fast OSL component and an isothermal TL signal in quartz from marine terraces off the coast of Korea. These signals lead to an inability to recover a known given dose using the standard SAR procedure. Experimental work demonstrated that these unwanted components could be removed by heating

the sample to at least 200°C, and so a higher cut-heat temperature was used in the analysis of these samples.

3) Where significant recuperation of the fast component of the OSL signal occurs. Stokes *et al*. (2000) found that the thermally transferred OSL signal could be as high as 50 % of the intensity of the natural signal in samples from coastal dunes in New Zealand. Murray and Wintle (2003) suggested that this was because of charge remaining in an optically-insensitive trap after measurement of the test dose OSL, some of which is then transferred to an optically-sensitive trap during the subsequent preheat step. In order to reduce recuperation experimentally, they proposed a modification to the 'standard' SAR protocol, which consisted of a high temperature (280°C) optical stimulation after measurement of the test dose (T_X).

5.3 TESTING THE APPROPRIATENESS OF THE SAR PROCEDURE

Initial tests characterising the OSL signal of the quartz studied in this thesis were described in Chapter 4. These indicated that for every sample, the OSL signal is dominated by the fast component, suggesting that the SAR protocol should be suitable for analysis of these samples. Prior to standard dating analysis of the samples, however, further tests must be conducted in order to check that no unusual results arise, and to select the most suitable preheat temperature for each sample.

5.3.1 Variation of D_e with preheat temperature

The D_e can be measured for aliquots given a range of preheat temperatures. The aliquots at different temperatures will undergo varying amounts of sensitivity change during the experimental procedure. This allows one to assess whether the D_e values remain consistent as the temperature changes, and if not, then one can select the most suitable preheat temperature for a particular sample. The temperature range that gives consistent results for the D_e values is termed the preheat plateau.

Murray and Wintle (2000) demonstrated for two samples that no preheat dependence of the D_e value was present over a preheat range of 160-300°C

(Fig. 5.6), but they noted that recuperation of the OSL signal did appear to be slightly more significant at temperatures >260°C. Conversely, Ward *et al.* (2003) urge caution owing to the presence of signal transfer from geologically unstable TL traps to those utilised for OSL dating in young fluvial samples, as this may lead to D_e overestimation. In their study, seven fluvial samples were investigated for preheat dependence of the D_e value. Of these, five showed some preheat dependence, and two very young samples from the Colorado River, Texas, USA (D_e values of 0.21 and 0.17 Gy) demonstrated rising D_e trends with preheat temperature (Fig. 5.7). This was attributed to incomplete bleaching of the traps in the 160-300°C TL region. Despite these results, many other previous studies demonstrate no significant trends in the D_e preheat plots for samples only a few thousand years old (e.g. Bailey *et al.*, 2001; Thomas *et al.*, 2005).

In this thesis, the variation in D_e with changing preheat temperature was investigated by using medium aliquots of quartz which were measured using the

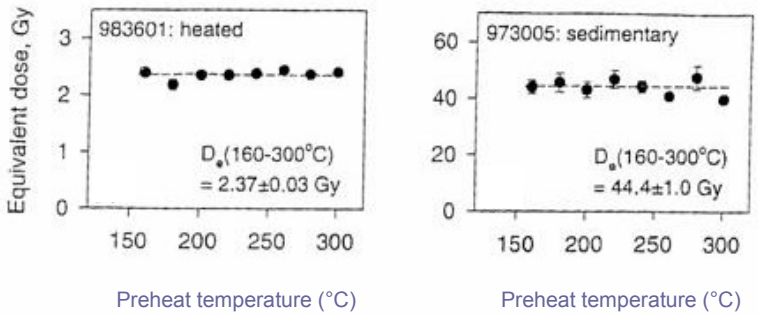

Figure 5.6: Plots of D_e as a function of preheat temperature for two samples of quartz. Each point is the average of three aliquots. From Murray and Wintle (2000).

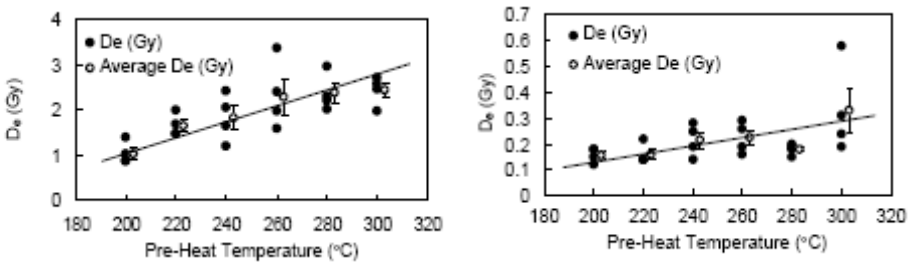

Figure 5.7: Plots of D_e as a function of preheat temperature for two samples of fluvial quartz. From Ward *et al.* (2003).

standard SAR procedure (Table 5.1) to derive the natural D_e. Twenty four discs were used in total for each sample and three aliquots were measured at each preheat temperature in 20°C steps over the range 160-300°C; a cut-heat temperature of 160°C was used as standard. This test was performed on samples 70KLA1-70KLA6. Plots of the D_e values obtained as a function of preheat temperature can be seen in Figure 5.8 where the results for each aliquot measured are shown. Samples 70KLA1 and 70KLA6 have relatively little scatter in the results, with a preheat plateau for both samples over the range 160-260°C and 160-280°C, respectively; the scattered points at the higher temperatures are likely to be caused by thermal erosion of the trapped charge in the 325ºC OSL trap. Samples 70KLA2, 4 and 5 have D_e values which are scattered, but no distinct trend with preheat temperature is evident. Despite the scatter in the results, there is nothing in the data to suggest a dependence of D_e on the preheat temperature. The results for 70KLA3 are different, with a falling trend occurring over the 160-200°C range and more consistent D_e values at temperatures >200°C. The D_e values for this sample are very close to saturation (see Fig. 5.9) which may cause this trend on the preheat plot; at this point of the growth curve, D_e derivation is less accurate than during the linear growth stage. In addition, some thermal erosion of a part of the OSL signal that is not stable over long time periods may occur at the higher temperature preheats.

It is likely that the scatter in the preheat plots (for 70KLA2-5) occurs because of heterogeneous bleaching, but it means that the appropriate preheat temperature for use in the SAR procedure cannot be selected. Instead, a dose recovery test over a range of preheats can be used to see at what temperatures a known given dose can be accurately recovered. This situation is not ideal as the thermal stability of the OSL signal from the natural irradiation may be different to that from a laboratory dose; a dose recovery test includes any thermally unstable signal induced by the laboratory irradiation unless, following irradiation, the aliquots are stored for a long time. In practice this is impractical, so a dose recovery test over a range of preheat temperatures is the best option for testing whether the SAR protocol is suitable for samples with heterogeneous bleaching.

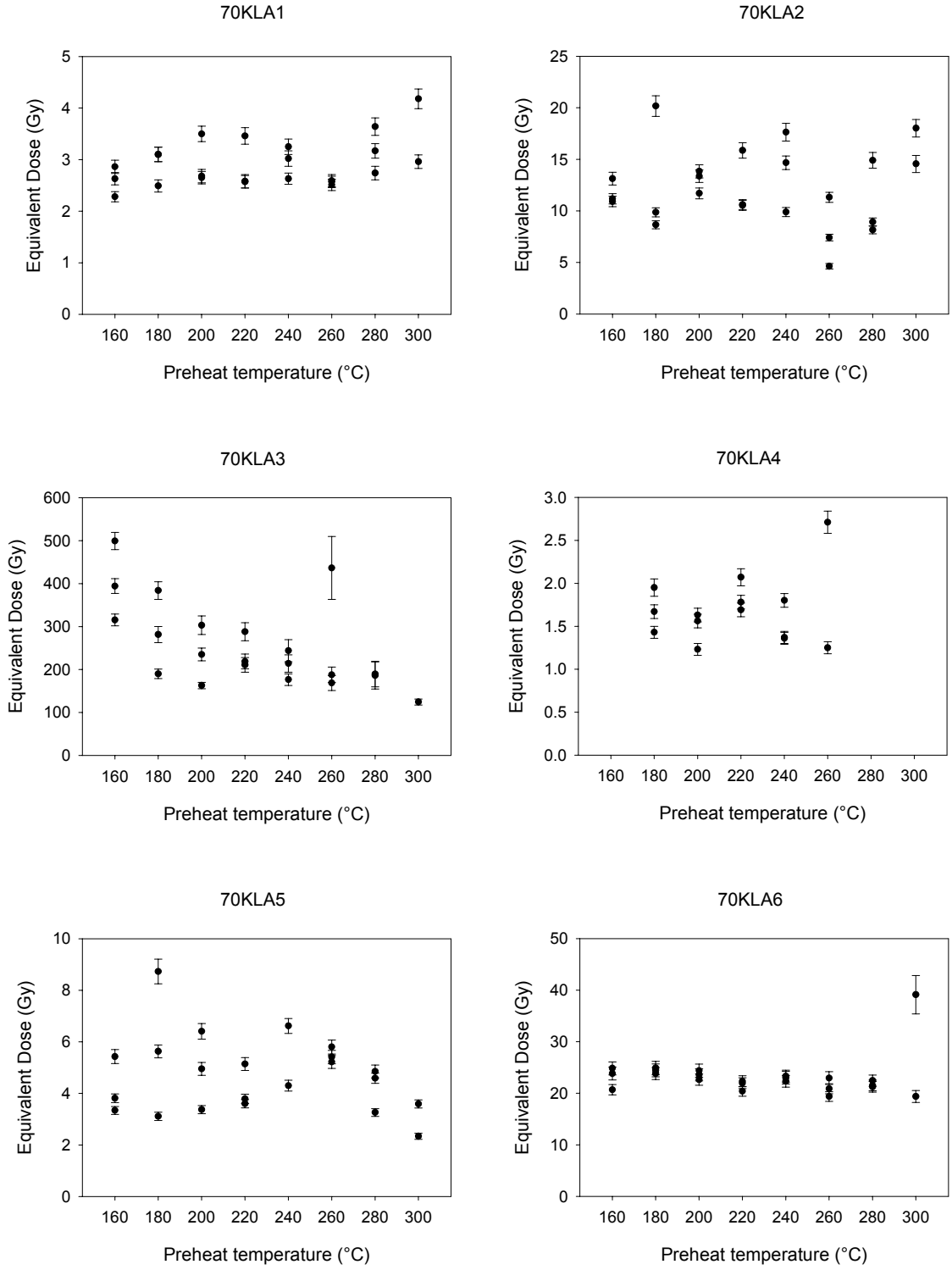

Figure 5.8: Preheat plots of samples 70KLA1-6.

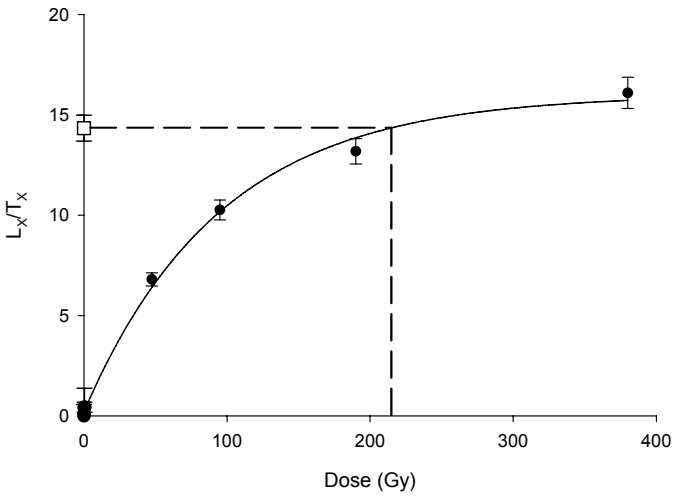

Figure 5.9: A typical growth curve for an aliquot of sample 70KLA3.

5.3.2 Dose recovery test

For this type of experiment, an aliquot has its natural signal removed by optical bleaching, followed by irradiation at room temperature in the laboratory. This laboratory dose is then treated as an unknown value and a D_e value is obtained using the SAR protocol. The ratio of the measured dose (calculated from construction of a growth curve following the standard SAR procedure) to the given dose (a known value from laboratory irradiation) should be consistent with unity if the SAR procedure is working successfully (Fig. 5.10).

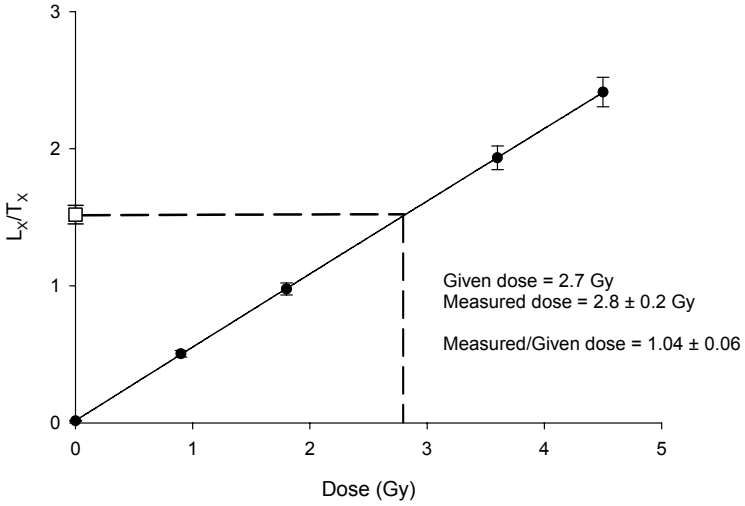

Figure 5.10: Results from dose recovery experiment (preheat of 220°C) on one aliquot of 70KLA1. The ratio of the measured dose to the given dose is consistent with unity.

The initial dosing of the aliquot should mimic nature as closely as possible so that the experiment is similar to obtaining a natural D_e value from each aliquot. However, the two primary differences between a natural situation and that in the laboratory are the temperature and dose-rate. Although the initial dosing is applied at room temperature and prior to any thermal treatment, the natural situation can never be truly simulated, particularly with respect to the dose-rate as this is typically higher in the laboratory than in nature by a factor of ~10^8.

5.3.3 Dose recovery as a function of preheat temperature

In this thesis, the suspected presence of heterogeneous bleaching meant that a preheat plateau could not be obtained for the samples analysed using standard methods (Fig. 5.8). Instead, a combined "dose recovery and preheat test" was developed. This experiment combined the two methods in order to investigate simultaneously the ability of SAR to recover a dose from a sample, and to choose the most suitable preheat temperature for use in the SAR procedure. For each sample, sixteen medium sized aliquots were analysed; initially, they were bleached for 100s at 125°C at maximum optical stimulation power (80 % for Risø 2 and 90 % for Risø 3) to entirely remove the natural signal (Jacobs, 2004: p62). The aliquots were then given a beta dose chosen to be close to the expected natural dose, as established from initial tests on two medium aliquots. The aliquots were then analysed using the SAR procedure. Two aliquots were preheated at each temperature between 160°C and 300°C in 20°C intervals, and a cut-heat of 160°C was used as standard. A graph of the ratio of the measured dose divided by the given dose as a function of the preheat temperature was then plotted. The results for samples 70KLA1-6 can be seen in Figure 5.11; these generally demonstrated ratios consistent with unity for temperatures between 160°C and 260°C. The plot for sample 70KLA3 shows a similar trend to the results found for the preheat test on the natural dose for this sample (Fig. 5.8). The dose recovery and preheat test suggests that for this sample in particular, using a preheat temperature >200°C is important to obtain the correct D_e for an aliquot. Plots of the dose recovery and preheat tests for every sample are shown in Appendix C, and details of the preheat plateaux identified for the samples are detailed in Table 5.2.

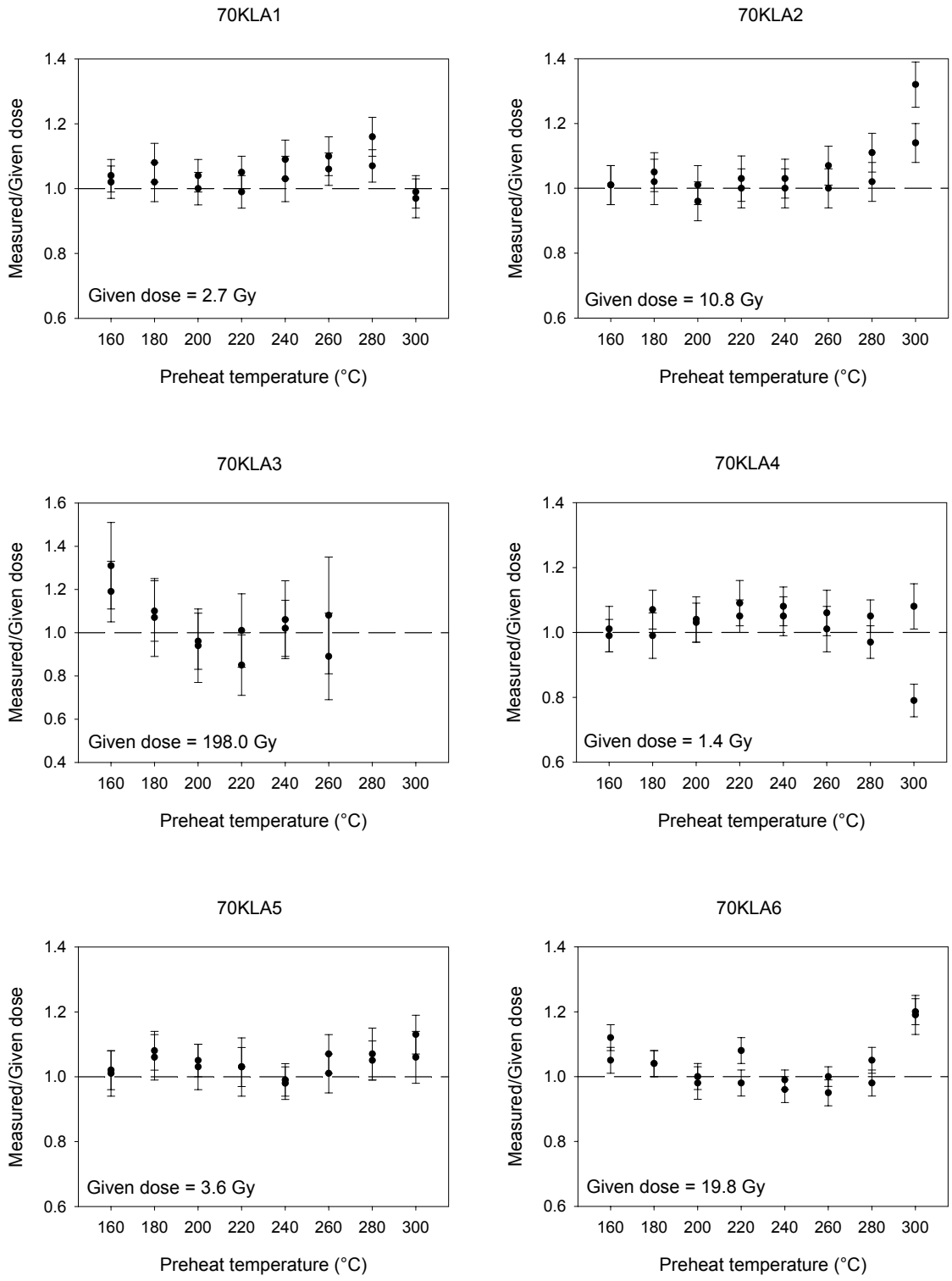

Figure 5.11: Dose recovery and preheat plots for samples 70KLA1-6. The aliquots of sample 70KLA3 with 280°C and 300°C preheats failed the recycling ratio test and therefore are not included in this graph.

Table 5.2. Details of dose recovery and preheat tests performed on samples from the Klip River and Schoonspruit.

Sample	Preheat plateau (°C)	Given dose (Gy)	Average ratio of measured/given dose over preheat plateau	Chosen preheat (°C)
70KLA1	160-300	2.7	1.04 ± 0.05	220
70KLA2	160-260	10.8	1.01 ± 0.03	220
70KLA3	200-260	198.0	0.98 ± 0.03	220
70KLA4	160-280	1.4	1.03 ± 0.04	220
70KLA5	160-260	3.6	1.03 ± 0.03	220
70KLA6	200-280	19.8	1.00 ± 0.04	220
75KL0308*		2.3	1.04 ± 0.02	220
75KL0309	160-280	2.3	1.05 ± 0.05	220
75KL0310	160-300	5.5	1.01 ± 0.06	200
75KL0311	160-300	11.0	1.02 ± 0.04	240
75KL0315	160-280	9.2	1.03 ± 0.04	240
75KL0316	160-260	2.3	1.03 ± 0.08	220
75KL0317	160-300	0.8	1.09 ± 0.09	220
75KL0318	160-300	1.1	1.03 ± 0.08	200
75KL0319	160-280	1.6	1.04 ± 0.09	200
75KL0320	160-280	2.0	1.02 ± 0.04	200
75KL0321	160-260	2.7	1.03 ± 0.03	200
75KL0322	160-300	3.2	0.99 ± 0.04	220
75KL0323	160-260	2.3	1.01 ± 0.03	240
75KL0324	160-280	1.3	1.02 ± 0.04	220
75KL0325	160-300	0.5	0.99 ± 0.04	220
75KL0326	160-260	0.3	1.01 ± 0.07	220
75KL0327	160-300	0.7	1.03 ± 0.06	220
75KL0328	160-300	3.2	1.04 ± 0.05	220
75KL0329*		3.7	1.00 ± 0.01	220
75KL0330	160-280	13.8	1.00 ± 0.08	220
75KL0331	160-280	29.3	1.02 ± 0.06	220
75KL0332	160-260	1.8	1.04 ± 0.04	220
75KL0333	160-280	1.8	1.03 ± 0.03	220
75KL0334	160-300	2.5	1.06 ± 0.05	220
75KL0335	160-260	2.8	1.05 ± 0.03	220
75KL0336**	160-200	36.7	1.03 ± 0.05	220
75KL0337**	160-200	45.8	1.03 ± 0.10	220
75KL0338	160-300	38.5	1.04 ± 0.07	220
75KL0339*		1.1	1.02 ± 0.04	220

75KL0340	160-300	1.8	1.05 ± 0.07	220
75KL0341	160-300	9.2	1.02 ± 0.07	220
75KL0342*		1.4	1.05 ± 0.02	220
91SC0401	160-300	3.7	1.03 ± 0.03	220
91SC0403	160-260	4.6	1.02 ± 0.02	220
91SC0404	160-300	4.6	1.01 ± 0.06	220
91SC0405	160-280	4.6	1.03 ± 0.02	220
91SC0406	160-260	1.8	1.03 ± 0.03	220
91SC0407	160-280	5.5	1.04 ± 0.04	220
91SC0408A	160-240	1.8	1.02 ± 0.02	200
91SC0409	160-280	9.0	1.01 ± 0.04	220
91SC0410	160-300	9.2	1.03 ± 0.04	220
92KL0401	160-300	1.8	1.02 ± 0.03	200

* Because of the small amount of quartz recovered for analysis, these samples did not have a full dose recovery and preheat experiment performed on them.

** The poor results from the experiment on these samples are dealt with in section 5.3.3.2.

5.3.3.1 Assessing sensitivity change using the dose recovery and preheat plot

The variation in sensitivity change of aliquots given different preheat temperatures can be assessed by plotting the OSL response to the test dose during each cycle of the SAR procedure. This procedure is described in Armitage *et al.* (2000) where variations in sensitivity change are plotted and investigated for two southern African quartz samples. In that study, different patterns of sensitivity change in the samples occurred between high temperature preheats (240-300°C) and low temperature preheats (160-220°C). The former group generally showed no substantial change or an increase in the sensitivity, whereas the latter group demonstrated a significant decrease in sensitivity.

Plotting data from the dose recovery SAR run in this manner allows the amount of sensitivity change occurring at each preheat temperature to be judged, thus aiding the selection of a suitable preheat temperature for routine analysis of a sample. Figure 5.12 shows the results for samples 70KLA1-6; with the exception of sample 70KLA3, the results show a similar trend to that found by Armitage *et al.* (2000) whereby aliquots with high temperature preheats show an increase in the sensitivity, and those aliquots with a low temperature preheat

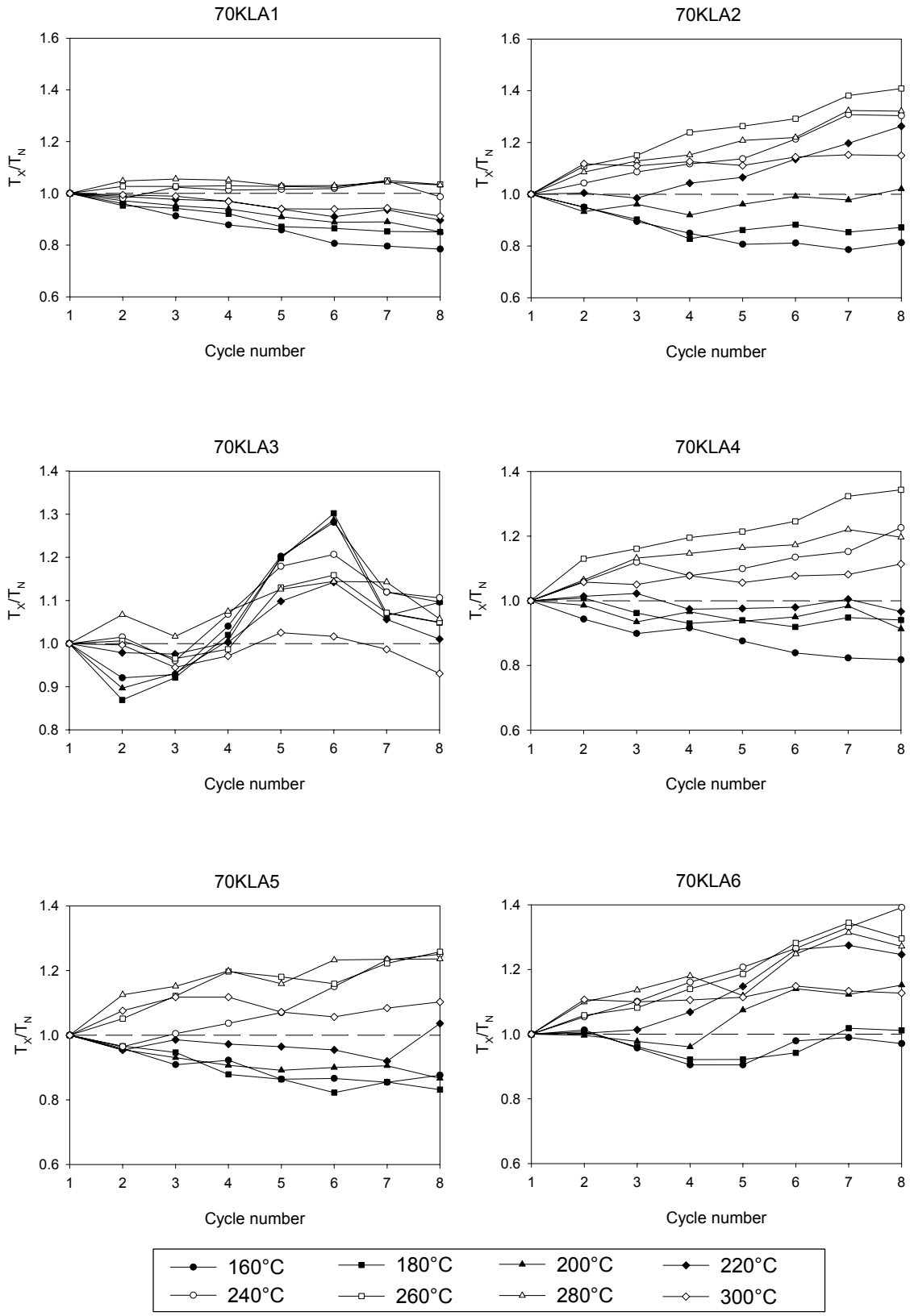

Figure 5.12: Plots of sensitivity change through the SAR procedure, for a range of preheat temperatures and plotted as a function of cycle number. Results are the mean of two aliquots.

show a decrease in sensitivity. The plot for sample 70KLA3 shows a different trend, with variation in the test dose OSL signal apparently reflecting the magnitude of the regenerated doses as opposed to sensitivity changes; the test dose signal initially increases (as the regenerative doses increase), then decreases after the sixth cycle (when a zero dose and the recycling doses are given). This suggests that, for this sample, relatively little sensitivity change occurs and instead the change in test dose response may be occur because of a small amount of the regenerated dose remaining in the grains after OSL stimulation. The extent of the remaining dose is relatively small for a preheat temperature of 220°C (<10 %) and does not appear to affect calculation of the given dose (Fig. 5.11) and thus no further measures to overcome it are necessary. For dating analysis of the samples in this thesis, a preheat temperature was selected that was both within the preheat plateau and showed minimal sensitivity change. For all the samples from the Klip River and Schoonspruit, a temperature between 200ºC and 240ºC was used (Table 5.2).

5.3.3.2 Increased cut-heat temperature

Although the majority of the samples demonstrated a clear preheat plateau (Appendix C, Table 5.2), two samples, 75KL0336 and 75KL0337, showed a monotonic decrease in D_e as the preheat temperature increased (Fig. 5.13a). The form of the OSL signal from these two samples was compared with that from sample 75KL0338, which was collected at a greater depth from the same auger hole as 75KL0337, and has a 'normal' dose recovery and preheat plot. Figure 5.14 shows the CW-OSL and LM-OSL curves following a range of doses for these three samples; the OSL has been normalised to the initial data point to make the curves comparable. No large difference between the normalised CW-OSL curves can be seen in either the natural or the laboratory doses; there is some evidence that the regenerated OSL for sample 75KL0338 has a slightly higher proportion of a medium or slow component than the other two samples, but this is unlikely to cause the effect seen in Figure 5.13a. Furthermore, the LM-OSL measurements confirm that there is no discernable difference between the components that form the luminescence signal of the samples. The temperature difference between the preheat and cut-heat also appears to have no effect on the OSL signals.

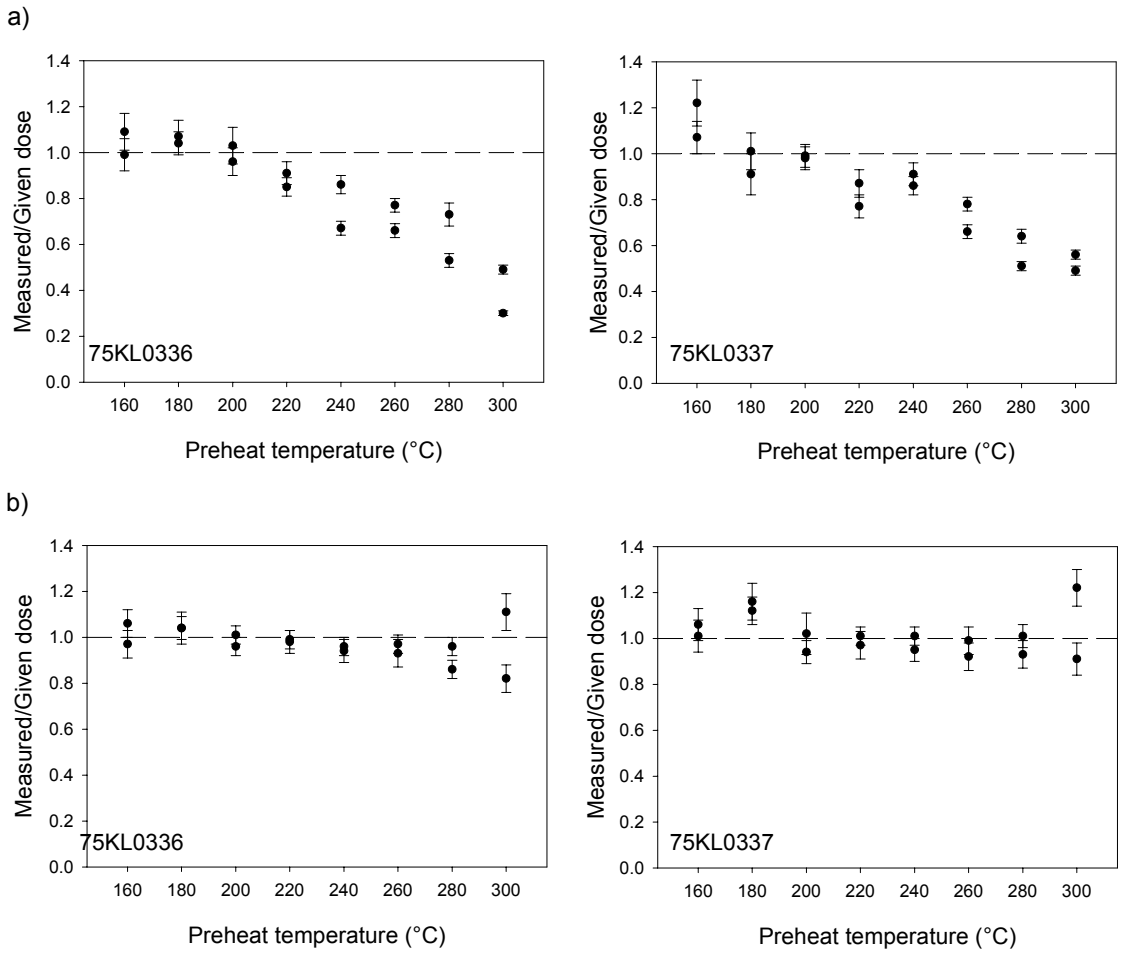

Figure 5.13: Dose recovery and preheat plots for samples 75KL0336 and 75KL0337 with a) a cut-heat of 160°C and b) a cut-heat 20°C less than the preheat temperature.

a)

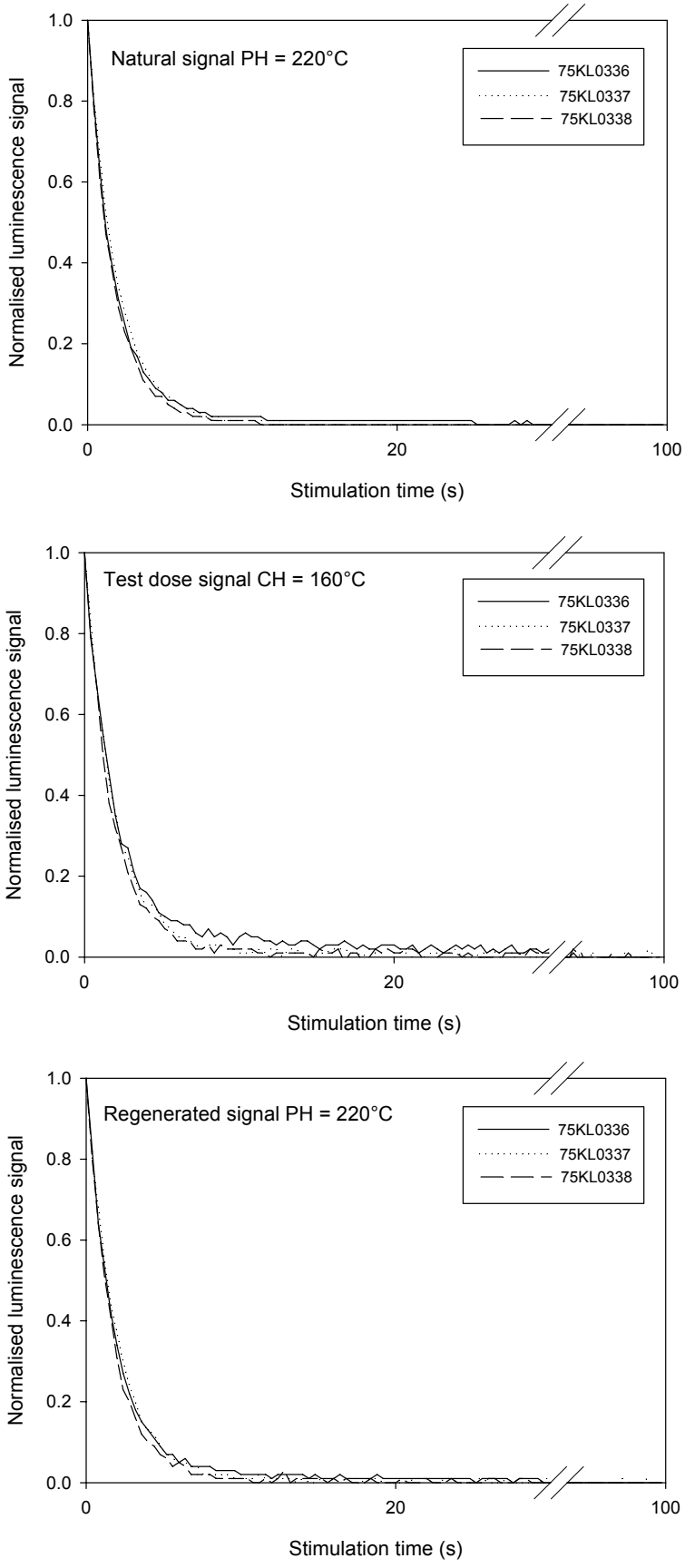

Figure 5.14: Comparison of a) CW-OSL- and b) LM- OSL curves, for samples 75KL0336-38.

b)

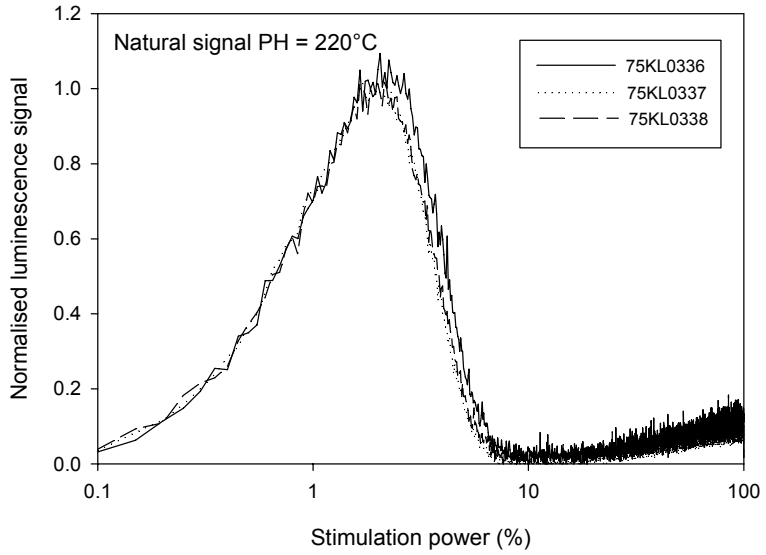

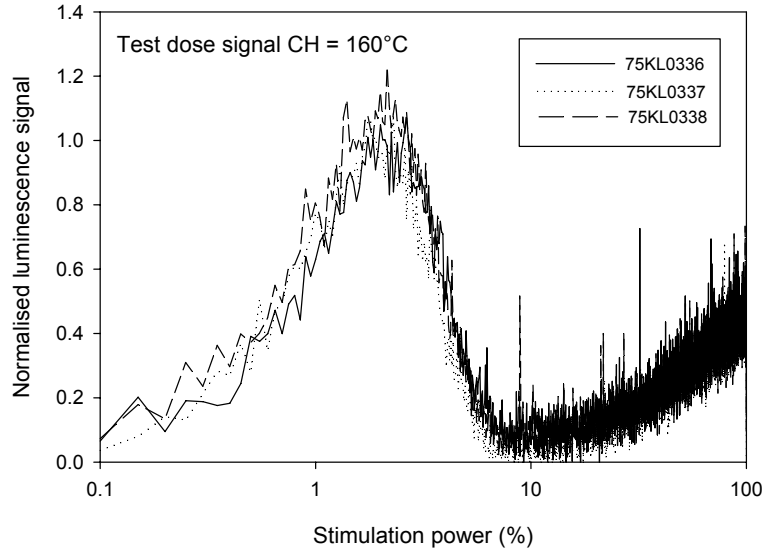

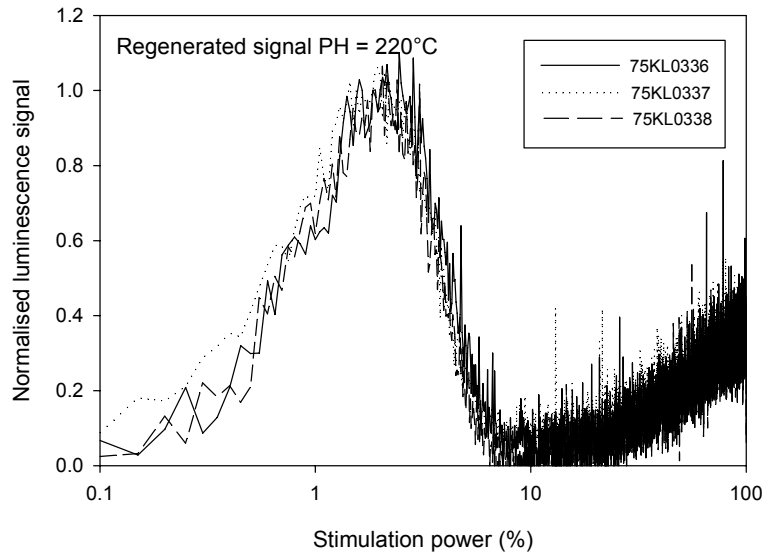

(Figure 5.14 continued)

Investigation into the L_X/T_X ratios for both the 'natural' (given dose) and the regeneration doses indicate that the L_N/T_N values fell as the preheat temperature increased, whereas plots of L_X/T_X against preheat temperature remained constant (Fig. 5.15). Roberts and Duller (2004) showed that when they plotted L_X/T_X as a function of preheat temperature for a sample of quartz from Australia, the values remained constant over the range 160-260°C, after which they were reduced owing to thermal erosion at the higher temperatures. The data shown in Figure 5.15 suggests that for some reason either the OSL signal associated with the 'natural' (i.e. given) dose decreases at temperatures >220°C, or the test dose following the 'natural' dose is enhanced at these temperatures.

The data in Figure 5.16a show that the sensitivity change occurring in the aliquots during the dose recovery and preheat plots did not follow the normal pattern for samples from the Klip River (Fig. 5.12); the sensitivity at higher cut-

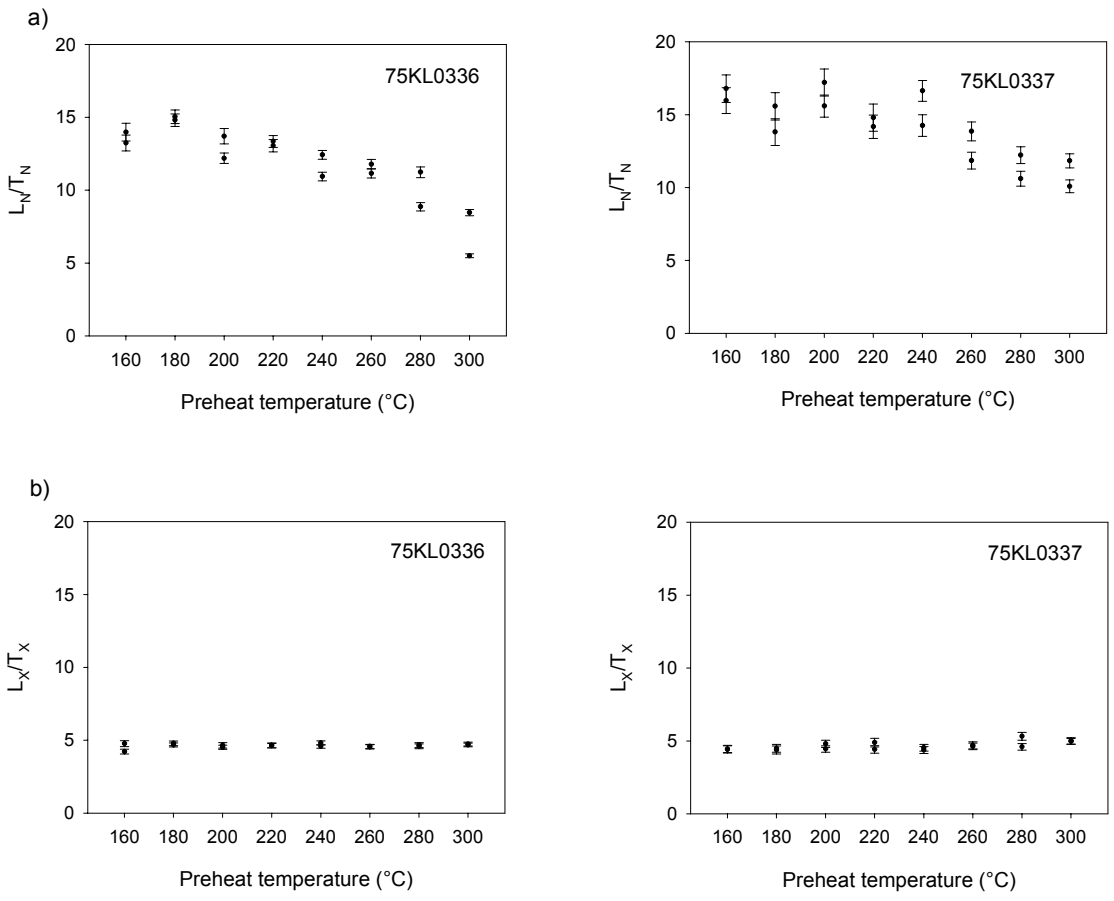

Figure 5.15: Plots of L_X/T_X for: a) the 'natural' (i.e. given dose); and b) a 9.5 Gy regenerative dose for samples 75KL0336 and 75KL0337.

heat temperatures (>220°C) fell dramatically, with the sensitivity after 8 cycles less than 50 % of the original level when a preheat of 300°C was used. This pattern of sensitivity change did not occur in any other samples from the Klip River. The recycling ratios for all the aliquots are consistent with unity, which indicates that the test dose is successfully correcting for this sensitivity change within the SAR sequence. However this test is not able to assess whether sensitivity change in the natural dose measurement cycle is accounted for correctly.

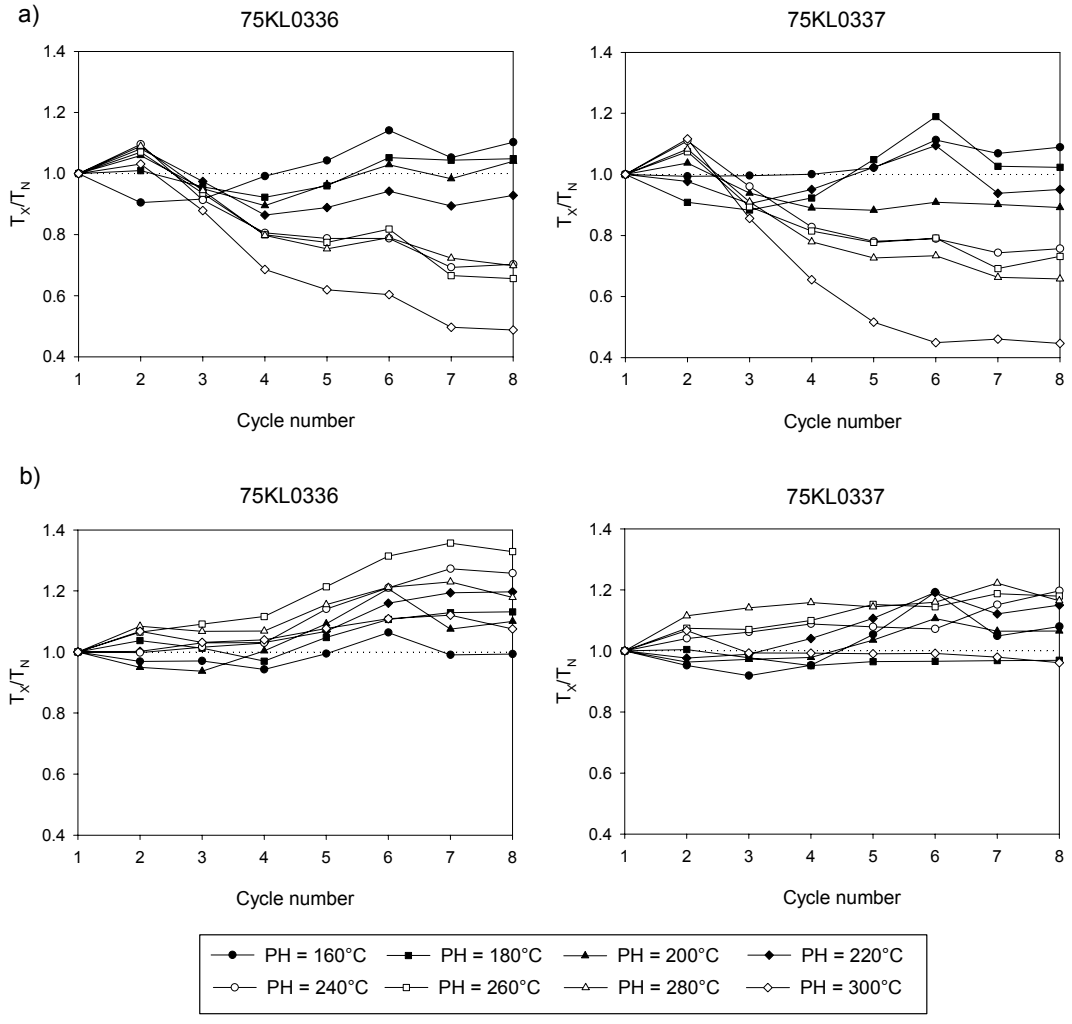

Figure 5.16: Plot of changing sensitivity over the SAR cycle for aliquots of samples 75KL0336 and 75KL0337 measured at different preheat temperatures; a) using a cut-heat of 160°C and b) with a cut-heat 20°C less than the preheat temperature. Each point is the average of two aliquots.

Previous studies where a given dose is unable to be recovered using the standard SAR have overcome the problem by using an increased cut-heat temperature prior to measurement of the test dose response procedure (e.g. Bailey, 2000; Choi et al., 2003b). In order to test whether this approach is suitable, a second dose recovery and preheat test was performed on the two samples, this time with a cut-heat that was 20°C less than the preheat temperature (previously it was fixed at 160°C). For both samples, this second dose recovery and preheat experiment yielded improved results, with the majority of the measured/given dose ratios consistent with unity (Fig. 5.13b). The sensitivity change that occurred during this experiment followed the pattern found in the other samples from the Klip River (Fig. 5.16b); with the sensitivity increasing at the higher preheat temperatures. Following these results, a SAR procedure with a preheat temperature of 220°C and a cut-heat of 200°C was used for dating of these two samples.

Samples 75KL0336 and 7KL0337 appear to behave differently to other samples collected from the Klip River site. The depositional unit from which they were collected is unlikely to contain grains derived from a different geological origin to the other units sampled, as the surrounding geology in the Klip River catchment is relatively homogeneous sandstones and shales intruded by dolerite (Section 2.2). Both samples, however, were taken from a silt/clay layer that was bluish in colour, whereas the other samples from the Klip River were collected from brown sand/clay deposits. Indeed, sample 75KL0338 was taken at a greater depth from the same auger hole as 75KL0337 and this sample demonstrated a 'normal' dose recovery and preheat plot when a cut-heat of 160°C was used. This suggests that the unusual behaviour of the two samples may be related to the depositional unit with which they are associated. The bluish colour of the sediment may be caused by a reducing environment in this relatively fine-grained layer. The unusual results from the dose recovery and preheat experiments for these two samples demonstrate the importance of performing a dose recovery experiment on every sample that is analysed.

5.3.4 IR checks

Duller (2004) suggested using infrared stimulation of an aliquot to check for the contribution of feldspars to the OSL signal that is measured. This test includes a second recycling dose within the SAR procedure (directly after the first recycling dose). Prior to blue LED optical stimulation, however, the disc is exposed to infrared (IR) stimulation to detect any IRSL arising from feldspars. If any feldspar is present, either in the form of feldspar grains contaminating the sample or feldspar inclusions within quartz grains, the OSL signal following the IR stimulation will be depleted relative to what would be expected. The ratio of this OSL signal over the signal arising from the initial recycling dose is termed the OSL-IR depletion ratio, and should be consistent with unity if no feldspars are present on the disc.

5.4 OBTAINING D_E VALUES

The standard SAR procedure, as described in Section 5.2.3, was used for analysis of the samples, with the extra step of the stimulations for the IR-OSL depletion ratio included. To be able to detect heterogeneous bleaching within a sediment, it is preferable to reduce the area of the disc containing quartz (Olley *et al.*, 1999), thereby reducing the number of grains in an aliquot and minimising averaging of the luminescence signal between the grains. If a sample is heterogeneously bleached, then minimising the number of grains should make it easier to detect differences between the D_e values of different grains. For dating of the samples in this thesis, an aliquot mask size of 2 mm diameter was used, and this is termed a "small aliquot". For each sample, a large number of aliquots were measured in order to enable investigation of the dose distributions.

Not every aliquot measured was used in subsequent analysis of the sample; a number of rejection criteria were used to exclude, from the D_e distributions obtained for each sample, aliquots that may give an erroneous value of equivalent dose. Calculation of the error on each D_e value is particularly important for heterogeneously bleached samples and the two main sources of error - counting statistics and systematic error - will be discussed later in this

section. Knowledge of the error on a D_e allows one to determine whether a high outlier occurs because the aliquot contains partially bleached grains, or because it is a poorly-known D_e value that, within errors, is consistent with the main population of D_e values.

5.4.1 Rejection of data

Aliquots were not included in the analysis of the D_e distribution of a sample if they failed any of the following criteria:

a) Signal levels

If no detectable OSL signal (i.e. no discernable decay curve) was present after a regeneration dose had been applied to an aliquot it was rejected (Fig. 5.17a). This situation will arise if none of the grains on the disc are capable of emitting a detectable OSL signal. In some instances, very low signal levels also caused a disc to be rejected but this was on the basis of one of the following criteria. On average, 5 % of the aliquots were rejected on this basis (Table 5.3).

b) Growth curve

If a simple exponential or exponential and linear function was not able to be fitted to the L_X/T_X points in order to form a growth curve, the disc was rejected. This occurred primarily when low signal levels were present (Fig. 5.17b), or if the OSL signal of the disc was not characterised by a dominant fast component (Fig. 5.17c). This can occur if one bright grain on an aliquot is dominated by the medium or slow components. If this occurs, these components can build up over the duration of the SAR cycle and create problems in the calculation of D_e. Although the grains are likely to be derived from the same geological source, it is possible that the components may vary on a grain-to-grain basis, although the reason for this remains unknown (Bulur *et al.*, 2002). 3 % of the aliquots that were measured were unable to have a growth curve fitted through the regenerated dose points (Table 5.3).

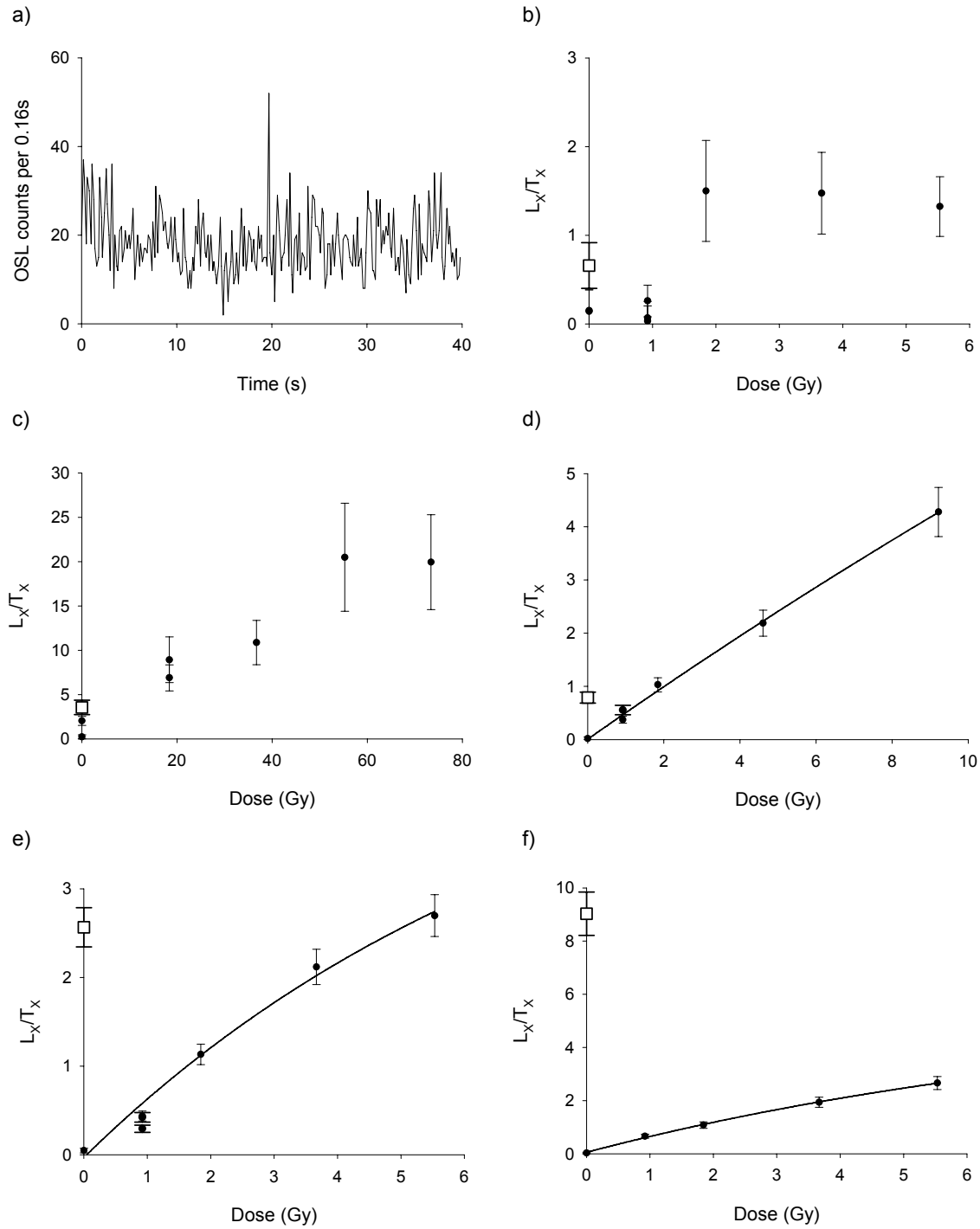

Figure 5.17: Graphs showing OSL signals and growth curves from aliquots which failed the rejection criteria listed in Section 5.4.1. The open square represents the L_N/T_N value, and the solid diamonds represent L_X/T_X points. a) an aliquot with no OSL decay after an ~2 Gy regenerative dose. Full SAR analysis of the aliquot resulted in the growth curve plotted in b); c) growth curve from an aliquot dominated by the medium component; d) the recycling ratio for this aliquot was 0.67 ± 0.22 indicating that sensitivity change is not corrected for appropriately; e) the IR-OSL ratio of this aliquot was 0.72 ± 0.15; f) the high L_N/T_N ratio did not intercept the growth curve.

Table 5.3: Details of aliquots rejected for dating analysis using the criteria detailed in the above section.

Sample	Total number of aliquots analysed	Low signal levels	Absence of growth curve	Poor recycling ratio	IR-OSL depletion ratio	No intercept with growth curve
70KLA1	166	14	4	9	17	0
70KLA2	175	17	7	8	16	0
70KLA3	133	0	1	9	21	2
70KLA4	169	23	4	13	18	0
70KLA5	102	14	2	9	12	0
70KLA6	161	10	2	6	17	0
75KL0308	116	14	11	29	6	0
75KL0309	96	3	2	5	7	1
75KL0310	96	2	0	3	10	0
75KL0311	96	2	2	9	4	0
75KL0315	96	1	4	5	5	2
75KL0316	96	19	4	13	8	0
75KL0317	68	6	2	2	6	0
75KL0318	71	1	4	4	7	0
75KL0319	72	7	0	8	3	1
75KL0320	72	5	2	7	1	0
75KL0321	72	0	1	5	8	0
75KL0322	72	2	1	3	4	1
75KL0323	72	3	5	3	1	0
75KL0324	72	8	2	5	4	0
75KL0325	72	1	4	6	5	1
75KL0326	96	19	7	11	9	0
75KL0327	72	3	0	13	5	1
75KL0328	96	3	2	7	8	0
75KL0329	96	11	4	13	12	0
75KL0330	96	1	3	9	8	1
75KL0331	96	2	3	5	6	2
75KL0332	96	1	0	6	12	0
75KL0333	96	3	3	12	8	0
75KL0334	96	7	4	21	7	2
75KL0335	96	1	0	10	11	0
75KL0336	95	0	3	5	5	1
75KL0337	96	3	9	2	1	1
75KL0338	96	0	8	3	4	0

75KL0339	96	7	2	11	18	3
75KL0340	96	1	0	8	10	1
75KL0341	96	1	0	4	16	2
75KL0342	96	4	2	14	13	0
91SC0401	96	0	1	4	2	1
91SC0403	96	0	0	2	3	0
91SC0404	104	0	5	7	2	0
91SC0405	96	1	2	4	0	1
91SC0406	96	0	0	5	0	4
91SC0407*	96	5	4	3	6	4
91SC0408	96	0	1	2	2	5
91SC0409	96	0	0	0	0	9
91SC0410	96	4	1	3	1	1
92KL0401	72	9	5	2	6	0
Total rejected (%)		5.1	3.1	7.9	8.2	0.7

*Nine aliquots of this sample were also rejected owing to unsuccessful irradiation of the test dose following measurement of the natural signal

c) Recycling ratio

If the ratio between L_X/T_X of the initial regeneration point and the final recycling dose was <0.6 or >1.4, or if it was not consistent with 0.9-1.1 within errors, then the disc was rejected (Fig. 5.17d). Failure of this test suggests that the sensitivity correction applied to the regeneration signals is not working adequately. For 8 % of the aliquots (Table 5.3), the test dose did not correct for sensitivity change appropriately.

d) IR-OSL depletion ratio

As discussed in section 5.3.4, an IR stimulation can check for the presence of feldspar contamination on an aliquot. If the IR-OSL depletion ratio was <0.6 or >1.4 or not consistent with 0.9-1.1 within errors, then the disc was rejected (Fig. 5.17e). 8 % of the aliquots showed evidence of a feldspar contribution to the OSL signal (Table 5.3). The level of contamination appears to vary on a sample-to-sample level, possibly because of small variations in the completeness of the HF etch during the sample preparation steps.

e) No intercept

Less than <1 % of aliquots measured (Table 5.3) demonstrated an OSL signal where the L_N/T_N value did not intercept with the growth curve (for an example, see Fig. 5.17f). Yoshida *et al.* (2000) have ascribed this phenomenon to what they term 'Class 3' grains.

Aliquots where L_N/T_N did not intercept the growth curve did not occur during the dose recovery and preheat tests, when a medium aliquot size was used. It is possible that, because of the rarity of 'Class 3' grains, their signal on medium aliquots is hidden by the 'normal' characteristics of the majority of the grains, or that their rare occurrence in the D_e datasets (Table 5.3) indicates that they contain very large doses.

5.4.2 Calculation of uncertainty on individual D_e values

The errors associated with the D_e values of aliquots can be important in analysis of the dose distribution of the sample. In particular, the error can help distinguish between a point that appears to be an outlier from the main population; if the error is large, the data point may actually be consistent with the population, but if the value is precisely known the D_e can be treated as a true outlier. When a dataset is shown graphically using a radial plot, correct assessment of the errors is critical in allowing one to visually define discrete populations of D_e values.

The errors associated with D_e values are derived from various sources, principally counting statistics, curve fitting, and instrument reproducibility. The way in which the error is calculated from the first two sources is outlined in Appendix D. Jacobs *et al.* (2006) stressed the importance of correctly assessing the uncertainty associated with the instrument reproducibility; if this is underestimated, the overdispersion of the dataset will be too great, and if it is overestimated, patterns of spread in the data may be hidden.

5.4.2.1 Instrument reproducibility error

The instrumental uncertainty is based on the reproducibility of various parameters, including the optical power, the aliquot position relative to the

irradiator, and the heating of the aliquot. As it is based on the instrument used for OSL analysis, as opposed to any characteristics of the grains characterised, the proportional value of this error is the same for every aliquot measured. It is essential to assess this error correctly to ensure that the precision of the D_e values is appropriate.

A value of instrument reproducibility was defined experimentally based on OSL measurements on quartz from the Klip River. Ten aliquots were analysed on Risø 3. Five small aliquots of two samples (70KLA4 and 75KL0308) were subjected to twenty-three cycles of regeneration and test doses of ~48 Gy and ~24 Gy respectively, allowing L_X/T_X to be found for each cycle (Fig. 5.18). The error from counting statistics was calculated for each L_X and T_X measured using equation D.1 (Appendix D); these values were combined in quadrature for each L_X/T_X value, and an average error from counting statistics was found for each aliquot (Table 5.4). The average L_X/T_X was found for each aliquot, and the relative standard deviation of this value was calculated. The error value associated with instrument reproducibility was found by subtracting the error from counting statistics from the relative standard deviation in quadrature; this

Table 5.4: Details of aliquots used for obtaining the error associated with instrument reproducibility.

Sample	Aliquot	Average L_X/T_X	Standard deviation on L_X/T_X	Error from counting statistics	Instrument reproducibility (%)
70KLA4	1	2.156	0.072	0.016	3.2
	2	1.998	0.048	0.021	2.1
	3	2.259	0.098	0.011	4.3
	4	1.843	0.041	0.016	2.1
	5	1.924	0.042	0.022	1.9
75KL0308	1	1.703	0.047	0.022	2.4
	2	1.889	0.053	0.015	2.7
	3	1.988	0.051	0.022	2.3
	4	1.667	0.134	0.029	7.9
	5	1.840	0.085	0.040	3.9

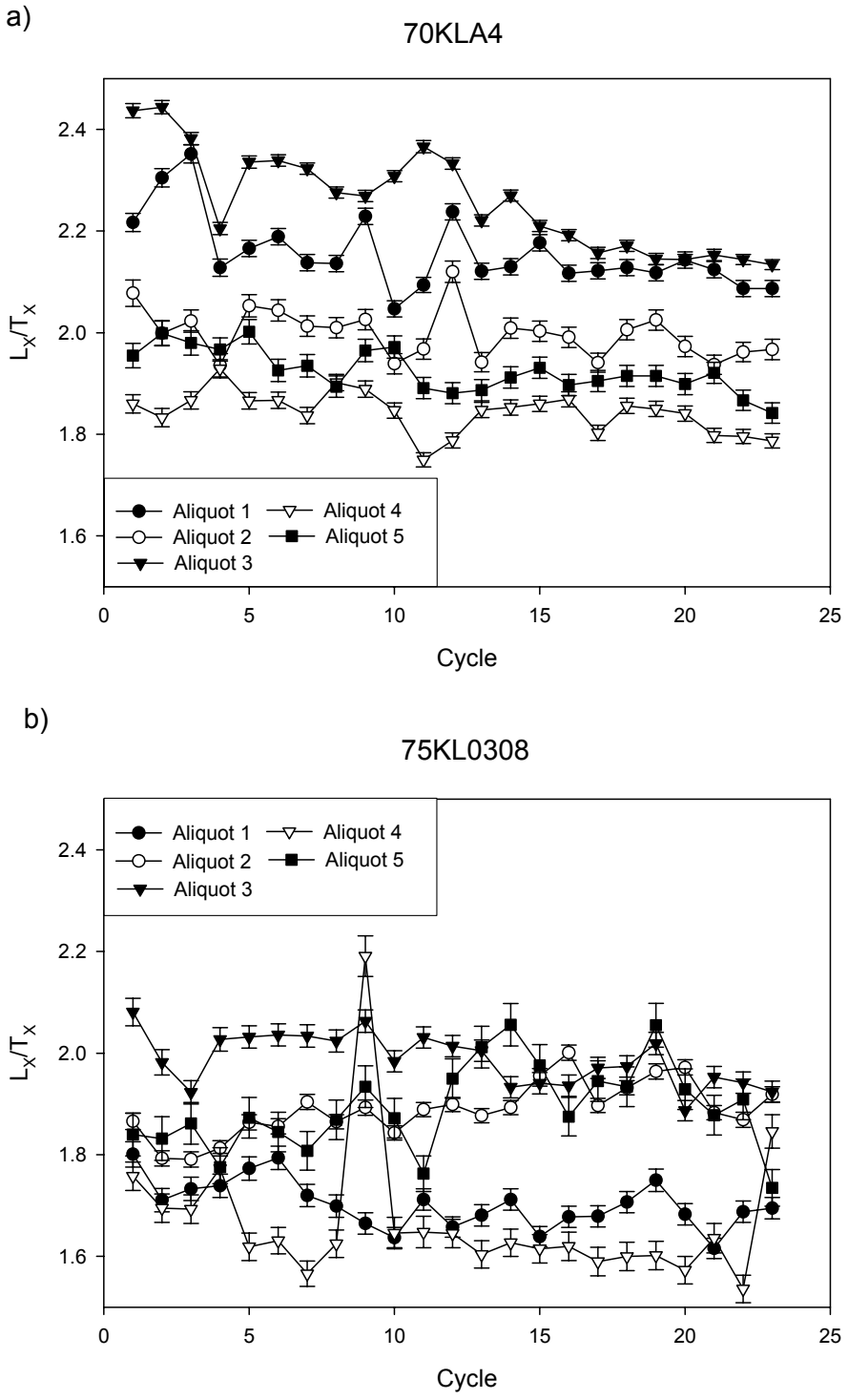

Figure 5.18: L_X/T_X values for the aliquots used for calculation of the error associated with instrument reproducibility for sample a) 70KLA4 and b) 75KL0308.

was then converted to a percentage error by dividing by the average L_X/T_X and multiplying by 100. As can be seen in Table 5.4, the values for the instrument reproducibility varied between 1.9 % and 7.9 %, but only two aliquots had values above 4 %. Aliquot 3 of sample 70KLA4 demonstrates a decreasing trend in the values for L_X/T_X (Fig. 5.18a), suggesting that sensitivity change is occurring above that corrected for by the test dose measurement; for this reason, this aliquot is not included in the analysis for instrumental reproducibility. The high standard deviation on aliquot 4 of sample 75KL0308 is caused by an anomalously high value for L_X/T_X at the ninth cycle. This aliquot was also rejected for calculation of the instrument reproducibility. Based on the remaining eight aliquots, an average value of 2.5 % (to the nearest 0.5 %) for the instrument reproducibility was calculated.

5.4.3 Calibration of beta sources

The D_e of each aliquot can be converted from a value in seconds to Grays by using a simple calculation involving the dose-rate of the relevant Risø reader. The calibration and calculation of the dose-rate for each reader is detailed in Appendix E.

5.5 GRAPHICAL DISPLAY METHODS

Graphical display of the different D_e values obtained for the suite of aliquots analysed for each sample is important in enabling the correct interpretation to be made, both in terms of the form of the dose distribution and in deriving a D_e value appropriate for age calculation. The most common types of graphical displays are variations of scatter plots, histograms, and radial plots. The variability in brightness of the luminescence signal from small aliquots of quartz leads to large variation in the errors associated with each D_e value, and so a display which indicates the errors on each point is preferable.

Plotting data in an appropriate graphical manner allows one to determine any coherent patterns in the data set, i.e. if the distribution is of a particular form. In some instances, the form of the distribution has been used to identify heterogeneous bleaching (Murray *et al.*, 1995) and sedimentary processes such

as pedoturbation (Bateman *et al.*, 2003), thereby enabling the appropriate D_e value to be derived.

5.5.1 Histograms

Histograms are a simple way of looking at the shape of a dose distribution for a sample. The D_e values are grouped into pre-determined ranges (bins) and the number of D_e values in each bin (frequency) is plotted as a function of D_e. The bin width for a sample can be arbitrarily selected; but Lepper *et al.* (2000) suggest using the median error value associated with the data set. This objective criterion was chosen so that the bin width correlates to the typical precision with which the D_e values are known. Although this objective approach has been used by a number of authors (e.g. Lepper and McKeever, 2002; Rowland *et al.*, 2005; Thomas *et al.*, 2005), others have presented histograms where the data is arbitrarily binned (e.g. Banerjee *et al.*, 2002; Rittenour *et al.*, 2003; Argyilan *et al.*, 2005).

Although plotting data in a histogram enables one to look at the shape of the dose distribution, no indication is given of the errors associated with the individual values, so it is impossible to differentiate between those D_e values that are well known and those that are poorly known (Galbraith *et al.*, 1999; Duller and Murray, 2000). Consequently, it is not possible to determine whether a point that appears as an outlier is in fact a true outlier, or instead is a D_e value that is very poorly known and, within errors, falls inside the main population. Despite this, histograms are valuable in providing a simple visual aid for interpreting the dose distribution of a sample and determining the appropriate method for derivation of the D_e value. Figure 5.19 shows a histogram of a sample with a dose distribution indicative of heterogeneous bleaching; the spread in the D_e values is obvious, but one is unable to tell the accuracy with which the high outliers are known.

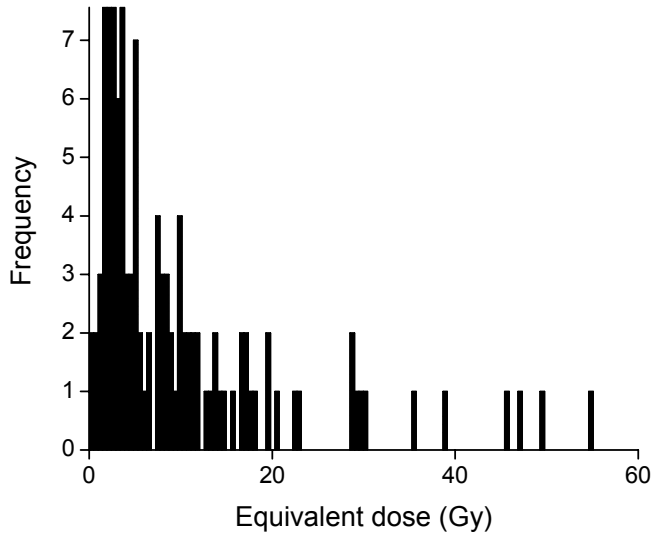

Figure 5.19: Histogram of sample 70KLA2. The bin width is the median error (0.49 Gy), and the total number of D_e values is 144.

5.5.2 Probability density plots

Probability density (PD) plots are a relatively common way of displaying the results from individual aliquots measured for OSL dating that takes into account the error on each D_e value (e.g. Bateman *et al.*, 2003; Jacobs *et al.*, 2003a,b; Rittenour *et al.*, 2003). Every data point is represented by a Gaussian curve (of equal area) with the peak height determined by the uncertainty on the D_e; the better known the value, the higher and narrower the peak (Fig. 5.20a). The individual Gaussians are then summed to create a plot of the relative probability of an equivalent dose for the population. Also shown are the individual D_e values obtained for each aliquot, ranked from lowest to highest. The dataset used for the histogram in Figure 5.19 is shown as a PD plot in Figure 5.20b. Plotting data in this manner for samples which are not normally distributed can lead to probability density functions consisting of a number of peaks, but these peaks do not necessarily correspond to discrete populations of grains within a sample. PD plots take into account the error on each aliquot, and, if the data points are plotted onto the graph, one can visually assess these errors.

Nevertheless, Galbraith (1998) published a critique of this type of plot stating a number of fundamental problems with PD plots, namely:

1) a PD plot dilutes the preciseness of data, concealing well-known points by weighting them with poorly-known points inappropriately.

2) the modes in PD plots do not necessarily represent discrete age components of a sample.

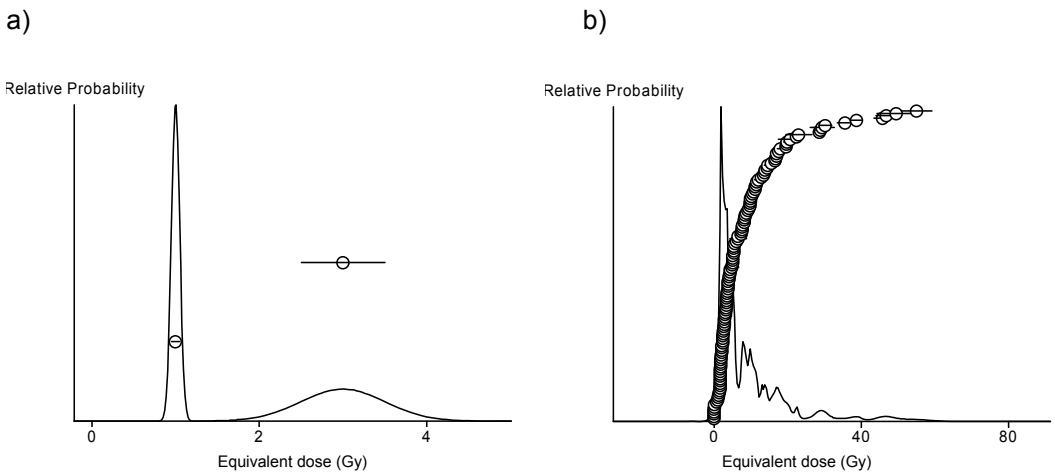

Figure 5.20: Probability density plots of a) two data points of 1.00±0.05 Gy and 3.00±0.50 Gy; and b) sample 70KLA2.

5.5.3 Radial plots

Galbraith *et al.* (1999) suggested the radial plot as a method of display for single grain D_e estimates. This type of plot was initially developed for use in fission track dating by Galbraith (1990), where individual data values have highly variable errors associated with them. A radial plot allows one to see both the D_e estimate of a value, and the error associated with it. The same data set plotted as a histogram in Figure 5.19 and a PD plot in Figure 5.20 is shown as a radial plot in Figure 5.21. In a radial plot, the D_e value of each point can be read off the right hand logarithmic scale by extending a straight line from the origin of

the left hand y-axis through the data point in question. The percentage relative error associated with this point can be found by dropping a line vertically to the top scale on the x-axis; the precision (reciprocal of the relative error) can be read off the bottom x-axis scale. D_e values with relatively small errors, and thus a high precision, fall to the right side of the diagram, whereas the less well known D_e estimates plot towards the left side. Accordingly, an appropriate error calculation for each D_e value is essential for plotting data values accurately in a radial plot, and enabling one to see the correct distribution of values. If a sample is not formed of a single population, less than 95 % of the data points will fall within the 2σ band. This situation can be seen in the radial plot shown in Figure 5.20. This sample demonstrates properties associated with heterogeneous bleaching; the values plotting above and to the right of the main data set are indicative of high outliers from aliquots with well-known D_e values, and these can be attributed to partially bleached grains.

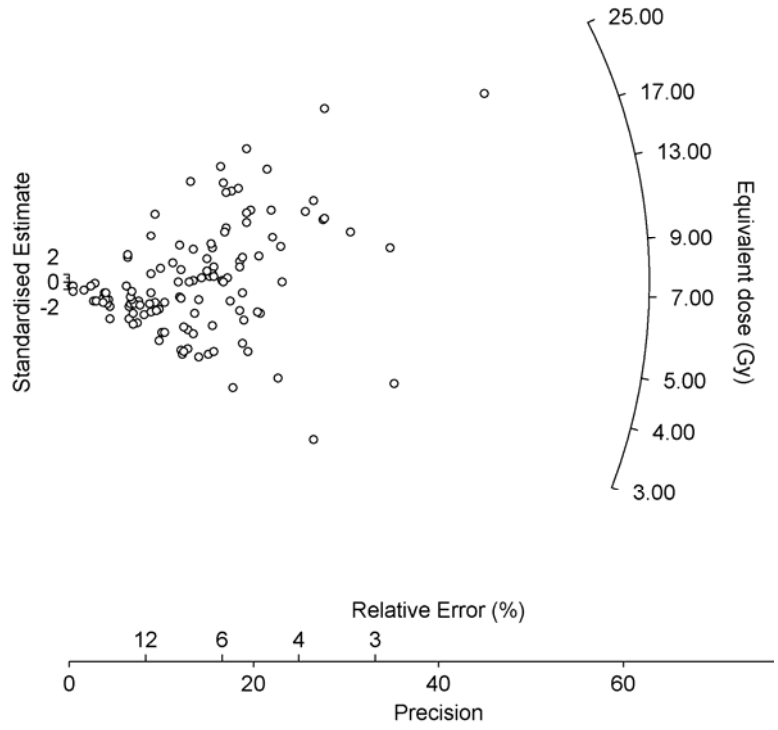

Figure 5.21: Radial plot of sample 70KLA2.

5.6 CONCLUSIONS

In this chapter, initial tests of the standard SAR protocol showed that it was appropriate for dating samples from the Klip River and the Schoonspruit. Selecting an appropriate preheat temperature using plots of the natural D_e as a function of preheat temperature, however, was complicated by scatter in the results, thought to be from heterogeneous bleaching of the quartz. Instead, a combined dose recovery and preheat test was undertaken on each sample. The preheat plateaux identified from these experiments, and assessment of the sensitivity change occurring over the SAR procedure at different preheat temperatures, allowed the appropriate preheat temperature for standard dating analysis of each sample to be selected. In general, this was 220°C, though in a few cases values of 200°C and 240°C were used. Although use of a dose recovery test to select the preheat temperature is not ideal, it is nevertheless the most appropriate method to use for samples where large scatter in the natural D_e values is present and heterogeneous bleaching is suspected.

The majority of the samples demonstrated a clear preheat plateau when a cut-heat of 160°C was used prior to measurement of the test dose. The exceptions were samples 75KL0336 and 75KL0337, which gave unusual forms in the dose recovery and preheat tests and thus necessitated further investigation. Increasing the cut-heat temperature overcame this problem by producing preheat plateaux, thus demonstrating that the standard SAR procedure is suitable for dating these samples, albeit with a higher cut-heat temperature than normal.

For each sample at least 68 aliquots were measured using the standard SAR procedure; a number of these were excluded from subsequent analysis of the D_e values on pre-defined rejection criteria. Sample data sets can be graphically displayed in various ways in order to look at the distribution; whilst both histograms and radial plots allow one to see the shape of the distribution, the radial plot has an advantage in that the errors associated with each value are also clearly represented. The statistical analysis of these D_e distributions is discussed in Chapter 6.

CHAPTER 6: DETECTION AND ANALYSIS OF INCOMPLETELY BLEACHED SEDIMENTS

6.1 INTRODUCTION

Understanding the dose distribution from a sample is essential for obtaining the appropriate burial dose (D_b). To allow one to assess the shape of a sample's dose distribution, a sufficient number of D_e values must be obtained. If a sediment consists of grains that were well bleached prior to deposition, and that were exposed to the same environmental dose-rate during burial, the resulting dose distribution would be Gaussian and the individual D_e values would be consistent with each other within errors. In some cases, however, grains are not exposed to sunlight of sufficient intensity and/or duration during sediment transport to remove fully the luminescence signal from the previous burial period, and hence residual trapped charge remains in the grains. When this occurs, the sediment is said to have been 'partially bleached'. Duller (1994) differentiated between two types of partially bleached sediments: 'type A' where all the grains are partially bleached to the same extent (i.e. homogeneously bleached); and 'type B' where different grains have been exposed to sunlight of differing intensity and/or duration causing varying amounts of residual trapped charge to remain in the grains (i.e. heterogeneously bleached). Analysis of sand-sized quartz grains from fluvial sediments has shown that they may be heterogeneously bleached (e.g. Murray *et al.*, 1995; Olley *et al.*, 1998; Lepper *et al.*, 2000), but no work has found evidence for homogeneous partial bleaching.

Two main approaches have been developed in order to allow one to detect heterogeneous bleaching in samples. First, signal analysis methods are based on the principle that different components of the OSL signal bleach at different rates. This allows one to calculate D_e values from an aliquot based either on parts of the decay curve dominated by the different components (fast, medium, slow), or solely on the individual components. Second, dose distribution methods analyse the spread in the distribution of D_e values from aliquots of the same sample, and the shape of this distribution. If the sample was heterogeneously bleached, one would expect the spread of D_e values in the dataset to be greater than expected;

this can be parameterised by statistical values. Furthermore, the histogram of a heterogeneously bleached sediment would be expected to show a skewed distribution with a high number of low values, and a tail up to high values, the latter owing to aliquots containing grains with residual doses.

In this chapter, two broad issues are discussed: 1) techniques developed to detect heterogeneous bleaching in a sediment sample (Sections 6.2 and 6.3); and 2) methods to then derive an appropriate D_b value from this type of distribution (Section 6.4). The D_e distributions obtained from the Klip River samples will be used to assess the reproducibility of OSL dating of fluvial samples, and the ages obtained using different methods of statistical analysis will be discussed to find which is the most appropriate method (Section 6.5).

6.1.1 Bleaching of luminescence signals underwater

Under normal daylight conditions, the OSL signal in a quartz grain is reduced to 1% of its initial level after 10 s of exposure to light (Godfrey-Smith *et al.*, 1988), but when a sediment is transported underwater, the bleaching rate will be greatly reduced. This reduction in bleaching rate occurs because of the decrease in the intensity of the light that the grains are exposed to, as controlled by both the depth and turbidity of the water column. Rendell *et al.* (1994) investigated the bleaching of the TL, OSL and IRSL signals from quartz and feldspars following three hours exposure to natural light at different depths within the water column. The results (Fig. 6.1) show that the OSL signal from quartz is more readily bleached underwater than the IRSL signal from feldspar. Contrary to this, Wallinga (2002) combined data on the light spectrum at depth in turbid water (Berger and Luternauer, 1987) with the bleaching efficiency of quartz and feldspar (Spooner, 1994a,b) to suggest that feldspar is likely to be bleached more readily at depth, whereas quartz is bleached more rapidly at the surface (Fig. 6.2). Regardless of the relative bleaching efficiency of feldspar, quartz is used in this study instead because of continuing uncertainty in the use of feldspar resulting from problems such as anomalous fading, and changes in the charge trapping probability from heating during measurement (Wallinga *et al.*, 2001).

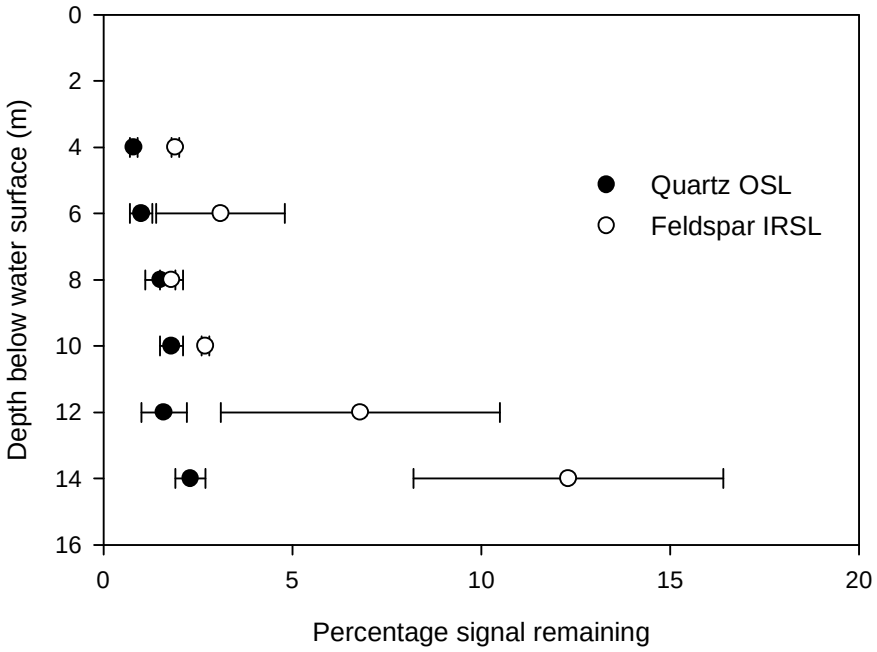

Figure 6.1: Percentage of initial signal remaining in quartz and feldspar grains after exposure to light for three hours at various depths within a water column. Data from Rendell *et al*. (1994).

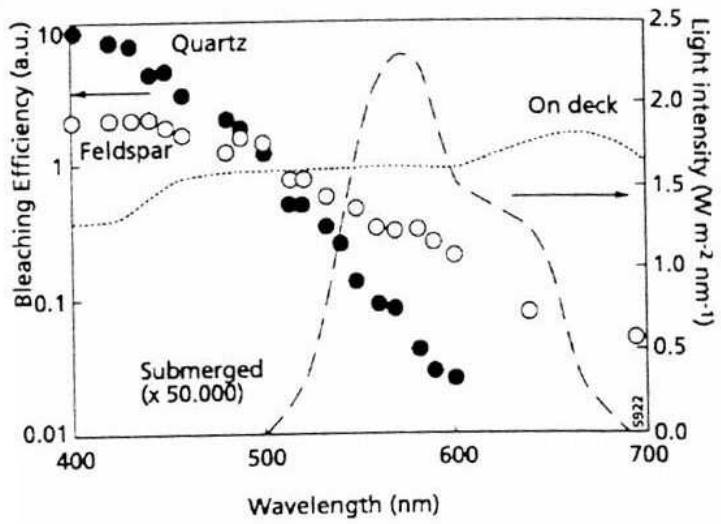

Figure 6.2: The light spectrum at both the water surface (dotted line) and at 4m depth (dashed line) in a turbid river (note that the light spectrum at depth has been multiplied by 50 000). The bleaching efficiency of quartz (filled circles) and feldspar (open circles) at the different wavelengths is also shown. Figure from Wallinga (2002).

6.1.2 Bleaching during fluvial transport

In a review of the bleaching of fluvial sediments, Jain *et al.* (2004) concluded that bleaching is primarily a function of transport distance and transport conditions. Comparisons between OSL ages and independent age estimates for samples from fluvial deposits generally showed no overestimation in the OSL age for samples older than 1000 years, but for samples younger than 1000 years heterogeneous bleaching was identified as a problem leading to age overestimation. When the minimum age model, rather than the mean value, was used to calculate D_b for the young samples, the OSL ages had a closer agreement with the independent age control.

The turbulent nature of flow in most natural rivers means that every grain will follow a different transport path in the water column. The Hjulström curve (Fig. 6.3) defines the flow velocity required for suspended and bedload transport for different grain sizes. For a river of given velocity, finer grains are more likely to be transported as suspended load than coarser grains (Hjulström, 1935), and thus would be expected to have a lower residual signal at deposition because they will have spent a greater proportion of their time near the water surface. However, analysis of quartz from flood deposits (Olley *et al.*, 1998) and point bars (Wallinga, 2002) found that the coarser grains provided values closer to those which were expected (Table 6.1; Fig.

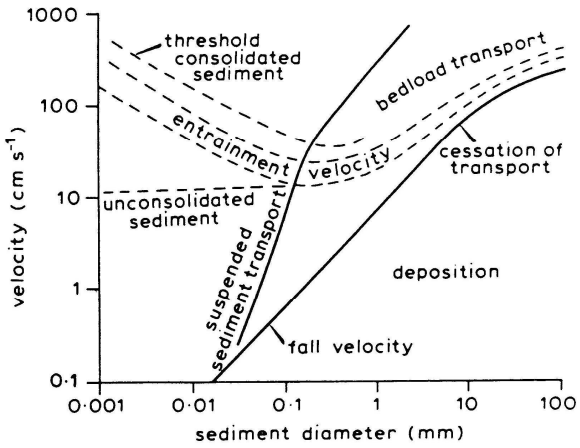

Figure 6.3: The Hjulström curve showing the expected form of sediment transport for grains of different transport size at varying flow velocity. From Richards (1982).

6.4). These ages still overestimated the expected age, indicating that a residual dose remained in all the grains, but the level of this residual dose was lower for the larger grain sizes. In these studies, the D_b value for the samples was based on the mean (and standard error) of the D_e values dataset. For each grain size, Olley *et al.* (1998) obtained 24 D_e values, and Wallinga (2002) obtained 16. Although the D_b values for all the grains sizes resulted in age overestimations, the coarser grains were better bleached. In this thesis, grains with diameters greater than 180 µm were used for analysis.

Table 6.1: D_b values and resulting ages from OSL analysis of different grain size fractions for two samples. The D_b value is calculated as the mean of the D_e dataset.

Grain size (µm)	Olley *et al.* (1998)* expected age = 0.07 ka		Wallinga (2002) expected age = 0.30 ± 0.02 ka	
	D_b (Gy)	Age (ka)	D_b (Gy)	Age (ka)
90-125	2.7 ± 0.4	0.73 ± 0.11	8.8 ± 3.9	6.84 ± 0.30
125-180	2.6 ± 0.4	0.69 ± 0.12		
180-212	1.5 ± 0.3	0.40 ± 0.07	1.9 ± 0.3	1.49 ± 0.27
425-500			0.9 ± 0.3	0.71 ± 0.28

* In this paper additional D_b values were obtained from analysis on more grain size fractions. Although the numerical values were not given, these data are shown graphically in Figure 6.4.

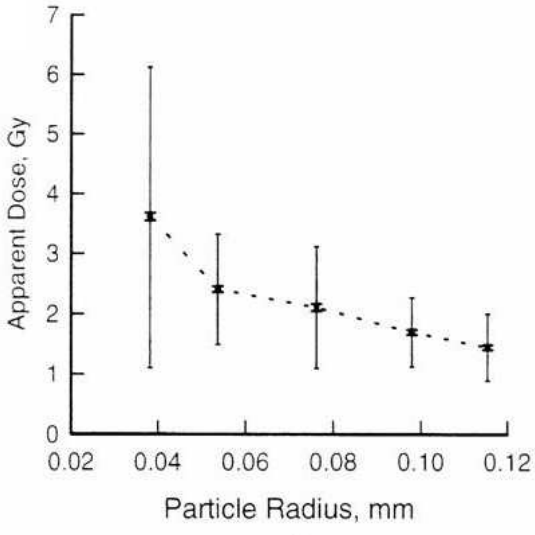

Figure 6.4: The mean apparent dose values (D_b), standard errors (just larger than the symbol representing the mean) and standard deviations of the D_e values found for different grain sizes, plotted against the median particle radius. From Olley *et al.* (1998).

Ditlefsen (1992) investigated the effect of turbidity on the bleaching of potassium feldspars, by measuring the IRSL signal after 20 hours of bleaching at 0.75 m depth in suspensions of sediment concentrations between 0.01 and 0.10 g/l. Only 5 % of the IRSL signal remained after bleaching in 0.01 and 0.02 g/l suspensions, however in the more concentrated suspensions little reduction was found in the IRSL at the end of the experiment. During high summer flows, the turbidity of the Klip River is greater than any of the experimental suspensions (1.5 g/l maximum; Tooth *et al.*, 2002) suggesting either that transport over many hours is necessary for complete bleaching within this river system, or that bleaching does not occur primarily during transport but rather during periods of temporary storage and remobilisation prior to final deposition.

Transport distance is another important factor determining the amount of bleaching. Stokes *et al.* (2001) investigated the residual signal in samples taken from the bedload of the Loire at different distances downstream of the river source. Although they found that the mean and median D_e values never reached zero (Fig. 6.5), the minimum D_e value from an aliquot was less than 1 Gy after 10 km transport.

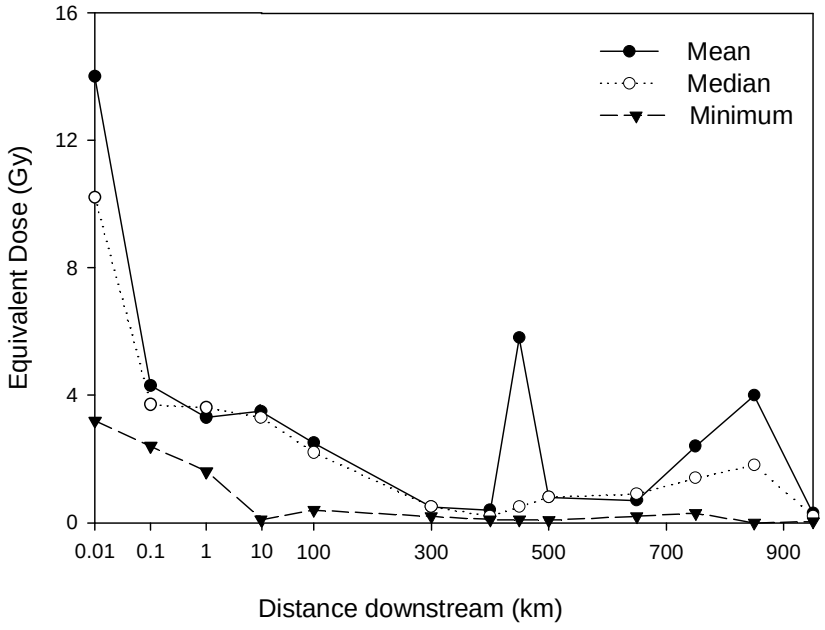

Figure 6.5: Equivalent dose values for bedload sediment samples as a function of distances downstream on the River Loire. Note the change in x-axis scale between 10 and 100 km. Redrawn from Stokes *et al.* (2001).

6.2 DETECTING HETEROGENEOUS BLEACHING: SIGNAL ANALYSIS METHODS

Bailey *et al*. (1997) demonstrated that the OSL decay curve at room temperature can be fitted by the sum of three exponential decay curves, each associated with a discrete component (as discussed in Section 4.4). They showed that the relative proportions of the fast and medium components varied with bleaching time (Fig. 6.6), because of the greater sensitivity to light of the fast component. Bailey *et al.* (1997) suggested that this differential bleaching of the OSL signal components would allow one to use the separated components to investigate whether a grain was partially bleached at deposition or not.

The relative rates at which the fast and medium components bleach varies with wavelength. As the wavelength increases, the medium component increasingly bleaches at a slower rate than the fast component (Singarayer and Bailey, 2004) (e.g. Bailey *et al.* (2003) calculated that at 500 nm the medium component bleaching rate is ~13 % that of the fast). At depth within water, the reduction in the light spectrum is reduced, with only longer wavelengths (>500 nm) remaining at 4 m depth in a turbid river (see Fig. 6.2). The differences expected in the underwater bleaching rates between the fast and medium components suggests

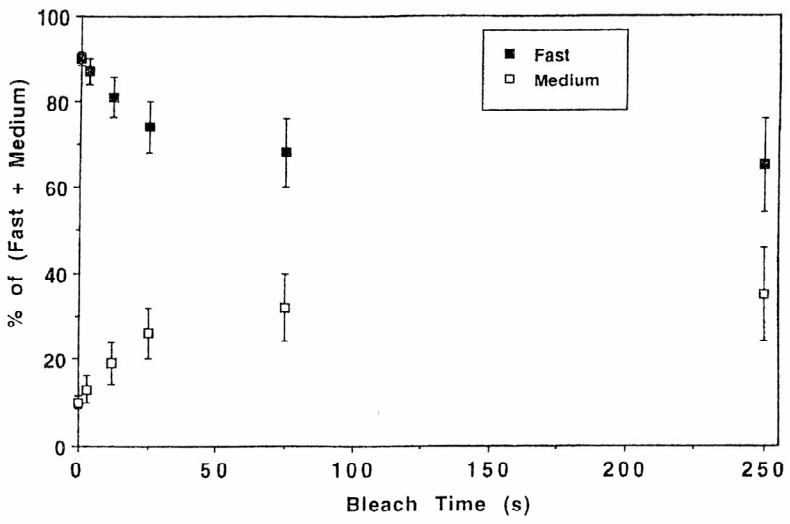

Figure 6.6: Effect of bleaching time on relative proportions of the fast and medium component in the Chaperon Rouge quartz OSL signal. Aliquots were bleached at room temperature using filtered green light. From Bailey *et al.* (1997).

that signal analysis methods should be a good technique for detecting partial bleaching in fluvial deposits.

Bailey *et al.* (1997) proposed a multiple-aliquot technique to detect homogeneous partial bleaching in sediments by exploiting the difference in the bleachability of the fast and medium components. They suggested constructing a regenerated growth curve in the normal manner and deriving the D_b from this. A separate aliquot of the sample is then fully bleached in the laboratory, prior to being dosed to the level of the D_b, and the OSL signal from this is recorded. The ratio of the fast to medium components in the natural and artificially dosed aliquots can then be compared; if there is a higher proportion of the medium component in the natural aliquot, the sediment is partially bleached.

Singarayer *et al.* (2005) used two procedures for using signal analysis methods to assess partial bleaching in single aliquots. The first method involved looking at variation in the D_e with stimulation time, as the OSL signal is increasingly dominated by harder-to-bleach components (termed a $D_e(t)$ plot). The second method mathematically resolved the different components of both LM-OSL and CW-OSL measurements, and calculated D_e values for each component. Aliquots from four modern fluvial samples, a fluvial sample with independent age control, and a coastal dune sample with independent age control, were measured to obtain D_b (based on the mean of at least eight D_e values) and were analysed using both methods. Five samples showed overestimation in D_b; aliquots of these samples showed rising $D_e(t)$ plots, and the D_e values obtained from the medium components were greater than those from the fast component. Thus, where overestimation in the age was found, the signal analysis methods indicated partial bleaching of the grains on the aliquot. The sample from the coastal dune showed no age overestimation and measurements on this sample gave flat $D_e(t)$ plots and consistent D_e values from the fast and medium components. From these results, Singarayer *et al.* (2005) concluded that $D_e(t)$ plots and LM-OSL curve deconvolution are equally suitable for detecting partial bleaching. The latter technique, however, has several drawbacks. First, complex fitting routines are necessary to extract the discrete components from the LM-OSL curve. Second, more time is involved in measurement of the LM-OSL signal, i.e. at least 200 s, as opposed to the 100 s needed for CW-OSL. Third, if a sample is heterogeneously

bleached, ideally small aliquots need to be used for analysis to reduce grain-to-grain averaging, but LM-OSL analysis on small aliquots containing only a few grains is difficult as the low signal levels do not lend themselves to viable curve deconvolution. Owing to these disadvantages, particularly the problems with the low signal levels from small aliquots, $D_e(t)$ plots are used in this thesis to detect partial bleaching instead of LM-OSL curve deconvolution.

6.2.1. Calculating D_e as a function of stimulation time

Calculating D_e as a function of stimulation time was first suggested by Huntley *et al.* (1985). They developed a 'shine plateau' test for use with the multiple-aliquot additive-dose technique. If D_e was found to increase with stimulation time, this was thought to be indicative of partial bleaching. This method was adapted and utilised for single aliquots by Bailey (2003a), with the resulting plot renamed a $D_e(t)$ plot. The OSL signal was now known to consist of a number of different components with varying detrapping probabilities which leads to different decay rates (e.g. Bailey *et al.*, 1997; Bulur *et al.*, 2000; Jain *et al.*, 2003). Thus, analysis of the D_e using different integrals of the decay curve should give D_e values initially dominated by the fast component, then as the stimulation time increases the medium component will become more significant. If the OSL signal of a sediment is not completely reset during transport, the fast component would be reset to a greater degree than the medium, and the medium component would have a greater residual dose, so a plot of the D_e obtained as a function of stimulation time should show a rising trend.

6.2.1.1 Analysis of samples partially bleached in the laboratory

Bailey (2003a) listed three experiments to test whether $D_e(t)$ plots can identify partial bleaching in an aliquot. Each experiment was used to answer a particular question:

1) Is $D_e(t)$ constant if the OSL signal has been fully reset?

2) How does the $D_e(t)$ plot change with increased homogeneous partial bleaching?

3) If an aliquot has been partially bleached and then irradiated, is the partially bleached signal preserved in a $D_e(t)$ plot?

Bailey (2003a) performed Experiments 1, 2 and 3 and demonstrated that a flat $D_e(t)$ plot could be obtained from a well-bleached sample (Fig. 6.7a, part i). In the second experiment, it was demonstrated that homogeneous partial bleaching of the aliquots leads to a rising trend in the $D_e(t)$ plots (Fig. 6.7a, parts ii-iv), with the relative increase in D_e with stimulation time greater for increased partial bleach times. In Experiment 3, the $D_e(t)$ plots for the 'natural' signal were obtained following dosing, partial bleaching, and a second dosing. Additionally, a 'replacement point' plot is used as a check to ensure that the aliquot would give a flat $D_e(t)$ plot if well-bleached; to obtain this 'replacement plot', one of the regenerated doses from the SAR procedure is treated as the natural. For all the samples investigated, partial bleaching could be detected, even if the aliquots were given a dose following the partial bleach (Fig. 6.7b).

6.2.1.2 Application to a Klip River Sample

The experiments suggested by Bailey (2003a) were undertaken on medium aliquots of sample 70KLA2 using Risø 3. This sample was collected from a palaeochannel deposit and the grains from this sample appear to be partially bleached to differing extents (Section 5.3.1; Fig. 5.8). For the OSL measurements, following the suggestion by Bailey (2003a), the blue LEDs were set at 50 % of full power, in order to reduce the stimulation power and allow greater resolution of the fast and medium components. The data was collected in 250 bins over 100 s stimulation, with each bin containing data from 0.4 s. The D_e is then obtained using different integrals of the OSL decay curve (Fig. 6.8).

Experiment 1

To ensure that the application of $D_e(t)$ plots to a sample is appropriate, it must be possible to obtain a flat plot from a fully bleached sample. In this experiment, a previously untreated aliquot (aliquot 1) was bleached using blue LEDs for 100 s at 160℃, prior to being given a beta dose of 18.8 Gy. T his dose was then treated as the natural, and the aliquot was analysed using the SAR procedure with four regeneration doses using a preheat of 260℃ and a cut- heat of 160℃, following

a) b)

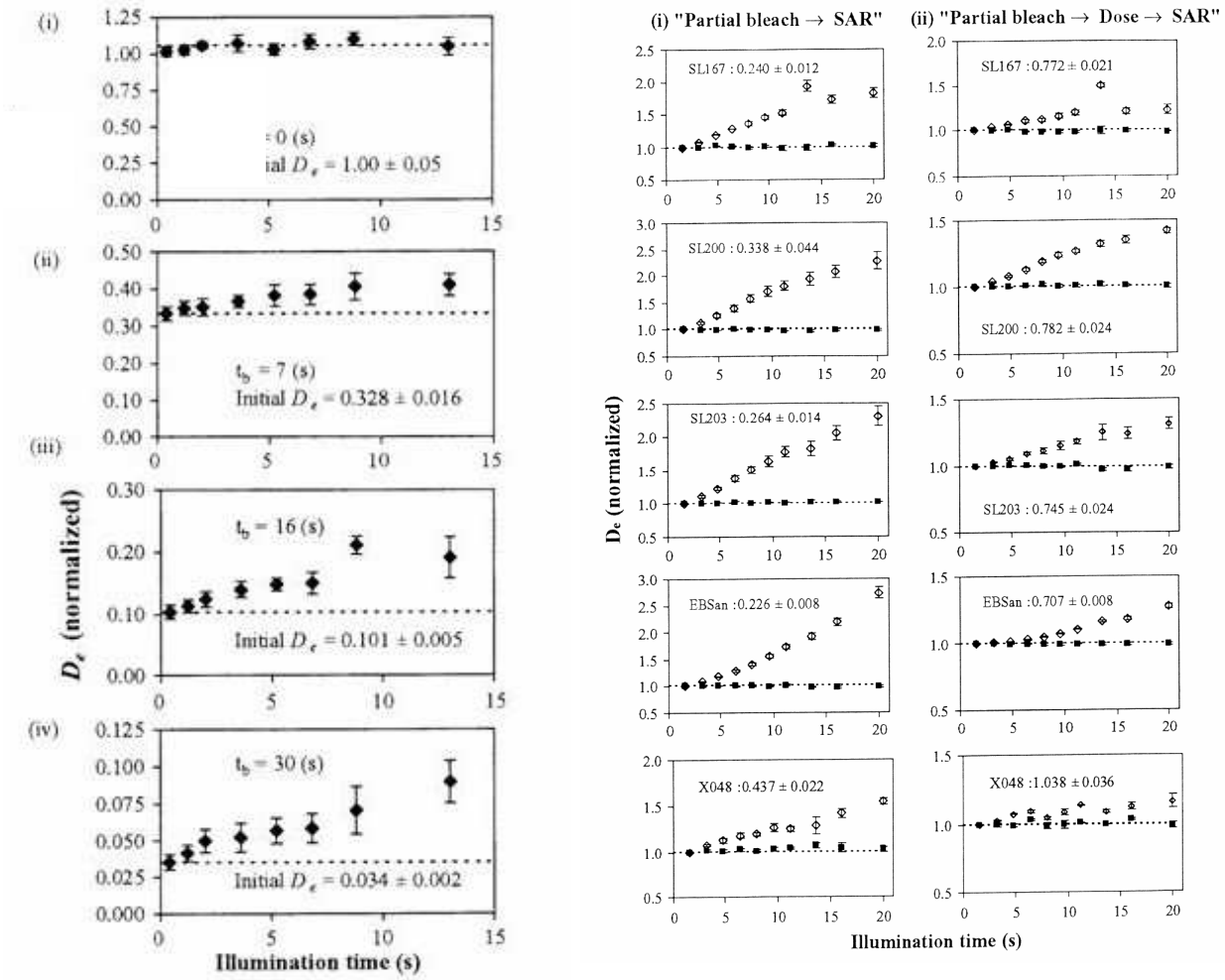

Figure 6.7: a) $D_e(t)$ plots for data obtained from experiments 1 and 2 by Bailey (2003a) for sample SL205 (an aeolian dune from Sri Lanka) over a range of bleaching times (0-30s). Each estimate of D_e is an average of four aliquots and has been normalised to the D_e obtained using the initial integral in part (i) where no partial bleaching occurred. The D_e value obtained using the initial integral is stated; the dashed line indicates the average of the eight estimates in part (i) and the level of the initial D_e in parts (ii) to (iv). b) $D_e(t)$ plots for data obtained from experiments 2 and 3 by Bailey (2003a). Each estimate of D_e is an average of four aliquots and has been normalised to the D_e obtained using the initial integral. The filled squares represent the values obtained using the replacement plot techniques, and the open diamonds represent the values from the 'natural' signal. The values are the relative signal magnitudes immediately following dosing, obtained from a 0.1 s OSL stimulations. (i) shows the data for experiment 2, (ii) shows the data for experiment 3. Both figures from Bailey (2003a).

test-doses of 1.9 Gy. Successive integrals of the decay curve were used to obtain D_e values. These were normalised to the given D_e (18.8 Gy) and are shown as a function of stimulation time (Fig. 6.9a). All the data points are consistent with the given dose, and the mean D_e is 19.1 ± 0.7 Gy. This experiment shows that a flat $D_e(t)$ plot can be obtained from an aliquot of 70KLA2 that has been fully bleached prior to irradiation.

Experiment 2

This next experiment replicates the case where a modern sample has undergone partial bleaching during the most recent transport event. Four previously untreated aliquots were bleached for 100 s, given a 18.8 Gy beta dose, and then bleached at 20℃ using the blue LEDs at 50 % power f or time t_b. For aliquots 2-5, t_b was 3, 7, 16 and 30 s, respectively. The aliquots were then analysed using the same SAR procedure as aliquot 1 and a $D_e(t)$ plot was constructed (Fig. 6.9b-e). These plots demonstrate that where the aliquots have been exposed to a bleach of 7 s or greater, a rising trend is evident, indicating partial bleaching.

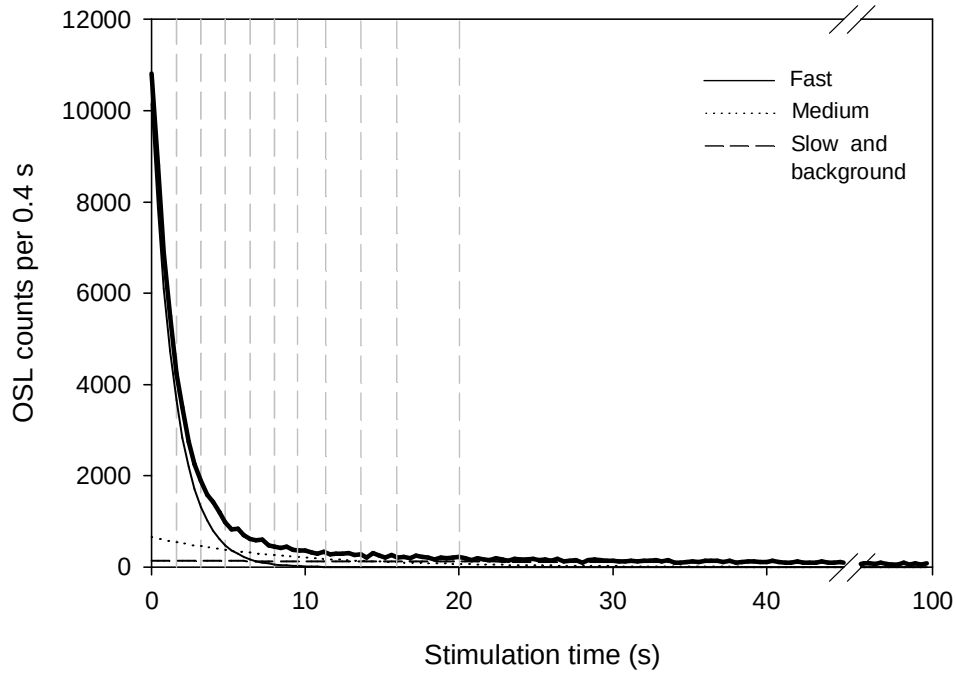

Figure 6.8: The thick black line shows the decay curve from an aliquot of 70KLA2 following an ~20 Gy dose. The integrals used in analysis of $D_e(t)$ plots are shown by dashed grey lines, and the deconvolved components forming the decay are also shown (the slow component and background counts have been combined).

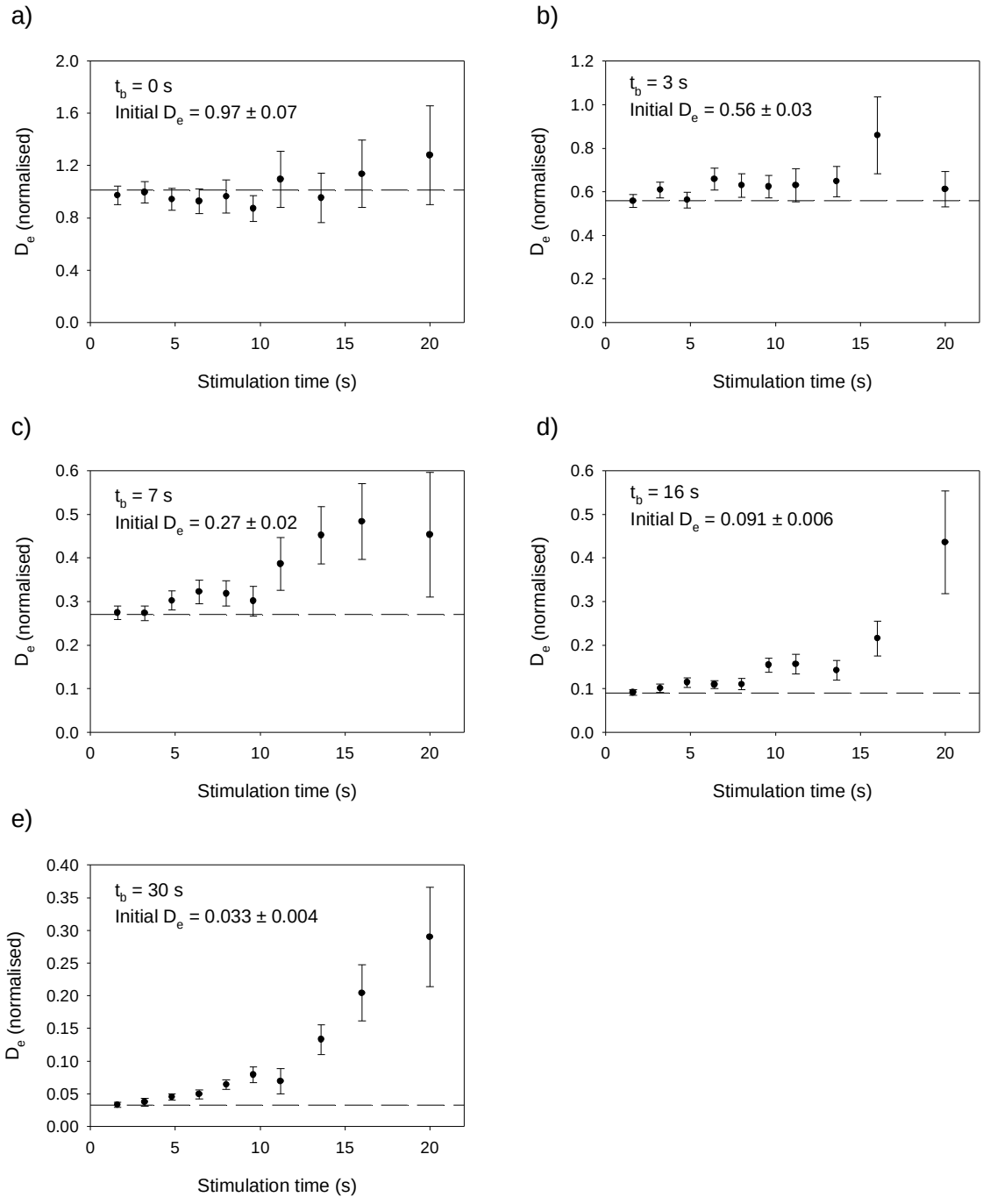

Figure 6.9: $D_e(t)$ plots constructed from a single aliquot following experiments 1 and 2 as described in the text. The bleaching time (t_b) is indicated on each plot and the D_e value calculated using the first integral is shown as a ratio to the known laboratory dose of 18.8 Gy to make these figures comparable with those of Bailey (2003). The dashed lines indicate the average D_e value in a), and the initial integral values in b) to e).

Following a 7 s bleach (where partial bleaching is first evident), the D_e value obtained from the initial integral of the decay curve is only 27 % of the given dose. After a 3 s partial bleach, no evidence of partial bleaching is present in the $D_e(t)$ plot, but the D_e value obtained using the initial integral is only 56 % of the given dose. Hence, despite the fact that after a 3 s partial bleach the D_e value considerably underestimates the true value, the result suggests that the bleach time is not sufficient to differentially bleach the fast and medium components and allow detection of partial bleaching through the use of a $D_e(t)$ plot. This bleaching time (3 s) was used in the experimental work by Bailey (2003a) but the results were not shown (see Fig. 6.7).

Overall, the results from the Klip River sample show that whilst severe partial bleaching (loss of ~75 % of the initial dose) can be detected through the use of $D_e(t)$ plots, the technique is not sensitive enough to detect a relatively short partial bleach, even when the bleaching has removed nearly 50 % of the initial dose.

Experiment 3

The final experiment is designed to replicate what would happen in cases where grains are partially bleached prior to being deposited and subsequently exposed to radiation during burial. Four previously untreated aliquots were bleached for 100 s, given a dose of 18.8 Gy, bleached for 7 s, given a further dose of 9.4 Gy, then analysed using the standard SAR procedure. In order to ensure that each aliquot is suitable for $D_e(t)$ analysis, Bailey (2003a) suggested using 'replacement plot' analysis, as discussed in Section 6.2.1.1. Figure 6.10a shows the D_e values for the four aliquots obtained using different integrals for both the ‘natural' (i.e. partially bleached) signal (filled symbols) and the regeneration dose signal (open symbols) used for the replacement plot. In Figure 6.10b, the mean D_e values are normalised to that obtained from the initial integral, and shown as a function of stimulation time. The rising trend in the 'natural' signal confirms that partial bleaching can be detected, even after a further dose. The replacement plot points scatter randomly about unity, showing that the aliquots are suitable for analysis using the $D_e(t)$ plot method. The mean normalised D_e value is 1.01 for the replacement plot points.

a)

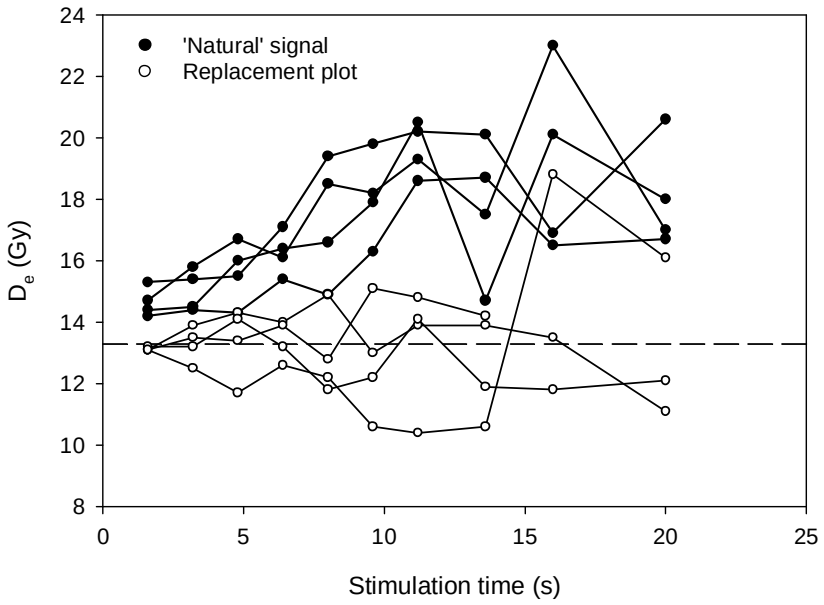

b)

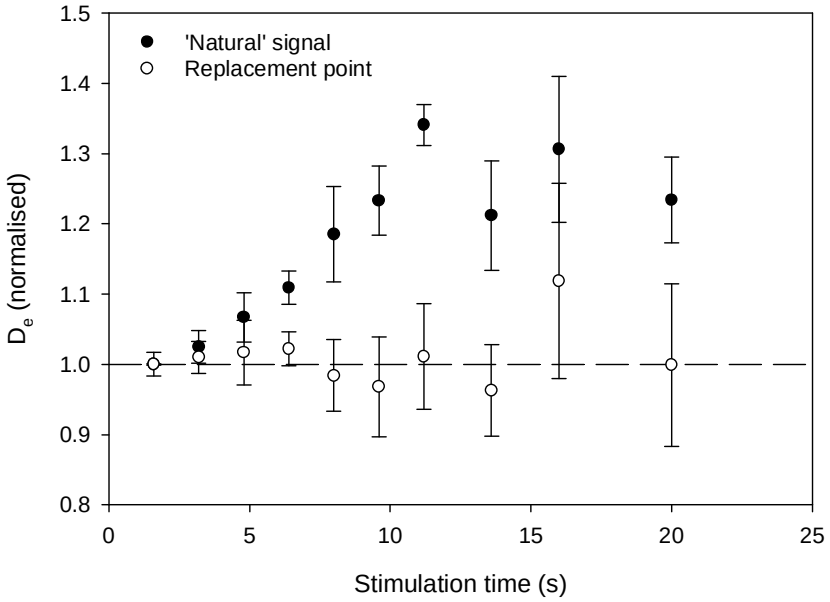

Figure 6.10: Results from Experiment 3. a) The actual D_e values obtained using the different integrals from the four aliquots. The filled circles show the D_e values from the 'natural' signals following an 18.8 Gy, 7 s bleach and 9.4 Gy dose. The open circles show the values obtained for a 13.3 Gy regeneration dose, treated as a 'replacement point'. The dashed line indicates 13.3 Gy. b) The average, normalised D_e values from the different integrals of stimulation time. Each point is the average of four aliquots, and is normalised to the initial integral D_e.

The three experiments detailed above all suggest that $D_e(t)$ plots may be suitable for the detection of partial bleaching of grains, and in each instance, the results confirm what Bailey (2003a) found. However, Figure 6.9b demonstrates that the method may not be very sensitive to partial bleaches of relatively short durations, even when the D_e value is reduced considerably.

6.2.2 "Z" plots

In fluvial environments where heterogeneous bleaching is anticipated, every aliquot may have been partially bleached to a different extent. To investigate the extent of heterogeneous bleaching in a sample, Bailey (2003b) suggested using a parameter called the Z value, defined as the ratio of the D_e obtained from a later integral of the OSL decay curve (dominated by the medium component) to the D_e obtained from the initial integral (dominated by the fast component). If an aliquot is well-bleached, the Z value will be consistent with unity, and if it is partially bleached, Z will be greater than 1. The relationship between D_e and Z, termed a 'Z plot', is shown schematically in Figure 6.11. The open triangle represents a situation where no bleaching occurred during the most recent transport event. Thus, the sediment is not partially bleached (Z=1), and the D_e is the sum of the burial dose from the most recent burial period and the entire pre-burial dose. As

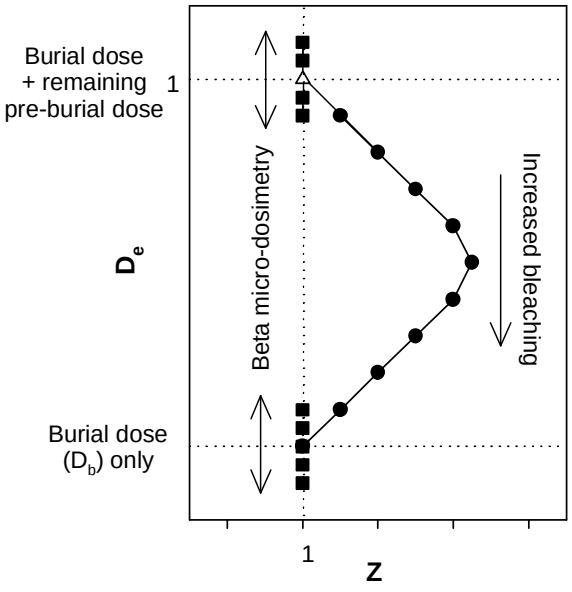

Figure 6.11: Schematic diagram showing how the D_e value and Z value are affected as the amount of partial bleaching increases. The potential effect of beta microdosimetry is also shown. Redrawn from Bailey (2003b).

the amount of bleaching that occurred during the transport event increases, the D_e value will decrease and the Z value will increase (Z>1). As the extent of bleaching continues to increase the effect of the residual signal decreases, leading to a reduction in the Z value (though Z remains above 1), and a continued decrease in D_e. This trend continues until a point where the sediment is completely bleached (Z=1), and no residual signal remains; at this point, the D_e value is the true burial dose (D_b). Figure 6.11 also shows that whilst variation in the beta microdosimetry of a sample may have an effect on the D_e, it will not affect the Z value of an aliquot.

6.2.2.1 Modelled data

Bailey (2003b) modelled the expected form of Z plots taking into account two variables: the extent of partial bleaching (*f*, the fraction of the residual pre-burial dose remaining), and the level of the pre-burial dose prior to partial bleaching (D_G). The Z plots produced from a number of simulated conditions are shown in Figure 6.12a and histograms of the D_e values from the same datasets are shown in Figure 6.12b. Bailey (2003b) shows that in theory, Z plots can successfully be used to identify heterogeneous bleaching of differing severities. When the data are plotted as histograms, heterogeneous bleaching can be detected in some circumstances, but a sediment may appear well-bleached (Fig. 6.12b, part iv) when in fact every grain retains a residual dose.

6.2.2.2 Application to a Klip River sample

A Z plot was constructed for sample 70KLA2 using Z values obtained from measurements made for dating purposes. The decay curves were recorded in 250 bins over 100 s stimulation using blue LEDs at 90 % full power. For derivation of the Z value, the integrals of bins 1-3 (0.0-1.2 s) and 10-12 (4.0-5.2 s) were used. The first integral was chosen to select part of the decay curve where the fast component is dominant, and the latter integral was chosen to reflect part of the decay curve which consists of a greater proportion of the medium component, but where the signal levels are sufficient to obtain a relatively precise value. For the decay curve shown in Figure 6.8, the ratio of the fast to medium component was 93:7 in the initial integral (bins 1-3) and 61:39 in the second integral (bins 10-12).

a)

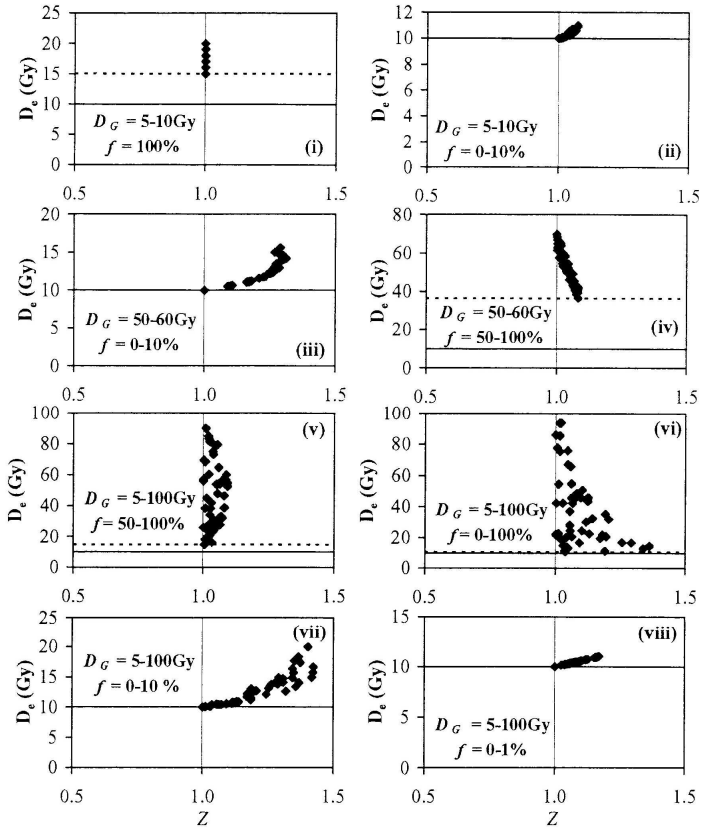

b)

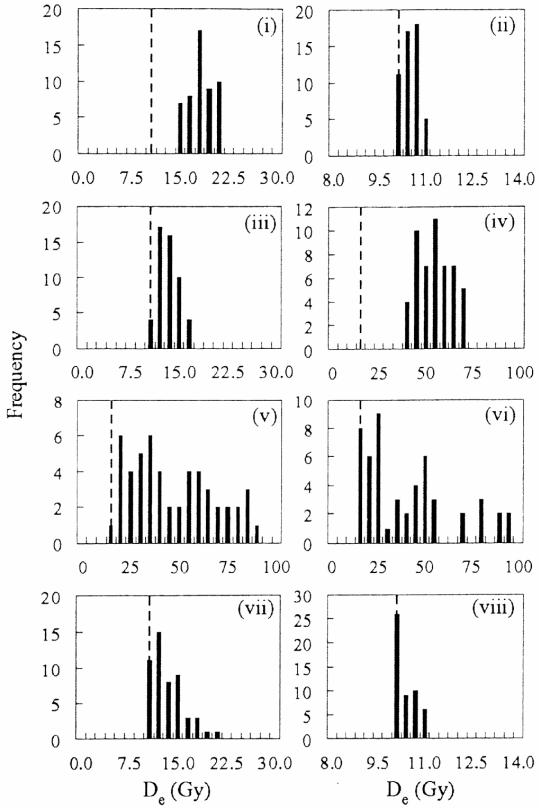

Figure 6.12: a) Plots of results showing the solutions to a model for deriving a Z value; for each graph, 50 solutions were obtained, each represented by a single data point. The dotted horizontal line shows the lowest D_e value obtained in the 50 solutions. The size of the pre-burial dose (D_G) and the fraction of residual pre-burial dose remaining (*f*) are indicated on each plot. In each case, the burial dose was 10 Gy, indicated by the solid horizontal line. b) The same data as shown in part a), plotted as a histogram. The dashed vertical lines represent the true burial dose (10 Gy). From Bailey (2003b).

Figure 6.13a shows the D_e value for every aliquot of 70KLA2 (deemed suitable for dating following application of the rejection criteria outlined in Section 5.5.1) plotted as a function of Z value. The right-hand side of the plot, where Z>1, shows the form expected when partial bleaching removes between 0 and 100 % of the residual dose (see Fig. 6.12, part vi). A large proportion of the data points, however, are plotted on the left-hand side of the plot, representing Z values less than one, something that is difficult to reconcile since it implies that the medium component is better bleached than the fast component. Furthermore, three aliquots give Z values that are negative. These occur because of low signal levels in the natural OSL which leads to a negative D_e value being obtained from the latter integral.

Bailey (2003b) suggested using a 'replacement point' check to ensure that all the aliquots are suitable for Z value analysis. Figure 6.13b is the same dataset as Figure 6.13a, but those points that failed the replacement point check (i.e. a Z value consistent with unity could not be obtained through analysis of a well-bleached regenerated signal) are shown as open circles. The points rejected using the replacement point criterion appear to fall indiscriminately around the Z=1 line. This suggests that the cause of the aliquots with Z values less than 1 is not a failure to produce a flat $D_e(t)$ plot when well bleached. To ensure that the Z values less than

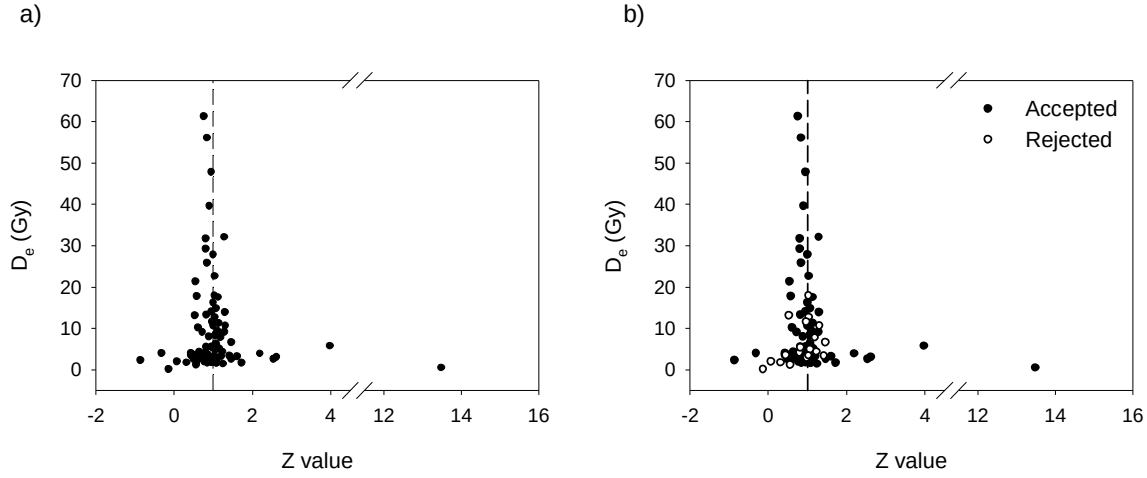

Figure 6.13: Z plots for sample 70KLA2: a) showing every data point and b) showing data points where the replacement point Z value was consistent with unity (accepted points - filled circles) and those where the replacement point Z value was not consistent (rejected points - open circles).

one are not caused by low signal levels, the Z values are plotted as a function of the natural signal and test dose signal in Figure 6.14. The results show that the Z value tends to 1 as the signal levels increase, and the scatter in Z increases as the signal levels decrease. However, no relationship between the presence of Z values less than one and the signal levels is evident.

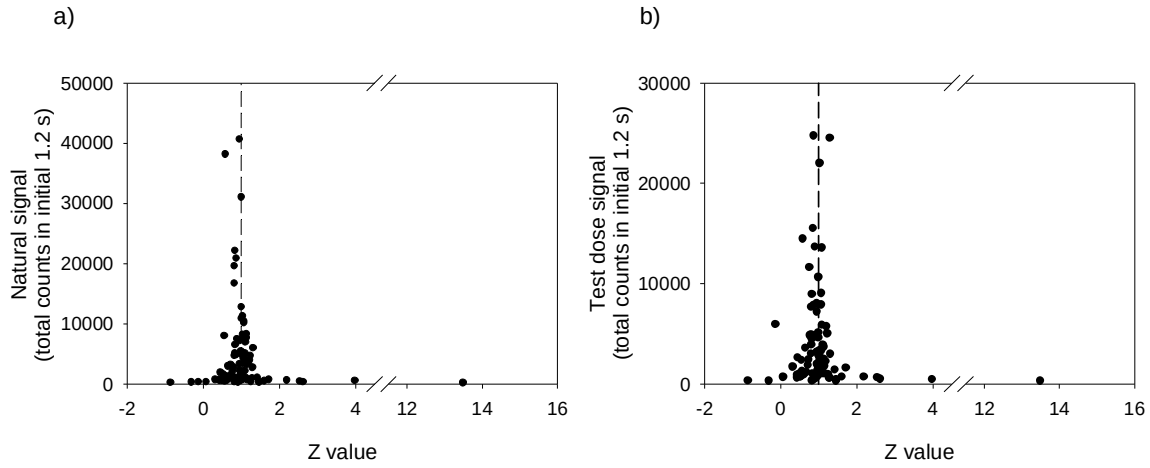

Figure 6.14: Plots for sample 70KLA2 showing a) the natural signal and b) the test dose signal as a function of the Z value.

An alternative method of representing the Z values is by plotting the D_e of the initial integral (bins 1-3) as a function of the latter integral D_e (bins 10-12). This display method also allows the errors on the D_e values to be shown, thus allowing one to determine if a Z value less than one is caused by large errors. The same aliquots that passed the 'replacement plot' test and are shown as accepted in Figure 6.13b are plotted in Figure 6.15. Z values that are consistent with unity (indicative of well-bleached aliquots or those that underwent no bleaching during the most recent transport event) fall along the Z=1 line, running diagonally across the plot. The Z values less than one fall above and to the left of the Z=1 line, and Z values greater than one fall to the right and below. From this plot, it can be seen that the majority of the aliquots have Z values that are consistent with unity. Only 10 % of the aliquots have Z values that are significantly above 1, indicative of partial bleaching, whereas 27 % have Z values that are less than 1 even taking into account the errors that are calculated. The low level of aliquots with Z greater than 1 suggests that the sample is quite well bleached, but these data points generally have large errors associated with the D_e values calculated from the

latter integral, causing them to be consistent with unity within errors. However, a large number of aliquots do have values of Z less than 1, and these are difficult to interpret. To investigate why the Z values less than one occur, 12 aliquots have been selected for further analysis (circled on Fig. 6.15, details in Table 6.2) and include four aliquots with Z values greater than 1, four with Z equal to 1, and four with Z less than one.

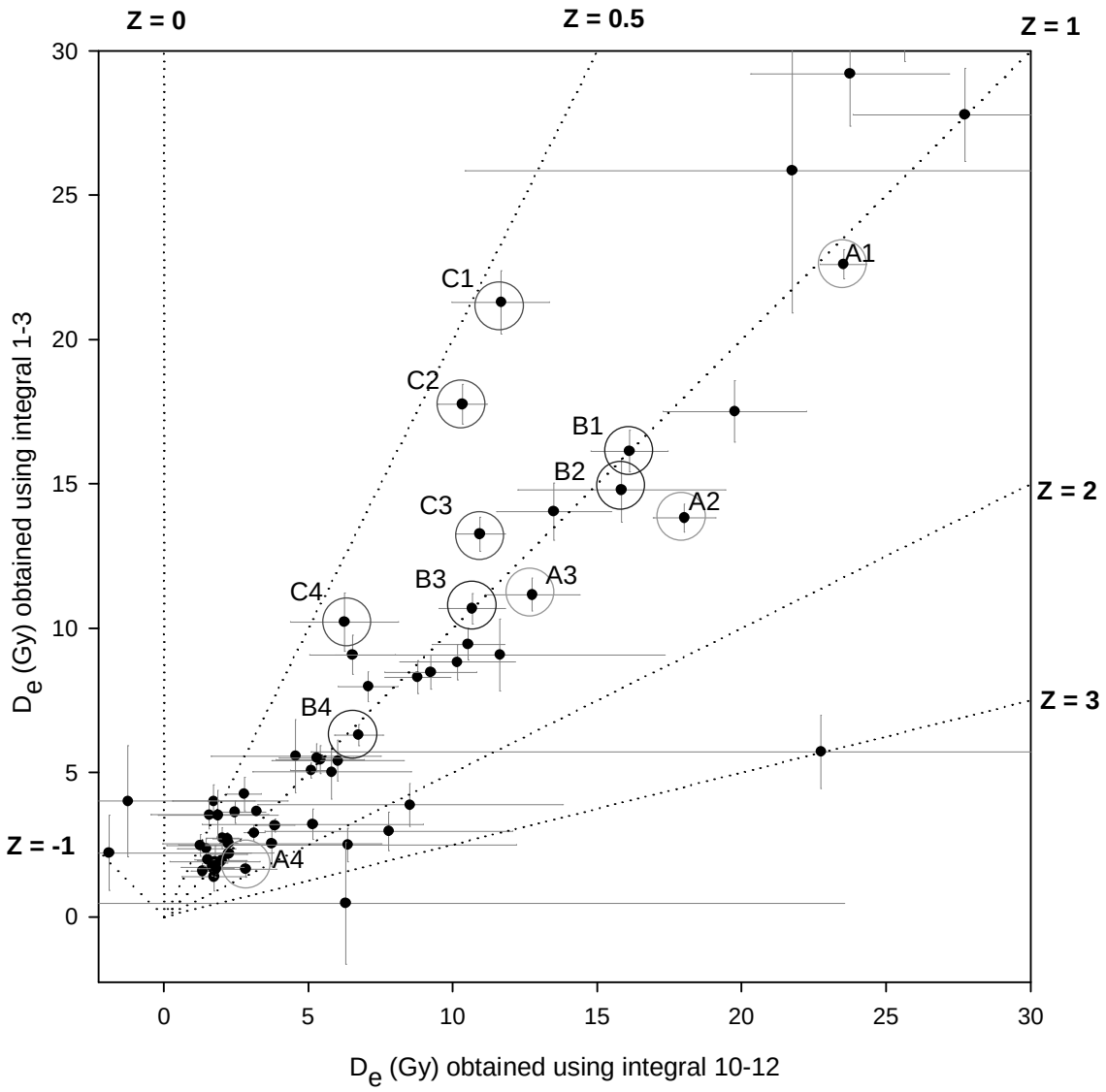

Figure 6.15: Graph showing the Z values for sample 70KLA2. The D_e values obtained using the initial integral are plotted against the D_e values obtained from the latter integral. Data points consistent with the Z=1 dotted line are those with Z values consistent with unity. The 12 data points circled were selected for further analysis (see Section 6.2.2.2).

Table 6.2: Details of aliquots chosen for further analysis, grouped into four aliquots with Z>1, four with Z=1 and four with Z<1. The Z values from the natural OSL signal and the replacement point OSL signal are detailed. The table also shows the D_e values calculated from the initial integral; and the ratio of the fast to medium (F:M) components in the first 1.2 s of stimulation in the natural (N) signal, and the mean of the F:M components in the regenerated and test dose (R & TD) signals. The final column details the test dose signal which indicates the brightness of the aliquot.

Aliquot		Z value (Natural)	Z value (Replacement plot)	D_e (Gy)	F:M (N) (%)	F:M (R & TD) (%)	Test dose signal
Z > 1	A1	1.04 ± 0.03	0.99 ± 0.04	22.60 ± 0.51	87±21 :13±2	94±1 : 6±1	95847
	A2	1.30 ± 0.09	0.96 ± 0.08	13.81 ± 0.48	93±0 : 7±0	95±0 : 5±0	24501
	A3	1.72 ± 0.70	0.81 ± 0.21	1.64 ± 0.28	96±2 : 4±2	8 4±1 : 16±0	1608
	A4	2.62 ± 1.56	0.75 ± 0.27	29.7 ± 0.67	90±15 : 10±9	73±3 : 27±3	489
Z = 1	B1	1.00 ± 0.09	1.02 ± 0.10	16.13 ± 0.72	100±0 : 0±0	98±1 : 2±1	10640
	B2	1.07 ± 0.26	0.96 ± 0.25	14.79 ± 1.11	99±1 : 1±0	96±1 : 4±1	1364
	B3	1.00 ± 0.12	1.07 ± 0.13	10.07 ± 0.52	100±1 : 0±1	100±0 : 0±0	5105
	B4	1.07 ± 0.15	1.05 ± 0.13	6.30 ± 0.36	100±1 : 0±1	99±0 : 1±0	7901
Z < 1	C1	0.55 ± 0.08	0.98 ± 0.18	21.29 ± 1.10	99±0 : 1±0	90±1 : 10±1	2347
	C2	0.58 ± 0.05	1.04 ± 0.10	17.76 ± 0.68	97±0 : 3±0	67±1 : 33±0	14464
	C3	0.83 ± 0.07	0.94 ± 0.09	13.26 ± 0.59	98±1 : 2±1	94±0 : 6±0	8953
	C4	0.61 ± 0.19	0.99 ± 0.25	10.22 ± 1.01	97±2 : 3±2	77±2 : 23±2	902

The normalised decay curves for the 12 aliquots chosen for further analysis were deconvolved assuming two exponential decaying components, a third exponential decaying component was not included because the majority of signal from any slow components would have been removed during the background subtraction. Additionally, in the part of the OSL decay curve of interest (first ~6 s) any contribution to the total signal from slow components is negligible. As an example, Figure 6.16 shows a deconvolved regenerated dose signal from aliquot A1. Deconvolution allowed calculation of the ratio of the fast:medium components in the natural signal (N), and the mean of the same ratio for the regenerative and test doses (R & TD) (Table 6.2).

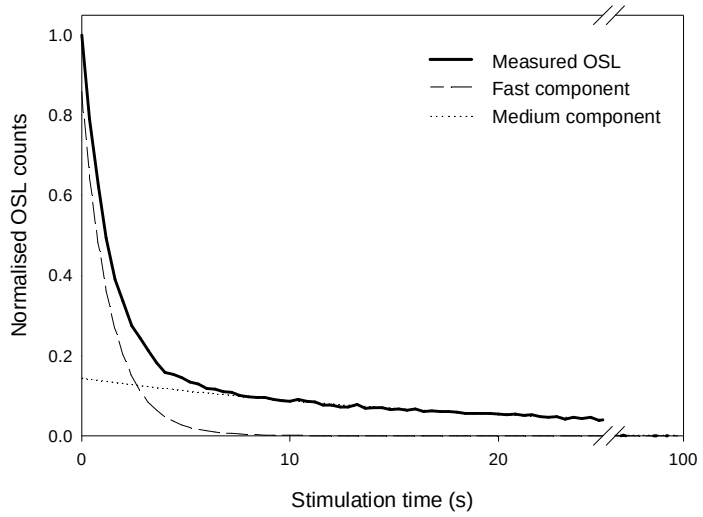

Figure 6.16: OSL decay from aliquot C2 following an ~33 Gy regeneration dose. The deconvolved fast and medium components are shown.

The normalised decay curves for the aliquots with Z greater than 1 are shown in Figure 6.17a. The results from the curve deconvolution (Table 6.2) show that for aliquots A1 and A2, a greater proportion of the OSL signal is derived from the medium component than the fast component in the natural (N) signal, compared to the mean of the regeneration and test dose (R & TD) signals. This is evident, particularly for aliquot A2, in the shape of the OSL decay curves shown in Figure 6.17a, where aliquot A2 has a natural signal that lies slightly above the regeneration signals. Aliquots A3 and A4 have ratios of the fast to medium component that are consistent within errors. While the Z values from these aliquots are greater than 1, the low signal levels give rise to scatter and hence Z is consistent with unity at two sigma. Although two of the aliquots demonstrate evidence of an increased medium component in the natural signal which would be interpreted as partial bleaching by Bailey (2003b), the results from aliquots A3 and A4 suggest that Z values greater than one are not necessarily caused by partial bleaching, and may arise from scatter in the D_e values obtained because of the low signal levels.

The decay curves for the four aliquots with Z values consistent with one are shown in Figure 6.17b. All the decay curves appear to overly each other, with

little evidence of change in shape between measurements. This is confirmed by the results of the curve deconvolution in Table 6.2. Interestingly, the curve deconvolution suggests that the OSL of aliquots B1, B3, and B4 has a negligible medium component; the only aliquot with convincing evidence of a medium component is B2, where a slight increase from 1 ± 0 % in the N signal to 4 ± 1 % in the R and TD signals is observed. If the OSL signal from an aliquot consists entirely of the fast component (disregarding the relatively constant effect of any slow components), the only possible Z value for that aliquot would be 1, since the D_e values from both integrals would be based on the fast component. Overall, the results from these aliquots are consistent with what one would expect where an aliquot has a Z value consistent with 1, i.e. the decay curves are similar for both natural and regeneration doses, although this is probably because of the fact that the OSL signal consists almost entirely of one component, as opposed to two bleachable components. It is interesting to note that the D_e values for the four aliquots range from ~6 Gy to ~16 Gy, consistent with the suggestion that a Z value consistent with 1 can represent two end-case situations, 1) where grains have been completely bleached; and 2) where grains were not bleached at all during the most recent transport event. This variation in D_e from apparently well-bleached grains may occur because of instances where the grains are partially bleached to an extent sufficient to significantly reduce the D_e, but not sufficient to allow the detection of partial bleaching (see Section 6.2.1.2). Following Bailey (2003b), the lowest value of D_e from an aliquot with Z value consistent with 1 is the most appropriate for the sediment, and the other aliquots with Z values consistent with 1 represent instances where the D_e is derived from both the most recent burial period and a residual dose.

Figure 6.17 (following three pages): The initial OSL decay for the natural, regeneration and test doses for four aliquots of sample 70KLA2 with a) Z>1; b) Z=1; and c) Z<1. The decay curves have been normalised, with the background (calculated from the last 20 s of stimulation (80-100 s)) subtracted.

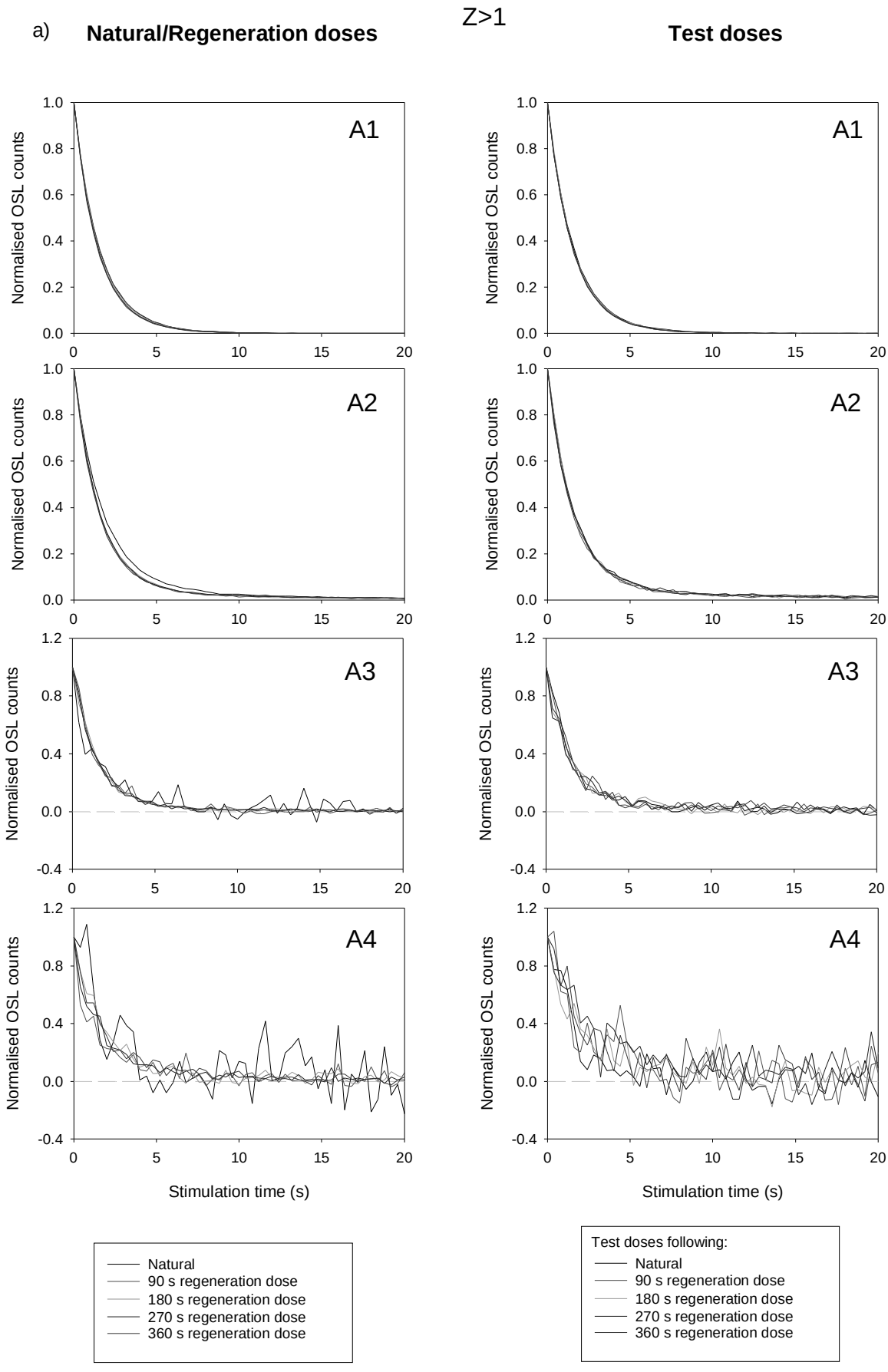
a)
Natural/Regeneration doses
Z>1
Test doses
A1
A2
A3
A4
Normalised OSL counts
Stimulation time (s)
Natural
90 s regeneration dose
180 s regeneration dose
270 s regeneration dose
360 s regeneration dose
Test doses following:
Natural
90 s regeneration dose
180 s regeneration dose
270 s regeneration dose
360 s regeneration dose

b)

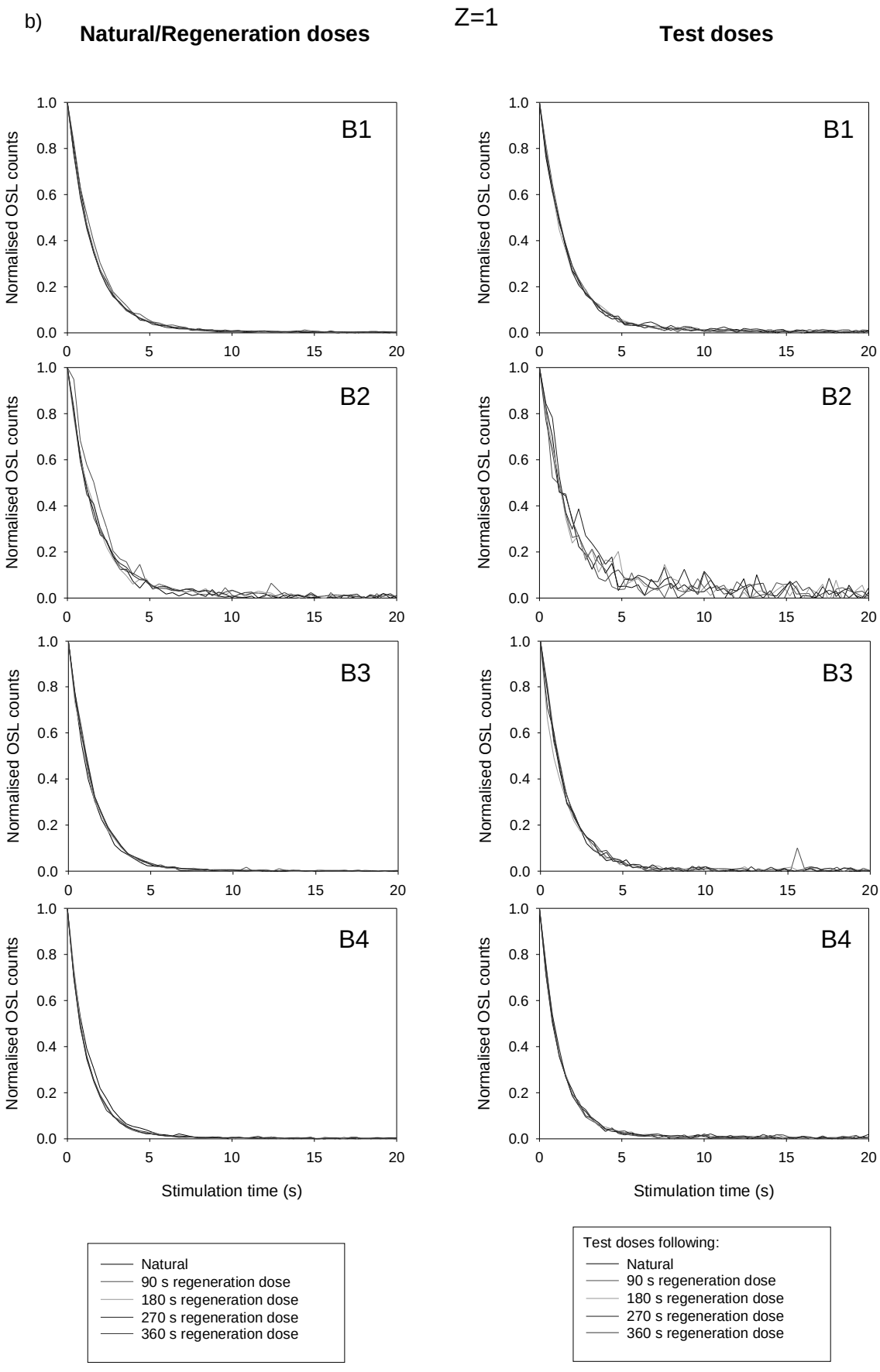
Z=1
Natural/Regeneration doses
Test doses
B1
B2
B3
B4
Normalised OSL counts
Stimulation time (s)
Natural
90 s regeneration dose
180 s regeneration dose
270 s regeneration dose
360 s regeneration dose
Test doses following:
Natural
90 s regeneration dose
180 s regeneration dose
270 s regeneration dose
360 s regeneration dose

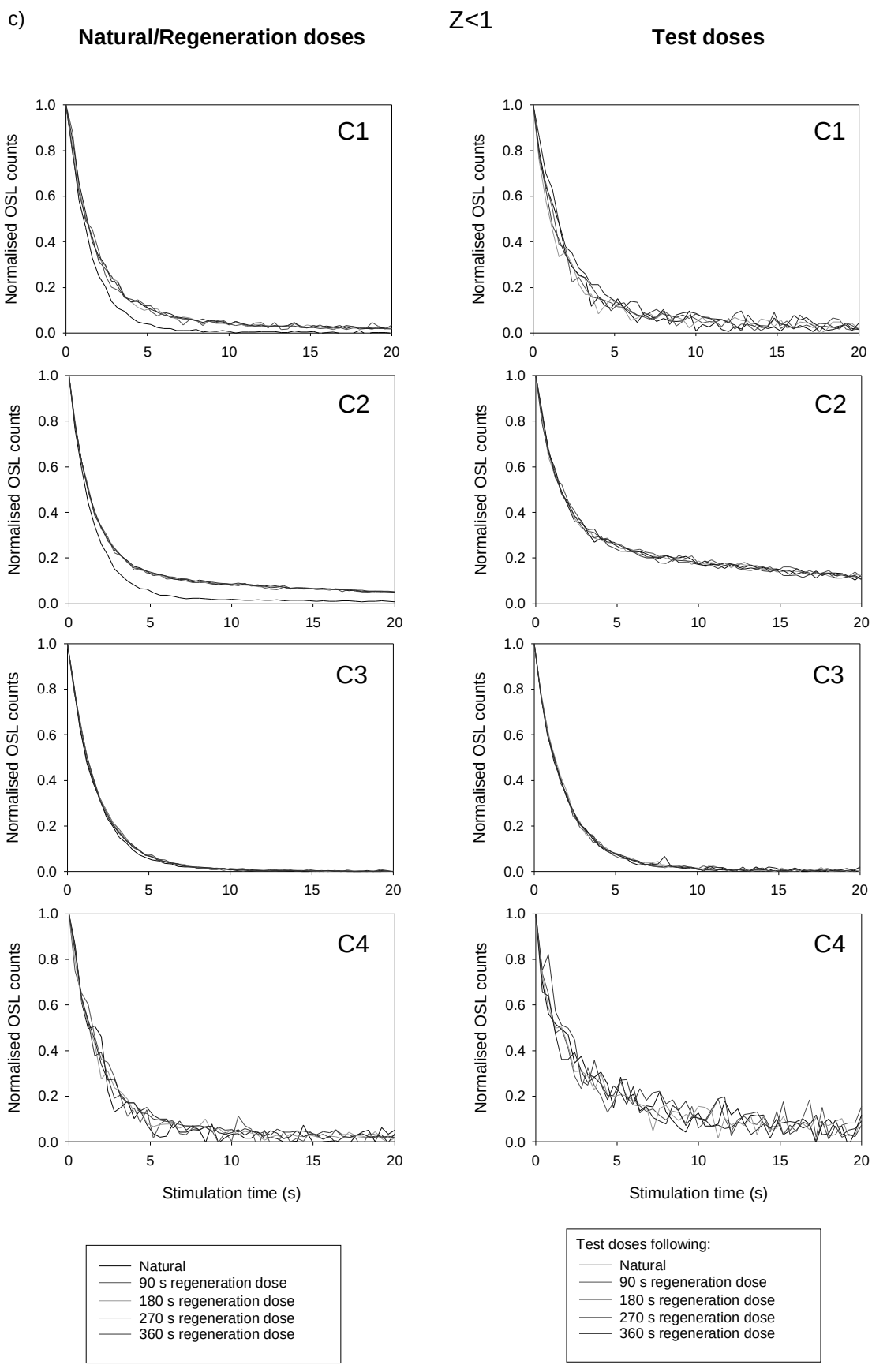
c)
Z<1
Natural/Regeneration doses
Test doses
C1
C2
C3
C4
Normalised OSL counts
Stimulation time (s)
Natural
90 s regeneration dose
180 s regeneration dose
270 s regeneration dose
360 s regeneration dose
Test doses following:
Natural
90 s regeneration dose
180 s regeneration dose
270 s regeneration dose
360 s regeneration dose

A Z value less than one should not occur as it suggests that the medium component was better bleached than the fast component during transport. Over a quarter of the aliquots analysed for the Z plot of sample 70KLA2 had Z values less than one (including errors). The normalised decay curves for the four aliquots chosen for further analysis (C1-C4) are shown in Figure 6.17c. Interestingly, the D_e values of aliquots C1-C4 are greater than some of those obtained for aliquots interpreted as being partially bleached (Z>1) and those considered to be well-bleached (Z=1) (Table 6.2). The graphs indicate that whilst the test dose responses of all the aliquots are consistent, the natural OSL decay curves of aliquots C1 and C2 contain a smaller proportion of the medium component than the regenerated signals. Curve deconvolution demonstrates that for all the aliquots (C1-C4), a greater proportion of the R and TD OSL signals is from the medium component than the N signal; for example, for aliquot C2 the mean proportion of the R and TD signals from the medium component is 30 % greater than in the N. This suggests that for these aliquots with Z values less than 1, the medium component is either unstable over geological periods, or thermally unstable and sensitises during the first elevated heat treatment (i.e. the preheat on the natural). Investigation into the thermal stability of the components of the OSL signal (Section 4.4.2) suggested that the medium component is thermally unstable in the Klip River quartz. This thermal instability may lead to the presence of an increased medium component in the R and TD signals, and thus a Z value less than 1. Nevertheless, the D_e values calculated for dating purposes from aliquots with this phenomenon should still be correct, as the part of the decay curve used in calculation of the D_e value is dominated by the fast component.

Bailey *et al.* (2003) found that a falling trend in $D_e(t)$ plots (which would yield a Z value less than one) occurred when old samples were investigated. They attributed this trend to a thermally unstable slow component (S_2, from Singarayer and Bailey, 2003). Modelling indicated that a significant decrease in the D_e with stimulation time could be expected from samples older than 20 ka. It is unlikely that this contributes to the Z values less than one for aliquots of 70KLA2, because the aliquot with the highest D_e (A4: 29.7 ± 0.67 Gy) has an age of ~16 ka.

The construction of $D_e(t)$ plots and/or derivation of Z values to detect partial

bleaching of sediment does not appear to work for the Klip River sample investigated. A large number of the aliquots had Z values less than 1, precluding them from inclusion in further analysis of the shape of the Z plot. Although some aliquots had Z values greater than 1, which would be interpreted as containing partially bleached grains by Bailey (2003b), a very small proportion had Z values significantly greater than 1 when the error terms on the D_e values were included. In part, this may occur because of the relatively small proportion of the medium component in the OSL signal; the magnitude of the fast component is generally at least 20 times larger than that of the medium component in sample 70KLA2 (Table 6.2), whereas Bailey *et al.* (2003b) found that in over 100 samples, the proportion of fast to medium component was 60:40. Additionally, the medium component in the quartz from the Klip River appears to be thermally unstable (Section 4.4.2), leading to the occurrence of an increased medium component in the regenerated and test dose signals.

Even if evidence of heterogeneous bleaching can be found in a sample through construction of a Z plot, it still does not enable one to determine the appropriate D_b for the sample. Bailey (2003b) suggested using the Z plot to determine the sub-population of well-bleached aliquots, and then taking the mean of these values. This approach leaves one with the problem of how to define the well-bleached grains. As demonstrated earlier, simply taking those aliquots with Z=1 is inappropriate as these aliquots may have widely ranging D_e values, possibly because of partial bleaching of an extent which is sufficient to leave a residual dose in the grains, but not severe enough to allow detection through $D_e(t)$ plots of the Z value.

6.3 DETECTING HETEROGENEOUS BLEACHING: DOSE DISTRIBUTION METHODS

An alternative method for detecting heterogeneous bleaching is by looking at the D_e distribution for a sample. If the D_e values are obtained from a sample where all the grains were bleached to the same extent during transport, and exposed to the same amount of radiation during burial, the resulting D_e distribution would be expected to be relatively narrow and symmetrical. In a fluvial sample, where each grain may have been reset to a different degree, the D_e values may be variable

and not consistent within errors. The shape and spread of a D_e distribution thus may allow one to detect the presence and severity of heterogeneous bleaching.

Olley *et al.* (1998) found that when D_e values were obtained for many aliquots of fluvial samples, asymmetric dose distributions were observed (Fig. 6.18). This had previously been noted by Murray *et al.,* (1995) who attributed the spread in the data, and shape of the histogram, to heterogeneous bleaching of the sediments. Olley *et al*. (1999) investigated the causes of asymmetric D_e distributions from small aliquots of fluvial quartz. They found that the more asymmetric the distribution, the greater the probability that the lowest D_e value represents the true burial dose. For aliquots containing different numbers of grains, they calculated the probability that an aliquot would be contaminated by partially bleached grains. Their results (Fig. 6.19) showed that where an aliquot contains 60 grains and the proportion of unbleached grains is >7 %, the probability of selecting an aliquot consisting entirely of well-bleached grains is effectively zero. By decreasing the number of grains on an aliquot, the probability of selecting only well bleached grains increases. Where variation in D_e exists, this reduces averaging of the grains, and allows a closer representation of the true D_e distribution to be attained (Wallinga, 2002).

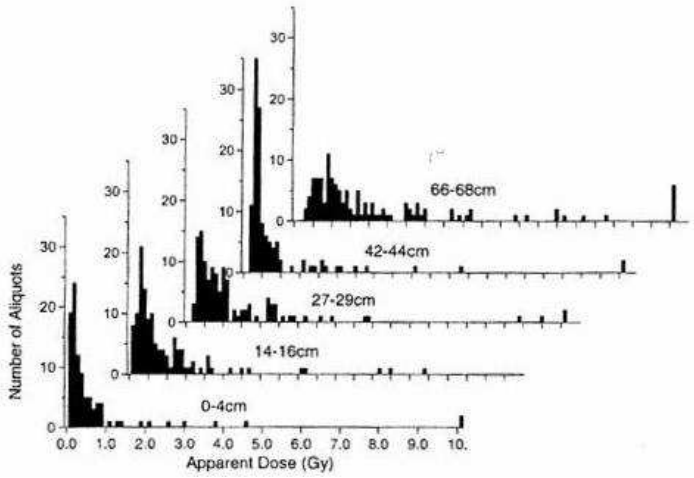

Figure 6.18: Dose distributions from various depths in a core from the Namoi River, Australia. From Olley *et al.* (1998).

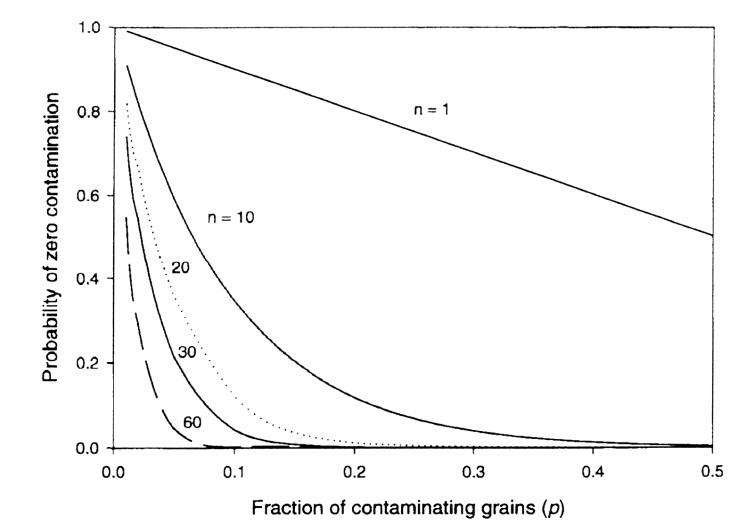

Figure 6.19: Plot showing the probability of selecting only well-bleached grains in aliquots consisting of n grains, as a function of the proportion of unbleached grains in a sample. From Olley *et al.* (1999).

6.3.1 Proportion of grains emitting luminescence

Murray and Roberts (1997) were the first to calculate equivalent dose values from single grains of quartz, and since then various papers have been published where a large number of grains have been analysed individually (Roberts *et al.*, 1999; Duller *et al.*, 2000; Yoshida *et al.*, 2000; Jacobs *et al.*, 2003; Olley *et al.*, 2004a,b; Jacobs *et al.*, 2006). Variability in several aspects of the signal from quartz on a grain-to-grain level has been noted, such as the saturation dose (Roberts *et al.*, 1999; Duller *et al.*, 2000), grain brightness (Duller *et al.*, 2000; Yoshida *et al.*, 2000), and the components in the OSL signal of grains from the same sample (Bulur *et al.*, 2002). For the current study, the OSL signal from single grains of quartz from some of the Klip River samples was measured to determine the proportion of grains that emit a measurable luminescence signal.

The number of grains that emit a measurable luminescence signal has been found to vary considerably on a sample-to-sample basis. Duller *et al.* (2000) first presented plots of the cumulative light sum (where the grains are ranked from brightest to dimmest), as a function of the proportion of grains, for various

samples. Their results (Fig. 6.20) showed a range in the behaviour of samples, with 95 % of the light sum originating from between 5 % and 50 % of the grains for the sedimentary samples; but the sample of calibration quartz demonstrated a more homogenous signal brightness from the individual grains. Results from further work into the brightness of grains in samples by Jacobs *et al.* (2003a) and Olley *et al.* (2004a) showed similar findings to that of Duller *et al.* (2000). For seven samples from a deep-sea core, Olley *et al.* (2004a) found that the proportion of grains with measurable D_e values varied between 21 % and 94 %. Jacobs *et al.* (2003a) investigated three samples of dune sand and found that <10 % of the grains contributed towards 90-95 % of the luminescence emitted when the burial dose was measured.

To investigate the proportion of grains emitting luminescence from the Klip River samples, the OSL signal was measured from 2000 grains from three samples: 75KL0315 (oxbow lake); 75KL0330 (palaeochannel); and 75KL0333 (palaeochannel) (Fig. 6.21). The CW-OSL signal from each grain was measured

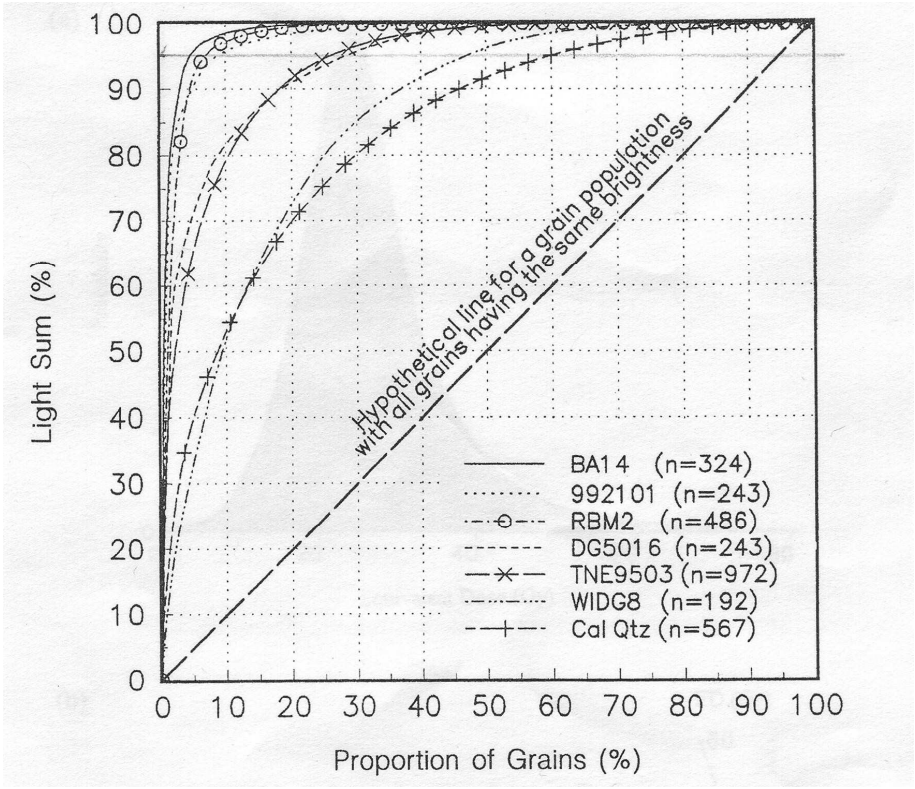

Figure 6.20: The proportion of the total OSL light sum from n grains, plotted as a function of the proportion of the total number of grains. For a population of grains which had the same brightness, the line would run diagonally from bottom-left to top-right. From Duller *et al.* (2000).

for 0.8 s at 125℃, after a 220℃ preheat (held fo r 10 s) following the natural dose, and a range of laboratory irradiations. Variability in the brightness of grains from the natural signal may be in response to variation in the D_e values from heterogeneous bleaching. Therefore the intensity of the luminescence signal following an ~43 Gy laboratory irradiation was used to compare the samples. 95 % of the total light sum emitted originates from 10 %, 8 % and 9 % of the grains for samples 75KL0315, 75KL0330 and 75KL0333, respectively (Fig. 6.21). Since all the sediment in the Klip River is thought to derive from the same geological source, one would expect the luminescence behaviour of the grains to be similar. This is demonstrated by the fact that the three samples investigated show similar proportions of bright grains, in contrast to other studies where this has varied widely on a sample-to-sample basis (Duller *et al.*, 2000). Because 95 % of the total light emitted derives from ≤10 % of the grains, if ~30 grains of Klip River quartz are used for analysis, the OSL signal measured would be expected to derive from only one to three grains, thereby minimising averaging of the individual grain D_e values. Thus, small aliquots (containing ~30 grains) should be suitable for detecting heterogeneous bleaching in these sediments and may be more accurate than using single grains because of the 9 % uncertainty associated with such measurements arising from factors such as instrument reproducibility, variable attenuation of the beta particles through the sample and beta source heterogeneity (Thomsen *et al*., 2005).

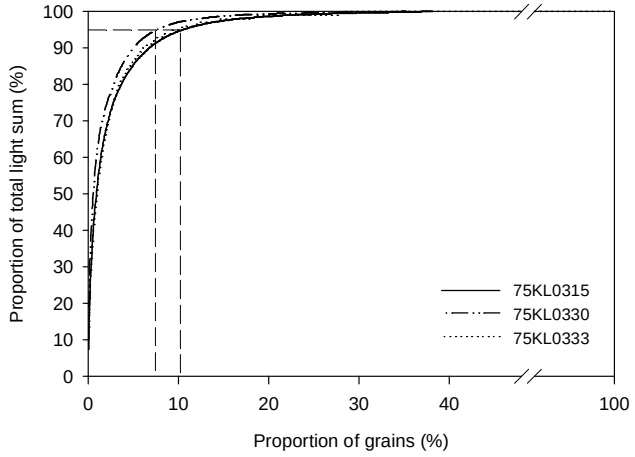

Figure 6.21: Percentage of the total light sum (following an ~43 Gy dose) as a function of the percentage of grains measured. 95 % of the luminescence emitted is derived from between 7.6 % and 10.2 % of the grains (indicated by dashed lines on the plot). The total number of grains measured for each sample was 2000.

6.3.2 Simple statistical measures of D_e distribution

Clarke (1996) and Clarke *et al.* (1999) suggested using the coefficient of variation (ν, the standard deviation divided by the mean) to detect heterogeneous bleaching, and defined a value of $\nu<0.1$ for a well-bleached sediment. Eitel *et al.* (2005) also found that artificially bleached samples consistently had ν values less than 0.1. Using this value as a threshold to determine whether a sample was well-bleached or not, six out of seven samples of fluvial silts from Namibia were found to be heterogeneously bleached. Further work on Namibian fluvial samples found that 26 out of 27 samples (25 fluvial, 2 aeolian) had $\nu>0.1$, with a mean value of 0.22 (Eitel *et al.*, 2006). Fuchs and Wagner (2003) used this parameter to analyse artificial mixtures of grains which had been bleached, irradiated and then partially bleached. As expected, they found that ν decreased as the number of grains on an aliquot increased. In conclusion, they stated that if using $\nu=0.1$ for the cut-off between a well-bleached and a heterogeneously-bleached sediment, an aliquot containing between 200 and 500 grains is preferable.

Rowland *et al.* (2005) calculated the ratio of the mean D_e to the median D_e (M/m) to determine whether a sample was heterogeneously bleached or not. If this ratio was 1.05 or less the sample was said to be well bleached, whereas ratios greater than 1.05 were associated with heterogeneously-bleached samples. They used this criterion to determine whether D_b should be calculated from the mean of the D_e values, or by using a "leading edge" approach on the sample. This approach was based on analysis of a larger data set by Lepper (pers. comm.) who found that for 94 % of his samples (n=31), the aeolian samples yielded M/m ratios less than or equal to 1.05, whilst fluvial samples had M/m ratios greater than 1.10. For each sample, between 51 and 315 D_e values were obtained.

Although both methods listed above do enable one to determine the spread in the distribution mathematically, neither of them takes into account the errors on the individual D_e values. With the exception of Eitel *et al.* (2005), the data used in the papers are not graphically represented so one is unable to gain any information about the spread in the errors on the D_e values. In Eitel *et al.* (2005), graphs of the D_e as a function of the normalised OSL suggest that the luminescence

intensity varies up to a factor of 28. As the errors associated with D_e values are based primarily on counting statistics, it is thus likely that the errors on these aliquots vary considerably. When looking at the results from small aliquots, with variable errors on D_e, it is important to take this into account. If errors are not included in the analysis, a poorly known value that is an outlier may influence the measure of spread considerably, whereas the data point may actually fall within the main population within errors. A preferable method of looking at the spread in the distribution would be one that incorporates the error value on each D_e determination.

6.3.3 The overdispersion parameter

The central age model described by Galbraith *et al*. (1999) allows one to calculate the overdispersion of a dataset. Using this model, the dataset is considered to be a single population where the log D_e values form a normal distribution (Fig. 6.22a) with mean δ and standard deviation $\sigma_{OD.}$ If σ_{OD}=0, then all the log D_e values ($\hat{\delta}_i$) must be equal to a common value within errors; this is the scenario assumed by the common age model (Fig. 6.22b) described in Galbraith *et al*. (1999). Thus, the overdispersion can be defined as the spread in a population that is in addition to the spread accounted for by the errors on individual D_e values. The maximum likelihood values of the parameters δ and σ_{OD} can be found using the equations:

$$\delta = \frac{\sum_{i=1}^{n} w_i \hat{\delta}_i}{\sum_{i=1}^{n} w_i}$$

and $$\sum_{i=1}^{n} w_i^2 \ (\hat{\delta}_i - \delta)^2 = \sum_{i=1}^{n} w_i$$

where $w_i = 1/(\sigma_{OD}{}^2 - s_i^2)$ Galbraith *et al.* (1999)

The parameter σ_{OD} is useful as it allows the spread in the distribution of D_e values to be compared between samples, taking into account the errors on D_e values.

Histograms and radial plots of samples 75KL0319 and 75KL0320 are shown in

Figure 6.23. From the histograms it can be seen that the spread in D_e values is similar for the two samples at just less than 3 Gy, but the σ_{OD} values are different - 12 % (75KL0319) and 26 % (75KL0321). The reason for this difference in σ_{OD} cannot be seen in the histograms. The high outlier seen in the histogram for 75KL0319 is not apparent in the radial plot because it has a large error (D_e = 2.75 ± 1.47 Gy) and thus falls within the main D_e population leading to the relatively small value for σ_{OD}. By contrast, 75KL0320 has a much larger spread in the radial plot leading to the relatively large value for σ_{OD} because of the occurrence of D_e values with small relative errors which fall outside the main D_e population.

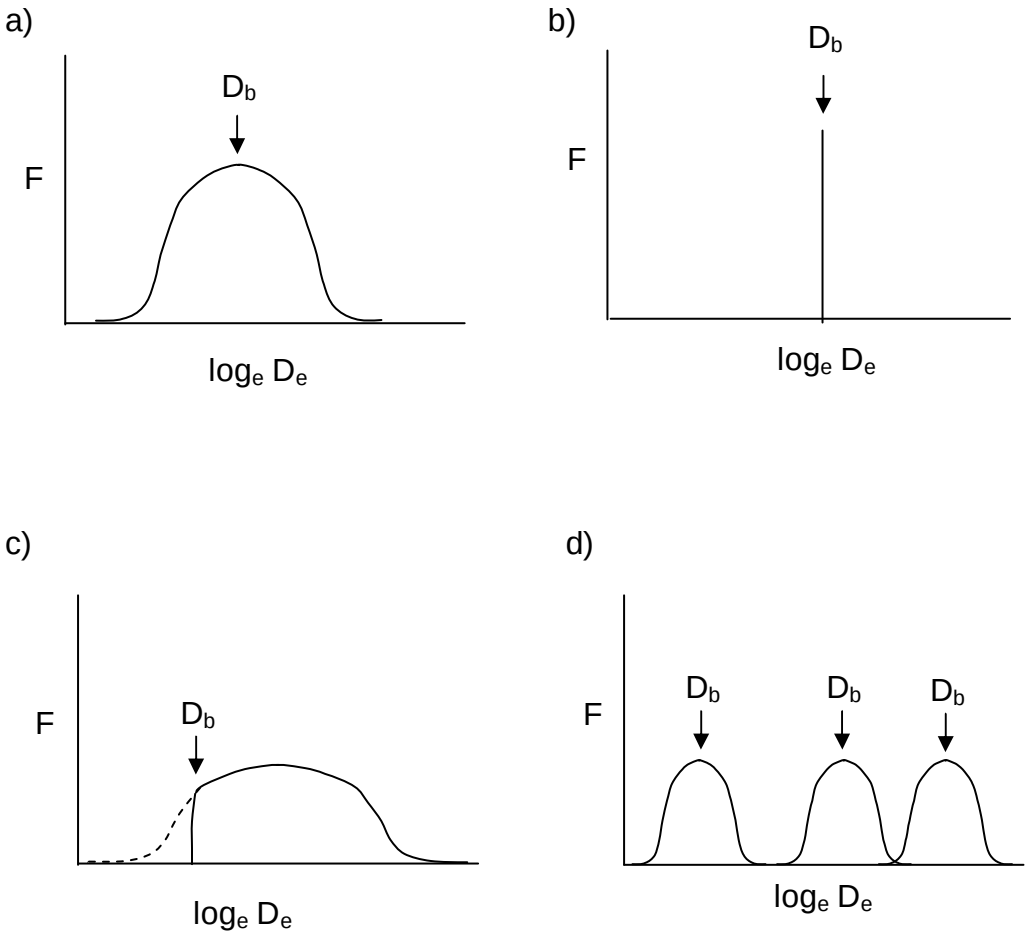

Figure 6.22: Schematic of the distribution of D_e values in various models: a) the central age model; b) the common age model: c) the minimum age model and d) the finite mixture model. The curves indicate the distribution of the D_e values (F represents the frequency), and the D_b values that would be calculated using the models.

a)

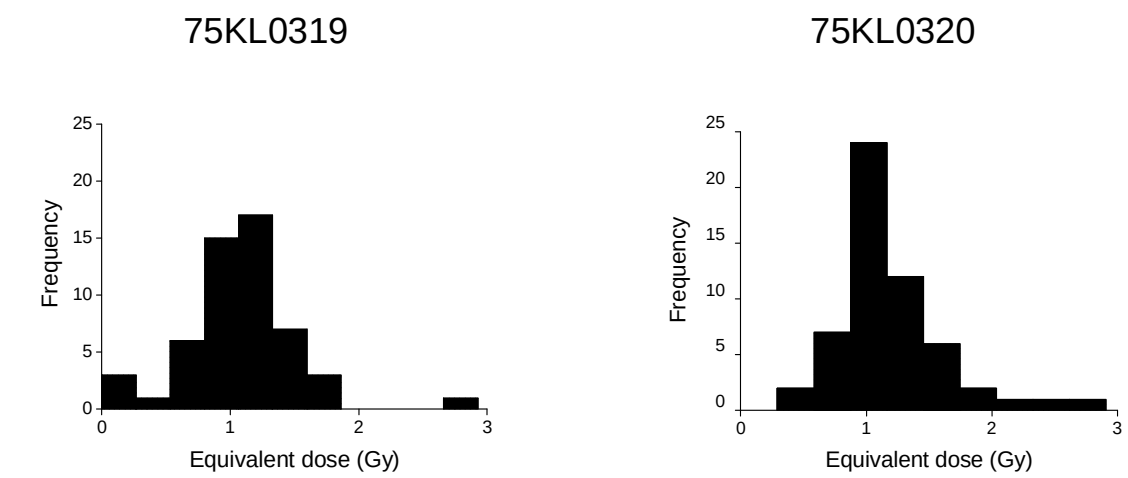

b)

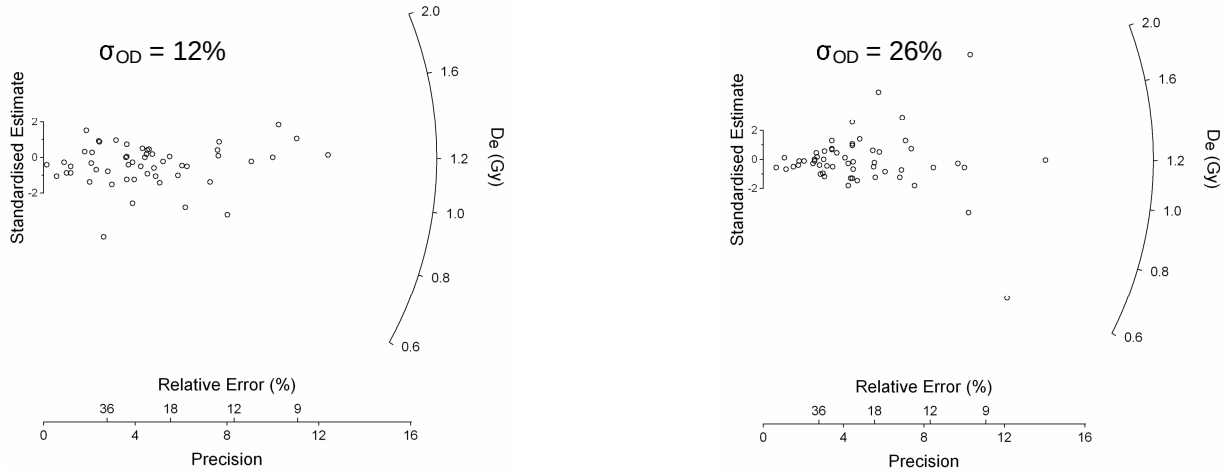

Figure 6.23: a) Histograms and b) radial plots of samples 75KL0319 and 75KL0320. Despite the similar spread in the D_e values, the overdispersion parameters vary considerably.

Galbraith *et al.* (2005) assessed the dispersion in D_e values that cannot be accounted for by the errors associated with experimental factors such as instrument reproducibility, counting statistics, and the beta-source heterogeneity, and the natural variability caused by factors such as non-uniform emptying of the optically-sensitive traps and thermal transfer. They investigated the values of σ_{OD} obtained for both naturally and laboratory irradiated samples (the naturally irradiated samples were thought to have been well bleached prior to deposition) in cases where three factors were varied: the test dose (0.5 Gy or 5 Gy); the preheat temperature (180℃ or 260℃); and the size of the al iquot (~8 or ~80 grains). As one would expect, the σ_{OD} was greater for the naturally irradiated aliquots than those that had undergone laboratory irradiation, and the smaller aliquots had higher σ_{OD} than the larger ones. For the aliquots consisting of ~8 grains, σ_{OD} varied between 7 % and 18 % for natural datasets and between 1 % and 12 % for datasets obtained after laboratory irradiation.

The overdispersion parameter was used by Olley *et al.* (2004a) to characterise the bleaching of marine sediments. They suggested that for single grain datasets, a value for σ_{OD} of <20 % indicates a well-bleached, single population. Values of σ_{OD} greater than this may be caused by factors such as heterogeneous bleaching, mixing of discrete populations of grains, or variation in beta microdosimetry. It might be expected that the amount of overdispersion in a well-bleached sample analysed using small aliquots would be less than that from single grain analysis, arising from some limited averaging of the signal from grains in the aliquot. Other literature which states the overdispersion values for samples includes Jacobs *et al.* (2003a) and Olley *et al.* (2004b). The former work included dating of three samples of dune sand from Blombos Cave, South Africa, using aliquots consisting of 500-800 quartz grains. Values of 9, 10 and 16 % were calculated for the σ_{OD}, and since the samples were expected to be well-bleached, this overdispersion was tentatively attributed to beta microdosimetry variations. In Olley *et al.* (2004b) single-grain measurements of lacustrine deposits had σ_{OD} values between 21 % and 42 % with a mean of 28 %, whereas fluvially transported deposits had a wider range from 1% to 85 %.

Although the overdispersion parameter allows one to assess the spread in the D_e

distribution, an arbitrary cut-off value still needs to be selected to differentiate between well-bleached and heterogeneously bleached sediments. Furthermore, a value of σ_{OD} for a single population is required for some statistical approaches such as the finite mixture model (Galbraith and Green, 1990). One method is to look at the σ_{OD} value that is obtained for a sample that is known to be well bleached. All of the samples collected for this project were deposited fluvially and so may be heterogeneously bleached and unsuitable. Therefore, sample TNE9517, collected from a linear dune system in Australia (Duller and Augustinus, in press), was analysed instead. This was expected to be completely bleached, as shown by modern dune samples from the region that gave residual ages of ~10 years. SAR analysis on 48 small aliquots of this sample gave a mean D_e value consistent with the value obtained using large aliquots of 22.2 ± 1.3 Gy, giving further confirmation that the sample was well-bleached prior to deposition (Fig. 6.24). The σ_{OD} value found for the D_e values from the small aliquot analysis of this sample was 10 %, in-line with the value that Olley *et al.* (2004a) suggested to define a well-bleached population. The σ_{OD} for multiple grain aliquots is likely to be less than that from single grain analysis owing to averaging of the D_e values when multiple grains are investigated. For this project, σ_{OD} was calculated for each sample, and the value of 10 % determined from TNE9517 was used as a cut-off to determine whether a sample was heterogeneously bleached or not.

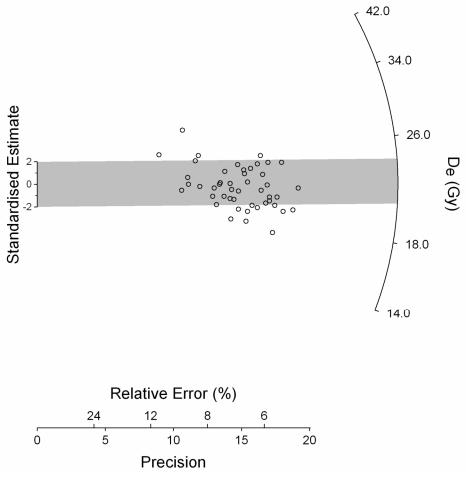

Figure 6.24: Radial plot of D_e values obtained from analysis of 48 small aliquots of TNE9517, a well-bleached sample from an Australian linear dune system. The grey shaded band indicates those values that are consistent within two sigma with the mean D_e value of 22.2 Gy calculated from large aliquot OSL analysis by Duller and Augustinus (in press).

6.4 STATISTICAL METHODS FOR OBTAINING AN APPROPRIATE D_B VALUE FROM A D_E DISTRIBUTION

Murray *et al*. (1995) first identified a spread in D_e values with an initial peak and a tail up to high values as indicative of heterogeneous bleaching. They analysed two modern samples and found that only a few aliquots had D_e values consistent with zero, presumably owing to an absence of unbleached grains on these aliquots. From these results, they inferred that for a heterogeneously bleached sediment, the lowest D_e values obtained are the best estimate of the true burial dose. Various studies have developed different statistical procedures for obtaining an appropriate D_b value from a heterogeneously bleached sediment; together these can be termed 'leading edge' models, as they use the low D_e values in the distribution for derivation of D_b. Some studies (e.g. Olley *et al.*, 1999, 2004b; Wallinga, 2002) have suggested using small aliquots or single-grain analysis for dating fluvial samples. If this is done, the errors on D_e are likely to be highly variable and thus it is important that they are included in analysis for the D_b calculation. The key papers that have discussed methods for obtaining an appropriate D_b value from heterogeneously bleached sediments are outlined below.

6.4.1 Methods based solely on the D_e values

6.4.1.1 Method 1: Olley et al. (1998)

In this paper, dose distributions were obtained by analysing aliquots of Australian quartz (125-180 µm) containing 60-100 grains. Two groups of samples were analysed, one from a known age deposit on the Murrumbidgee River, and one from varying depths down a core collected from the Namoi River (Fig. 6.18). For the Murrumbidgee River sample, the mean of the lowest 5 % of D_e values gave an age of 64 ± 7 years, consistent with the known age of 70 years. Following this, the ages from the Namoi River samples were obtained using the mean of the lowest 5 % of D_e values, and the ages calculated generally increased with depth.

6.4.1.2 Method 2: Fuchs and Lang (2001)

Sample pre-treatment on sediments collected from fluvial deposits from the

Peloponnese yielded small amounts of quartz, so for this research only nine or ten aliquots (each consisting of 3 mg of 90-200 µm grains) were analysed per sample. The results showed scattered D_e values which were assumed to be from heterogeneous bleaching. Measurement of aliquots which had been artificially bleached and irradiated yielded a maximum standard deviation of 4 % in the D_e values. To calculate a D_b from the natural D_e values, based only on those aliquots which contained well-bleached grains, the D_e values for each sample were ranked in order from youngest to oldest. Starting with the youngest value, and including one additional aliquot at a time, the mean D_e and percentage standard deviation was calculated. This was repeated, including aliquots with increasing values of D_e until the standard deviation of the mean was 4 %; this mean value was taken to be the most appropriate estimate of D_b. Although no independent age control was available for the samples, the ages increased with depth as expected.

6.4.1.3 Method 3: Lepper et al. (2000) and Lepper and McKeever (2002)

Three stratigraphic levels of fluvial deposits in central Oklahoma were investigated by Lepper *et al*. (2000). Using the results from treating a regeneration dose as an unknown dose in the SAR procedure they characterised the effect the experimental error distribution would have on a D_e distribution. They suggested that experimental errors can be removed from the distribution by deconvolution, leaving a distribution of D_e arising solely from natural sedimentary processes. An algorithm (Agersnap-Larsen, unpublished) requiring the input of the natural D_e values and the D_e values obtained from treating a known dose point as unknown, was used to deconvolve the data. The leading edge of the deconvolved D_e distribution was then used to calculate the D_b using the equation:

$$D_b = [(D_{e\text{-mode}} + D_{e\text{-min}})/2\} \pm \{(D_{e\text{-mode}} - D_{e\text{-min}})/2]$$

No independent age control was available for the samples studied in this paper, so the accuracy of the method could not be tested. A simpler method of analysis was proposed by Lepper and McKeever (2002). After plotting the D_e dataset in a histogram, with the bin widths calculated as the median of the error values on the D_e values, a Gaussian curve was fitted through the data points represented by the (x,y) co-ordinates obtained from the centre of the bin and the frequency of D_e

values in that bin (Fig. 6.25). The second derivative of this Gaussian was then used to calculate D_b.

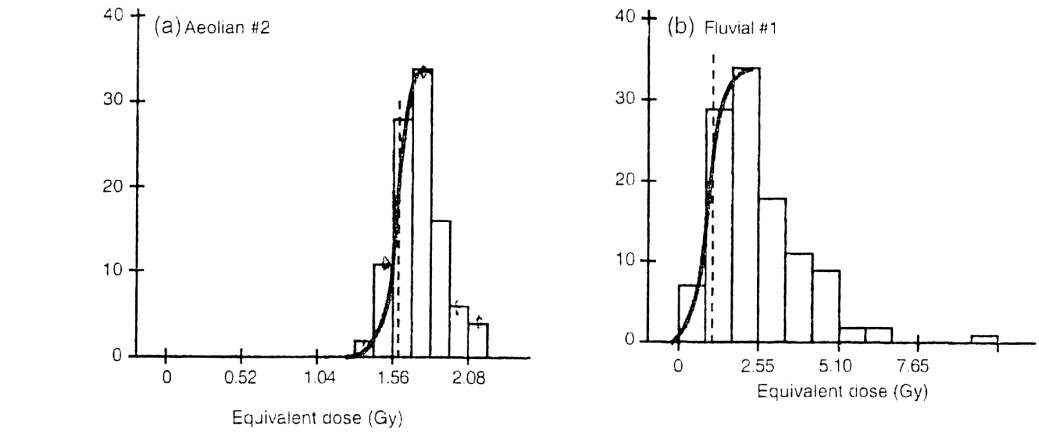

Figure 6.25: Examples of D_e distributions from a) an aeolian dune sand, and b) a floodplain deposit. The bold line shows the Gaussian curve fitted to the leading edge of the distribution to enable derivation of the burial dose (D_b) at the point of inflection (dashed line). From Lepper and McKeever (2002).

6.4.1.4 Method 4: Zhang et al. (2003)

Zhang *et al.* (2003) studied fluvial sand from palaeochannels on the Beijing Plain using the SAR procedure. The large amount of scatter in the D_e values was investigated through the various luminescence properties of the aliquots. They took the scatter in the normalised OSL of regeneration doses (L_X/T_X) from a sample as being representative of a well-bleached situation; in this case, the scatter arises from the varying luminescence properties of the grains, and experimental error. They used this value to calculate a D_b from a sample following a procedure very similar to that described by Fuchs and Lang (2001). Initially, the relative standard deviation (RSD) of the scatter in the normalised OSL signal from the first regenerative dose was calculated. The aliquots were then ranked from the lowest to the highest value of sensitivity-corrected natural OSL signal, assuming that the aliquot with the lowest normalised OSL signal also would have the lowest D_e value. The cumulative RSD of the natural OSL signals was found, starting from the aliquot with the lowest OSL signal, and including aliquots one at

a time, until the RSD of the first regenerative dose OSL dataset was reached. The aliquots taken into account up to this point were determined to be well-bleached, and the D_e values were averaged to find D_b for the sample. Only one sample studied in the paper had independent age control; this was provided by archaeologists who placed the pottery shards at 0.7 ka. The corresponding OSL age of 0.68 ± 0.04 ka for this sample was in good agreement.

6.4.2 Methods incorporating the uncertainty on D_e

If the brightness of the OSL signal is highly variable on an aliquot to aliquot basis, the errors on the D_e values will also vary considerably, as is commonly the case when single grains or small aliquots are being analysed. A value that may appear to be a low outlier can actually form part of the main distribution within errors, but this will not be taken into account in the methods covered in Section 6.4.1. The following methods incorporate the errors on the D_e values into the analysis for determination of D_b.

In the models outlined in Sections 6.4.2.2 and 6.4.2.3 (the minimum age model and finite mixture model) the data are initially transformed by taking the natural logarithm (ln) of the D_e values prior to subsequent analysis (Fig. 6.22c-d).

6.4.2.1 Method 5: Thomsen et al. (2003)

A method to derive the correct D_b from dose distributions obtained from single grain analysis of quartz from irradiated blocks was described by Thomsen *et al*. (2003). Relatively strict acceptance criteria were applied to the grains included in the analysis, i.e. if the uncertainty on the D_e value for a grain was >15 % or >0.5 Gy, the grain was rejected. On all the accepted grains, a 10 % uncertainty was combined with the D_e error to account for the variation found in results from a dose recovery experiment on single grains. To calculate a D_b value based on those grains from the well-bleached part of the distribution, the ratio of the external measurement of uncertainty (α_e) to the internal measurement of uncertainty (α_i) is used. The equations for these two values are:

$$\alpha_e^{\,2} = \frac{\sum_{i=1}^{n} (x_i - \bar{x})^2 \Big/ \sigma_i^{\,2}}{(n-1)\sum_{i=1}^{n} 1 \Big/ \sigma_i^{\,2}} \qquad \alpha_i^{\,2} = \frac{1}{\sum_{i=1}^{n} 1 \Big/ \sigma_i^{\,2}}$$

where x_i is the dose estimate from each individual grain, σ_i is its uncertainty, $\bar{x}$ is the weighted mean, and *n* is the number of measurements. α_e combines information on individual estimates of uncertainty for each grain and the deviation from a weighted mean. If there is no other source of error except for the uncertainty on the individual data points then α_e reduces to α_i, so for a large, normal population α_e/α_i tends to unity (i.e. where the overdispersion is 0). In a distribution containing heterogeneously-bleached grains, this ratio can be used to determine which grains are well bleached, i.e. where the distribution in x_i is consistent with σ_i. Any additional variance because of heterogeneous bleaching will increase α_e relative to α_i. By ranking the individual equivalent doses from lowest to highest and calculating α_e/α_i for n = 2,3…x until $\alpha_e/\alpha_i = 1 \pm (2(n-1))^{-0.5}$, only the well-bleached grains are used in the estimate of D_b. Any grain giving a D_e above this point is assumed to be partially bleached.

6.4.2.2 Method 6: Galbraith and Laslett (1993) –Minimum Age Model

The minimum age model was developed for samples where heterogeneous bleaching is evident (Galbraith *et al.*, 1999). It derives a D_b value from a truncated normal distribution fitted to the individual D_e values, with the truncation point giving the value of D_b (Fig. 6.22c) (Galbraith and Laslett, 1993). To describe the distribution fitted to the dataset, four parameters and their errors need to be calculated: (1) the proportion of grains that were fully bleached prior to burial; (2) the truncation point of the distribution (i.e. the logarithm of the D_b value); (3) the value which would be the mean of the normal distribution fitted to the dataset; and (4) the overdispersion of this distribution. Relatively complex equations are needed to optimise these various parameters used within the model, and a program written by Geoff Laslett for S-Plus (Galbraith, pers. comm.) has been adapted for running in the statistics package 'R'. This allows the parameters to be found using optimisation routines.

6.4.2.3 Method 7: Galbraith and Green (1990) –Finite Mixture Model

Galbraith and Green (1990) describe the finite mixture model. This model is appropriate for sediments containing grains of more than one discrete population, where each population (component) has been well bleached and can be described by the central age model (Section 6.3.3) (Fig. 6.24d). For this model, the user is required to enter the number of components (k) and the overdispersion parameter for the components, into the program code. The program fits the components to the dataset, and for each component it gives D_b and its error. Additionally, it gives two parameters; the log likelihood and the Bayesian Information Criterion (BIC). These parameters are used to assess the most appropriate number of components to fit to a dataset. The software can be run repeatedly on a dataset, steadily increasing the number of components (k). BIC reduces down to a minimum at the best fit, and then increases again.

Although this model has been designed for a distribution consisting of a discrete number of populations, it can be applied to a heterogeneously bleached sample. As the model selects populations based on D_e values that are consistent with one another (within a set σ_{OD} defined by the user), the D_b of the lowest population will essentially be derived from a normal distribution of the lowest D_e values. Thus, if the dataset contains some D_e values measured from well-bleached grains, this lowest population should allow one to obtain the appropriate D_b value for a sample. In addition to the D_b value for each population, the output for this model contains the percentage of the D_e values that form each individual population, so one is able to gain understanding of the extent of heterogeneous bleaching.

6.4.3 How many D_e values are needed to obtain a reproducible estimate of D_b?

The number of individual D_e values needed to characterise accurately a distribution will depend upon the complexity of that distribution. Thus, heterogeneously-bleached samples would be expected to require a larger number of aliquots than homogeneously-bleached ones. Murray *et al.* (1995) first investigated the extent of bleaching in water-lain sediments through the analysis of at least 120 D_e values for each sample. In many studies more than 50 D_e

values are obtained per sample (e.g. Olley *et al.*, 1998; Lepper *et al.*, 2000; Folz *et al.*, 2001; Rowland *et al.*, 2005), but other studies concerned with the detection of heterogeneous bleaching in sediments obtain less than 10 D_e values (e.g. Colls *et al.*, 2001; Fuchs and Lang, 2001; Srivastava *et al.*, 2001).

To determine how many D_e values are needed to characterise a distribution, 116 D_e values were obtained for 70KLA2 (Fig. 6.26). This sample shows evidence of

a)

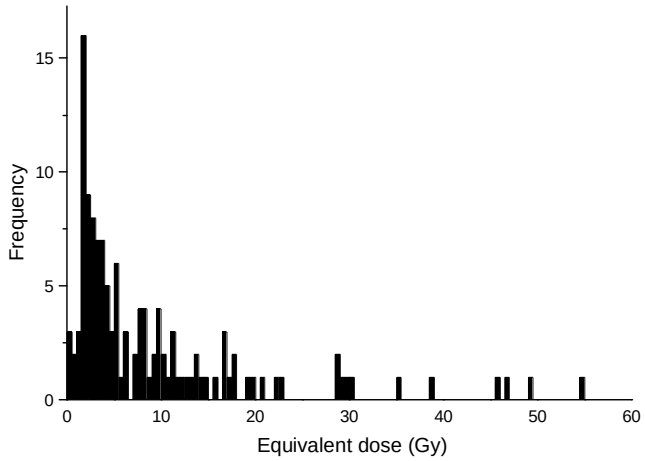

b)

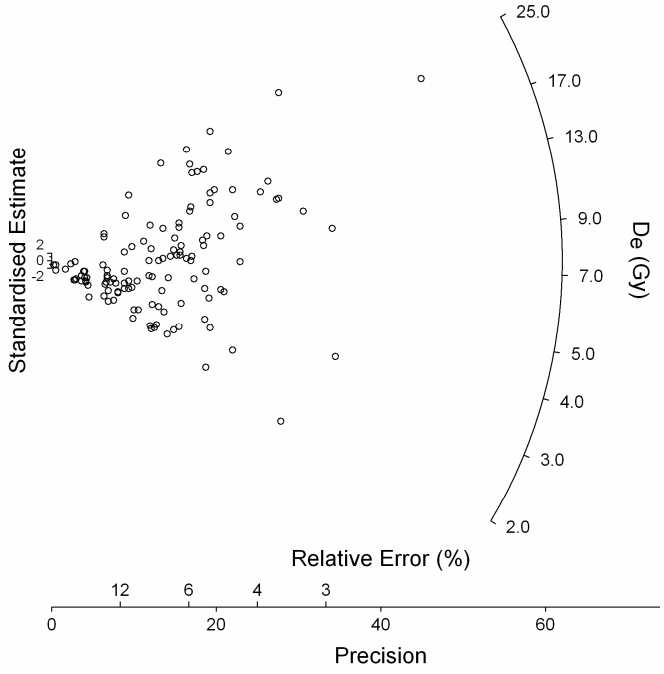

Figure 6.26: a) Histogram and b) radial plot showing the D_e distribution for sample 70KLA2.

heterogeneous bleaching both in the shape of the distribution (Section 6.3), and in the high overdispersion parameter (σ_{OD} = 97 %). From this dataset of D_e values, sub-samples containing 5, 10, 15, 20, 30, 40, 50 and 60 D_e values were randomly selected, and this was repeated 20 times for each sub-sample size resulting in 160 datasets. When the sub-sample contains more than five D_e values there will be some replication of the D_e values in the datasets, but the analysis still allows one to investigate the reproducibility of a heterogeneously-bleached distribution.

Each of the 160 sub-samples (of 5, 10, 15 … 60 D_e values) was tested for normality using the 1 sample Kolmogorov-Smirnov test. The results (Fig. 6.27) demonstrate that for sample 70KLA2, at least 50 D_e values need to be measured to be certain of obtaining a dataset that is statistically non-normal. If the dataset contains less than 20 aliquots, there is a greater than 50 % chance that a distribution from this heterogeneously-bleached sample will appear normal.

The D_b value was obtained for each of the 160 sub-samples using a variety of statistical techniques including the weighted mean, central age model, Method 1 (Section 6.4.1.1), Method 2 (Section 6.4.1.2), Method 5 (Section 6.4.2.1), Method 6 (minimum age model), and Method 6 (finite mixture model).

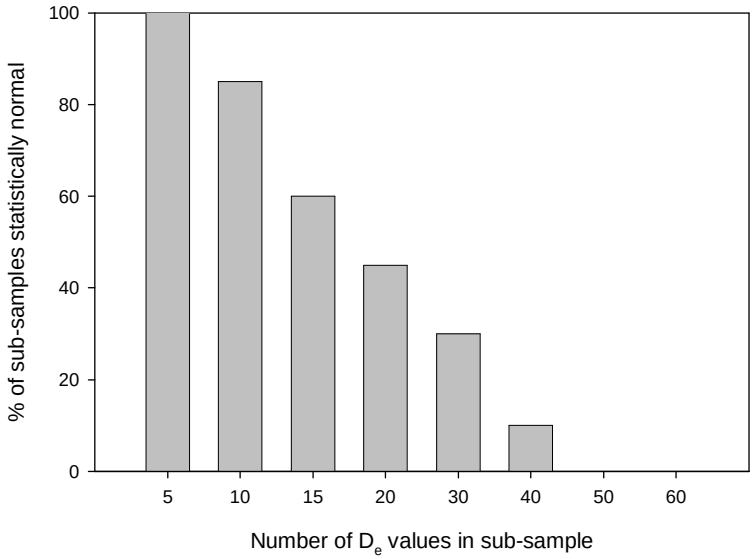

Figure 6.27: Bar chart showing the percentage of sub-sample datasets from sample 70KLA2 that are statistically normal using the 1-sample Kolmogorov-Smirnov test.

The results using the weighted mean are shown in Figure 6.28a. The D_b value calculated for each of the 160 datasets is plotted as a filled circle as a function of the number of values in the sub-sample. The error bars indicate the absolute error associated with the greatest D_b value calculated for each sub-sample size. For D_b values calculated using the weighted mean, the absolute error remains relatively consistent, regardless of the number of D_e values in the sub-sample size, because this method assumes the dataset is derived from a normal distribution. The grey line joins the mean D_b values for each sub-sample size, and demonstrates that changing the sub-sample size does not lead to a systematic change in the D_b values calculated. Using the weighted mean, regardless of the sub-sample size, D_b is approximately 2.5 Gy. However, the relative standard deviation (RSD) calculated for the 20 D_b values for each sub-sample size shows that, as expected, as the number of D_e values in the sub-sample increases, the RSD decreases from ~12 % (when the weighted mean is based on 5 D_e values), to <3 % if more than 30 D_e values are included in the calculation. Although this method produces reproducible results with small errors on the individual D_b values, this type of analysis is inappropriate for a heterogeneously-bleached sample because it assumes the D_e distribution is normal.

The results from the central age model show high scatter in the D_b values for sub-samples containing <30 D_e values (Fig. 6.28b). In particular, a D_b of ~5 Gy is obtained for a sub-sample with 5 D_e values; this arises from two high outlying D_e values which also cause the high error on this D_b, and the high value for RSD for the D_b values. In general, as one would expect, the D_b values remain consistent for all sub-samples sizes at ~2.6 Gy, although like the weighted mean, this type of analysis is unsuitable for a heterogeneously-bleached sample.

Figure 6.28 (following pages): Results from analysis of different sub-samples of the D_e dataset for 70KLA2. The same sub-sample datasets were used to derive D_b values (left-hand axis) using six different statistical methods, the D_b for each sub-sample is shown as a filled circle; the errors associated with the largest D_b value for each sub-sample size are also shown. The grey line shows the mean D_b values for each sub-sample size. The relative standard deviation of the D_b values for each size grouping are plotted as triangles using the right-hand axis.

a)

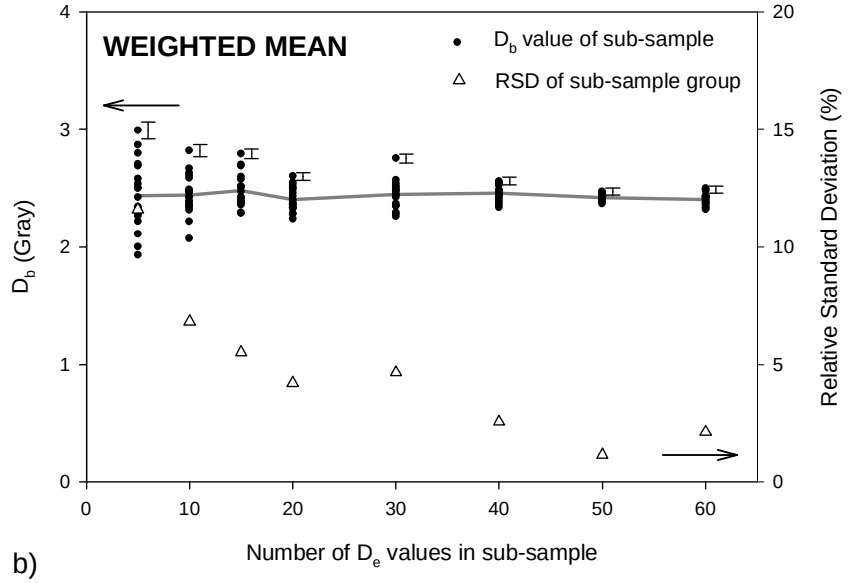
WEIGHTED MEAN
D_b value of sub-sample
RSD of sub-sample group
D_b (Gray)
Relative Standard Deviation (%)
Number of D_e values in sub-sample

b)

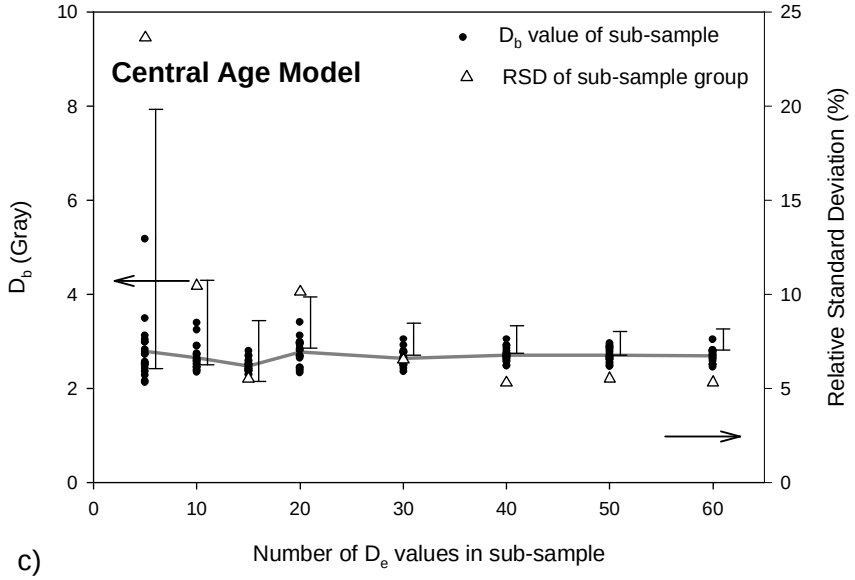
Central Age Model
D_b value of sub-sample
RSD of sub-sample group
D_b (Gray)
Relative Standard Deviation (%)
Number of D_e values in sub-sample

c)

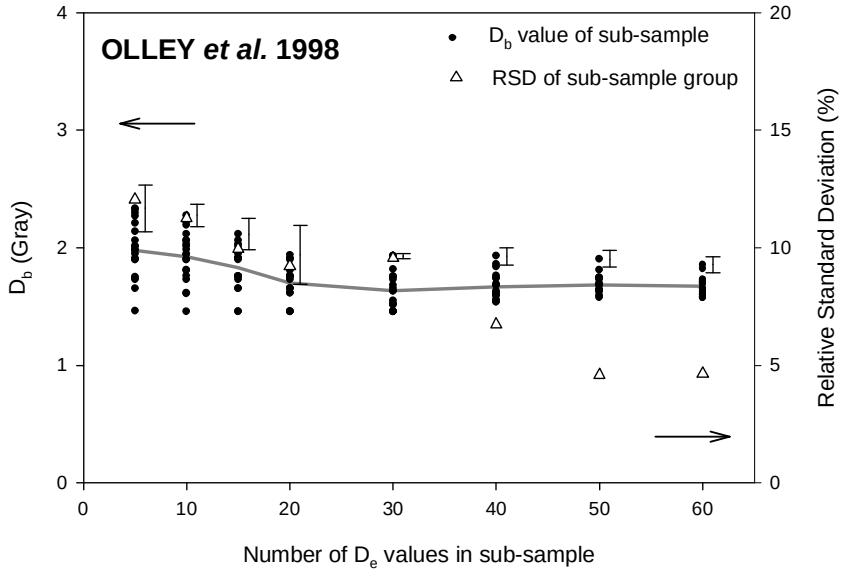
OLLEY *et al.* 1998
D_b value of sub-sample
RSD of sub-sample group
D_b (Gray)
Relative Standard Deviation (%)
Number of D_e values in sub-sample

d)

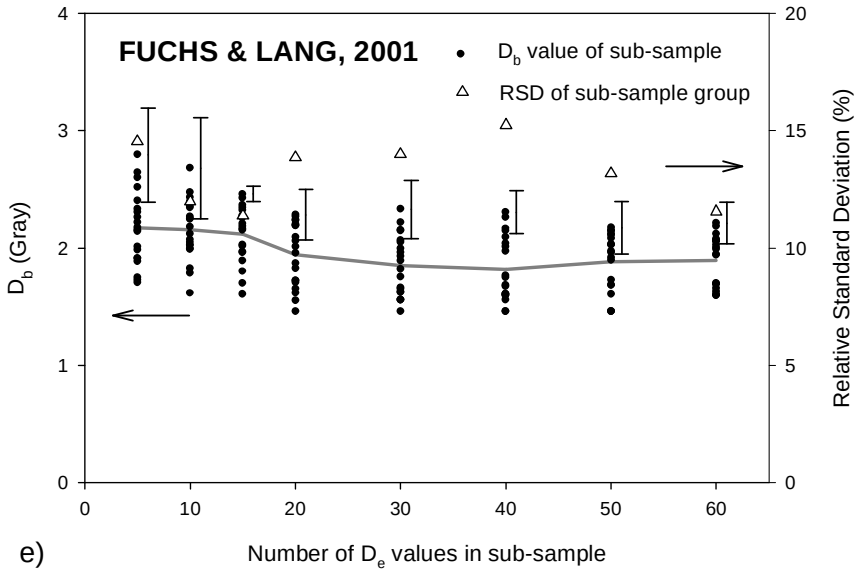
FUCHS & LANG, 2001
D_b value of sub-sample
RSD of sub-sample group
D_b (Gray)
Relative Standard Deviation (%)
Number of D_e values in sub-sample

e)

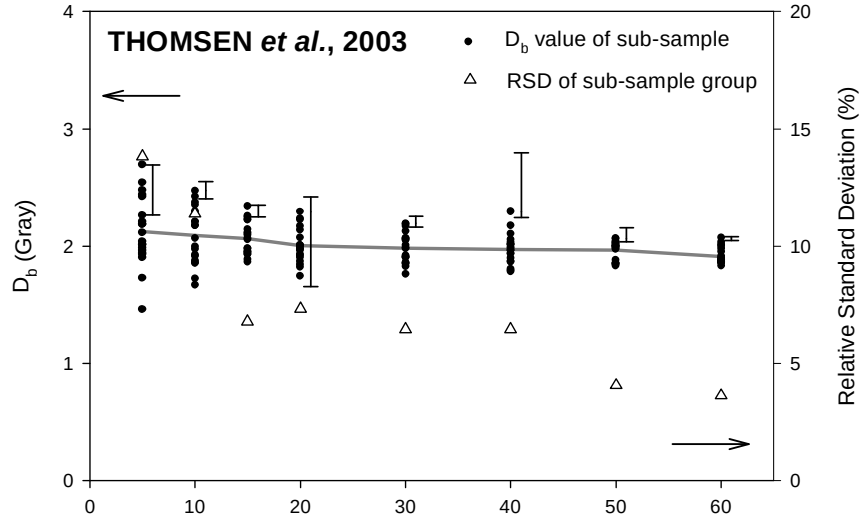
THOMSEN et al., 2003
D_b value of sub-sample
RSD of sub-sample group
D_b (Gray)
Relative Standard Deviation (%)

f)

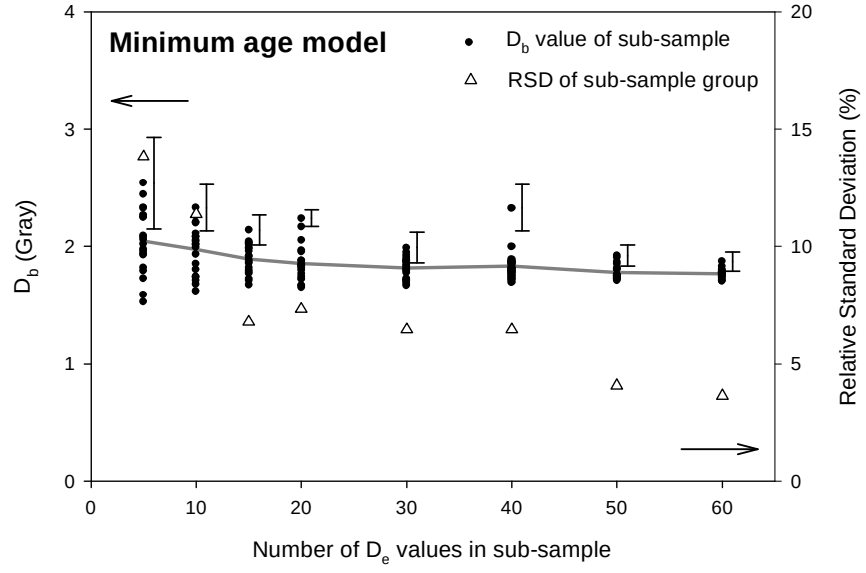
Minimum age model
D_b value of sub-sample
RSD of sub-sample group
D_b (Gray)
Relative Standard Deviation (%)
Number of D_e values in sub-sample

g)

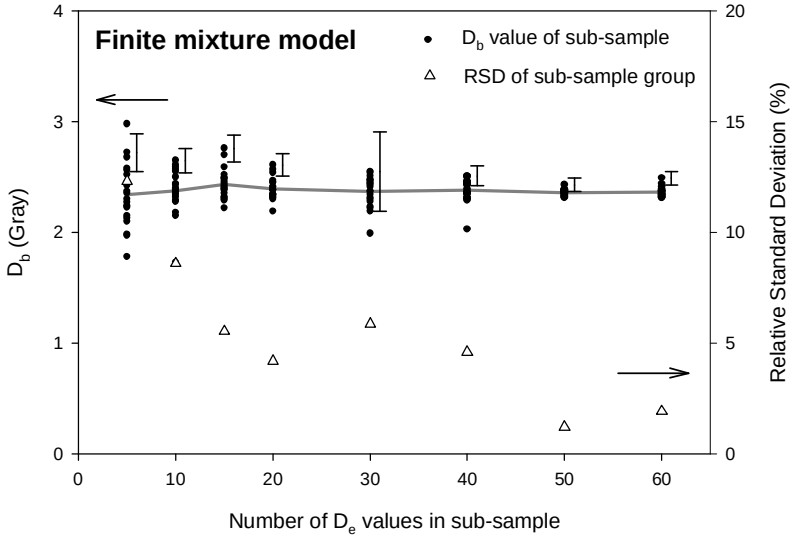

Method 1 (Olley *et al.*, 1998) gives consistent values of mean D_b when the sub-sample consists of more than 20 D_e values (Fig. 6.28c). Datasets with ≤20 D_e values will have a D_b derived from the lowest D_e value only, while D_b for the 60 D_e sub-sample is based on the lowest 3 D_e values. As this technique takes into account very few aliquots from the lower end of the distribution, each D_b value is essentially based on the same few D_e values. This is demonstrated by the mean D_b values for each sub-sample size that decrease monotonically for between 5 and 20 D_e values, and then remain consistent, at about 1.8 Gy. The RSD of the results falls to <5 % when at least 50 D_e values are included in the analysis.

The RSD of the D_b values obtained following Method 2 (Fuchs and Lang, 2001) shows poor reproducibility in the results (Fig. 6.28d). This poor reproducibility arises owing to the sensitivity of the procedure to a high RSD in the lowest two or three D_e values in the sub-sample. For instance, if the first few D_e values vary considerably, a high RSD results and D_b is calculated from only these few values. The instances where this occurs can be seen by the D_b points which plot below the main body of D_b values.

A similar situation also arises with sub-samples consisting of <15 D_e values when Method 5 (Thomsen *et al.*, 2003) is used (Fig. 6.28e), although this method is less sensitive to these low outlying values because it takes into account the errors on

the D_e values. The mean D_b value for the different sub-sample sizes is relatively consistent at ~2.1 Gy, and the reproducibility of the D_b values is <5 % when 50 D_e values are included in the analysis. However, the errors associated with D_b are highly variable using this technique, owing to the manner in which the α_e/α_i ratio is used to derive the errors.

When D_b is calculated using Method 6 (minimum age model) and Method 7 (finite mixture model) (Fig. 6.28f-g) the RSD of the D_b values decreases to <5 % when the sub-samples contain 50 or more D_e values. The mean D_b values decrease slightly as the number of D_e values in the sub-sample increases, before remaining constant (~1.9 Gy) when at least 20 D_e values are included in the minimum age model analysis (Fig. 5.28f). The mean D_b values, calculated using the finite mixture model, remain constant (~2.2 Gy) for all sub-sample sizes. The finite mixture model shows less variability in the results than the minimum age model, with the relative standard deviation generally <5 % when the sub-sample contains at least 10 D_e values (Fig. 6.28g). As one would expect, the minimum age model consistently derives lower D_b values than the finite mixture model.

The variation in the D_b values calculated using the different methods shows that techniques that are based on the inclusion of increasing D_e values, until a pre-defined parameter is reached, encounter problems with low, outlying values. With the exception of the method detailed by Fuchs and Lang (2001), the RSD of the D_b values calculated from sub-samples containing the same number of D_e values is generally <5 % for sub-samples containing 50 D_e values. This level of 50 D_e values is consistent with the sub-sample size needed for 100 % of the sub-samples to be considered statistically non-normal (Section 6.4.2) and this is recommended as the minimum sample size.

6.4.4 Which method to use for D_b analysis?

The method of including the lowest 5 % of D_e values as described by Olley *et al.* (1998) may be problematic when the extent of heterogeneous bleaching within a set of samples is not consistent. In addition, if a sample is well bleached, such a method cannot be used for D_b calculation. As mentioned previously, the methods based on ranking data from the lowest D_e values have problems in deriving

suitable D_b values where low outliers are present in the datasets. For selecting the most appropriate method for obtaining D_b values, it should ideally: 1) take into account the errors on D_e values; 2) be able to cope with outlying low D_e values; and 3) be applicable to both well-bleached and heterogeneously-bleached sediments.

In this study, the two procedures deemed most applicable are the minimum age and finite mixture models. Both methods should be equally suitable for well-bleached and heterogeneously-bleached samples. In the following section, the minimum age model and finite mixture model are used to derive D_b from samples which would be expected to be heterogeneously bleached owing to their fluvial deposition. The finite mixture model can be reduced to the central age model by fitting a single component to the dataset.

6.5 INVESTIGATING THE REPRODUCIBILITY OF D_E DISTRIBUTIONS

Section 6.4.3 demonstrated that for sample 70KLA2, at least 50 D_e values were needed to obtain a D_e distribution that yielded reproducible values of D_b. A further test of reproducibility can be undertaken by looking at D_e distributions from samples taken from the same depositional context. The reproducibility of distributions can be looked at in two ways: 1) similarity in the shape of the distributions; and 2) agreement in the ages derived from samples that would be expected to give consistent results. In this section, the samples investigated were taken from locations specifically selected to enable direct comparison of the results. The reproducibility of the Klip River samples was investigated at three spatial scales:

a) Replicates of samples: for five samples, two discrete datasets (termed A and B), each consisting of at least 50 D_e values, have been obtained.

b) Samples collected 0.3 m apart: samples 75KL0308 and 75KL0309 were collected from within a palaeochannel reach at the same depth in auger holes a distance of 0.3 m apart.

c) Samples from the same palaeochannel reach: from some of the palaeochannel reaches (Fig. 2.15), multiple samples of the uppermost bedload sand were taken

at different locations within the same reach.

For these samples, the D_b was calculated using both the minimum age model (MAM) and finite mixture model (FMM). The number of components in the FMM was increased for each sample until the best fit was found based on the BIC figure. The lowest dose population containing >10 % of the D_e values was selected to represent the well-bleached part of the distribution and used to obtain D_b. The 10 % cut-off was selected so that populations based on one or two D_e values only, were not used for derivation of the sample D_b. The components fitted had σ_{OD} = 10 %; this value was derived from small aliquot analysis of a well-bleached Australian dune sand (Section 6.3.3). To make the FMM and MAM analyses comparable, a 10 % overdispersion value was also added in quadrature to the D_e dataset prior to analysis using the MAM.

6.5.1 Results

6.5.1.1 Replicates of samples

The smallest scale test for the reproducibility of the D_e distributions and D_b values was made by obtaining two separate datasets (termed A and B) of D_e values for five samples. The datasets were constructed by measuring a large number of aliquots for each sample, ranking the D_e values in order of measurement, then splitting the dataset in half. The five samples analysed were collected from different reaches of palaeochannels and had sample codes 70KLA1-70KLA4 and 70KLA6 (locations shown in Fig. 2.15).

The replicate datasets of the five samples are shown as radial plots in Figure 6.29, and illustrate that for each sample the range of D_e values and extent of scatter is similar between the two datasets. Table 6.3 details the σ_{OD} and D_b values calculated using both the MAM and FMM for each dataset; the parameters associated with the D_b value obtained from the FMM are also included. In every case, σ_{OD} is similar for the two replicate datasets, indicating comparable spread in the data. Every sample demonstrates heterogeneous bleaching, with σ_{OD} generally around 40 %, but for sample 70KLA2 is it significantly greater at 91-101 %. The central values of the components fitted to each dataset using the finite

Dataset A

Dataset B

KLA1

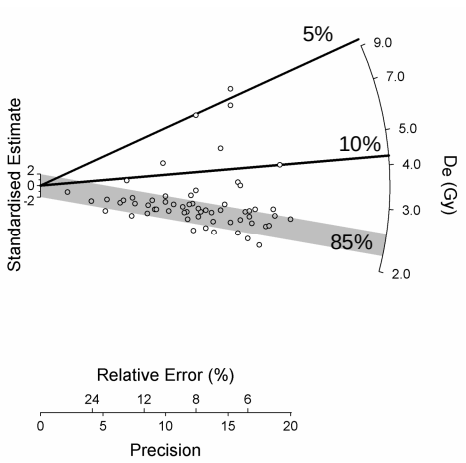

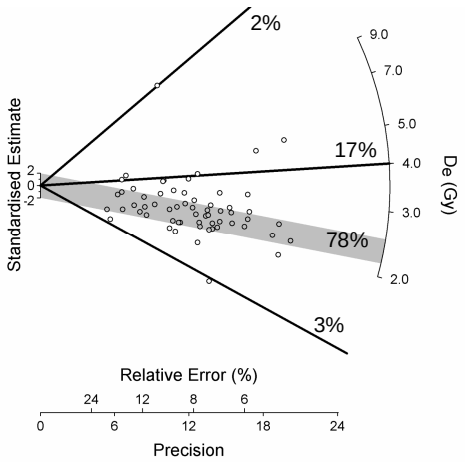

KLA2

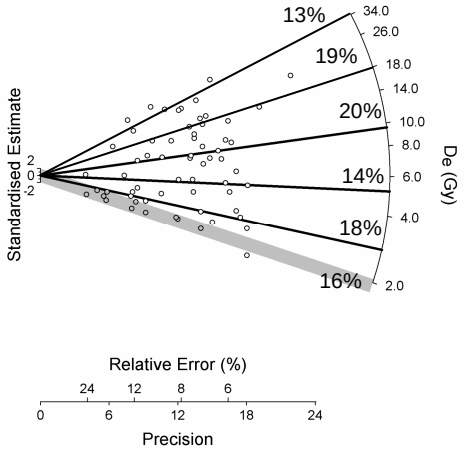

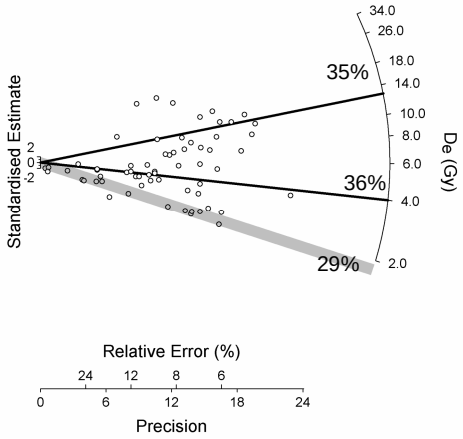

KLA3

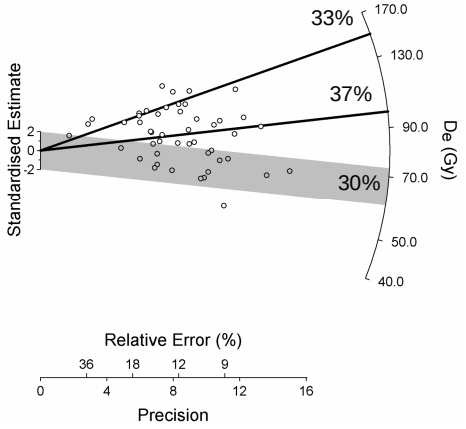

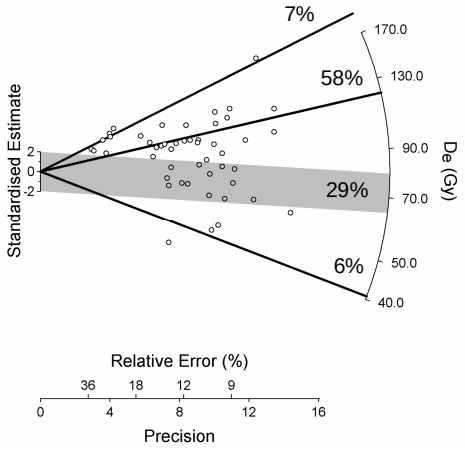

(Figure 6.29: details overleaf)

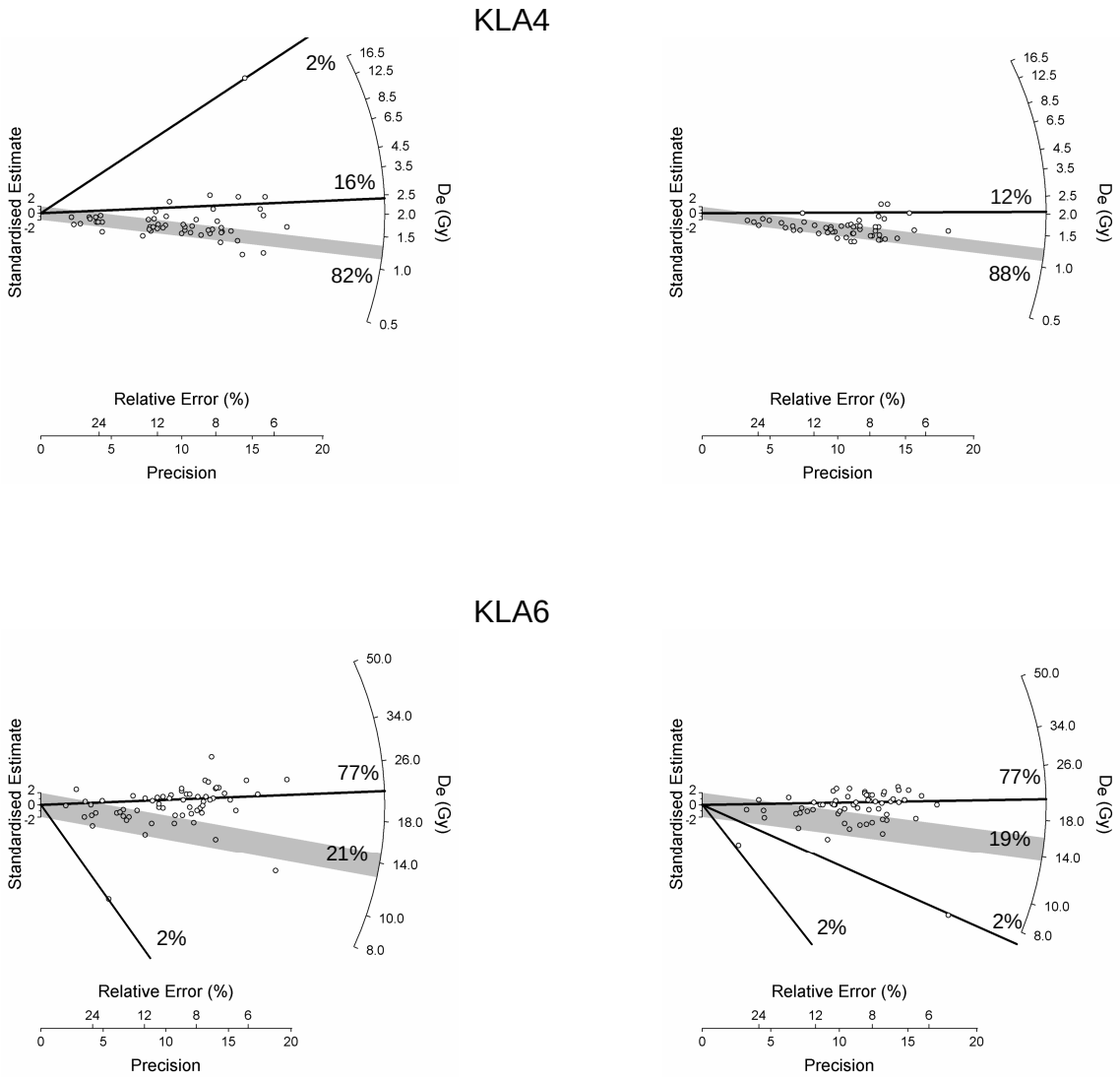

Figure 6.29: Radial plots of replicate datasets for samples 70KLA1-4, 6. The grey shaded bands show the D_e values within 2σ of the D_b values calculated using the finite mixture model, and the percentage of the D_e dataset that value is based on is indicated. The solid straight lines indicate the central value of the other populations found using the finite mixture model, and the percentage of the D_e dataset the value is based on is also given.

mixture model, and the percentage of D_e values associated with each component, are shown on Figure 6.30; the D_e values consistent within 2 sigma errors of the component selected for derivation of the D_b value are shown in the shaded band. The cause of the high number of components fitted to dataset 70KLA2A can be seen in Figure 6.29, where a number of precisely known, relatively high D_e values have discrete components associated with them.

For all the samples, the D_b values calculated using the MAM and FMM are consistent within two sigma errors for datasets A and B. In every instance, the MAM D_b is lower than that calculated by the FMM, owing to the manner in which the models are fitted. This difference in fitting procedures also leads to greater errors associated with the D_b derived using the minimum age model.

The results confirm that the number of D_e values obtained is adequate to obtain a reproducible estimate of D_b, even for samples with very high overdispersion factors indicative of severe heterogeneous bleaching.

Table 6.3: Results for replicate datasets of samples. Showing the number of D_e values in the dataset (n); the overdispersion parameter (σ_{OD}); the D_b value calculated using the minimum age model; the D_b value calculated using the finite mixture model; the number of components fitted (k); and the proportion of the D_e dataset that D_b is based on.

				Minimum age model	Finite mixture model		
Sample		n	σ_{OD} (%)	D_b (Gy)	D_b (Gy)	k	Proportion (%)
70KLA1	A	61	40	1.83 ± 0.09	2.39 ± 0.03	3	85 ± 5
	B	61	35	1.71 ± 0.09	2.35 ± 0.03	4	78 ± 6
70KLA2	A	63	91	1.64 ± 0.13	1.94 ± 0.07	6	16 ± 5
	B	64	101	1.37 ± 0.12	1.78 ± 0.04	3	29 ± 6
70KLA3	A	50	44	62.7 ± 4.9	66.2 ± 2.0	3	30 ± 8
	B	50	36	56.1 ± 4.4	71.7 ± 2.1	4	29 ± 7
70KLA4	A	55	30	0.84 ± 0.06	1.23 ± 0.02	3	82 ± 5
	B	56	59	0.93 ± 0.05	1.17 ± 0.02	2	88 ± 5
70KLA6	A	63	22	12.0 ± 1.0	13.9 ± 0.5	3	21 ± 7
	B	63	39	13.7 ± 0.8	14.8 ± 0.5	4	19 ± 7

6.5.1.2 Samples 0.3 m apart

A medium scale test of the reproducibility of D_e distributions and D_b values was made by collecting two samples from a very short distance apart. Samples 75KL0308 and 75KL0309 were taken from palaeochannel reach B (locations shown on Fig. 2.15) from auger holes ~0.3 m apart at exactly the same depth (0.9 m). These samples should yield similar dose distributions and ages as the samples probably would have been transported and deposited at the same time under very similar conditions.

The radial plots for samples 75KL0308 and 75KL0309 are shown in Figure 6.30 and visual inspection indicates that there is a similar amount of scatter. This is confirmed by σ_{OD} values 30 % and 29 %, respectively (Table 6.4), suggesting that they were bleached to a similar extent during transport prior to burial. Although these samples were collected from very near to one another, the environmental dose-rate of the samples varies, and thus comparison of the burial ages, as opposed to the D_b values, is necessary. The D_b values and ages calculated using both models can be found in Table 6.4, and show that the ages calculated using

a) KL0308 b) KL0309

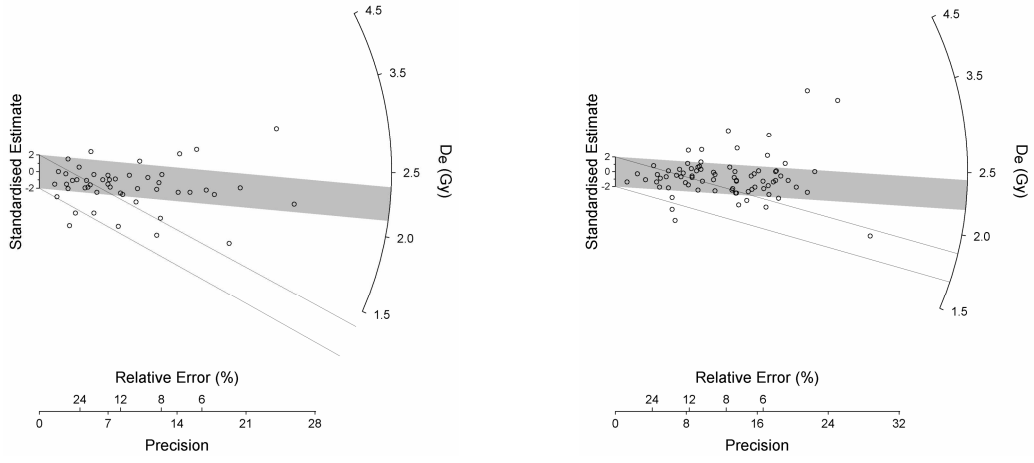

Figure 6.30: Radial plots for samples 75KL0308 and 75KL0309. The shaded and outlined bands show those D_e values that are consistent with the D_b derived using the finite mixture model and minimum age model, within two sigma errors, respectively.

the MAM are not consistent within two sigma errors. This model is strongly influenced by a few, imprecise D_e values for sample 75KL0308, leading to this disparity in the results. By contrast, the D_b values derived using the FMM lead to ages that are consistent within errors.

The results again confirm that 50 D_e values are adequate to obtain reproducible distributions on a small spatial scale, but they suggest that the MAM is unable to derive an appropriate estimate of D_b if a few scattered and imprecise D_e values are present in the dataset. By comparison, the consistent results obtained with the FMM demonstrate that this method is able to derive reproducible burial ages for the two samples investigated.

6.5.1.3 Samples from the same palaeochannel reach

The largest scale test of the reproducibility of OSL dating of palaeochannel deposits was undertaken on samples of the uppermost bedload sand collected from palaeochannel reaches at distances up to ~3 km apart. As a palaeochannel is probably abandoned over a time period of decades to centuries, one would only expect the samples to provide broadly similar values for the age of abandonment. Results for the replicate samples from the different palaeochannel reaches are grouped together in Table 6.4.

The samples collected for Reach B were spread over ~1 km of channel. As expected, burial ages derived using the MAM are consistently younger than those calculated using the FMM. The ages for the four samples are not consistent within two sigma errors when the MAM is used, but the ages calculated using the FMM are consistent within errors.

The samples taken from an ~1.5 km section of Reach C show that 70KLA2 has a burial age of at least 8 ka younger than the other samples for this reach. Samples 75KL0330 and 75KL0331 have results consistent within errors when the FMM is used, whereas the results for the MAM are not consistent. Sample 70KLA2 was taken from a location very close to Reaches B and E (see Fig. 2.15); both these reaches were active recently (within the last ~1.1 ka), so this sample may represent a flood deposit originating from these younger channels. In addition,

Table 6.4: Results for the replicate palaeochannel samples from the Klip River. Showing the overdispersion parameter (σ_{OD}); the environmental dose-rate; the burial dose (D_b) and age calculated using the minimum age model; the burial dose (D_b), number of components fitted to the D_e dataset (k), proportion of D_e values in the population used for D_b calculation, and the age calculated using the finite mixture model (with the 1 sigma error).

				Minimum age model (MAM)		Finite mixture model (FMM)			
Reach	Sample	σ_{OD} (%)	Dose-rate (Gy/ka)	D_b (Gy)	**Age (ka)**	D_b (Gy)	k	Proportion (%)	**Age (ka)**
B	70KLA1	37	1.84 ± 0.10	1.77 ± 0.07	**0.96 ± 0.06**	2.38 ± 0.02	5	83 ± 4	**1.29 ± 0.07**
	75KL0308	30	2.10 ± 0.12	1.24 ± 0.10	**0.59 ± 0.06**	2.24 ± 0.04	4	72 ± 8	**1.07 ± 0.06**
	75KL0309	29	1.80 ± 0.10	1.73 ± 0.08	**0.96 ± 0.07**	2.30 ± 0.03	4	87 ± 4	**1.28 ± 0.07**
	75KL0329	43	2.13 ± 0.12	1.80 ± 0.11	**0.85 ± 0.07**	2.28 ± 0.04	4	57 ± 8	**1.07 ± 0.06**
C	70KLA2	97	1.82 ± 0.10	1.50 ± 0.09	**0.82 ± 0.07**	2.56 ± 0.02	3	47 ± 4	**1.41 ± 0.08**
	75KL0330	20	1.94 ± 0.10	31.3 ± 1.3	**16.1 ± 1.1**	31.5 ± 0.9	2	26 ± 8	**16.2 ± 1.0**
	75KL0331	25	2.10 ± 0.12	18.6 ± 1.4	**8.8 ± 0.8**	31.1 ± 0.4	4	89 ± 4	**14.8 ± 0.8**
E	70KLA4	48	2.11 ± 0.12	0.87 ± 0.04	**0.41 ± 0.03**	1.16 ± 0.01	4	76 ± 6	**0.55 ± 0.03**
	75KL0332	26	2.13 ± 0.12	1.43 ± 0.06	**0.67 ± 0.05**	1.79 ± 0.02	3	86 ± 6	**0.84 ± 0.05**
	75KL0333	45	2.15 ± 0.12	1.30 ± 0.07	**0.60 ± 0.05**	1.61 ± 0.02	3	59 ± 6	**0.75 ± 0.04**
	75KL0339	33	1.91 ± 0.10	0.81 ± 0.05	**0.43 ± 0.04**	1.10 ± 0.02	4	84 ± 6	**0.57 ± 0.03**
	75KL0342	58	1.89 ± 0.07	0.94 ± 0.07	**0.50 ± 0.04**	1.26 ± 0.03	4	47 ± 7	**0.66 ± 0.03**
G	70KLA6	30	2.06 ± 0.12	12.9 ± 0.6	**6.28 ± 0.47**	14.4 ± 0.3	4	20 ± 5	**6.99 ± 0.43**
	75KL0336	26	2.23 ± 0.13	20.3 ± 1.0	**9.1 ± 0.7**	24.0 ± 0.4	2	68 ± 8	**10.8 ± 0.7**
	75KL0337	20	2.35 ± 0.14	30.1 ± 1.3	**12.8 ± 0.9**	25.0 ± 1.0	2	12 ± 4	**10.7 ± 0.7**

this sample is very poorly bleached (σ_{OD} = 97 %) in comparison to the other samples from the reach, suggesting that it may have been derived from a different depositional event. Although both models give a greater burial age for sample 75KL0330 than 75KL0331, the difference in the ages may be occur because of gradual abandonment and infilling which slowly progressed from downstream (location of sample 75KL0330) to further upstream.

Five samples were taken from Reach E over a distance of ~3 km. The burial ages calculated using both models are not consistent within two sigma errors and show similar degrees of scatter. The difference in the ages also may be explained by a pattern of abandonment that started at the downstream end and gradually progressed upstream. Despite the difference in the ages, over the entire 3 km reach they vary by less than 300 years.

Of the samples taken from Reach G, 70KLA6 was located very close to the modern channel, with the other two samples taken ~0.5 km downstream. Using the MAM, all the burial ages are widely scattered over a range of ~6 ka. The results for the samples obtained using the FMM are more consistent, with samples 75KL0336 and 75KL0337 having very similar burial ages. The sample taken close to the modern channel (70KLA6) has an anomalously low burial age, so this may represent a younger flood deposit derived from the nearby modern channel.

Overall, the ages calculated using the FMM are more reproducible along a palaeochannel reach than those calculated using the MAM. This is particularly demonstrated by the results for channel reaches C and G. In Reach C, samples 75KL0330 and 75KL0331 have consistent ages calculated using the FMM, with 70KLA2 being a clear outlier, whereas the ages derived for the former two samples using the MAM vary by a factor of 2. In Reach G, the ages calculated using the FMM for samples 75KL0336 and 75KL0337 are very similar, with 70KLA6 clearly being younger. In comparison, the results from the MAM for the three samples are all inconsistent, with no indication of which sample age is the most appropriate for estimating the timing of abandonment of this palaeochannel.

6.5.1.4 Conclusions from the ages calculated

The results from the samples collected from the same palaeochannel reach (Section 6.5.1.3), in addition to the results from samples 75KL0308 and 75KL0309 (Section 6.5.1.2), indicate that the MAM has problems in obtaining reproducible estimates of burial ages for replicate samples. The FMM derives more reproducible burial ages, suggesting that this method is more appropriate for derivation of D_b values from these fluvial samples.

6.5.1.5 Overdispersion values

Additionally, the overdispersion parameter (σ_{OD}) was investigated by depositional environment for all the Klip River samples to see if any distinct differences were evident. The overdispersion values for the samples, grouped by their depositional environment, are shown in Table 6.5. The oxbow lake and scroll-bar samples are shown next to the reach of river with which they are associated. No clear differences are detectable in the overdispersion values between the depositional environments, but the mean value for the channel fills deposits (σ_{OD} = 43 %) is greater than that for the oxbows and scroll-bars (33 % and 31 %, respectively). Overall, the values are consistent with what one might expect; Olley *et al.* (2004b) calculated σ_{OD} values between 1 % and 85 %, with a mean of 44 %, for fluvial samples from a range of depositional environments within Australia. The scroll-bar samples might be expected to have the lowest overdispersion values as the sediment forming the scroll ridges is thought to derive from point bars which may be exposed to sunlight for long durations during low river flows. Overall, the majority of the samples from the channel fill and oxbow lake deposits have σ_{OD} >20 % indicating that heterogeneous bleaching is prevalent in sediments from the Klip River.

Table 6.5: Overdispersion values (σ_{OD}) for all the samples from the Klip River, grouped by depositional environment.

Channel reach	Channel fill		Oxbow lakes		Scroll bar samples	
	Sample	σ_{OD} (%)	Sample	σ_{OD} (%)	Sample	σ_{OD} (%)
A	75KL0310	19				
	75KL0311	21				
B	70KLA1	37	75KL0315	55		
	75KL0308	30	75KL0328	26		
	75KL0309	29				
	75KL0329	43				
C	70KLA2	97				
	75KL0330	20				
	75KL0331	25				
D	70KLA3	40				
E	70KLA4	48	75KL0334	21		
	75KL0332	26	75KL0335	28		
	75KL0333	45				
	75KL0339	33				
	75KL0342	58				
F	70KLA5	63				
G	70KLA6	30				
	75KL0336	26				
	75KL0337	20				
	75KL0338	19				
MODERN	75KL0316	94			75KL0317	44
					75KL0318	9
					75KL0319	12
					75KL0320	26
					75KL0321	17
					92KL0401	16
	75KL0326	83			75KL0322	11
	75KL0327	122			75KL0323	24
					75KL0324	66
					75KL0325	83

6.6 COMPARISON WITH ^{14}C RESULTS

Samples for radiocarbon analysis were taken from three different OSL sample sites: 75KL0308, 75KL0310; and 75KL0342 (Fig. 2.15). The locations chosen were in different palaeochannel reaches and were selected to cover a range of ages. The purpose of these samples was primarily to obtain independent age control, for without this the accuracy of the OSL dates cannot be established. As covered in Section 2.5.2, the samples for ^{14}C analyses were taken from the organic-rich mud directly overlying the sediment collected for OSL dating; the details of the ^{14}C analysis are in Appendix F. Table 6.6 contains the results from both the OSL and ^{14}C analyses, and the results are also shown graphically in Figure 6.31.

Using the MAM for analysis, only one sample (75KL0310) gives an OSL age greater than the ^{14}C result. Sample 75KL0308 has a burial age considerably younger than the ^{14}C age and 75KL0342 has an OSL age just consistent with the younger end of the one sigma error range for the ^{14}C analysis. Using the FMM, both 75KL0310 and 75KL0342 have ages in the appropriate stratigraphic order with the corresponding ^{14}C age, and the burial age calculated for sample 75KL0308 is consistent with the ^{14}C result. These results suggest that the MAM tends to underestimate the burial age of a sample; this may be because this model can be biased towards a low D_b value if one or two low D_e values are present in the dataset (Section 6.5.1).

Table 6.6: Information on the associated OSL and ^{14}C ages.

OSL sample	Minimum age model age (ka)	Finite mixture model age (ka)	**Associated ^{14}C sample**	Age range (cal ka)*
75KL0308	0.59 ± 0.06	1.07 ± 0.06	**Beta – 197148**	1.01 – 1.11
75KL0310	4.27 ± 0.29	4.60 ± 0.26	**Beta – 197149**	3.90 – 4.04
75KL0342	0.35 ± 0.03	0.66 ± 0.03	**Beta – 197150**	0.35 – 0.53

* Age range given as one sigma error range to enable direct comparison with OSL ages.

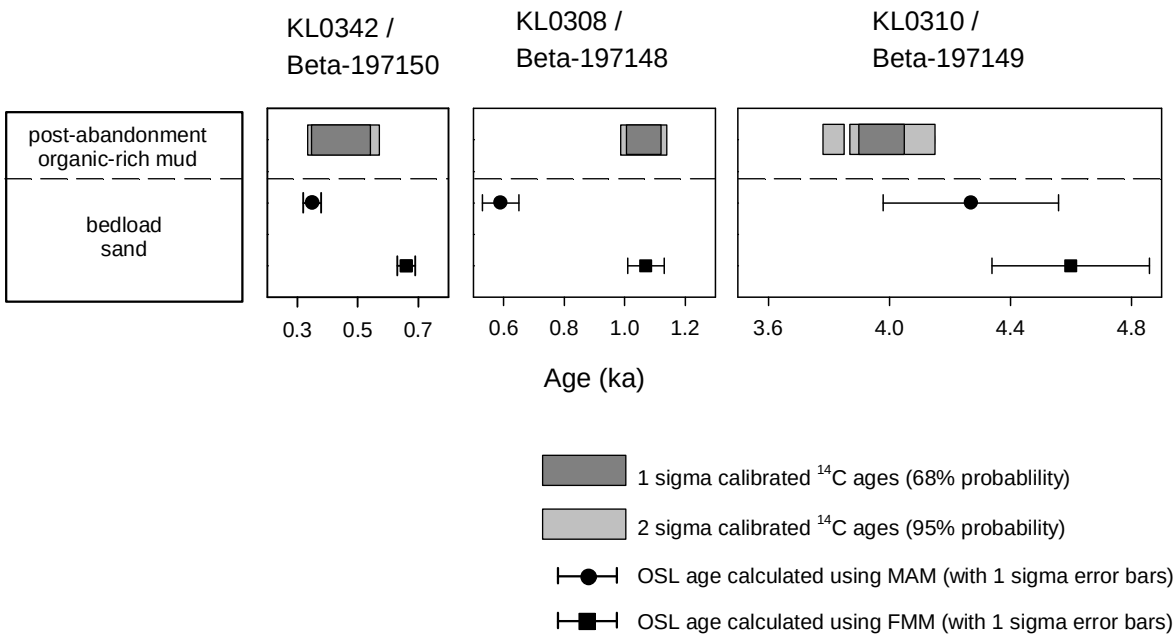

Figure 6.31: Schematic comparison between the OSL ages calculated using the minimum age model (MAM) and finite mixture model (FMM), and the radiocarbon ages of the overlying sediment.

6.7 CONCLUSIONS

Detecting partial bleaching in the sediments from the Klip River using signal analysis methods such as $D_e(t)$ plots and assessing the Z values of aliquots, appears to be problematic for samples from the Klip River. In part, this may arise because of the relatively low proportion of the medium component in the quartz OSL signal, and the thermal instability of this component. The experiments proposed by Bailey (2003a) to assess the applicability of $D_e(t)$ plots appeared to demonstrate their suitability to the Klip River sample studied, but the method did not appear to be sensitive to partial bleaches for relatively short durations, even when the D_e value was considerably reduced. Overall, signal analysis methods for detecting partial bleaching of grains do not appear suitable for the samples studied in this thesis.

The overdispersion parameter was suggested as the most appropriate method to detect and quantify heterogeneous bleaching in a sediment. A σ_{OD} value of 10 %

was calculated from small aliquot analysis of a well-bleached sample, suggesting that values greater than this are indicative of heterogeneous bleaching. The majority of the samples from the Klip River were found to be heterogeneously bleached, with values of overdispersion up to 101 %. Various methods proposed in the literature for obtaining an appropriate D_b value from a heterogeneously-bleached sample were investigated by using D_e values from sample 70KLA2. The results indicated that most methods were able to calculate reproducible and stable values of D_b. The majority of the methods outlined are applicable only to heterogeneously-bleached samples. Further investigation into the MAM and FMM was undertaken because these methods should also be suitable for well-bleached samples, as well as those that have been heterogeneously bleached. Analysis of the reproducibility of the D_b values derived indicated that ~50 D_e values are necessary to obtain a reproducible D_e distribution.

Application of the MAM and FMM demonstrated that the latter model is more appropriate for analysis of the Klip River samples. The ages calculated using the FMM for samples from the same reach of palaeochannel were more reproducible than the ages calculated from the MAM. Furthermore, when compared with ^{14}C ages from the overlying sediment, the ages calculated using the FMM were in the correct stratigraphic order, in contrast to those calculated using the MAM. The MAM tends to calculate a D_b value that is too low, because it is strongly influenced by low dose outliers which occur in the dataset. At present, no formal rejection criteria exists for these types of D_e values. Because the FMM allows one to reject these low D_e values on the basis that they are not consistent with the main population of well-bleached grains, it therefore performs better. On the basis of the results discussed in Sections 6.5 and 6.6, the FMM was used to calculate D_b value for the samples from the Klip River and Schoonspruit. Knowledge of the D_b value, and the environmental dose-rate for each sample, enables the burial age to be calculated, and these are presented in the next chapter.

CHAPTER 7: CALCULATION OF AGES AND INTERPRETATION OF RESULTS

7.1 INTRODUCTION

This chapter discusses the OSL ages for samples from various depositional environments of the Klip River and Schoonspruit, focussing in particular on determination of the rates of key processes of channel change outlined in Chapter 1 (lateral migration, meander cutoff, avulsion, and incision). From knowledge of the ages of deposits, and the rates of these channel change processes, an assessment is made as to whether changes in these fluvial systems are autogenically controlled or predominantly influenced by allogenic factors, such as climatic change.

7.2 LATERAL MIGRATION AND MEANDER CUTOFF

7.2.1 Waaihoek site

The geometry of the Waaihoek meander indicates that lateral migration at this site occurs by extension (expansion) of the meander bend (Fig 7.1) (Knighton, 1998; Bridge, 2003). At this location, the meander loop is part of the active river so in addition to the scroll-bar samples on the inner bank, samples were taken from the modern point bar and left-hand river bank (Fig 7.1). Radial plots and histograms showing the D_e distributions for each sample are shown in Figure 7.2; the samples are ordered by age from youngest (modern samples 75KL0326 and 75KL0327) to oldest (scroll-bar sample 75KL0322).

Heterogeneous bleaching is clearly evident in three of the samples (75KL0327; 75KL0325; 75KL0324) both from the shapes of the D_e distributions (Fig. 7.2) and in the overdispersion parameters (Table 7.1). For these samples, the D_e distributions in the radial plots show a band of data points with a diffuse cloud of scattered data points above this band, and in the histograms a sharp initial rise and a long tail extending to high D_e values. Sample 75KL0326 also has an overdispersion parameter of 76 % indicating heterogeneous bleaching; however the radial plot shows that only three data points fall outside the main population

of D_e values. This suggests that this point bar sample is in fact relatively well bleached. Although the absolute spread in the D_e datasets for the scroll-bar samples (75KL0322-75KL0325) is comparable at ~4 Gy (Fig. 7.2b), the two older samples (75KL0322 and 75KL0323) have distributions where the majority of the D_e values are consistent within 2 sigma errors (Fig 7.2a), and that appear Gaussian in shape in the histograms (Fig 7.2b). These D_e distributions suggest that the two samples were well bleached prior to deposition, and that the spread in the data is as a result of the poor precision of the D_e values.

The D_b values obtained by the finite mixture model are shown on the radial plots by the dashed line, and the grey shaded band shows those D_e values that are consistent with it within two sigma errors (Fig. 7.2a). The results show that the proportion of the D_e dataset that forms the population that D_b is based on,

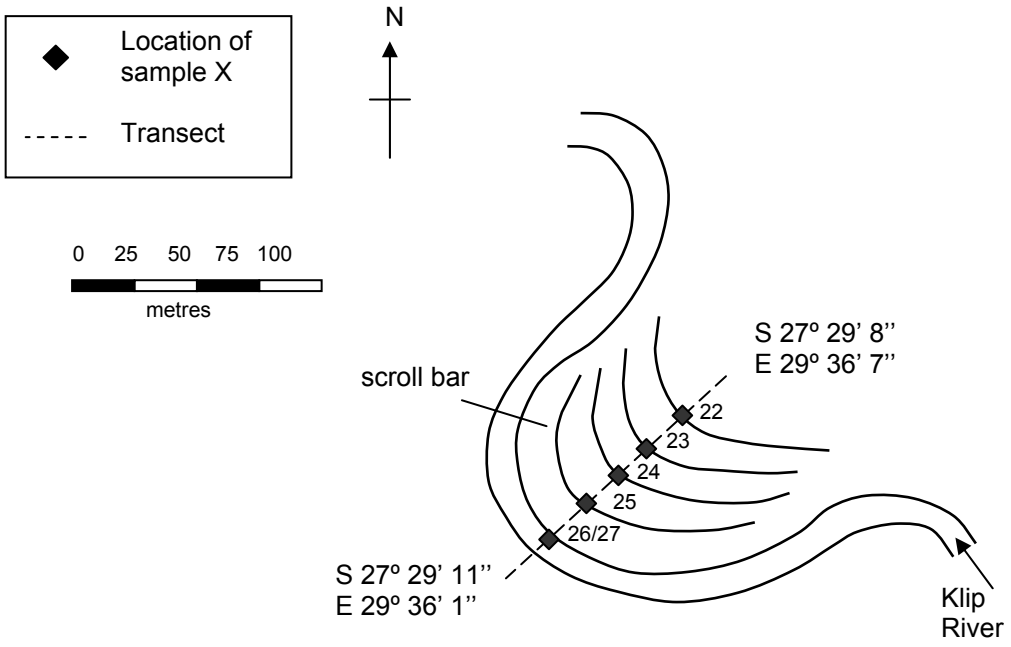

Figure 7.1: Schematic of the meander and associated scroll bars at the Waaihoek The numbers indicate the samples for OSL dating (prefixed by 75KL03-); sample 75KL0322 is from the youngest scroll bar, and 75KL0326 and 75KL0327 are from the modern point bar and river bank, respectively.

a)

75KL0326

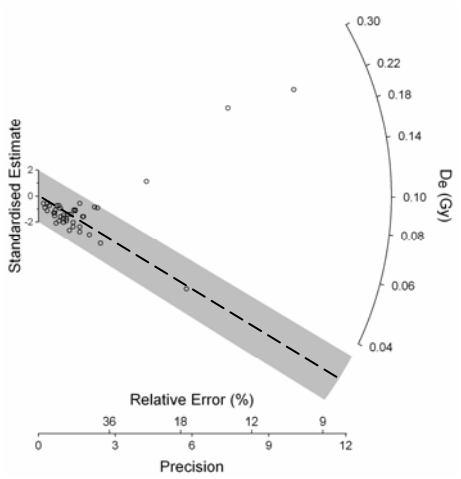

75KL0327

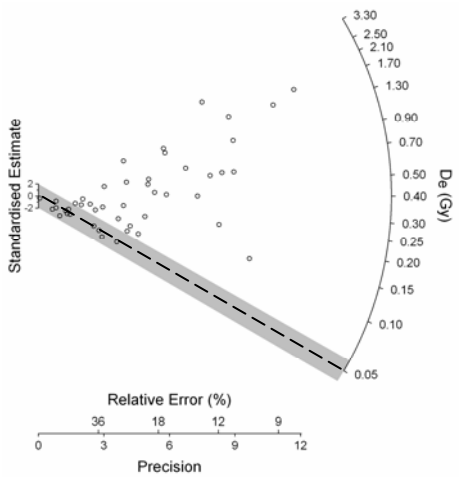

75KL0325

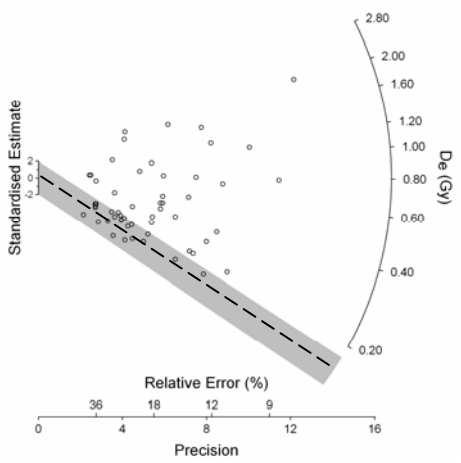

75KL0324

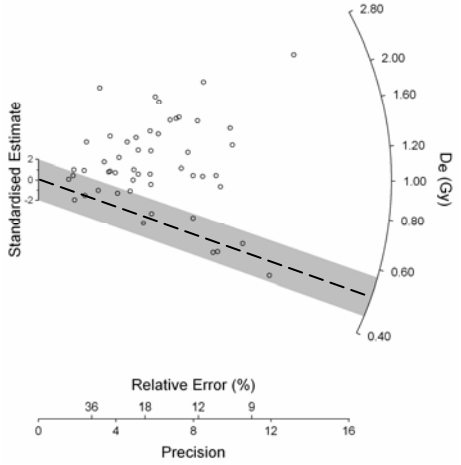

75KL0323

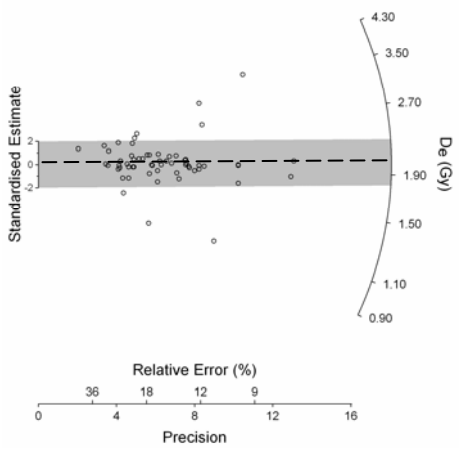

75KL0322

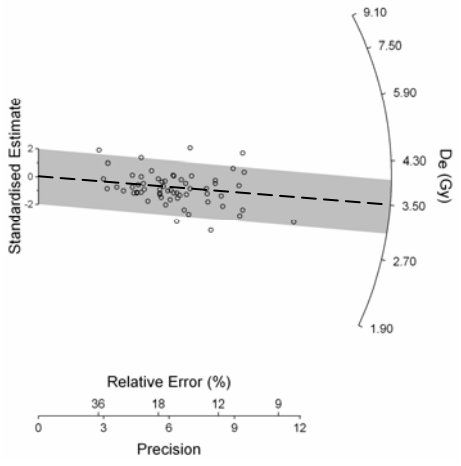

b)

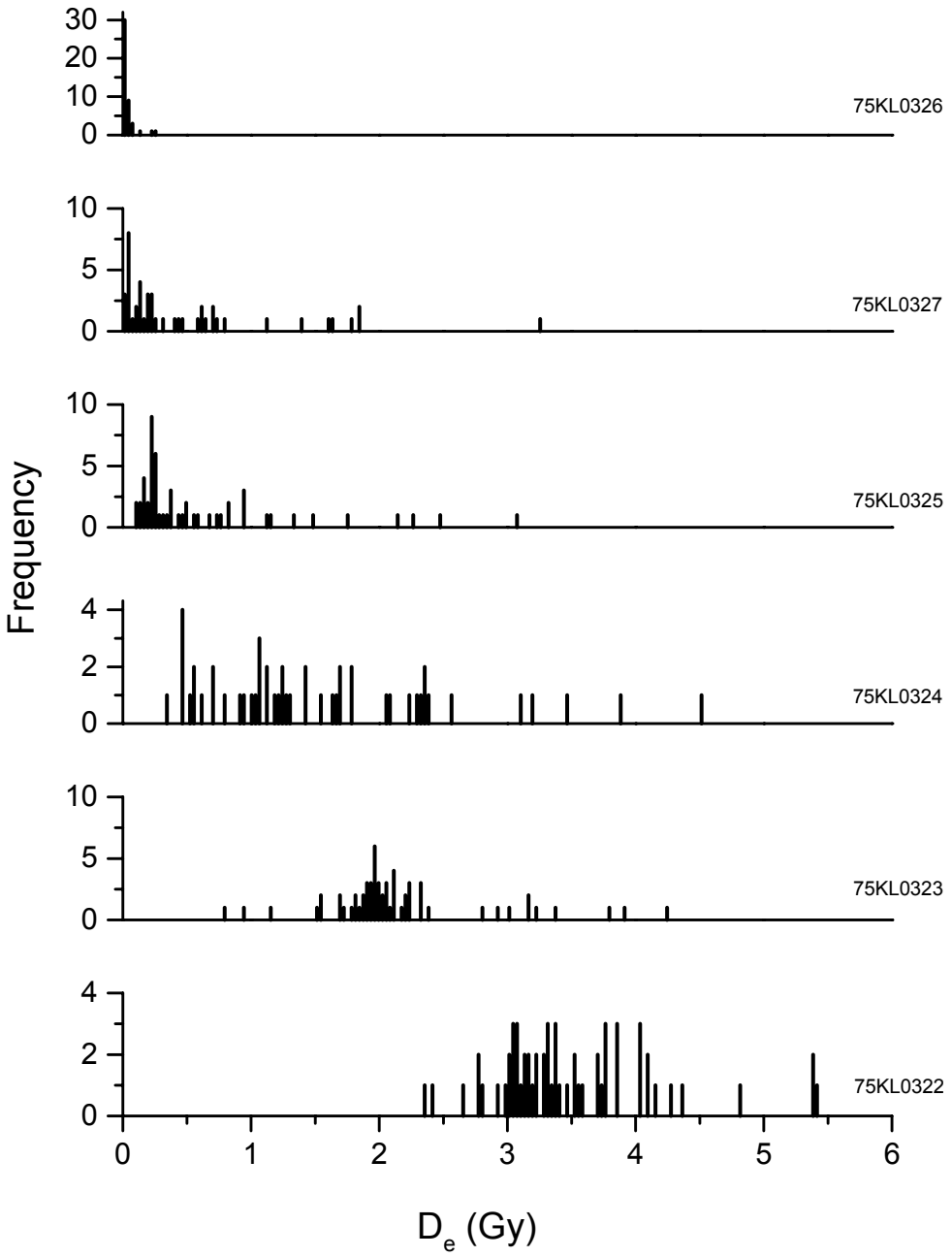

Figure 7.2: a) Radial plots of the D_e values for the six samples from the Waaihoek site. The D_b value calculated is indicated by the dashed line, and the grey shaded band shows those D_e values that are consistent with it within 2σ. b) Histograms showing the frequency of D_e values for the Waaihoek site samples. Note the different y-axis scales.

Table 7.1: Results from OSL analysis of samples from the Klip River and the Schoonspruit. Table headers include sample code; location; sampling environment; number of aliquots (n) in each dataset; overdispersion parameter (σ_{OD}); number of components (k) fitted using the finite mixture model; the proportion of D_e values in the population that the burial dose is based on; the burial dose (D_b) for the sample; the environmental dose-rate; and the burial age of the sample.

Sample	Location	Environment	n	OD (%)	k	Proportion (%)	D_b value (Gy)	Dose-rate (Gy/ka)	Burial age (ka)
Klip River									
70KLA1	Reach B	Palaeochannel	122	37	5	83 ± 4	2.38 ± 0.02	1.84 ± 0.11	1.30 ± 0.08
70KLA2	Reach C	Palaeochannel	127	97	3	47 ± 4	2.56 ± 0.02	1.82 ± 0.11	1.41 ± 0.08
70KLA3	Reach D	Palaeochannel	100	40	4	29 ± 5	69.6 ± 1.6	2.31 ± 0.13	30.2 ± 1.9
70KLA4	Reach E	Palaeochannel	111	48	4	76 ± 6	1.16 ± 0.01	2.11 ± 0.12	0.55 ± 0.03
70KLA5	Reach F	Palaeochannel	65	63	4	17 ± 6	2.09 ± 0.07	1.51 ± 0.08	1.39 ± 0.09
70KLA6	Reach G	Palaeochannel	126	30	4	20 ± 5	14.4 ± 0.3	2.06 ± 0.12	6.99 ± 0.44
75KL0308	Reach B	Palaeochannel	56	30	4	72 ± 8	2.24 ± 0.04	2.10 ± 0.12	1.07 ± 0.06
75KL0309	Reach B	Palaeochannel	78	29	4	87 ± 4	2.30 ± 0.03	1.74 ± 0.10	1.32 ± 0.07
75KL0310	Reach A	Palaeochannel	81	19	3	34 ± 9	9.26 ± 0.19	2.01 ± 0.11	4.60 ± 0.27
75KL0311	Reach A	Palaeochannel	79	21	3	56 ± 14	9.97 ± 0.39	1.65 ± 0.09	6.03 ± 0.41
75KL0315	Reach B	Oxbow	79	55	5	32 ± 6	3.60 ± 0.14	1.96 ± 0.11	1.84 ± 0.13
75KL0316	Kadies Drift	Oxbow	51	94	3	41 ± 9	0.08 ± 0.02	1.32 ± 0.09	0.06 ± 0.02
75KL0317	Kadies Drift	Scroll bar	50	44	2	45 ± 8	0.39 ± 0.02	2.08 ± 0.15	0.19 ± 0.02
75KL0318	Kadies Drift	Scroll bar	56	9	1	100 ± 0	0.92 ± 0.04	2.63 ± 0.19	0.35 ± 0.03
75KL0319	Kadies Drift	Scroll bar	53	12	2	98 ± 2	1.12 ± 0.05	2.30 ± 0.17	0.49 ± 0.04
75KL0320	Kadies Drift	Scroll bar	56	26	2	92 ± 5	1.13 ± 0.05	2.57 ± 0.19	0.44 ± 0.04
75KL0321	Kadies Drift	Scroll bar	58	17	2	98 ± 2	2.88 ± 0.11	2.74 ± 0.20	1.05 ± 0.09
75KL0322	Waaihoek	Scroll bar	61	10	1	100 ± 0	3.48 ± 0.09	2.49 ± 0.17	1.40 ± 0.10
75KL0323	Waaihoek	Scroll bar	60	24	3	89 ± 5	2.02 ± 0.05	3.03 ± 0.24	0.67 ± 0.06
75KL0324	Waaihoek	Scroll bar	53	66	4	20 ± 6	0.51 ± 0.02	2.76 ± 0.22	0.18 ± 0.02
75KL0325	Waaihoek	Scroll bar	55	83	4	47 ± 8	0.15 ± 0.02	2.12 ± 0.17	0.07 ± 0.01
75KL0326	Waaihoek	Point bar	50	76	2	92 ± 5	0.03 ± 0.00	1.64 ± 0.11	0.02 ± 0.00
75KL0327	Waaihoek	River Bank	50	122	4	19 ± 8	0.05 ± 0.01	2.40 ± 0.19	0.02 ± 0.00

75KL0328	Reach B	Oxbow	76	26	2	99	±	1	2.86	±	0.04	1.74	±	0.10	1.65 ± 0.10
75KL0329	Reach B	Palaeochannel	56	43	4	57	±	8	2.28	±	0.04	2.13	±	0.12	1.07 ± 0.06
75KL0330	Reach C	Palaeochannel	74	20	2	26	±	8	31.5	±	0.9	1.94	±	0.11	16.2 ± 1.0
75KL0331	Reach C	Palaeochannel	78	25	4	89	±	4	31.1	±	0.4	2.10	±	0.12	14.8 ± 0.8
75KL0332	Reach E	Palaeochannel	77	26	3	86	±	6	1.79	±	0.02	2.13	±	0.12	0.84 ± 0.05
75KL0333	Reach E	Palaeochannel	70	45	3	59	±	6	1.61	±	0.02	2.16	±	0.13	0.75 ± 0.05
75KL0334	Reach E	Oxbow	55	21	3	19	±	2	2.82	±	0.06	1.53	±	0.08	1.84 ± 0.11
75KL0335	Reach E	Oxbow	74	28	3	87	±	6	2.25	±	0.06	1.32	±	0.07	1.70 ± 0.10
75KL0336	Reach G	Palaeochannel	81	26	2	68	±	8	24.0	±	0.4	2.23	±	0.14	10.8 ± 0.7
78KL0337	Reach G	Palaeochannel	80	20	2	12	±	4	25.0	±	1.0	2.34	±	0.14	10.7 ± 0.8
75KL0338	Reach G	Palaeochannel	81	19	4	76	±	8	21.8	±	0.9	1.85	±	0.11	11.8 ± 0.8
75KL0339	Reach E	Palaeochannel	55	33	4	84	±	6	1.10	±	0.02	1.91	±	0.11	0.57 ± 0.03
75KL0340	Reach E/F/G	Oxbow	76	43	4	77	±	8	1.32	±	0.04	2.23	±	0.13	0.59 ± 0.04
75KL0341	Reach F	Oxbow	73	71	4	57	±	6	5.13	±	0.11	2.14	±	0.13	2.40 ± 0.15
75KL0342	Reach E	Palaeochannel	63	58	4	47	±	7	1.26	±	0.03	1.89	±	0.07	0.66 ± 0.03
92KL0401	Kadies Drift	Scroll bar	50	16	2	97	±	4	2.26	±	0.04	2.45	±	0.18	0.92 ± 0.07
Schoonspruit															
91SC0401	Upper floodplain	Oxbow	88	51	4	31	±	6	3.98	±	0.06	2.52	±	0.19	1.58 ± 0.12
91SC0403	Upper floodplain	Overbank	91	56	5	53	±	6	3.40	±	0.11	2.68	±	0.21	1.27 ± 0.11
91SC0404	Upper floodplain	Overbank	90	38	3	84	±	4	3.39	±	0.03	2.65	±	0.21	1.28 ± 0.10
91SC0405	Upper floodplain	Overbank	88	36	3	48	±	7	3.92	±	0.06	2.64	±	0.21	1.48 ± 0.12
91SC0406	Upper floodplain	Overbank	87	121	6	50	±	6	0.36	±	0.02	2.95	±	0.24	0.12 ± 0.01
91SC0407	Inset floodplain	River bank	84	157	6	14	±	5	0.15	±	0.02	2.78	±	0.23	0.05 ± 0.01
91SC0408	Inset floodplain	River bank	86	153	8	10	±	3	0.20	±	0.07	2.35	±	0.18	0.08 ± 0.03
91SC0409	Inset floodplain	River bank	87	94	8	14	±	4	4.65	±	0.17	2.57	±	0.19	1.81 ± 0.15**
91SC0410	Upper floodplain	Oxbow	86	53	5	15	±	4	3.34	±	0.09	2.76	±	0.22	1.21 ± 0.10

* All the samples located in a "Reach" are from the Seekoeivlei Nature Reserve part of the floodplain

** This sample was deemed undateable (see Section 7.4.1)

reflects the extent of heterogeneous bleaching in the sample. For instance, the D_b value for the well bleached samples is based on the majority of the D_e values (e.g. D_b for 75KL0326 is calculated from 92 % of the D_e values), whereas the D_b value for the poorly bleached samples is based on a smaller proportion of the D_e dataset (e.g. D_b for 75KL0327 is calculated from 19 % of the D_e values) (Table 7.1).

The ages calculated from the D_b values for the Waaihoek site are shown in Figure 7.3 along a transect across the scroll-bar sequence. The ages calculated for the samples from the modern point bar and the river bank are 0.02 ± 0.00 ka in both instances. This demonstrates that despite the variation in the extent of heterogeneous bleaching of these samples (Table 7.1; 75KL0326 and 75KL0327), when using the finite mixture model the ages are consistent within errors. The ages calculated for these samples indicate that at deposition, a small residual charge equating to ~20 years may remain in the quartz grains. For the scroll-bar samples, all the ages calculated are in the correct order for the depositional sequence. Overall, the results from the scroll-bar sequence indicate that the meander migrated ~70 m in ~1.4 ka, giving an average lateral migration rate of ~0.05 m/a.

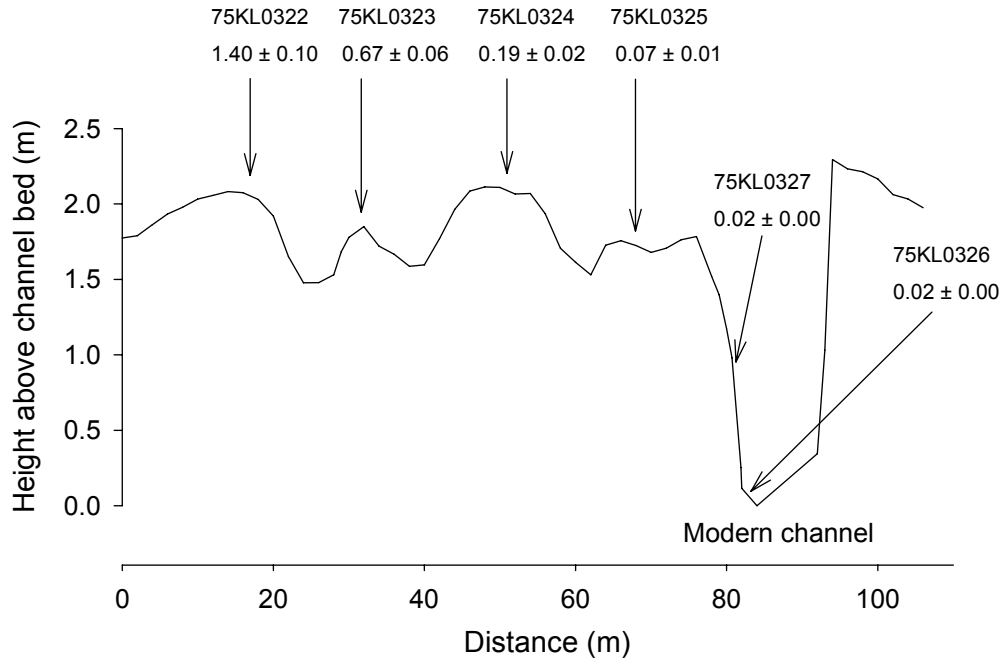

Figure 7.3: Transect (VE = 20) across the Waaiheok scroll-bar sequence (see Fig 7.1 for location). Sample locations and calculated ages (ka before AD 2004) are shown.

7.2.2 Kadies Drift site

The geometry of the Kadies Drift meander indicates that lateral migration involved extension of the bend, eventually resulting in abandonment by neck cutoff (Fig. 7.4) (Knighton, 1998; Bridge, 2003). Following abandonment, the ends of the former meander were plugged by sediment from the currently active channel, thus preventing further bedload deposition around the apex of the bend. Independent age control from aerial photographs indicates that the cutoff occurred between AD 1954 and 1979 (Section 2.6.1). A schematic of the meander bend with the sample locations marked is shown in Figure 7.4; samples numbered 16 – 21 (prefixed 75KL03- for analysis) were collected in 2003, and sample numbered 01 (prefixed 92KL04-) was collected the following year. The D_e dataset for each sample is shown in radial plots and histograms in Figure 7.5; the samples are in order from youngest (75KL0316) to oldest (75KL0321). Both the radial plots and the histograms suggest that only the channel fill sample (75KL0316) was heterogeneously bleached. Sample

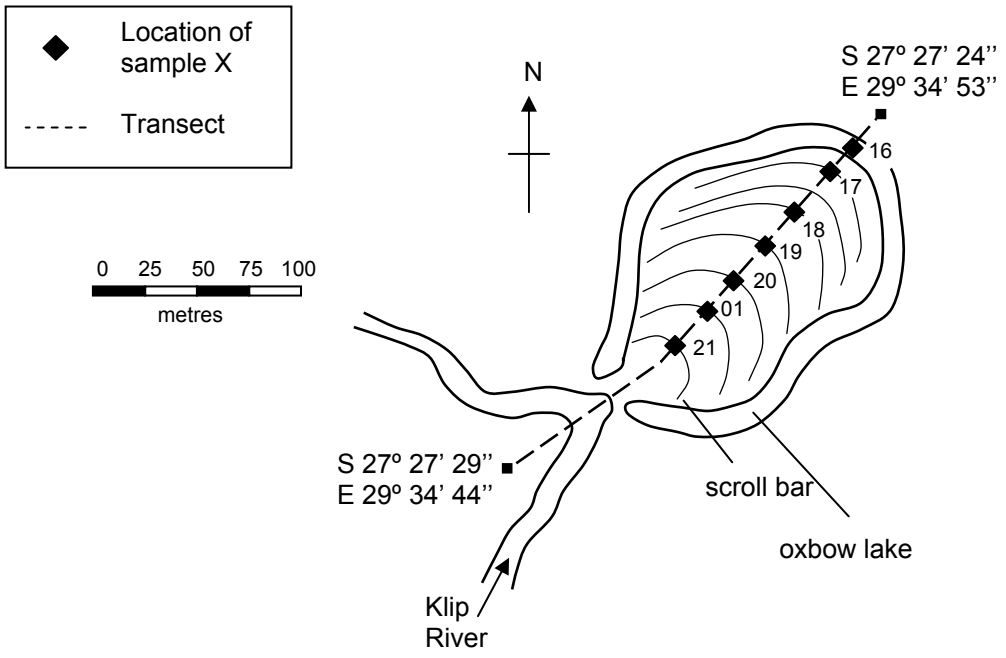

Figure 7.4: Schematic of the meander and associated scroll bars at the Kadies Drift site. The numbers indicate the samples for OSL dating (01 is prefixed by 92KL04-, and 16-21 are prefixed by 75KL03-); sample 75KL0316 is from the channel fill of the oxbow, and 75KL0321 is from the oldest scroll bar.

a)

75KL0316

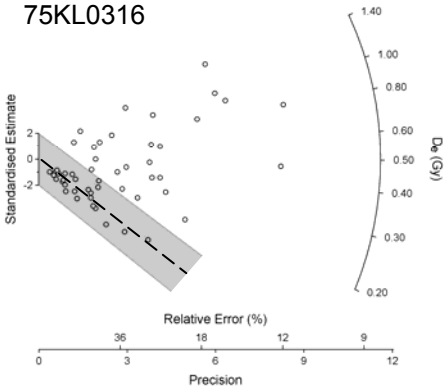

75KL0317

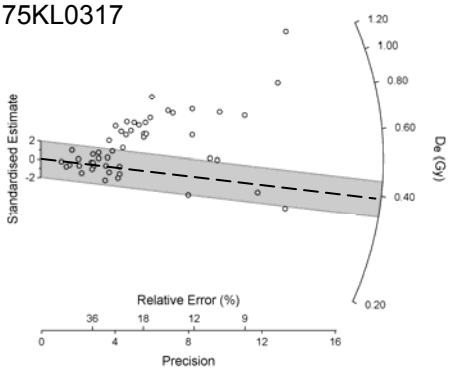

75KL0318

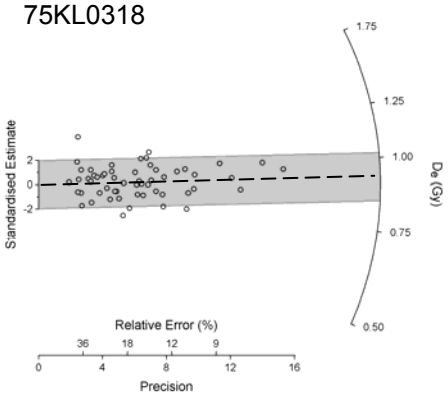

75KL0319

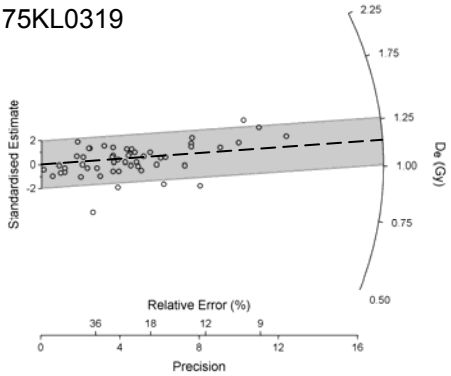

75KL0320

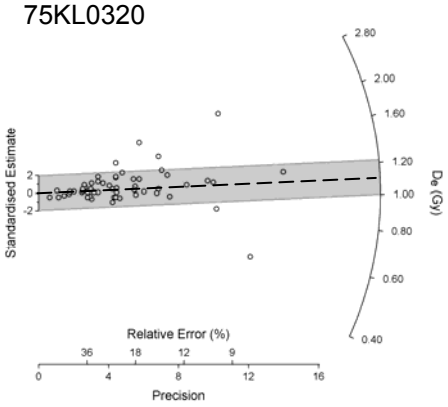

92KL0401

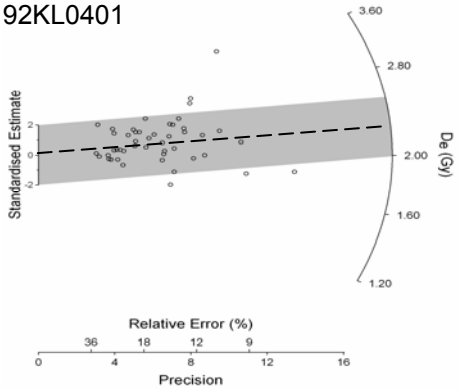

75KL0321

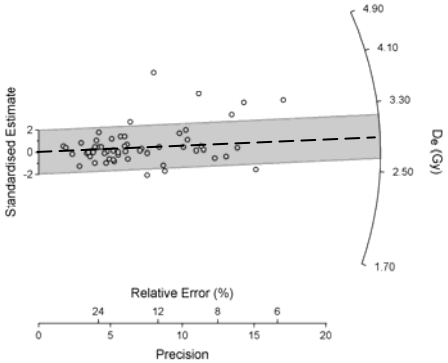

b)

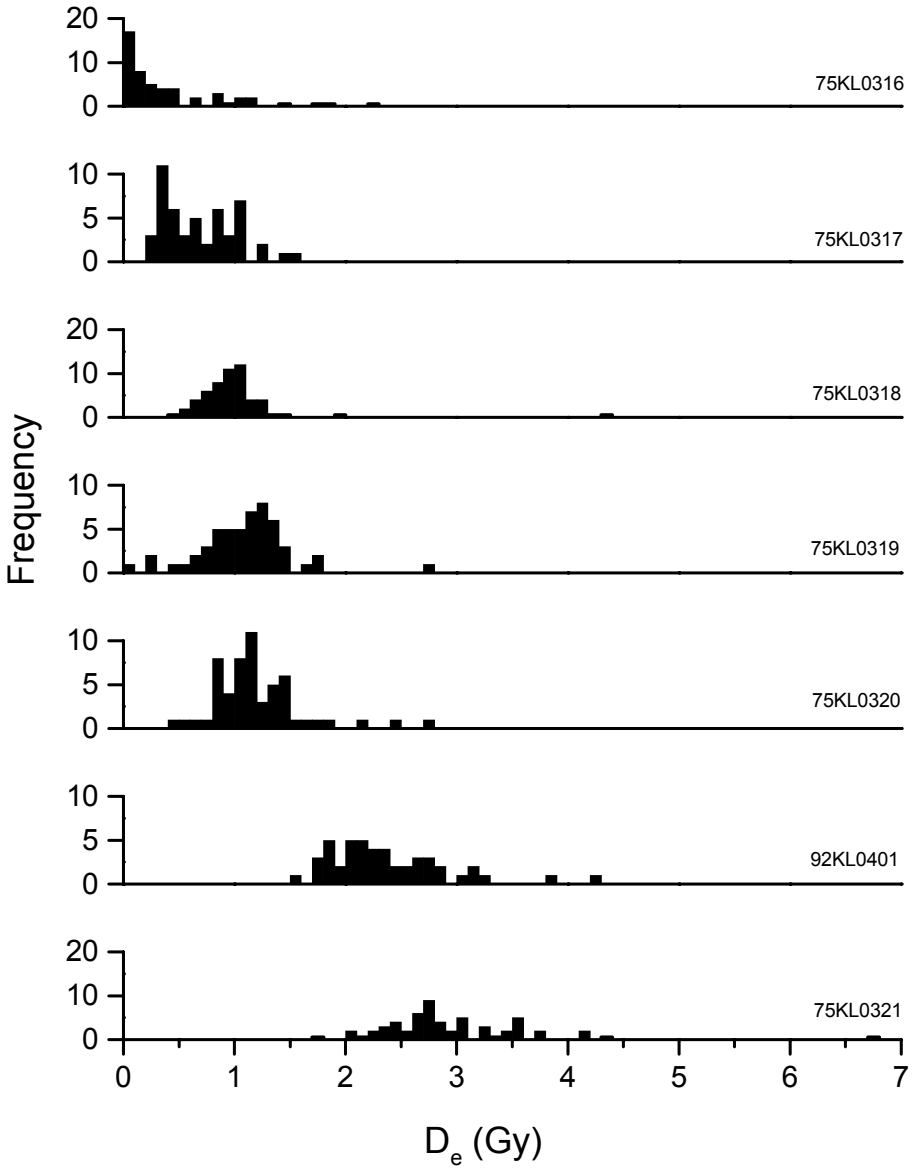

Figure 7.5: a) Radial plots of the D_e values for the seven samples from Kadies Drift. The D_b value calculated is indicated by the dashed line, and the grey shaded band shows those D_e values that are consistent with it within 2σ. b) Histograms showing the frequency of D_e values for the Kadies Drift site samples. Note the difference in the y-axis scales.

75KL0317 appears to have two discrete populations within the D_e distribution, as is evident from both the radial plot and histogram. This is supported by the results from the finite mixture model that reveal that the D_e dataset consists of two populations of values, each containing approximately half the D_e values.

The radial plots of the remaining scroll-bar samples (75KL0318-21 and 92KL0401) show D_e datasets that consist of a single dominant population with a few outlying points. The finite mixture model picked out these outliers as discrete populations based on only one or two values, and the D_b values for the samples were based on the main, dominant population.

The ages calculated from the D_b values for the Kadies Drift site are shown in Figure 7.6 along a transect across the scroll-bar sequence. The sample from the oxbow lake (75KL0316) has an age 0.06 ± 0.02 ka (Table 7.1), this equates to a central age of AD 1942 (one sigma error range: AD 1926-1958). This result is consistent with the known age of meander cutoff which occurred between AD 1954 and 1979. As expected, this sample is slightly older than the cutoff event itself because it is associated with bedload transport prior to meander abandonment. With the exception of sample 75KL0320 (0.46 ± 0.04 ka), the central values of the ages for the scroll bars fall in the correct chronological order for the depositional sequence (Fig. 7.6). The age calculated

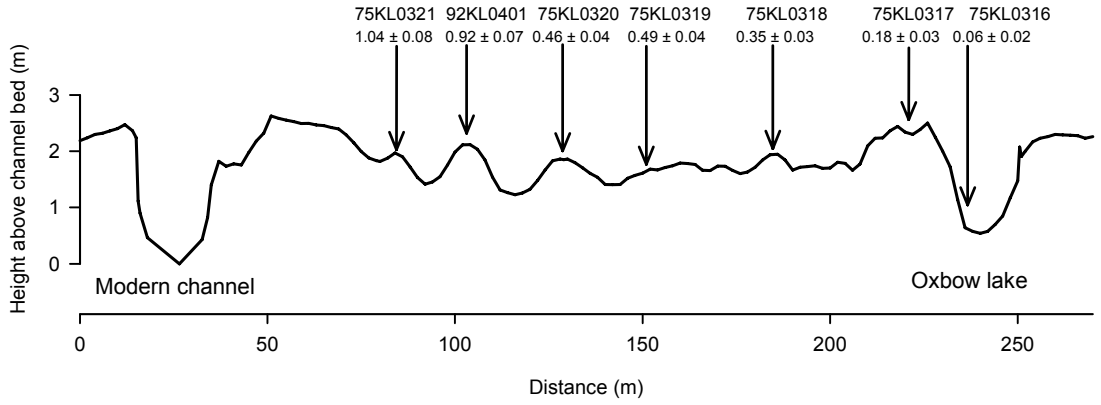

Figure 7.6: Transect (VE = 15) across the Kadies Drift scroll-bar sequence (see Fig. 7.3 for location). Sample locations and calculated ages (ka before AD 2004) are shown.

for sample 75KL0320, however, is nonetheless consistent within errors of the age found for 75KL0319 (493 ± 37 years) located ~27 m to the northeast. These results may indicate a short-lived increase in the lateral migration rate around this time; overall, the results indicate that the meander migrated ~160 m over a period of ~1000 years, giving an average lateral migration rate of ~0.16 m/a.

7.2.3 Discussion

Although the scroll-bar sequences at the two sites are of a similar age, the D_e distributions show dissimilar patterns of bleaching. At the Waaihoek site, the two younger scroll-bar samples (75KL0324 and 75KL0325) are heterogeneously bleached, whilst the older samples are well bleached (75KL0322 and 75KL0323). None of the scroll-bar samples from the Kadies Drift site show evidence of heterogeneous bleaching, although sample 75KL0317 shows evidence of partial bleaching in the form of two discrete populations of grains being present (Fig. 7.5a). For the younger samples, the river bank sample from Waaihoek (75KL0327) and the channel fill sample from Kadies Drift (75KL0316) are heterogeneously bleached (Fig. 7.2 and 7.5), whilst the point bar sample from Waaihoek is generally well bleached. The difference in the extent of bleaching of the samples is probably a reflection of the different depositional environments. Grains on the surface of a point bar are likely be exposed to direct sunlight above the water level for a large proportion of the year, whilst the channel fill and river bank sediments are less likely to be exposed to sufficient light to fully bleach the grains during transport in the water column prior to deposition and subsequent burial. In general, the scroll-bar samples appeared to be well bleached. Since scroll-bar ridges may originate from point bars (Section 1.3.1.1) one might expect the form of the D_e distributions to be similar, but a greater spread is evident in the D_e distributions for the scroll-bar samples, as compared to the point bar sample. This may arise from older material being incorporated into the deposit during scroll-bar formation.

Despite the difference in the extent of bleaching of the young and modern samples, using the finite mixture model allows one to calculate ages that are

appropriate, and thus can be used to determine lateral migration rates. For the meander bends at the Waaihoek and Kadies Drift sites, the average lateral migration rates obtained using OSL dating were ~0.05 m/a and ~0.16 m/a, respectively. These values are broadly similar to those found for other low or moderate energy, meandering rivers around the world (e.g. Hickin and Nanson, 1975; Dietrich *et al.*, 1999; Brooks, 2003; Tooth and McCarthy, 2004). The average rates, however, conceal temporal differences in the pattern and rate of lateral migration on the two meander bends. Figure 7.7 shows the ages of the deposits as a function of the distance across the sequence. The Waaihoek meander (Fig. 7.7a) initially had a slow rate of lateral migration (~0.04 m/a between 1.40 ± 0.10 ka and 0.07 ± 0.01 ka), and subsequently the rate increased to ~0.30 m/a after 0.07 ± 0.01 ka. Analysis of the most recent aerial photographs for this site indicates that the r/w ratio (see Section 1.3.1.1) for this bend was ~5 in 1979 (0.03 ka). Previous work (Section 1.3.1.1) has found that the maximum rate of lateral migration tends to occur at r/w ratios between 1 and 3, suggesting that the lateral migration rate of the Waaihoek bend has yet to reach a maximum. Unfortunately, because the aerial photographs are not of sufficient resolution, changing curvature of the bend as individual scroll-bar ridges were formed cannot be reconstructed in detail, so one is unable to investigate how r/w has changed through time. Nevertheless, the initial slow migration rate in what was probably a broader and more open bend (high r/w), and the increase in the lateral migration rate as the bend tightened (lower r/w), suggests that lateral migration at this location is primarily controlled by the bend curvature, as argued by Hickin and Nanson (1975; 1984). From the limited palaeoclimatic records for the Highveld (Section 2.7.2), there is no evidence to suggest climatic changes have had an influence on the lateral migration rate.

At Kadies Drift, the rate of lateral migration has been more constant at ~0.16 m/a (Fig. 7.7b), although possibly with a short lived increase in the rate at ~0.4 ka, as suggested by the results from 75KL0319 and 75KL0320. This possible increased rate coincides with part of the Little Ice Age, which is characterised by generally colder and drier climate but with periods of increased storminess (Section 2.7.3). Hence, the period of increased migration rate could be related to a period of higher discharges on the Klip River during the LIA;

a)

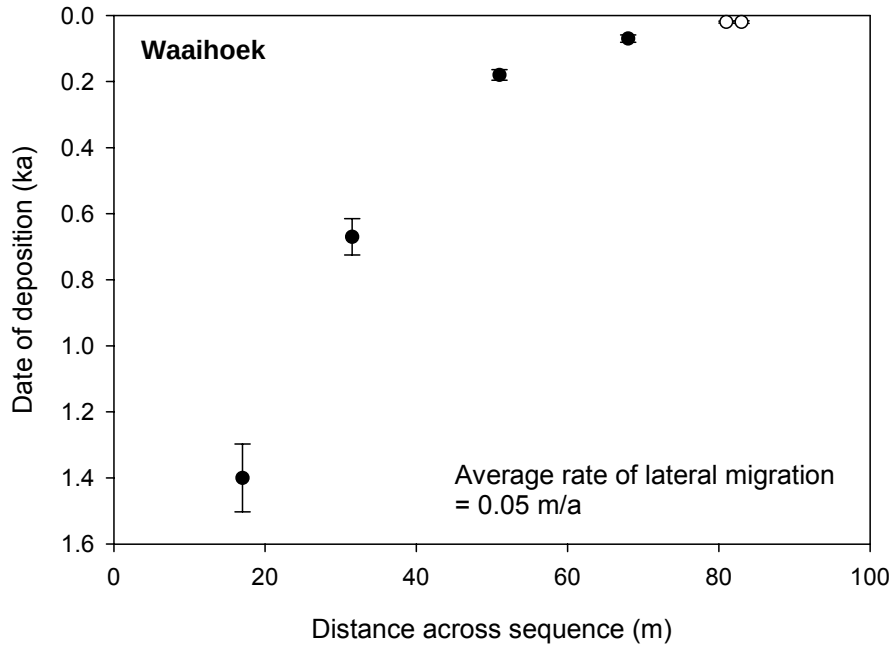

b)

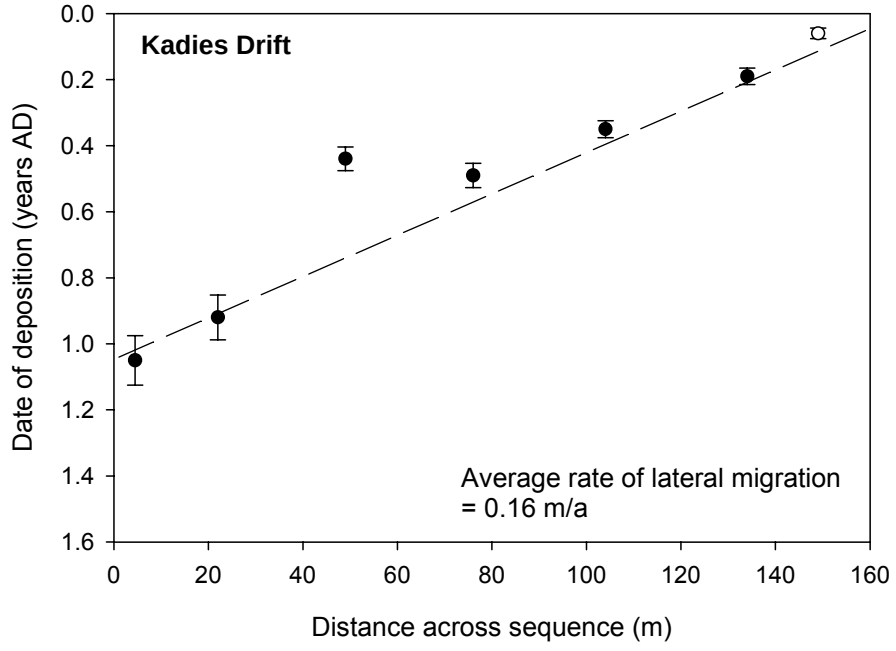

Figure 7.7: Graphs showing the date of deposition (ka) as a function of the distance across the scroll-bar sequence (from an arbitrary starting position) for a) Waaihoek site and b) Kadies Drift site. The scroll-bar samples are shown as solid circles, and the samples from other depositional environments are shown as open circles. The dashed line in b) indicates the average rate of lateral migration.

however the lack of high-resolution palaeoclimate records for the Highveld means that this assertion can remain only speculative. Alternatively, the increase in the lateral migration rate could be related to changing bend curvature. The extensional growth of the meander, and its eventual cutoff, will have resulted in a decrease in r/w over time to its present value of ~3. Unfortunately, erosion by the upper and lower limbs of the meander during bend development has removed much of the original scroll-bar topography, such that the changing curvature of the bend cannot be reconstructed. Nevertheless, this pattern of meander bend growth would be broadly consistent with Hickin and Nanson's (1975; 1984) pattern of a faster migration rate being related to an initially more open bend and a slower migration rate related to further tightening of the bend prior to cutoff.

Variation in the rates of lateral migration on meander bends of the lower Mississippi River has been attributed to the strong influence of local controls on lateral migration (Hudson and Kesel, 2000). The differences in the pattern of lateral migration on the Klip River meanders may also occur because of the influence of local variations such as minor differences in bank strength related to subtle variations in the bank material and/or vegetation, and/or differences in the floodplain morphology such as the presence of levees, scroll bars, oxbows etc. To investigate this further, many more scroll-bar sequences from the Klip River would have to be dated, and the relationship between the pattern of scroll-bar migration and local controls would have to be explored.

7.3 AVULSION AND MEANDER CUTOFF

The results from replicate samples of the uppermost bedload sand from reaches of the palaeochannels in the Seekoeivlei part of the Klip River floodplain wetland were discussed in Section 6.5.1.3. The results from replicate samples covering various spatial scales showed that the finite mixture model is the most appropriate for D_b calculation, and the ages of abandonment of palaeochannels with more than one OSL sample of the uppermost bedload sand were determined. In this section, the timing of abandonment of all the discrete palaeochannel reaches is discussed. Additionally, the ages of the

samples taken from a greater depth in the bedload sand, and the ages from the oxbow samples, are also detailed.

Figure 7.8 shows the map of the sample locations for the Seekoeivlei site. The palaeochannel samples taken from the uppermost bedload sand allow one to derive the timing of the final bedload transport in the channel (i.e. abandonment). The samples taken from a greater depth in the bedload sand should be older and therefore provide relative age control, and allow one to calculate a broad estimate of the rate at which the channels aggraded whilst they were active. The oxbow samples allow the longevity of the palaeochannel reaches to be investigated; the oldest oxbow will give a minimum age for initiation of flow along a given palaeochannel reach. As the oxbows must have been formed prior to the palaeochannel they are associated with, the oxbow ages also provide relative age control for the palaeochannel samples. The radial plots for every sample are shown in Appendix G, and the ages calculated are detailed in Table 7.1.

7.3.1 Results

Along Reach A, only one sample (75KL0310) was taken from the uppermost bedload sand, thus the calculated age of 4.60 ± 0.27 ka is the most appropriate for the date of abandonment. This OSL age is consistent with the ^{14}C age of 3.9-4.0 cal ka (1 sigma error age range) obtained from the overlying post-abandonment infill. An additional sample of bedload sand was also taken from this reach; 75KL0311 was sampled from the same auger hole as 75KL0310, at a depth ~0.4 m greater. 75KL0311 has an OSL age of 6.03 ± 0.41 ka and thus the chronology is consistent with the stratigraphy. Whilst this result does not enable one to gain further insight into the timing of abandonment, it indicates that this reach was active for a minimum of ~1.4 ka, and that the rate of aggradation of the channel bed was ~0.3 m/ka whilst it was active.

As covered in Section 6.5.1.3, the four samples taken from Reach B (70KLA1; 75KL0308; 75KL0309; 75KL0329) have ages indicating abandonment at ~1.1 ka. This is verified by a ^{14}C age for post-abandonment infill of 1.01-1.11 cal ka (1 sigma error age range). The recent abandonment is also suggested by

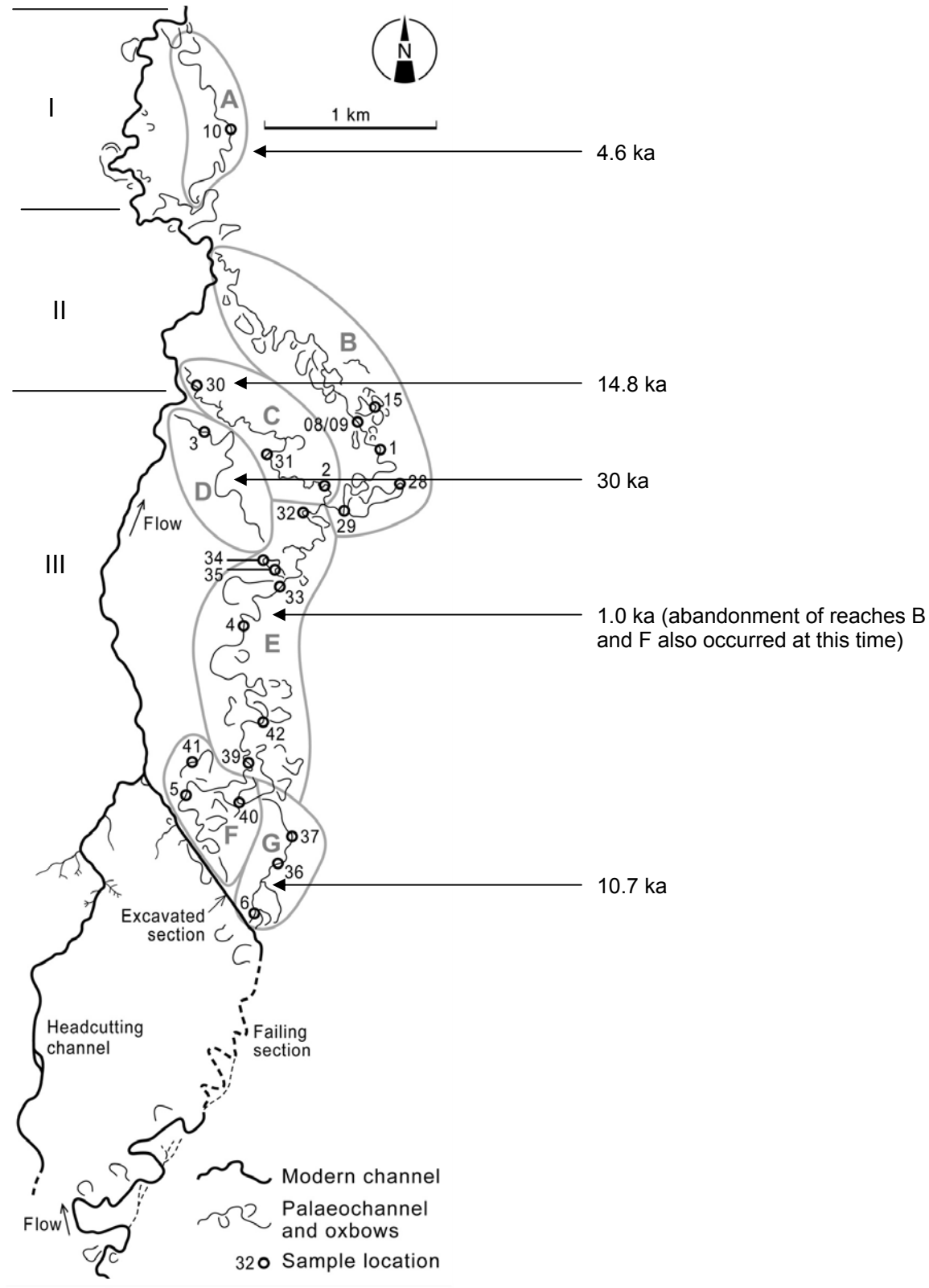

Figure 7.8: Map of the Seekoeivlei site showing the sample locations (prefixed 70KLA- for samples 1 to 6, and 75KL03- for all other samples) and discrete palaeochannel reaches. The modern channel is divided into three sections marked as I – III. Samples 11 and 38 (not shown) were taken at the same locations as samples 10 and 37, respectively, but at a greater depth (see text for discussion). The timing of abandonment of the different reaches of channel is also indicated.

the high level of preservation of meanders and oxbows along this reach. Two oxbows associated with this reach were also sampled; samples 75KL0315 and 75KL0328 have OSL ages of 1.84 ± 0.13 ka and 1.65 ± 0.10 ka, respectively. These ages are older than the ~1.1 ka abandonment and therefore are consistent with the expected age relationships. The ages are not much older than the timing of abandonment, however, and therefore indicate only that the channel was active for a minimum of ~0.6 ka prior to abandonment. These results suggest that meander cutoffs on the Klip River occur frequently.

Samples 75KL0330 and 75KL0331 from Reach C have OSL ages of 16.2 ± 1.0 ka and 14.8 ± 0.8 ka respectively (Table 7.1), indicating that the reach was last actively transporting bedload ~14.8 ka. Although the ages are consistent within errors, the greater age is obtained from the more downstream sample, possibly demonstrating that reach abandonment was initiated at the downstream end and gradually progressed upstream. A third sample, 70KLA2, was also taken from the very upstream end of this reach, but it has a much younger OSL age (1.41 ± 0.08 ka) that was attributed to sampling of younger flood deposits derived from a more recently active palaeochannel reach (B or E).

Only one sample was taken from Reach D, so the age of 30.2 ± 1.9 ka calculated for sample 70KLA3 is the most appropriate for the date of abandonment. Owing to a greater degree of post-abandonment infilling, this reach is very poorly defined both in aerial photographs and on the ground, strongly supporting the assertion that this is the oldest section of palaeochannel evident in the Seekoeivlei part of the floodplain wetland.

Five palaeochannel samples were taken from Reach E. Although the results were not consistent within errors, with the exception of sample 70KLA4, the ages decreased upstream, again suggesting a pattern of abandonment that started at the downstream end and gradually progressed upstream, finally ending ~0.6 ka. The most downstream sample (75KL0332) has an age of 0.84 ± 0.05 ka, whilst the most upstream sample (75KL0339) has an age of 0.57 ± 0.03 ka. Over a distance of ~3 km, the absolute difference in the ages is less than 0.3 ka, equivalent to a rate for the upstream progression of abandonment of <10 m/a. A ^{14}C sample taken from the post-abandonment infill directly above

sample 75KL0342 has an age of 0.35-0.53 cal ka (1 sigma error age range), consistent with abandonment around ~0.6 ka. In addition to the palaeochannel fill samples, three oxbows were also sampled from Reach E. Oxbow samples 75KL0334 and 75KL0335 were taken directly adjacent to palaeochannel sample 75KL0333. The position of the oxbows is such that the outermost oxbow sample (75KL0334) must be older than the sample from the innermost one (75KL0335) (Fig. 7.8). The ages for 75KL0334 and 75KL0335 are 1.84 ± 0.11 ka and 1.70 ± 0.10 ka, respectively. Therefore these results are in the appropriate chronological order for the depositional sequence, and are older than the corresponding channel fill sample (75KL0333: 0.75 ± 0.05 ka). The ages indicate meander cutoff on the Klip River occurs frequently, as previously suggested by the results from Reach B. The results from the oxbows show that the reach was active for at least 1.4 ka prior to being abandoned ~0.6 ka.

Only one palaeochannel sample (70KLA5) was taken from Reach F; and has a burial age of 1.39 ± 0.09 ka. The most appropriate estimate for the abandonment of this reach is thus ~1.4 ka. An additional sample was taken from an oxbow associated with this reach. This sample (75KL0341) has a burial age of 2.40 ± 0.15 ka, indicating that the reach was active for at least 1 ka.

Three palaeochannel samples were taken from Reach G. One of these, 70KLA6, has an anomalously low age (6.99 ± 0.44 ka) which was attributed to more recent deposits derived from a nearby younger channel. Samples 75KL0336 and 75KL0337 have very similar ages indicating abandonment at ~10.7 ka. From the same auger hole as 75KL0337, an additional sample (75KL0338) was taken at a depth 0.8 m greater. This sample has an age of 11.8 ± 0.8 ka, consistent with the younger age of 10.7 ± 0.8 ka for 75KL0337, and suggests a rate for bed aggradation along the reach of ~0.7 m/ka.

Sample 75KL0340 was taken from an oxbow located at the junction of Reaches E, F, and G, and the age is 0.59 ± 0.04 ka. This young age, together with the location of the oxbow relative to the palaeochannel reaches, suggests that it is associated with Reaches E or F, rather than Reach G.

7.3.2 Discussion

The results from OSL dating of the Klip River palaeochannels show that the avulsions identified in the Seekoeivlei site occurred between ~30 ka and ~0.6 ka. The layout of the palaeochannel reaches shows that for a continuous section of channel to occur, Reach E must have acted as a link between the upper and lower sections of palaeochannel (Fig. 7.8); either Reach F or G, and either Reach B or C, must have been active at the same time as Reach E. The abandonment of Reach E terminated at ~0.6 ka, this value is based on consistent results from a relatively large number of OSL palaeochannel and oxbow ages, and a corresponding ^{14}C sample, and therefore one can be confident in this age. Upstream, OSL dating puts abandonment at ~1.4 ka and ~10.7 ka for Reach F and Reach G, respectively. The relative age order of these two palaeochannel reaches is confirmed by the relative preservation of the channel form in aerial photographs and field mapping (Fig. 7.8), which show that the meanders and oxbows of Reach F are more distinct than those of Reach G. Thus it is likely that Reach F was abandoned at approximately the same time as Reach E, and that the OSL age of ~1.4 ka for Reach F may be a slight overestimation.

Downstream of Reach E, Reaches B and C were abandoned ~1.1 ka and ~14.8 ka, respectively. The relative preservation of the reaches in aerial photographs and field mapping (Fig. 7.8) again confirms the relative age order. This indicates that Reach B was active at approximately the same time as Reach E. Therefore, reaches B, E, and F must have formed a continuous channel prior to being abandoned gradually over a few centuries.

The results from dating of the palaeochannels indicates that the Klip River has undergone at least five avulsions in the last ~30 ka, occurring at ~30 ka, 14.8 ka, 10.7 ka, 4.6 ka, and 1.0 ka. For the majority of the reaches, the timing of abandonment is based on more than one OSL age, or confirmed by additional analyses, so one can be confident in the value. The timing of abandonment of Reaches D and F, however, are based on single samples, and thus should be treated with caution. Although the advanced degree of infilling strongly supports the assertion that Reach D is the oldest palaeochannel reach at the

Seekoeivlei site, additional samples will be necessary to confirm the age of abandonment.

In the field, collecting subsurface samples that accurately reflect the last bedload transport in the palaeochannels is difficult because no distinct stratigraphic units are visible when augering. Sampling could only be undertaken using the texture of material being augered as a guide to the location of the transition between the bedload sand and post-abandonment infill of organic-rich sandy clay. If minor scour and fill structures are present in the bedload sand these cannot be identified, even though they might contribute to variations in the burial ages derived for a reach of palaeochannel. Additional variation in the ages may occur from sampling deposits associated with later activity along nearby, younger channels, as evident from the anomalously young ages for samples such as 70KLA2 and 70KLA6. These results demonstrate the importance of taking replicate samples wherever possible in complex depositional environments such as floodplain wetlands with extensive reaches of palaeochannel.

Although avulsions are thought to be mainly a feature of aggrading floodplains (Makaske, 2001; Slingerland and Smith, 2004), the Klip River experiences periodic avulsions with a local aggradation rate of essentially zero. The low aggradation rate is demonstrated by the fact that the channel bed remains grounded on bedrock throughout the reach, the limited (<4 m) thickness of floodplain sediments, the low rate of aggradation of active channels (OSL dating of bedload at depth in the palaeochannels indicates infilling rates <1 m/ka whilst active), and the incomplete filling of the palaeochannels even after ~30 ka of abandonment. Over the last ~30 ka, the avulsion frequency has been <0.2 per 1 ka, with a slight increase to <0.3 per 1 ka since ~15 ka. These rates of avulsion are significantly lower than those found on other river systems with relatively high aggradation rates (Section 1.3.2.2). This supports the hypothesis that the avulsion frequency and aggradation rate are positively coupled (e.g. Bryant *et al.*, 1995; Mackey and Bridge, 1995; Slingerland and Smith, 1998).

From the results for the Seekoeivlei part of the Klip River floodplain wetland, the reaches that were active at the same time in the past can be identified (Table

7.2); the modern channel has been divided into three sections (denoted I – III) as they would have been initiated at different times in the past. The results show that section II of the modern river is likely to have been active in the past, prior to abandonment and subsequent recapturing of flow at ~0.6 ka. In order to obtain an estimate of the longevity of the palaeochannels, samples for OSL dating were taken from some of the oxbows. In every instance, the ages obtained from oxbows were older than those from the related palaeochannel reach. However, none of the oxbow ages were more than 2 ka older than the timing of abandonment of the reach. Based on the ages of the palaeochannel reaches as a whole, most of the reaches must have been active for ~15 ka (Table 7.2). Thus it appears that none of the oxbow samples is old enough to allow the longevity of a channel reach to be determined using these samples. To determine the longevity of the palaeochannels, additional oxbow samples would be necessary, however it is likely that a large proportion of the older oxbows will be consumed during lateral migration of more recent channels, thereby skewing the record.

Table 7.2: Reaches of palaeochannel (A – G) and presently active sections of the Klip River (I – III) that were active for different time intervals over the last ~30 ka.

Time (ka)	Active reaches/sections of the Klip River at the Seekoeivlei site
~ 0 – 0.6	III – II – I
~ 0.6 – 4.6	F – E – B – I
~ 4.6 – 10.7	F – E – B – A
~ 10.7 – 14.8	G – E – B – A
~ 14.8 – 30	G – E – C – II – A
> ~ 30	G – E – D – II – A

The timing of the avulsions on the Klip River does not show any coherent or consistent link with palaeoclimatic changes in the region, identified from other palaeoclimatic proxies or records (Section 2.7.3). Broadly, the absence of avulsions during the period from ~15 ka to ~30 ka may be indicative of reduced fluvial activity around the last glacial maximum, when rainfall was less than at present. The avulsions during the Holocene, however, do not correspond to any known climatic variations in southern Africa. Thus the chronology of

avulsion on the Klip River suggests that this process occurs autogenically, as opposed to being allogenically forced.

7.4 INCISION

7.4.1 Results

To determine the timing of incision along the Schoonspruit, samples were taken from the upper and lower floodplain (Fig 2.16). The upper floodplain samples, and additional samples from oxbows located on this floodplain give a maximum age for the initiation of incision. The two oxbow samples, 91SC0401 and 91SC0410, have OSL ages of 1.58 ± 0.15 ka and 1.21 ± 0.10 ka respectively (Table 7.1). Both these samples are heterogeneously bleached, as demonstrated by the spread in the D_e values (Fig. 7.9) and the high overdispersion parameters (Table 7.1). These results show that the river was active on the upper floodplain until at least ~1.2 ka, and thus incision occurred at a later date.

The samples taken from the upper floodplain at the incisional face (91SC0403-06) also have radial plots and overdispersion parameters indicative of heterogeneous bleaching (Fig. 7.9; Table 7.1). The ages calculated for the upper floodplain samples are shown on surveyed transects (Fig 7.10). The results for samples 91SC0404 and 91SC0405 (Transect 2) are consistent with their stratigraphic order giving values of 1.28 ± 0.10 ka and 1.48 ± 0.12 ka, respectively. Although the results are consistent within errors, they suggest that prior to the most recent incisional episode the Schoonspruit had aggraded at ~2 m/ka. The age obtained for sample 91SC0403 (Transect 1) is consistent with the results for Transect 2, but sample 91SC0406 (Transect 3) has an age of 0.12 ± 0.01 ka (Table 7.1), which is not consistent with the results for other samples from the upper floodplain. This sample also has a very high overdispersion parameter (121 %; Table 7.1). During laboratory preparation of this sample, it was clear that there was a high degree of root penetration in the sampled sediment, which was not the case with any of the other samples. This may have caused an anomalously young age because during growth the roots

91SC0401

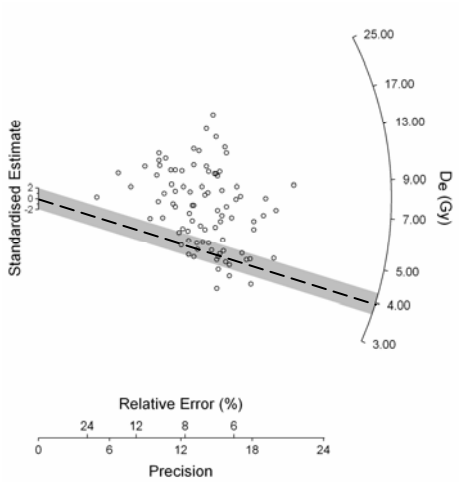

91SC0403

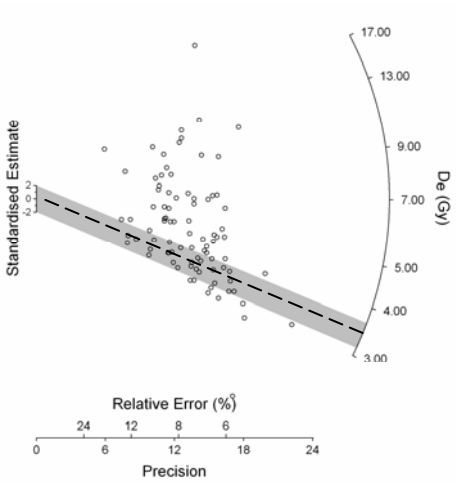

91SC0404

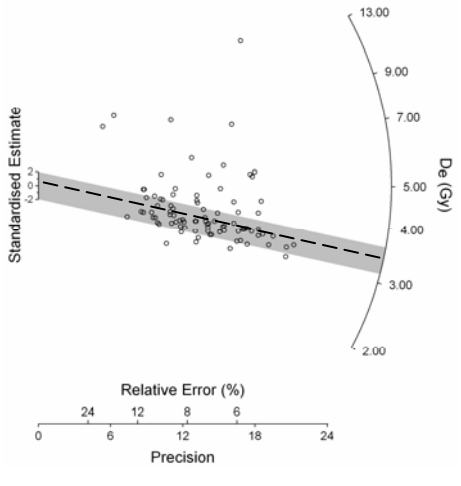

91SC0405

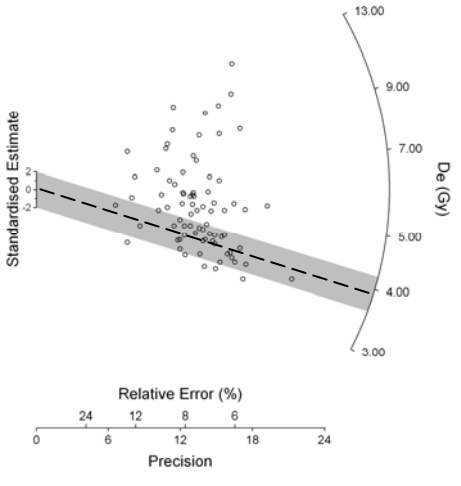

91SC0406

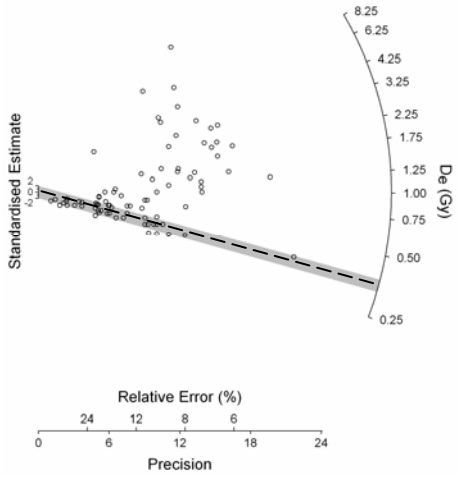

91SC0407

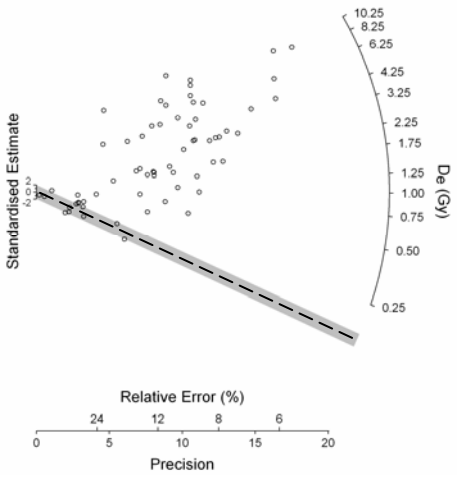

91SC408

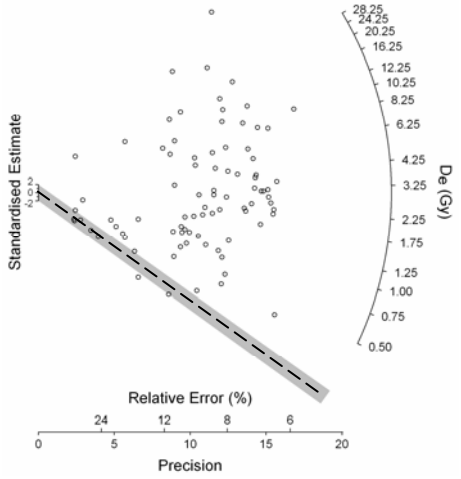

91SC0409

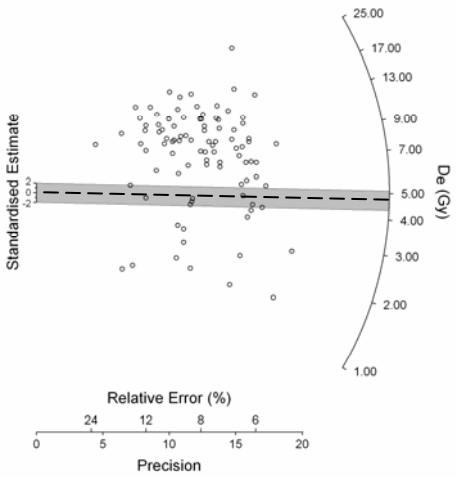

91SC0410

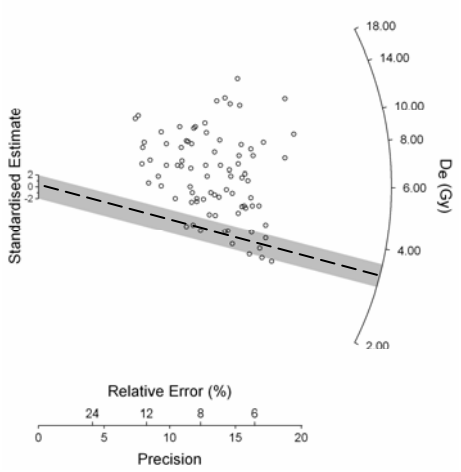

Figure 7.9: Radial plots of the D_e values for the nine samples from the Schoonspruit. The D_b value calculated is indicated by the dashed line, and the grey shaded band shows those D_e values that are consistent with it within 2σ.

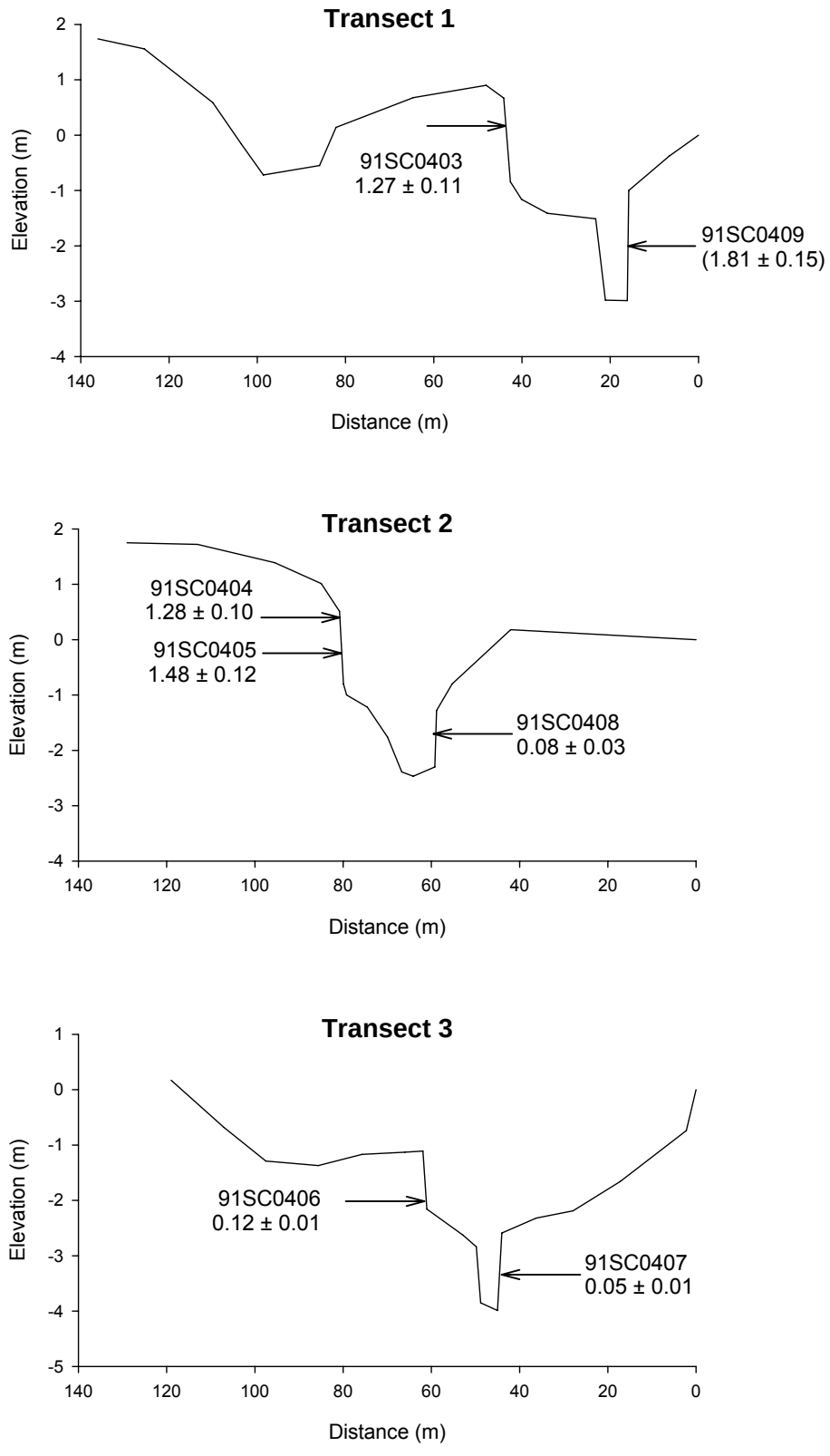

Figure 7.10: Transects 1-3 perpendicular to the Schoonspruit (for location, see Figure 2.16), showing the location of the samples (VE = 12.5). The ages (in ka) of the samples are shown. The result for sample 91SC0409 is shown in brackets because this sample was deemed undateable (see text for discussion).

can create a downward mixing profile by pushing down younger grains from upper layers of sediment. If this has occurred, it would also lead to a higher degree of mixing and therefore explain the greater overdispersion. Thus, the anomalously low age for this sample was attributed to pedoturbation, and the sample was not taken into consideration for the timing of incision on the Schoonspruit.

The samples from the lower floodplain of the Schoonspruit reflect more recent depositional events. Samples 91SC0407 and 91SC0408 have OSL ages of 0.05 ± 0.01 ka and 0.08 ± 0.03 ka, respectively. These results are consistent within errors, and indicate deposition during the last 100 years. The radial plots (Figure 7.9) and the high overdispersion parameters (~105 %) demonstrate that they are very heterogeneously bleached, with only a few well-bleached grains. The sample taken from Reach 1, 91SC0409, has a greater burial age of 1.81 ± 0.15 ka (Table 7.1). This sample is also very heterogeneously bleached but has a slightly lower overdispersion value of 94 %. The radial plot for this sample, however, shows a slightly different shape to the other samples. Whilst the spread in D_e values is similar, the D_e distribution for sample 91SC0409 contains a few scattered, relatively low D_e values (consisting of ~11 % of the D_e dataset), with the majority of the data points forming a group of higher D_e values (Fig. 7.9). The other samples have D_e distributions with a more even spread of data points across the range of values. The low number of relatively well-bleached grains for sample 91SC0409 causes problems when the finite mixture model is used for D_b selection. Using the standard procedure for D_b calculation (Section 6.5), the D_b value is based on the lowest population containing at least 10 % of the D_e values. The pattern of spread in the D_e dataset of 91SC0409 is such that the low D_e values do not form a consistent population, but instead form three discrete populations each consisting of <5 % of the D_e values (Fig. 7.11). Therefore, when the D_b value is calculated from a population containing at least 10% of the grains, the lowest 11 % of D_e values are excluded from the analysis. This leads to an inappropriately high D_b value (4.65 ± 0.17 Gy), and thus age overestimation occurs. This sample is the only one analysed in this thesis where >10 % of the D_e values are less than the D_b value calculated. The 10 % criterion was used to avoid basing the D_b value for a sample on a

population that consists of one or two outlying points. The lack of consistent low D_e values and the age overestimation, suggests that sample 91SC0409 does not contain sufficient well-bleached grains to enable the correct D_b value to be calculated. Therefore, the sample is deemed as being undateable. The high level of poorly bleached grains in the sample may be because of the presence of extensive dongas (gullies) in the locality (Fig. 2.16), that may have introduced a mix of poorly bleached sediment to the river. Why only this sample would be affected however, is unclear. If material from the dongas has been washed downstream to the location of sample 91SC0409, it is unlikely that the short transport distance would be sufficient to form a well bleached deposit, and instead resulted in a very heterogeneously bleached sample.

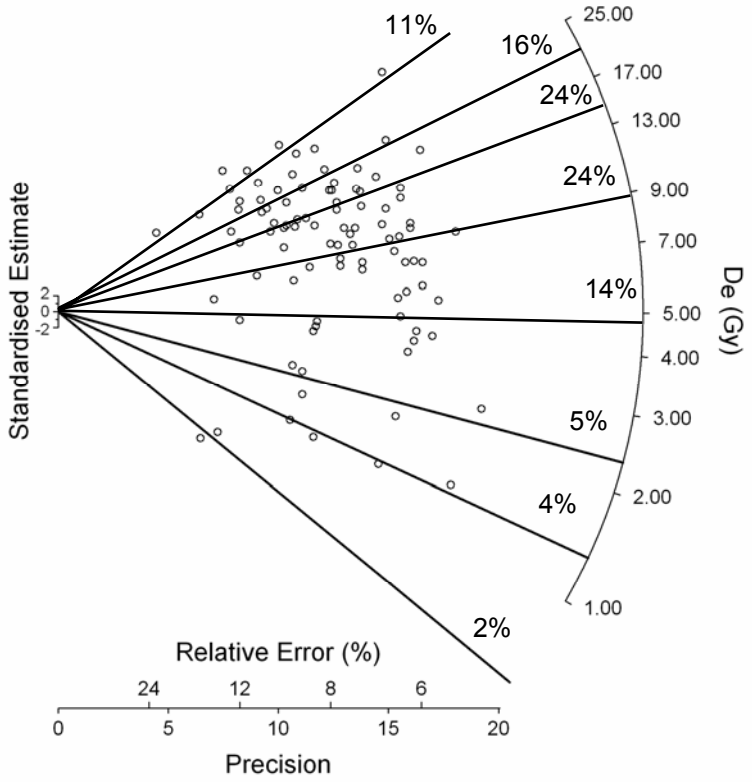

Figure 7.11: Radial plot for sample 91SC0409. The solid lines show the D_b values for the nine populations identified by the finite mixture model, and the proportion of the D_e dataset that forms each population is indicated.

7.4.2 Discussion

From the results for the accepted samples (i.e. excluding 91SC0406 and 91SC0409) the timing of incision along the Schoonspruit can be determined. The ages from the oxbows and the upper floodplain deposits indicate that deposition was active until ~1.2 ka, after which incision commenced. As expected, the samples from the lower floodplain have very young ages demonstrating the cessation or slowing of incision, and renewed deposition to form an inset floodplain in the incisional slot within the last 100 years. The transects across the Schoonspruit show incision is 3-4 m into both alluvium and bedrock, giving an average rate of incision of ~2-3 mm/a. This is comparable with rates of incision obtained from other rivers (Section 1.3.4.2). No previous work has been published on the incision rates of rivers with similar geomorphic and geological settings as the Schoonspruit, however, and therefore one is unable to compare the rate of incision with rates from similar river settings. Given that incision is an erosional process, the lack of any deposits recording the changing level of the Schoonspruit during incision is unsurprising, but it means that one is unable to determine if there has been any variation in the rate of incision during the last ~1.2 ka.

This most recent episode of incision on the Schoonspruit was initiated by breaching of a downstream dolerite sill, leading to local base-level lowering (Group 2 following the notation of Schumm (2005), containing geomorphic causes). Baselevel lowering results in the generation of knickpoints that have since migrated upstream (Tooth *et al.*, 2004). Knickpoints have been identified at locations upstream of the reach studied in this work, indicating ongoing incision in places, but along most of the study reach an inset floodplain has formed in the incision slot. This suggests that incision along this reach of the Schoonspruit has either slowed or has finished, with baselevel stabilising once more.

7.5 SUMMARY

The application of OSL dating to sediment samples from the Klip River and the Schoonspruit was successful, and allowed the rates of channel change

processes such as lateral migration, cutoff development, avulsion, and incision to be derived. The vast majority of the samples showed evidence of heterogeneous bleaching in both the radial plots and in the overdispersion parameters, but some of the scroll-bar samples appeared to be well bleached. This pattern of bleaching is consistent with what one would expect from the different depositional mechanisms of the samples. Those from the palaeochannel infill, oxbows, and floodplain sediments would have been deposited following transport within the water column, where limited exposure to sunlight means that the rate of bleaching is greatly diminished. Scroll-bar samples are thought to derive from point bar deposits, where the sediment grains may lie exposed to direct sunlight above the water level for a large proportion of the year and thus have an increased rate of bleaching. Whilst use of the finite mixture model enabled D_b values to be obtained from most of the samples, one sample from the lower floodplain of the Schoonspruit was so poorly bleached it was deemed undateable.

Luminescence dating of the scroll-bar sequences at Waaihoek and Kadies Drift was successful. Low residual ages were found in modern samples, and the channel fill sample from Kadies Drift had an OSL age consistent with that expected from aerial photographs. With the exception of one sample, the results for the scroll-bar samples were in the correct chronological order for the depositional sequence. The lateral migration rate at the two sites was different, suggesting that lateral migration may be influenced by local controls. The principle influence on the lateral migration rate appeared to be changing r/w ratio caused by changing bend curvature. No clear evidence of allogenic forcing from climatic changes was apparent; however a possible increase in the lateral migration rate of the Kadies Drift meander during the early 16th Century coincided with the LIA.

The use of replicate samples allowed a chronology of avulsion on the Klip River to be established. The occurrence of anomalously young results for some palaeochannel reaches was attributed to the sampling of flood deposits derived from later channel activity, and demonstrated the importance of understanding the sampling context and taking multiple samples were possible. Where the samples are taken from a subsurface environment, with only the texture of the

material being augered as a guide, it can be difficult to accurately sample material associated with the final bedload transport as one is unable to see the subsurface structures. Nevertheless, by interpreting the results from the multiple channel fill samples, the timings of avulsions on the Klip River were established, with five having occurred since ~30 ka. There is no apparent link to periods of climatic change, suggesting that avulsions on the Klip River occur autogenically.

In general, dating the upper and lower floodplains of the Schoonspruit was also successful. Problems were encountered, however, with samples that had either been subjected to mixing from root penetration, or that did not have sufficient well-bleached grains to allow the sediment to be dated using OSL. For the majority of samples, however, the finite mixture model was able to derive a D_b value from the well-bleached population, leading to ages that are consistent within depositional units. Through the use of multiple samples from the same level of floodplain, the timing of incision was dated successfully.

7.6 CONCLUSION

In conclusion, with the possible exception an increase in the lateral migration rate at Kadies Drift that coincided with the Little Ice Age, no connection between palaeoclimatic records for South Africa and channel change processes on the Klip River and Schoonspruit is evident. The results suggest that the changes in these river systems are dictated largely by processes inherent to river activity (autogenic controls), which in turn may be influenced by local controls (e.g. floodplain morphology). Climatic changes appear to have only a relatively minor influence on river activity over the time period studies here, and leave little tangible morphological or sedimentary evidence. Over time, any possible climatic signals may be obscured by morphological or sedimentary features resulting from autogenic channel changes, suggesting that these systems do not provide discernible archives of palaeoenvironmental change. Until more high resolution late Quaternary palaeoclimatic records are available for the Highveld region of South Africa, however, this conclusion can only remain tentative.

CHAPTER 8: CONCLUSIONS

In this thesis, OSL dating was successfully used to obtain accurate chronologies of channel change for two South African floodplain wetlands. Robust methods were developed for the analysis of D_e datasets from small aliquots to give depositional ages for sediments from a variety of fluvial environments. No conclusive evidence was found for a link between records of climate and fluvial change, and therefore the likelihood is that the primary control on channel change is autogenic (inherent to river activity).

8.1 SUMMARY OF PRINCIPLE FINDINGS

To determine whether changes in channel form in South African floodplain wetlands occur as a result of autogenic processes, or in response to allogenic forcing, chronologies of channel change on the Klip River and the Schoonspruit were established using OSL dating. In this thesis, the SAR procedure was used to obtain D_e values for small aliquots of quartz consisting of ~30 grains. Investigations into the proportion of grains emitting a light signal demonstrated that for aliquots of this size, the measurable OSL signal only derives from two or three grains (Chapter 6). For each sample, at least 50 D_e values were measured in order to obtain reproducible D_e distributions. The overdispersion parameter was calculated for each sample and used to determine whether heterogeneous bleaching was present. In general, palaeochannel and oxbow samples were heterogeneously bleached and this was observed for samples up to ~30 ka, in contrast to the suggestion by Jain *et al.* (2004). The scroll-bar samples were generally well bleached and the D_e datasets were typically characterised by a single dominant dose population (Chapter 7). This difference in the bleaching characteristics was attributed to the different mechanisms of deposition at the various sample locations. Although heterogeneous bleaching could be detected from the D_e distributions, the signal analysis method of $D_e(t)$ plots was unable to identify partial bleaching of grains. This was because of a number of reasons: 1) the small proportion of the CW-OSL signal arising from the medium component; 2) sensitisation of the components at different rates (Chapter 4); and 3) instability of the medium

component over geological periods, and therefore only dose distribution methods were used in this thesis.

It was shown that when at least 50 equivalent dose (D_e) values were used, the finite mixture model gave consistent D_b values. Using this model to calculate ages for different samples from the same palaeochannel reach generally gave abandonment ages that were consistent within errors, or that were indicative of gradual abandonment initiated at the downstream end of the channel. However, some samples that were believed to be from the last bedload transport in a reach of palaeochannel gave ages that were significantly younger than expected from other related samples, highlighting the importance of high-density sampling in areas of high channel activity, particularly where the stratigraphy is not visible.

Comparison between the results obtained from OSL dating and independent methods of age calculation also verified the suitability of the finite mixture model for calculation of D_b for fluvial samples. For three of the channel fill samples, independent age control was available from radiocarbon (^{14}C) dates for the overlying post-abandonment channel fill. In all three locations, the OSL age obtained using the finite mixture model for D_b calculation is older than the corresponding ^{14}C age, as expected from the stratigraphy. Additionally, aerial photography places the timing of oxbow formation at the Kadies Drift site to between 1954 and 1979. The OSL age calculated for a sample from the oxbow (0.06 ± 0.02 ka) is consistent with this range within errors; the central value is slightly older than the cutoff itself as expected, because it is associated with the final episode of bedload transport prior to meander abandonment.

The reproducibility of the ages obtained, and the consistency of the OSL ages with independent age estimates, confirms the suitability of OSL dating applied to fluvial deposits from the Klip River, provided that appropriate sampling, analytical and interpretative procedures are followed. Therefore, OSL dating can be a valuable tool in investigating the development of channels and floodplains along fluvial systems such as the Klip River and Schoonspruit. In particular, using the OSL dates calculated for samples taken from scroll bars, meander cutoffs, palaeochannels, and different levels of floodplains, enabled

the rates associated with different processes of channel change (lateral migration, avulsion, and incision) to be obtained. On the Klip River, lateral migration rates of ~0.05 and 0.16 m/a were obtained for meanders at Waaihoek and Kadies Drift, respectively. Dating of the palaeochannels in the Seekoeivlei part of the Klip River floodplain wetland gave an avulsion frequency of <0.2 per 1 ka over the last ~30 ka. Incision on the Schoonspruit has occurred at an average rate of ~2-3 mm/a over the last ~1.2 ka, following breaching of a dolerite sill downstream of the study site.

With the possible exception of an increase in the lateral migration rate at Kadies Drift that coincided with part of the Little Ice Age, no apparent connection between the chronology of channel change on the Klip River and Schoonspruit and the palaeoclimatic records for South Africa is evident. The results from this study, therefore, indicate that the channel changes on the rivers investigated occur principally in response to autogenic forcing, as opposed to allogenic variations such as climate change. The apparent lack of concordance between channel change and external factors, however, may arise from the limited number of sites studied, and the current paucity of high resolution records of late Quaternary palaeoclimatic changes across the South African Highveld. Before one is able to state unequivocally that channel changes in South African floodplain wetlands occur primarily in response to autogenic forcing, further chronologies of channel change for different rivers, and more high resolution palaeoclimatic records for the region, need to be developed.

In conclusion, this study demonstrates the validity of the OSL technique in obtaining rates of channel change for river systems transporting quartz-rich sand in general, provided that large numbers of D_e values are measured and the appropriate statistical techniques are employed. The OSL technique will be of particular value for changes that occurred before the start of documentary records, and where preservation of organic material is limited, but where a relatively closely-spaced series of samples are needed to determine detailed rates and timescales of channel change.

8.2 FUTURE RESEARCH DIRECTION

Arising from this thesis, a number of issues occur, primarily concerning the wider application and development of the OSL dating methods used in this work, and further investigations into the relationship between climatic and fluvial change in South Africa

The finite mixture model was found to be appropriate for obtaining accurate and reproducible D_b values for heterogeneously bleached samples younger than ~15 ka. The minimum age model was found to be affected by the presence of a small proportion of outlying data points with low D_e values, present in the datasets for some samples. Currently, the reason for these low D_e values is unknown; they occur because of either experimental causes (e.g. grains inappropriate for SAR analysis), or natural causes (e.g. grains intruded from another deposit, or localised low dose-rates). Investigation of these aliquots with the low D_e values may allow one to identify the cause of the outliers, and thereby tighten up the dose distribution.

The reliability with which dose distributions can be measured and analysed for older samples with growth curves near saturation is uncertain. As the OSL signal approaches saturation level the precision, and possibly the accuracy, may decrease. Additionally, for older samples with an increased burial period and hence accrued dose, other factors such a beta microdosimetry may start to become important. An indication of this was found in the oldest sample from the Klip River (70KLA3: ~30 ka), where the D_e values covered a large range and had relatively large individual errors associated with them. To examine whether the methods used in this thesis are appropriate for older samples similar procedures to those used in this work need to be used to date older fluvial deposits, where independent age control is available. If beta microdosimetry was thought to be a problem, Z plots potentially allow one to differentiate between this and partial bleaching. However, as seen in this study, not all samples have a stable medium component of sufficient magnitude for allowing this method to be used for the detection partial bleaching of grains.

The procedures developed in this thesis are also likely to be applicable to other heterogeneously bleached samples, where a population of well-bleached grains

exists. Glacial deposits are often very poorly bleached and the methods developed here have begun to be applied to samples from this environment (Duller, in press). To establish the suitability of the finite mixture model for samples from other environments, however, studies with independent age control and/or using replicate samples from depositional units would have to undertaken, possibly utilising single grain OSL dating if necessary.

The results from OSL dating of two South Africa floodplain wetlands in this study showed no evidence of a link between climatic and fluvial change. Further investigation into whether such a relationship exists could be done in two ways. First, by developing additional chronologies of channel change for similar floodplain wetlands in the same geographical region, thereby ensuring that the climate in the past would have been the same. Despite the lack of high resolution palaeoclimatic records in this area, if specific periods of increased fluvial change were identified on different rivers, the evidence would suggest allogenic control of channel change. Second, by applying the techniques used in this study to investigate rates of channel change in other regions of southern Africa, where detailed records of climate change exist, one would be able to identify a relationship between climatic and fluvial change with more ease, if such a relationship existed.

APPENDIX A: CALCULATION OF ENVIRONMENTAL DOSE-RATE

For all the samples analysed in this thesis the environmental dose-rate was calculated in LDB2005 based on the results from thick source alpha counting and beta counting. To ensure that the software was working correctly, the stages of calculation performed in the database were done individually and checked against the database values for sample 70KLA1. The values obtained for the final dose-rate and its error, and all the values calculated throughout the working, are identical to those produced in the LDB2005, indicating that the automated dose-rates calculated in LDB2005 are correct.

Alpha counting

The results from alpha counting on sample 70KLA1 are shown below. The data was collected between 30.03.2004 and 08.04.2004, using an active counting area of 15.45 cm^2.

	Count time (ks)	Total counts (cnts)	Pairs counts (cnts)	Count-rate (cnts/ks)	Background subtracted count-rate (cnts/ks)
Background	86.4	3	-	0.035	
Unsealed	262.6	3017	81	11.488	11.453
Sealed	177.9	2096	68	11.781	11.747

Sealed/Unsealed ratio *(11.747 cnts/ks / 11.453 cnt/ks)* 1.03 ± 0.03

Background counts expected on unsealed measurement (cnts) *(0.035 cnt/ks * 262.6 ks)* 9.12

Error on unsealed count-rate (cnts/ks) *(√(9.12 + 3017)/262.6)* 0.2095

Use of pairs counts to determine U and Th concentrations (from unsealed counts)

The following is derived from the description by Aitken (1990):

Observed pairs counts	81
Count time (ks)	262.6
Observed pairs count-rate (pairs/ks)	0.3084
Dead time per ks (with coincidence time of *0.4 – 0.02 s = 0.38 s*)	0.00038
Gate open (ks) *(0.00038 * 11.488)*	0.0044
Random coincidence pairs count-rate (pairs/ks) *(0.0044 * 11.488)*	0.0502
True pairs count-rate (pairs/ks) *(0.3084 – 0.0502)*	0.2583
True pairs count-rate per area (pairs/ks/cm^2)	0.0167

Using relationship from Huntley and Wintle (1981) which states that the Th concentration (in ppm) is related to the true pairs count-rate (p) by:

Th = p/0.0022a

where a is the proportion of pairs measured in the 0.02 – 0.40 s coincidence window; in this instance this value is 0.76 (Daybreak model 583 Users Manual).

Th concentration (ppm) *(0.0167/(0.0022 * 0.76))*	**9.998**
Error on Th (ppm) *((9.998 * √(0.3084 * 262.6))/(0.2583 * 262.6))*	1.327

From Adamiec and Aitken (1998) Table 7, the expected count-rate (cnts/ks) for 1 ppm of parent is known:

	Values from Adamiec and Aitken (42 mm diameter detector screen)	Values for a 15.45 cm^2 detector screen (used in Aberystwyth)
Thorium	0.483	0.539
Natural Uranium	1.67	1.862

Th count-rate (cnts/ks) *(9.998 * 0.539)* Error on Th count-rate (cnts/ks) *(1.327 * 0.539)*	5.385 ± 0.715
U count-rate (cnts/ks) *(11.453 - 5.385)* Error on U count-rate (cnts/ks) *(√(0.2095² + 0.715²))*	6.068 ± 0.747
U concentration (ppm) *(6.068/1.862)* Error on U (ppm) *(0.747/1.862)*	**3.258 ± 0.400**

GM-beta counting

Operation of the GM-beta counter was described in Section 3.5, including determination of the error on the calculated beta dose-rate.

Measured beta dose-rate (Gy/ka) Error on measured beta dose-rate (Gy/ka)	1.638 ± 0.026

One can combine the TSAC and GM-beta counting to obtain an estimate of the K concentration.

From Adamiec and Aitken (1998) Tables 5 and 6, the dose-rate (Gy/ka) for given quantities of parent:

	Alpha	Beta	Gamma
Thorium (1 ppm)	2.78	0.146	0.133
Natural Uranium (1 ppm)	0.732	0.0273	0.0476
Potassium (1%)		0.782	0.243

Using U and Th concentrations calculated from TSAC:

Beta dose-rate from U (Gy/ka) *(3.258 * 0.146)*	0.476 ± 0.058
Error on beta dose-rate from U (Gy/ka) *(0.476 * 0.400/3.258)*	
Beta dose-rate from Th (Gy/ka) *(9.998 * 0.0273)*	0.273 ± 0.036
Error on beta dose-rate from Th (Gy/ka) *(0.273 * 1.327/9.998)*	
Beta dose-rate from U and Th (Gy/ka) *(0.476 + 0.273)*	0.749 ± 0.069
Error on beta dose-rate from U and Th (Gy/ka) $(\sqrt{(0.058^2 + 0.036^2)}$	
Beta dose-rate from K (Gy/ka) *(1.638 – 0.749)*	0.889 ± 0.073
Error on beta dose-rate from K (Gy/ka) $(\sqrt{(0.026^2 + 0.069^2)}$	
K concentration (%) *(0.889/0.782)*	**1.137 ± 0.094**
Error on K concentration (%) *(1.137 * 0.073/0.889)*	

TOTAL DOSE-RATE

Beta dose-rate

Measured total beta dose-rate (Gy/ka)

1.638 ± 0.026

Error on measured total beta dose-rate (Gy/ka)

Attenuated beta dose-rate (see Section 4.8.1)

Grain size (180-121 µm) - beta attenuation factor of 0.879

Total beta dose-rate (Gy/ka) *(1.638 * 0.879)*

1.440 ± 0.024

Error on total beta dose-rate (Gy/ka) $(1.440 * \sqrt{((0.004/0.879)^2 + (0.026/1.638)^2)}$

Corrected for water content (see Section 4.8.2)

Water content for this sample was 50 ± 10 %.

Total beta dose-rate (Gy/ka) *(1.440/(1 + (1.25*0.5)))*

0.886 ± 0.070

Error on total beta dose-rate (Gy/ka) $(0.886 * \sqrt{(0.125/1.625)^2 + (0.024/1.440)^2)}$*

Gamma dose-rate

Gamma dose-rate from U (Gy/ka) *(3.258 * 0.113)*

0.368 ± 0.045

Error on gamma dose-rate from U (Gy/ka) *(0.368 * 0.400/3.258)*

Gamma dose-rate from Th (Gy/ka) *(9.998 * 0.0476)*

0.476 ± 0.063

Error on gamma dose-rate from Th (Gy/ka) *(0.473 * 1.327/9.998)*

Gamma dose-rate from K (Gy/ka) *(1.137 * 0.243)*

0.276 ± 0.023

Error on gamma dose-rate from K (Gy/ka) *(0.276 * 0.094/1.137)*

Total gamma dose-rate (Gy/ka) *(0.368 + 0.476 + 0.276)*

1.120 ± 0.081

Error on total gamma dose-rate (Gy/ka) $(\sqrt{(0.045^2 + 0.063^2 + 0.023^2)}$

Corrected for water content (see Section 4.8.2)

Total gamma dose-rate (Gy/ka) *(1.120/(1 + (1.14*0.5)))*

0.714 ± 0.073

Error on total gamma dose-rate (Gy/ka) $(0.714 * \sqrt{(0.114/1.570)^2 + (0.081/1.120)^2})$*

Cosmic dose-rate

Thickness of overburden = 0.9 m. Cosmic dose-rate calculated using equation from Prescott and Hutton (1988).

Total cosmic dose-rate (Gy/ka)

0.239 ± 0.024

Error on total cosmic dose-rate (Gy/ka)

*The (0.125/1.625) and (0.114/1.570) terms in these error calculations derive from the propagation of the error on the water content through the equation.

TOTAL DOSE-RATE FOR SAMPLE 70KLA1

Total dose rate (Gy/ka) *(0.000 + 0.886 + 0.714 + 0.239)*

1.839 ± 0.104

Error on total dose-rate (Gy/ka) $(\sqrt{(0.070^2 + 0.073^2 + 0.024^2)})$

The final dose-rate and associated error, and all the values calculated throughout the working are identical to those produced in LDB2005, indicating that it is working correctly.

APPENDIX B: PARAMETERS OBTAINED FROM FITTING OF LM-OSL CURVES

The table below details the photoionisation cross-sections (cm^2) calculated for the components obtained from curve deconvolution of LM-OSL measurements of the natural (N) and regenerated (R) signals from six Klip River samples (70KA1-6) and two samples from the Schoonspruit (91SC0408 and 91SC0410).

	70KLA1		70KLA2		70KLA3	
Component	N	R	N	R	N	R
Fast	2.20×10^{-17}	1.71×10^{-17}	2.43×10^{-17}	2.25×10^{-17}	2.32×10^{-17}	2.55×10^{-17}
Medium	2.12×10^{-18}				5.82×10^{-18}	8.99×10^{-18}
Slow 3			7.86×10^{-19}		1.43×10^{-20}	
Slow 4	9.52×10^{-21}	4.76×10^{-21}	9.52×10^{-21}	4.76×10^{-21}		4.76×10^{-21}

	70KLA4		70KLA5		70KLA6	
Component	N	R	N	R	N	R
Fast	2.22×10^{-17}	2.44×10^{-17}	2.57×10^{-17}	2.50×10^{-17}	2.26×10^{-17}	2.64×10^{-17}
Medium		7.59×10^{-18}	6.70×10^{-18}	3.63×10^{-18}	4.14×10^{-18}	9.36×10^{-18}
Slow 3						
Slow 4	4.76×10^{-21}	4.76×10^{-21}	9.52×10^{-21}	4.76×10^{-21}	4.76×10^{-21}	4.76×10^{-21}

	91SC0408		91SC0410	
Component	N	R	N	R
Fast	2.32×10^{-17}	2.30×10^{-17}	2.59×10^{-17}	2.54×10^{-17}
Medium	3.14×10^{-18}	2.52×10^{-18}	1.42×10^{-18}	
Slow 3	1.93×10^{-19}	3.67×10^{-19}		
Slow 4	1.21×10^{-20}	8.09×10^{-21}	1.32×10^{-21}	9.66×10^{-21}

The tables below contain the parameters derived from curve deconvolution of LM-OSL curves., detailing the number of trapped electrons (n) and the detrapping probability (b). The best fit number of component is highlighted in bold. Error values are not included for clarity.

Sample: 70KLA1

	Natural				Regenerated dose (4.6 Gy)			
Number of components:	2	3	4	5	2	3	4	5
R^2	***0.691***	***0.691***	***0.704***	***0.704***	***0.949***	***0.792***	***0.791***	***0.791***
n1	4.33×10^4	4.33×10^4	**3.51×10^4**	3.51×10^4	**8.06×10^4**	8.01×10^4	8.06×10^4	8.06×10^4
b1	0.3527	0.3527	**0.4621**	0.4618	**0.3595**	0.3625	0.3593	0.3595
n2	2.05×10^6	1.03×10^6	**2.11×10^4**	2.11×10^4	**3.29×10^6**	2.32×10^5	1.65×10^6	1.08×10^6
b2	0.0002	0.0002	**0.0445**	0.0444	**0.0001**	0.0008	0.0001	0.0001
n3		1.03×10^6	**1.08×10^6**	7.17×10^5		7.83×10^7	1.65×10^6	1.08×10^6
b3		0.0002	**0.0002**	0.0002		0.0000	0.0001	0.0001
n4			**1.08×10^6**	7.17×10^5			5.93×10^5	1.08×10^6
b4			**0.0002**	0.0002			0.0000	0.0001
n5				7.17×10^5				3.55×10^6
b5				0.0002				0.0000

Sample: 70KLA2

	Natural				Regenerated dose (4.6 Gy)			
Number of components:	2	3	4	5	2	3	4	5
R^2	***0.922***	***0.923***		***0.922***	***0.900***	***0.904***	***0.900***	***0.297***
n1	1.53×10^5	**1.51×10^5**		1.53^5	1.05×10^5	**1.03×10^5**	1.05×10^5	1.46×10^6
b1	0.5034	**0.5110**		0.5032	0.4730	**0.4871**	0.4730	0.0001
n2	4.29×10^6	**1.43×10^4**		1.48×10^7	4.83×10^6	**4.78×10^6**	2.41×10^6	1.46×10^6
b2	0.0002	**0.0165**		0.0001	0.0001	**0.0001**	0.0001	0.0001
n3		**4.44×10^6**		4.87×10^0		**2.00×10^5**	2.41×10^6	1.46×10^6
b3		**0.0002**		0.0000		**0.0000**	0.0001	0.0001
n4				1.31×10^3			5.67×10^{-2}	2.59×10^{-2}
b4				9.22×10^5			0.0000	0.0000
n5				-2.07×10^7				1.34×10^0
b5				0.0000				0.0000

Sample: 70KLA3

	Natural				Regenerated dose (4.6 Gy)			
Number of components:	2	3	4	5	2	3	4	5
R^2	***0.994***	***0.998***	***0.994***	***0.998***	***0.932***	***0.935***	***0.932***	***0.932***
n1	1.95×10^{6}	**1.72×10^{6}**	1.95×10^{6}	1.68×10^{6}	1.83×10^{5}	**1.29×10^{5}**	1.83×10^{5}	1.83×10^{5}
b1	0.4337	**0.4864**	0.4337	0.4933	0.4111	**0.5345**	0.4111	0.4111
n2	7.97×10^{6}	**3.29×10^{5}**	4.01×10^{6}	3.53×10^{5}	6.14×10^{6}	**6.47×10^{4}**	3.07×10^{6}	2.05×10^{6}
b2	0.0003	**0.1222**	0.0003	0.1460	0.0001	**0.1887**	0.0001	0.0001
n3		**8.19×10^{6}**	4.01×10^{6}	1.00×10^{5}		**6.21×10^{6}**	3.07×10^{6}	2.05×10^{6}
b3		**0.0003**	0.0003	0.0063		**0.0001**	0.0001	0.0001
n4			7.92×10^{6}	4.10×10^{6}			1.44×10^{-1}	2.05×10^{6}
b4			0.0000	0.0003			0.0000	0.0001
n5				5.50×10^{6}				2.25×10^{-1}
b5				0.0001				0.0000

Sample: 70KLA4

	Natural				Regenerated dose (4.6 Gy)			
Number of components:	2	3	4	5	2	3	4	5
R^2	***0.910***	***0.910***	***0.910***	***0.859***	***0.932***	***0.933***	***0.680***	***0.680***
n1	**2.51×10^4**	2.51×10^4	2.51×10^4	8.40×10^4	9.23×10^4	**8.49×10^4**	2.57×10^6	1.68×10^6
b1	**0.4653**	0.4653	0.4653	0.4900	0.4771	**0.5119**	0.0001	0.0001
n2	**6.71×10^6**	3.35×10^6	3.35×10^6	1.03×10^7	1.06×10^7	**9.88×10^3**	2.57×10^6	1.68×10^6
b2	**0.0001**	0.0001	0.0001	0.0001	0.0001	**0.1594**	0.0001	0.0001
n3		3.35×10^6	3.35×10^6	8.34×10^4		**1.07×10^7**	4.10×10^6	1.68×10^6
b3		0.0001	0.0001	0.0000		**0.0001**	0.0000	0.0001
n4			8.47×10^{-2}	9.26×10^4			5.51×10^6	9.16×10^6
b4			0.0000	0.0000			0.0000	0.0000
n5				-1.84×10^7				5.18×10^6
b5				0.0000				0.0000

Sample: 70KLA5

	Natural				Regenerated dose (4.6 Gy)			
Number of components:	2	3	4	5	2	3	4	5
R^2	***0.859***	***0.860***	***0.860***	***0.859***	***0.904***	***0.905***	***0.400***	***0.399***
n1	8.39×10^{4}	**7.56×10^{4}**	7.56×10^{4}	8.40×10^{4}	1.11×10^{5}	**1.05×10^{5}**	4.67×10^{6}	2.32×10^{1}
b1	0.4902	**0.5393**	0.5394	0.4900	0.4937	**0.5240**	0.0001	0.0111
n2	3.32×10^{6}	**1.20×10^{4}**	1.20×10^{4}	1.03×10^{7}	4.94×10^{6}	**1.25×10^{4}**	1.51×10^{4}	1.10×10^{2}
b2	0.0002	**0.1406**	0.1410	0.0001	0.0001	**0.0762**	0.0000	0.0013
n3		**3.35×10^{6}**	3.35×10^{6}	8.34×10^{4}		**5.00×10^{6}**	6.89×10^{3}	8.43×10^{4}
b3		**0.0002**	0.0002	0.0000		**0.0001**	0.0000	0.0050
n4			0.00×10^{0}	9.26×10^{4}			0.00×10^{0}	1.22×10^{7}
b4			2.72×10^{7}	0.0000			0.0000	0.0001
n5				-1.84×10^{7}				-9.69×10^{6}
b5				0.0000				0.0000

Sample: 70KLA6

	Natural				Regenerated dose (4.6 Gy)			
Number of components:	2	3	4	5	2	3	4	5
R^2	***0.914***	***0.916***	***0.904***	***0.915***	***0.824***	***0.825***	***0.824***	***0.824***
n1	1.50×10^{5}	**1.38×10^{5}**	1.50×10^{5}	1.50×10^{5}	4.09×10^{4}	**2.60×10^{4}**	4.09×10^{4}	4.09×10^{4}
b1	0.4380	**0.4746**	0.4356	0.4379	0.4003	**0.5548**	0.4003	0.4003
n2	4.47×10^{6}	**1.99×10^{4}**	8.75×10^{6}	1.26×10^{7}	4.59×10^{6}	**1.73×10^{4}**	2.29×10^{6}	1.53×10^{6}
b2	0.0001	**0.0870**	0.0001	0.0001	0.0001	**0.1966**	0.0001	0.0001
n3		**4.55×10^{6}**	3.26×10^{5}	-1.50×10^{7}		**4.63×10^{6}**	2.29×10^{6}	1.53×10^{6}
b3		**0.0001**	0.0000	0.0000		**0.0001**	0.0001	0.0001
n4			0.00×10^{0}	6.02×10^{0}			1.38×10^{-2}	1.53×10^{6}
b4			1.15×10^{7}	0.0000			0.0000	0.0001
n5				1.45×10^{-2}				5.67×10^{-2}
b5				1.41×10^{6}				0.0000

Sample: 91SC0408

	Natural				Regenerated dose (4.6 Gy)			
Number of components:	2	3	4	5	2	3	4	5
R^2	***0.930***	***0.964***	***0.991***	***0.991***	***0.977***	***0.989***	***0.994***	***0.993***
n1	1.17×10^6	1.16×10^6	**1.03×10^6**	1.02×10^6	1.12×10^6	2.42×10^6	**1.02×10^6**	1.02×10^6
b1	0.4172	0.4258	**0.4882**	0.4918	0.4348	78410.0000	**0.4844**	0.4853
n2	1.87×10^7	3.78×10^6	**2.60×10^5**	2.46×10^5	2.40×10^7	1.13×10^6	**2.22×10^5**	2.07×10^5
b2	0.0004	0.0014	**0.0661**	0.0761	0.0002	0.4282	**0.0532**	0.0572
n3		3.44×10^9	**8.49×10^5**	5.48×10^5		3.56×10^9	**1.69×10^5**	1.56×10^5
b3		0.0000	**0.0041**	0.0059		0.0000	**0.0077**	0.0104
n4			**2.20×10^7**	4.44×10^6			**2.65×10^7**	6.00×10^6
b4			**0.0003**	0.0007			**0.0002**	0.0003
n5				3.17×10^7				3.33×10^7
b5				0.0001				0.0001

Sample: 91SC0410

	Natural				Regenerated dose (4.6 Gy)			
Number of components:	2	3	4	5	2	3	4	5
R^2	***0.988***	***0.995***	***0.994***	***0.994***	***0.988***	***0.889***	***0.987***	***0.995***
n1	3.25×10^{6}	**3.14×10^{6}**	1.57×10^{6}	3.09×10^{6}	1.78×10^{6}	2.27×10^{-4}	1.78×10^{6}	**1.68×10^{6}**
b1	0.5232	**0.5455**	0.5447	0.5537	0.5345	3.26 x 10+08	0.5347	**0.5761**
n2	3.14×10^{7}	**5.13×10^{5}**	1.57×10^{6}	3.65×10^{5}	4.81×10^{7}	1.80×10^{6}	1.34×10^{7}	**3.57×10^{5}**
b2	0.0003	**0.0299**	0.5463	0.0605	0.0002	0.5261	0.0003	**0.0465**
n3		**3.25×10^{7}**	5.13×10^{5}	4.03×10^{5}		1.02×10^{10}	1.34×10^{7}	**9.70×10^{6}**
b3		**0.0003**	0.0299	0.0059		0.0000	0.0003	**0.0003**
n4			3.25×10^{7}	3.16×10^{6}			3.49×10^{7}	**9.18×10^{6}**
b4			0.0003	0.0006			0.0001	**0.0003**
n5				3.40×10^{7}				**4.39×10^{7}**
b5				0.0002				**0.0001**

APPENDIX C: DOSE RECOVERY AND PREHEAT PLOTS

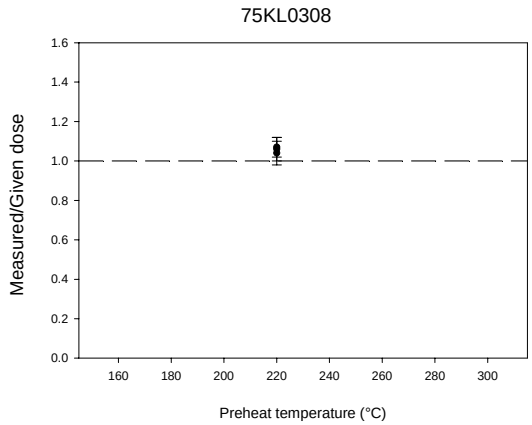

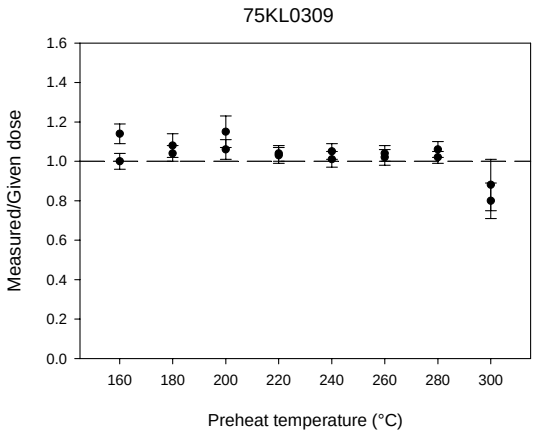

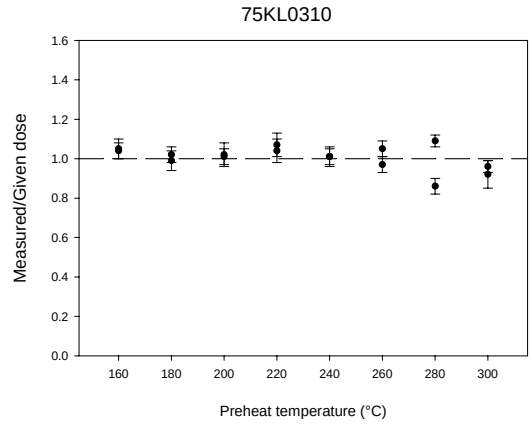

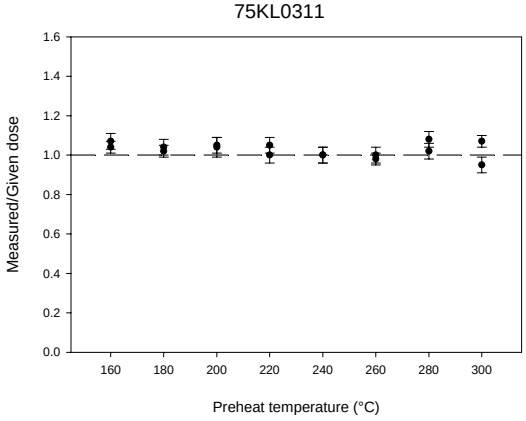

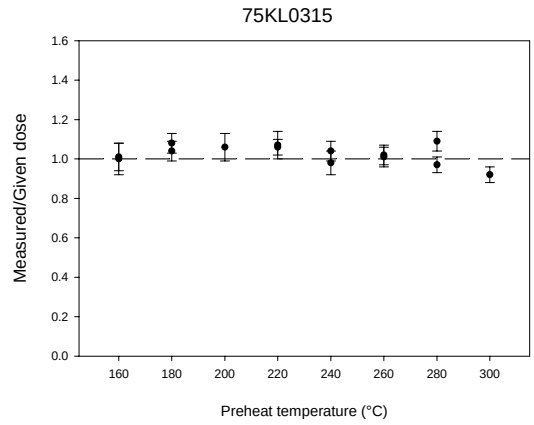

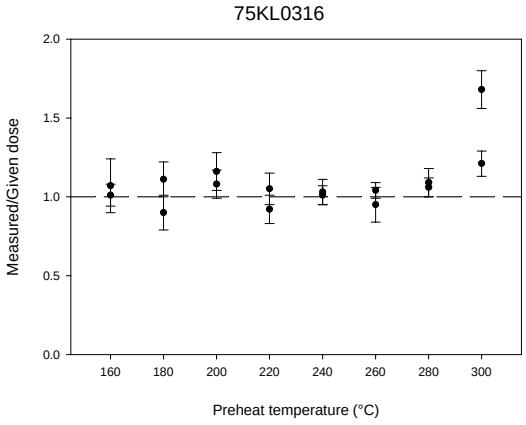

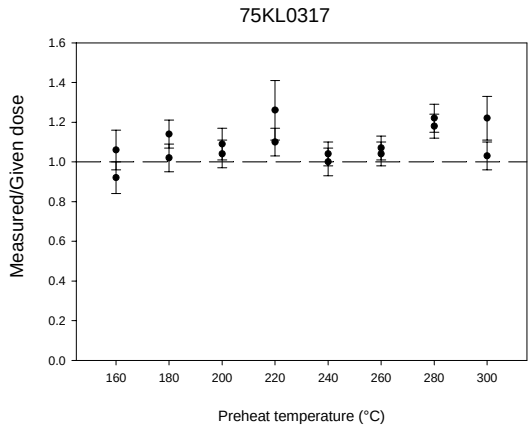
75KL0317
Measured/Given dose
Preheat temperature (°C)

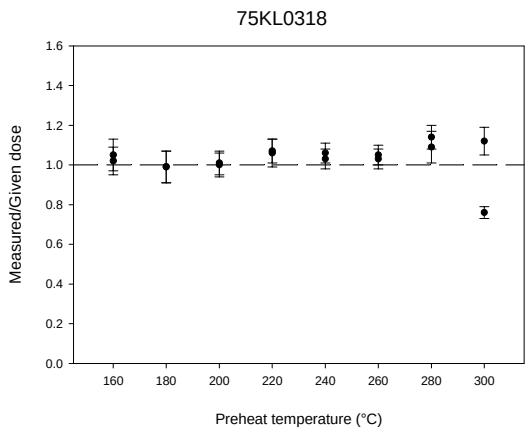
75KL0318
Measured/Given dose
Preheat temperature (°C)

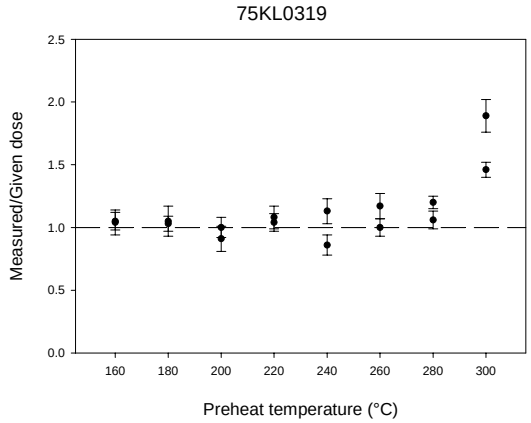
75KL0319
Measured/Given dose
Preheat temperature (°C)

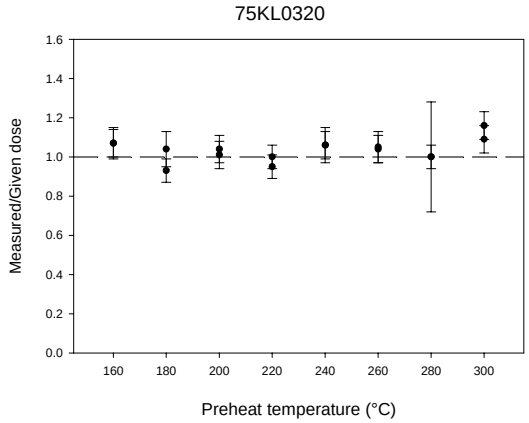
75KL0320
Measured/Given dose
Preheat temperature (°C)

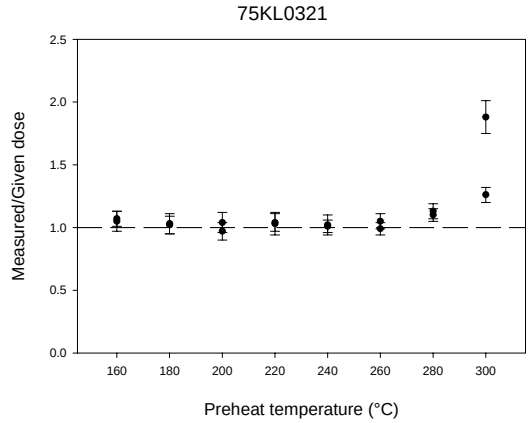
75KL0321
Measured/Given dose
Preheat temperature (°C)

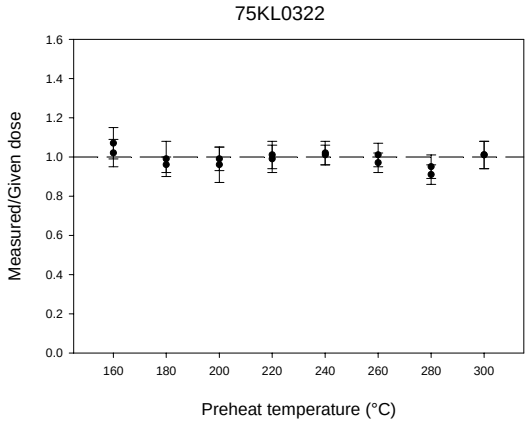
75KL0322
Measured/Given dose
Preheat temperature (°C)

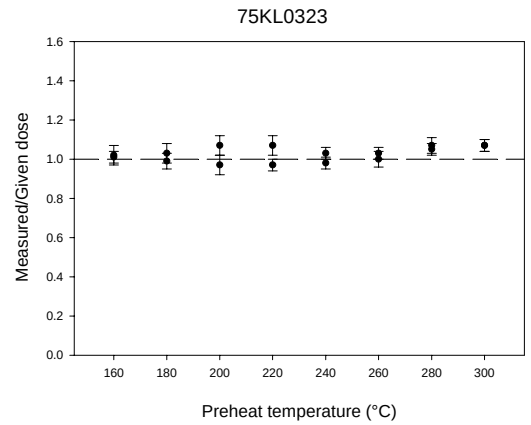
75KL0323
Measured/Given dose
Preheat temperature (°C)

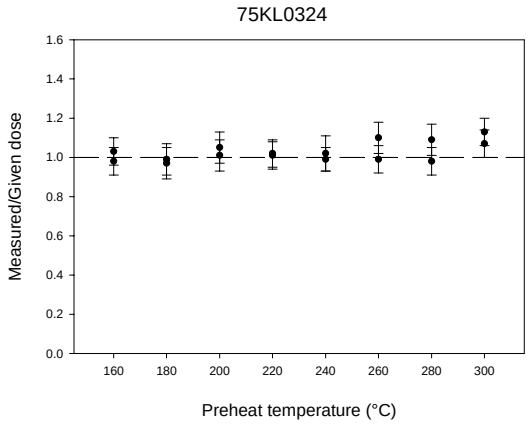
75KL0324
Measured/Given dose
Preheat temperature (°C)

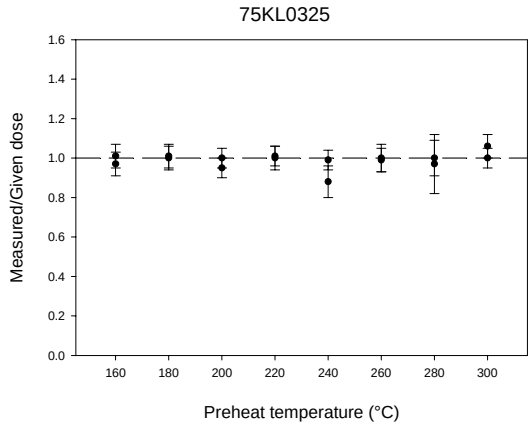
75KL0325
Measured/Given dose
Preheat temperature (°C)

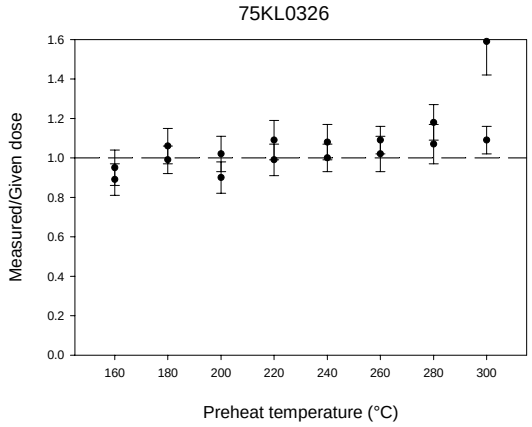
75KL0326
Measured/Given dose
Preheat temperature (°C)

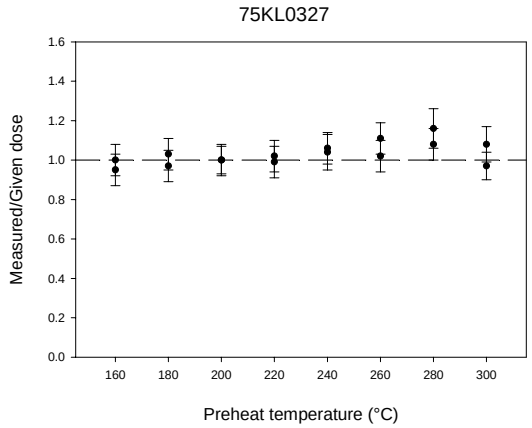
75KL0327
Measured/Given dose
Preheat temperature (°C)

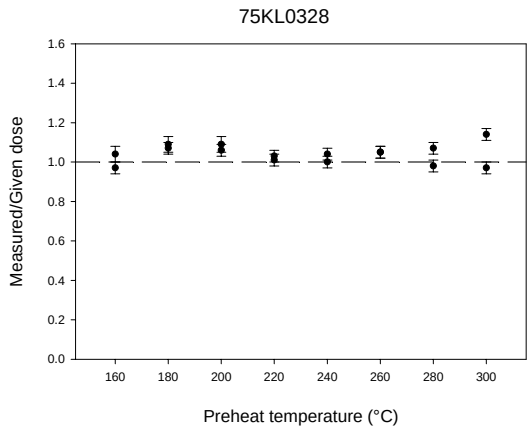
75KL0328
Measured/Given dose
Preheat temperature (°C)

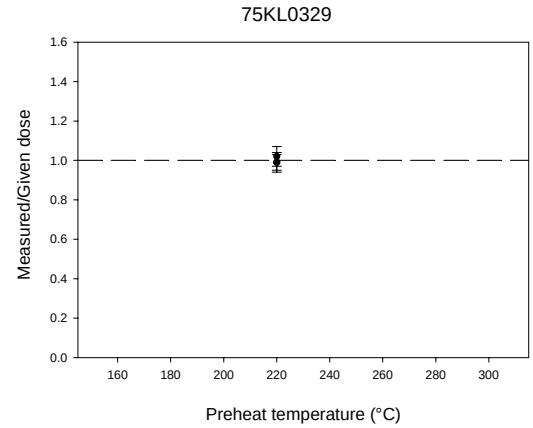
75KL0329
Measured/Given dose
Preheat temperature (°C)

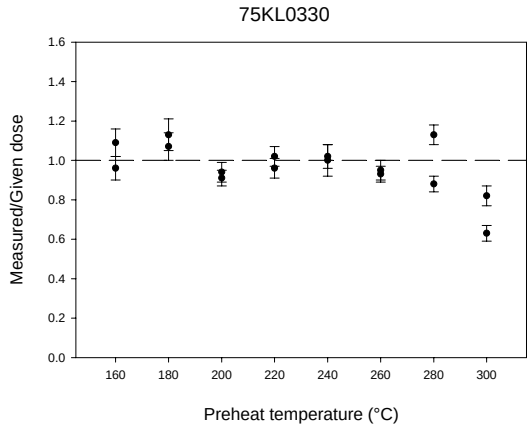
75KL0330
Measured/Given dose
Preheat temperature (°C)

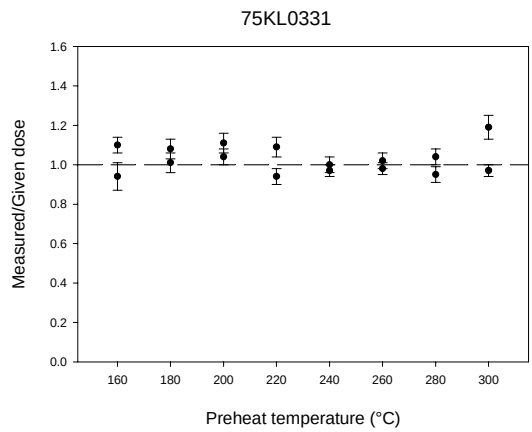
75KL0331
Measured/Given dose
Preheat temperature (°C)

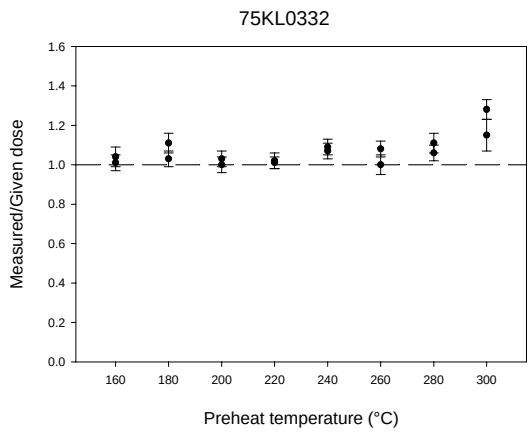
75KL0332
Measured/Given dose
Preheat temperature (°C)

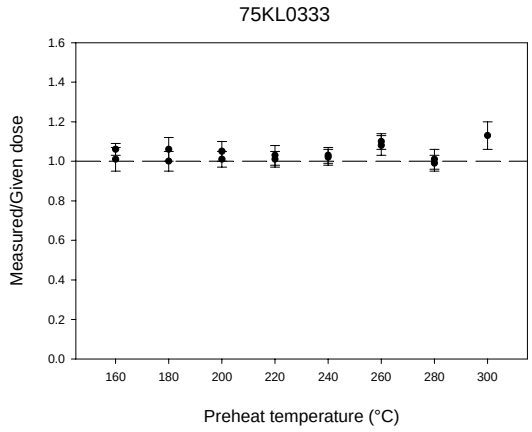
75KL0333
Measured/Given dose
Preheat temperature (°C)

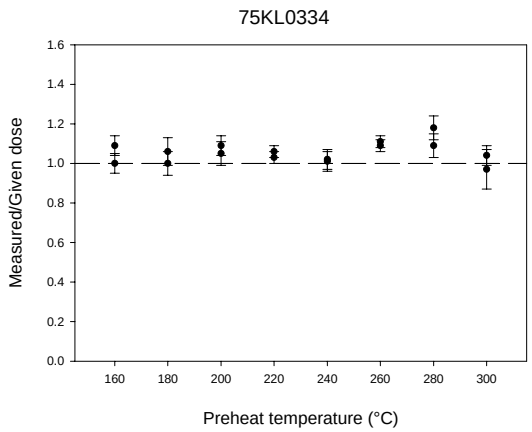
75KL0334
Measured/Given dose
Preheat temperature (°C)

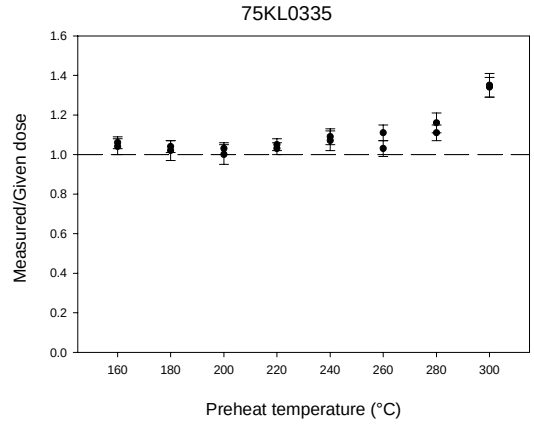
75KL0335
Measured/Given dose
Preheat temperature (°C)

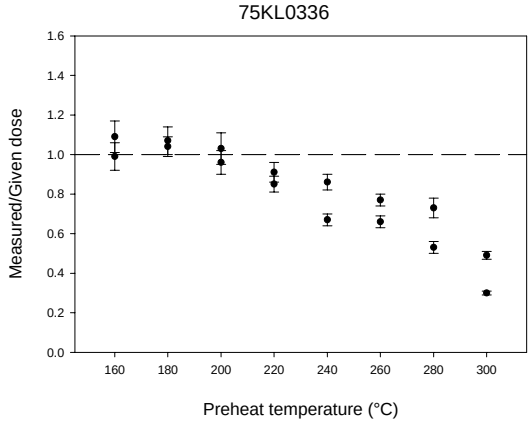
75KL0336
Measured/Given dose
Preheat temperature (°C)

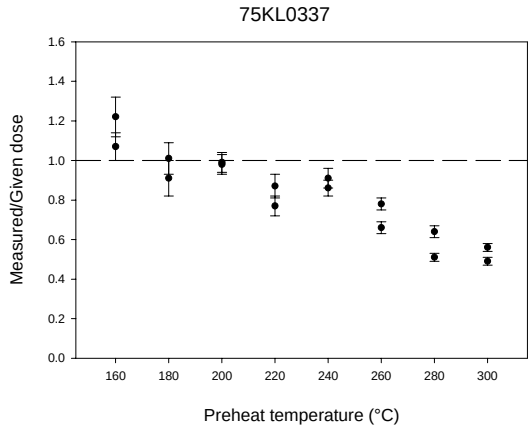
75KL0337
Measured/Given dose
Preheat temperature (°C)

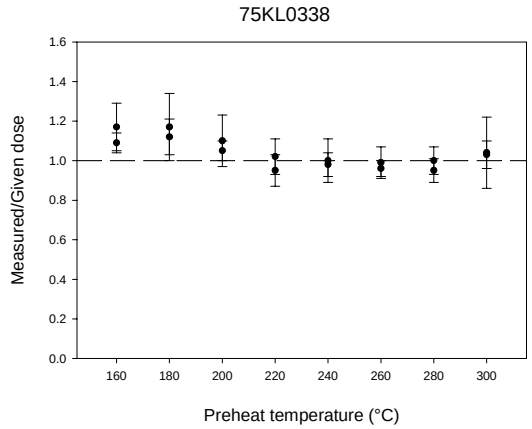
75KL0338
Measured/Given dose
Preheat temperature (°C)

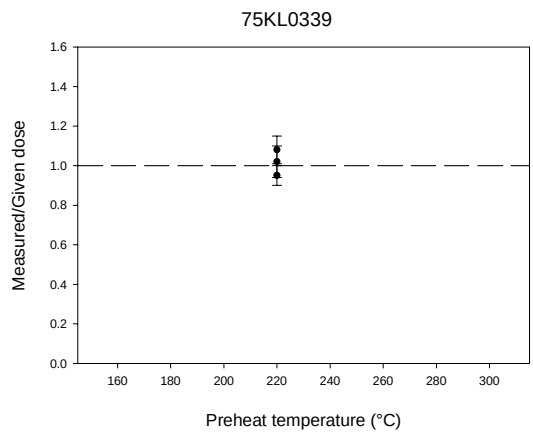
75KL0339
Measured/Given dose
Preheat temperature (°C)

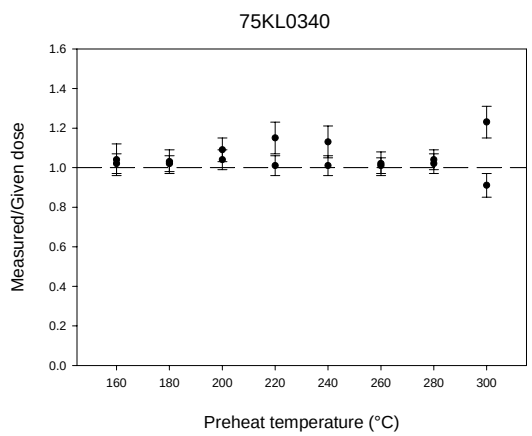
75KL0340
Measured/Given dose
Preheat temperature (°C)

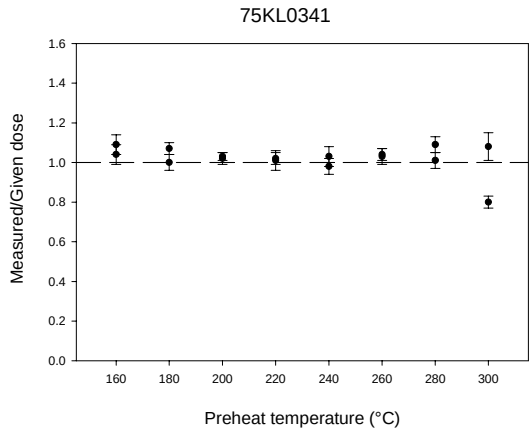
75KL0341
Measured/Given dose
Preheat temperature (°C)

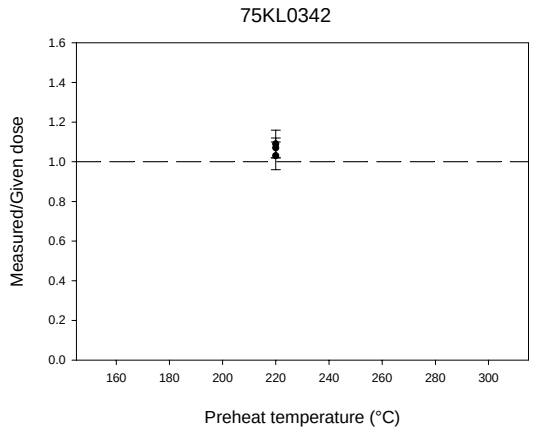
75KL0342
Measured/Given dose
Preheat temperature (°C)

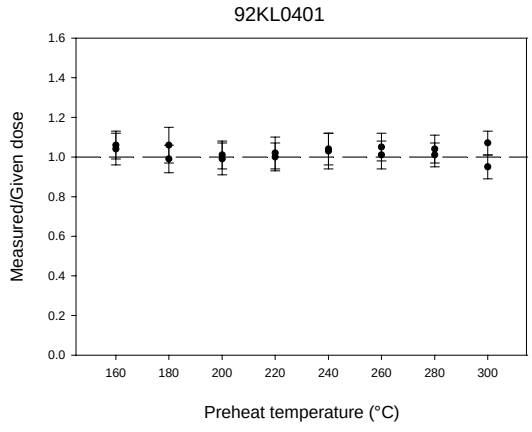
92KL0401
Measured/Given dose
Preheat temperature (°C)

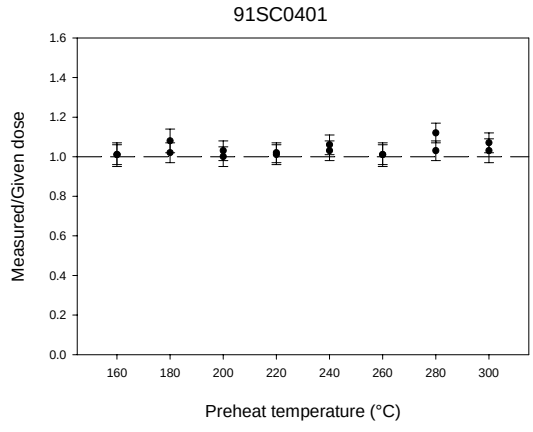
91SC0401
Measured/Given dose
Preheat temperature (°C)

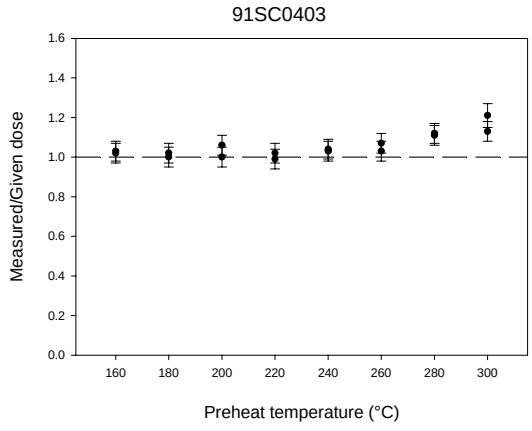
91SC0403
Measured/Given dose
Preheat temperature (°C)

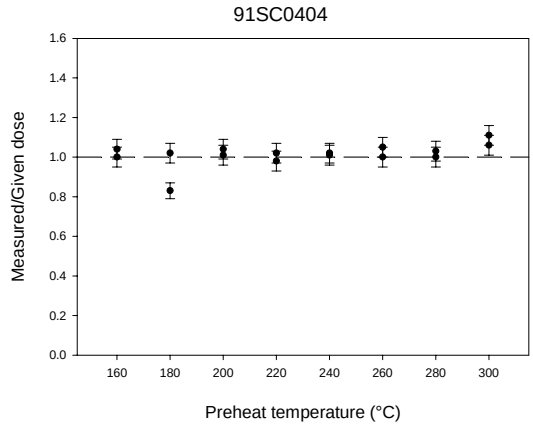
91SC0404
Measured/Given dose
Preheat temperature (°C)

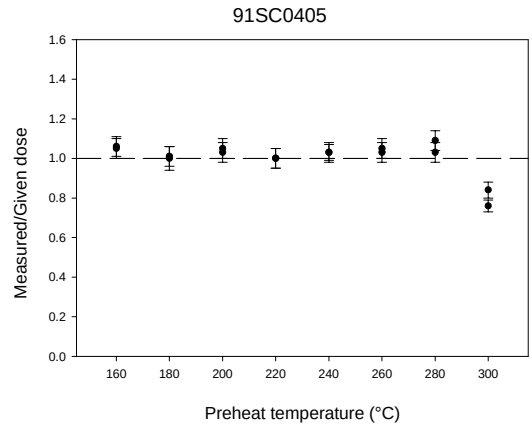
91SC0405
Measured/Given dose
Preheat temperature (°C)

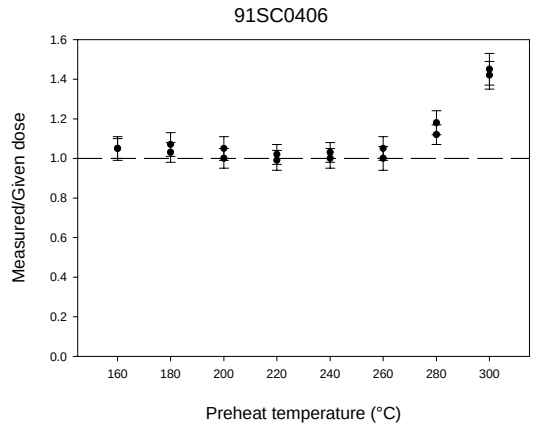
91SC0406
Measured/Given dose
Preheat temperature (°C)

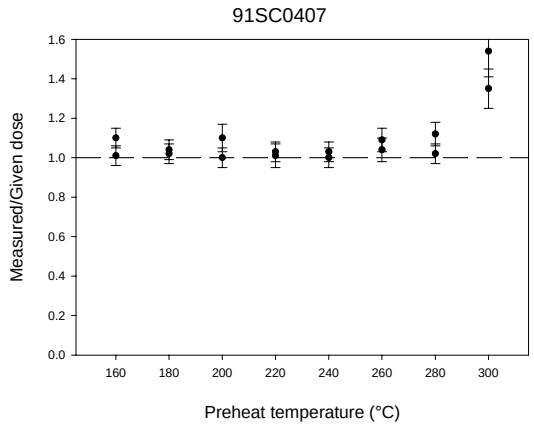
91SC0407
Measured/Given dose
Preheat temperature (°C)

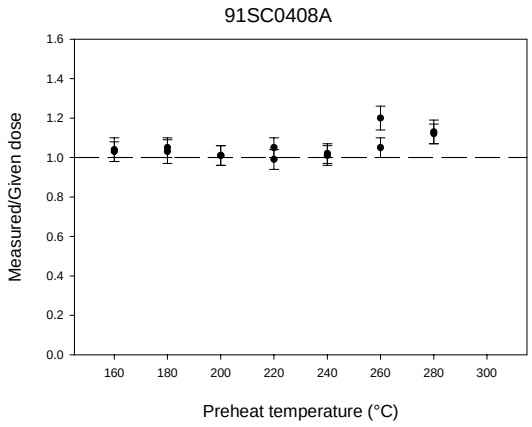
91SC0408A
Measured/Given dose
Preheat temperature (°C)

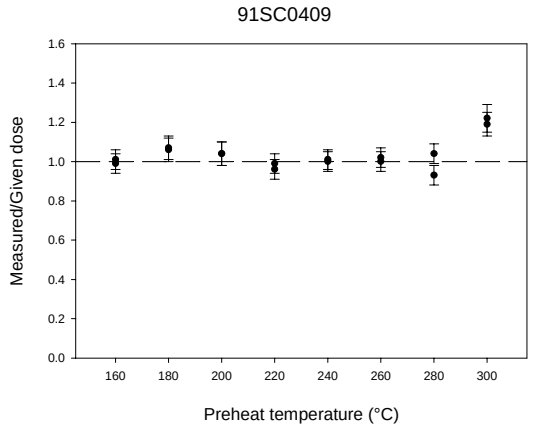
91SC0409
Measured/Given dose
Preheat temperature (°C)

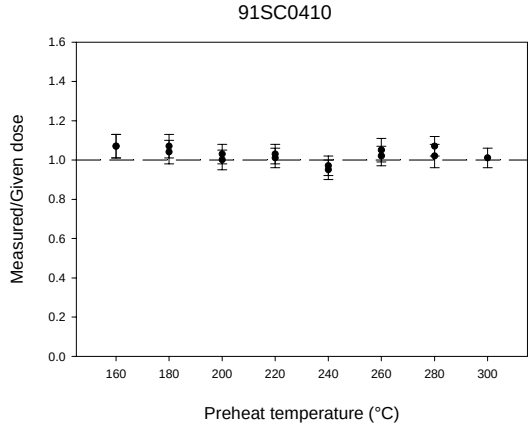
91SC0410
Measured/Given dose
Preheat temperature (°C)

APPENDIX D: CALCULATION OF ERRORS ASSOCIATED WITH COUNTING STATISTICS AND CURVE FITTING

The errors associated with each OSL measurement (L_X and T_X) are calculated, then combined to get an error for each L_X/T_X ratio, and then incorporated into the uncertainty for the fitting of the growth curve. The error on each OSL measurement is found using the equation described by Galbraith (2002), as a correction of the equation first proposed by Banerjee *et al.* (2000). The relative standard deviation (rse) on each OSL signal can be calculated, taking into account background counts, using the equation:

$$rse = \frac{\sqrt{Y_0 + \left(\overline{Y}/k\right)}}{Y_0 - \overline{Y}} \qquad \text{[Eqn. D.1]}$$

where Y_0 is the integral of the counts in the initial five bins (used to obtain L_X or T_X), $\overline{Y}$ is the mean background count (scaled using *k* to be equivalent for the number of channels used for Y_0). After the rse is calculated for each OSL stimulation, it is combined in quadrature to give the error on each L_X/T_X ratio due to counting statistics.

Once a growth curve is fitted through the L_X/T_X data points, the deviation of the fit from the actual points is used to calculate the uncertainty of the fit (Duller, 2005). This is calculated using the equation:

$$Deviation = \frac{\sqrt{\sum_1^n \left(calculated\ L_X/T_X - actual\ L_X/T_X\right)^2}}{n} \qquad \text{[Eqn. D.2]}$$

where *n* is the number of regenerated doses. The figure for the deviation of the fitted growth curve from the actual data is combined with the uncertainty associated with L_N/T_N, to determine the error on the D_e value due to counting statistics and the curve fitting procedure.

APPENDIX E: CALIBRATION OF BETA SOURCES AND CALCULATION OF DOSE-RATE

During the course of this study, the beta sources on Risø 2 and 3 were calibrated by H. Roberts or myself using a “calibration quartz” (180-212 µm) which has been previously gamma irradiated to a known dose (4.65 Gy or 5.10 Gy), provided by A.S. Murray. For calibration, at least five medium aliquots of the calibration quartz were measured using the standard SAR procedure. The resulting mean D_e value (in seconds) was then used to calculate the beta dose-rate. The results from the calibration performed on the readers used in this study are shown in Figure E.1. The dose-rate at times between calibrations can be calculated using the equation:

$$N(t) = N_0 e^{-\lambda t}$$

where N_0 is the dose-rate at time t = 0, and λ is the probability of decay per unit of time related to the half-life ($\tau_{1/2}$) by $\lambda = 0.693/\tau_{1/2}$ (Aitken, 1985). The half-life of $^{90}Sr/^{90}Y$ is known to be 28.79 years (Chu *et al.*, 1999). From the above equation, the dose-rate at any point in time can be calculated, and used to convert the D_e values from seconds to Gray.

a)

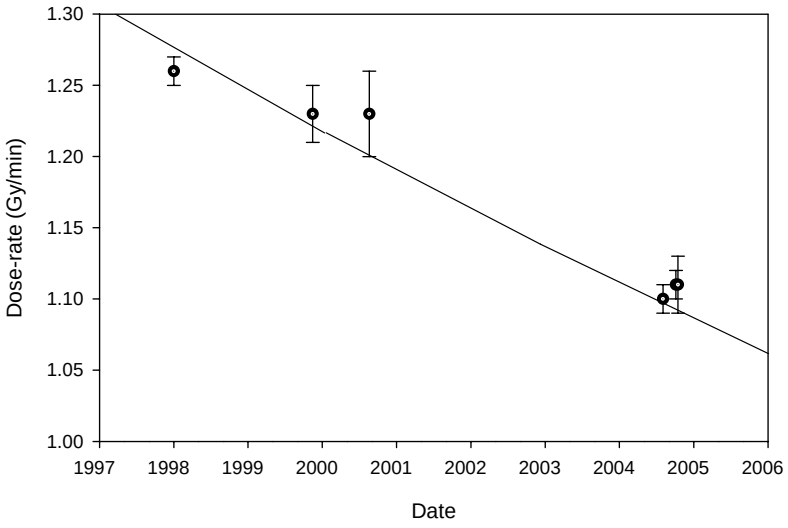

b)

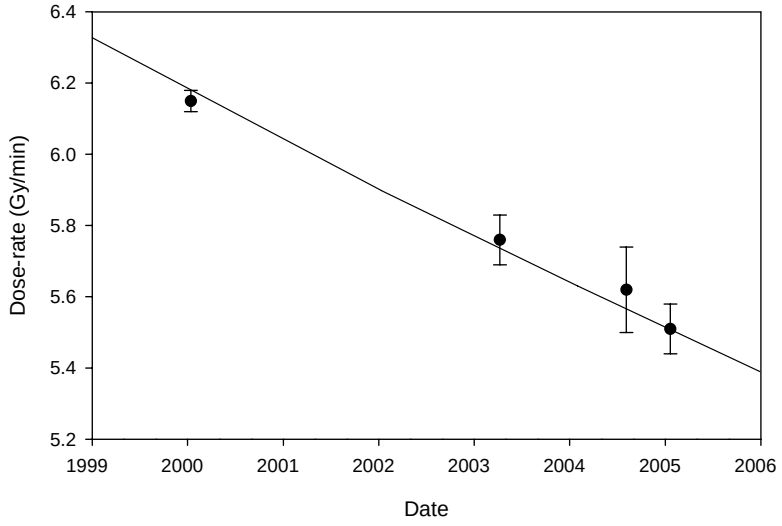

Figure E.1: Dose-rate of beta sources in a) Risø 2, and b) Risø 3. The solid circles represent values obtained from calibrations, and the solid line indicates the calculated dose-rate through time.

APPENDIX F: DETAILS OF RADIOCARBON ANALYSES

^{14}C sample	Associated OSL sample	Measured ^{14}C age	Conventional ^{14}C age	2σ calibrated results* (cal BP)	2σ calibrated results* (cal BP)	δ ^{13}C	Method of analysis	Material
Beta-197148	75KL0308	1100 ± 40 BP	1110 ± 40 BP	1080 - 940	1060 - 960	-24.2 ‰	AMS	charred material
Beta-197149	75KL0310	3510 ± 50 BP	3620 ± 60 BP	4090 - 3820 3780 - 3730	3990 - 3850	-18.5 ‰	Radiometric: bulk low C analysis	organic sediment
Beta-197150	75KL0342	310 ± 60 BP	330 ± 60 BP	510 - 290	480 - 300	-23.8 ‰	AMS	peat

* Calibrated using the Intcal98 database (Stuiver *et al.*, 1998). No correction for the southern hemisphere was deemed necessary.

APPENDIX G: RADIAL PLOTS OF PALAEOCHANNEL AND OXBOW SAMPLES FROM THE KLIP RIVER

Radial plots of the D_e values for samples from the Seekoeivlei Nature Reserve part of the Klip River floodplain. The D_b value calculated is indicated by the solid line, and the grey shaded band shows those D_e values that are consistent with it within 2σ.

70KLA1

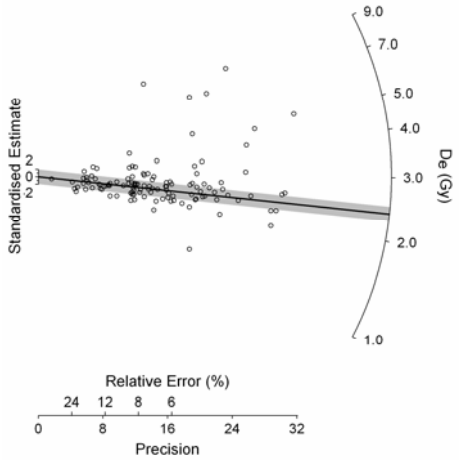

70KLA2

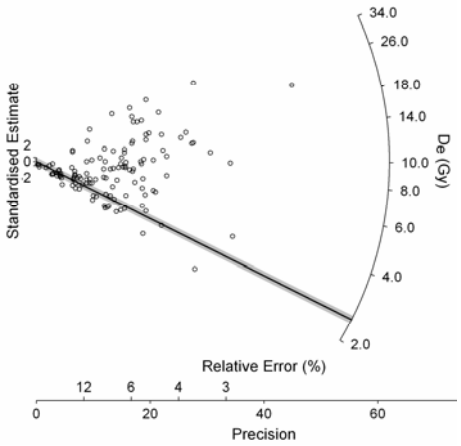

70KLA3

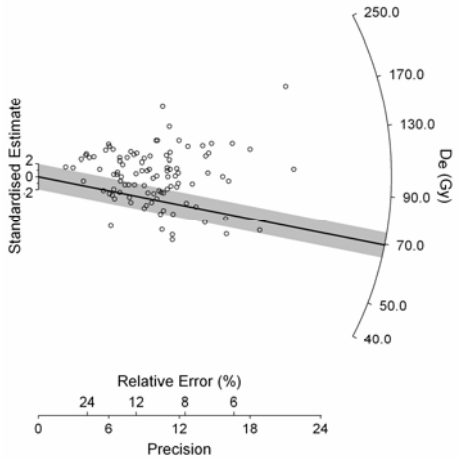

70KLA4

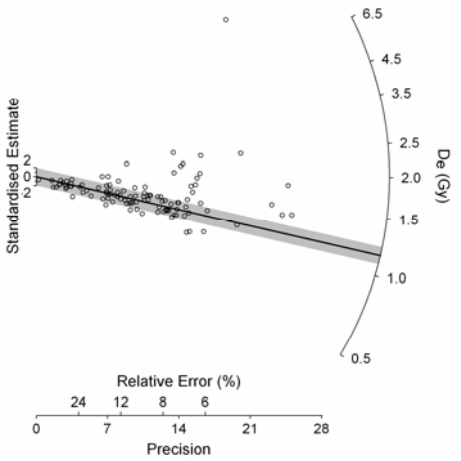

70KLA5

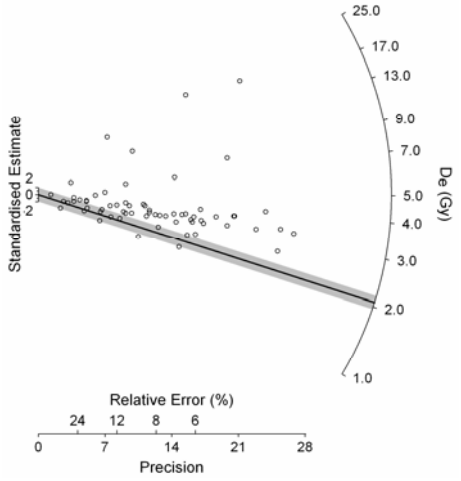

70KLA6

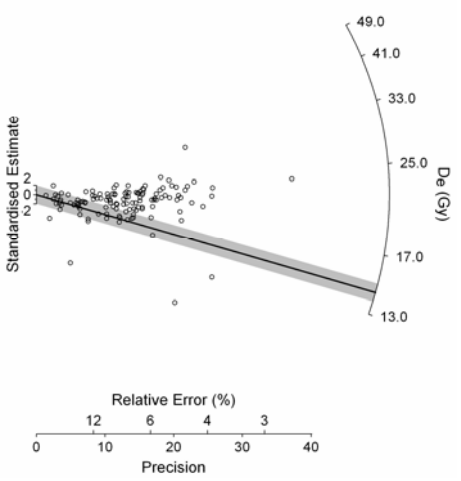

75KL0308

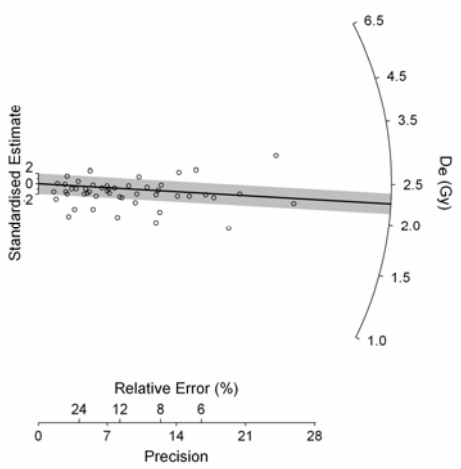

75KL0309

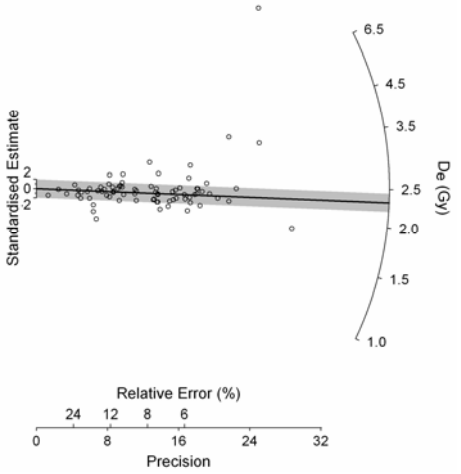

75KL0310

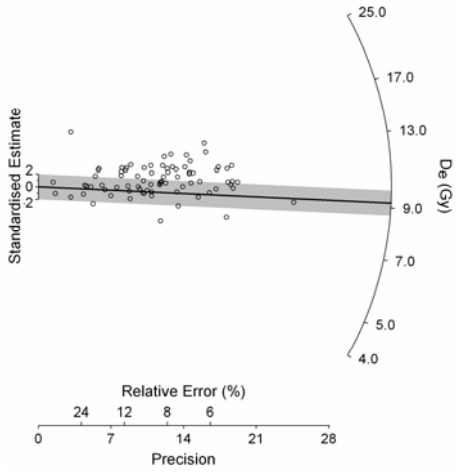

75KL0311

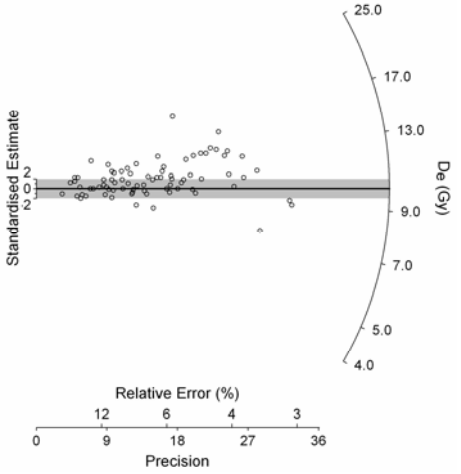

75KL0315

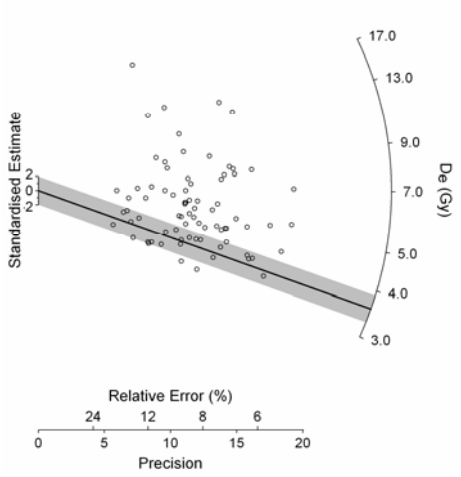

75KL0328

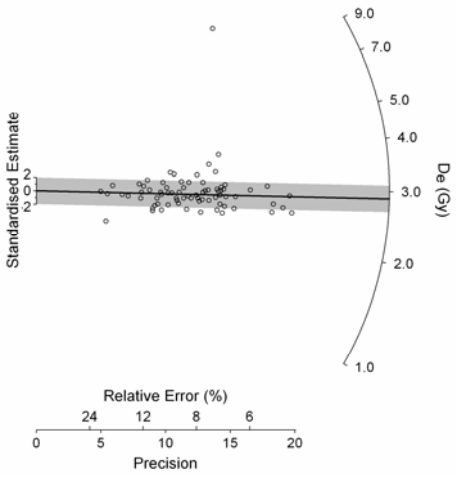

75KL0329

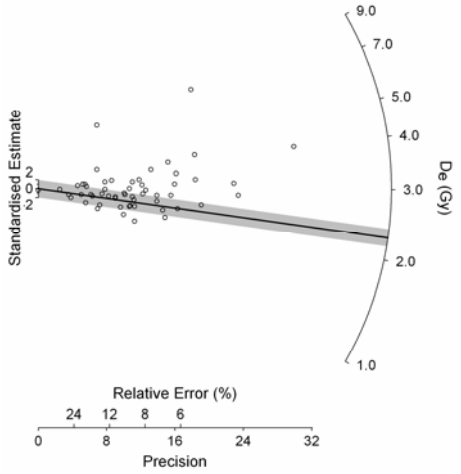

75KL0330

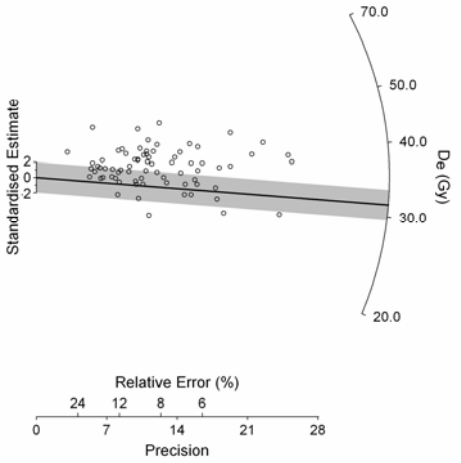

75KL0331

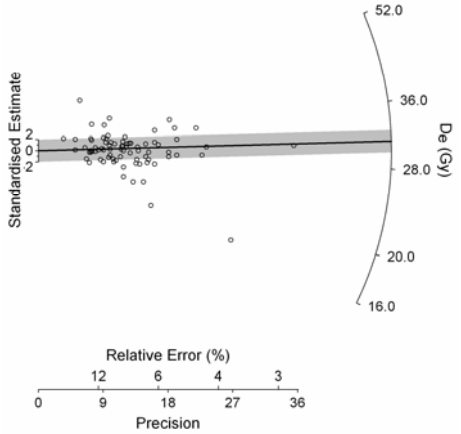

75KL0332

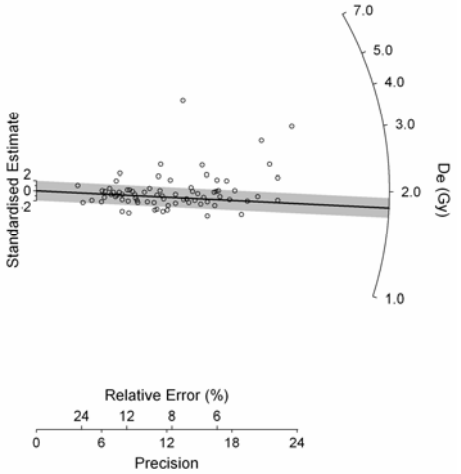

75KL0333

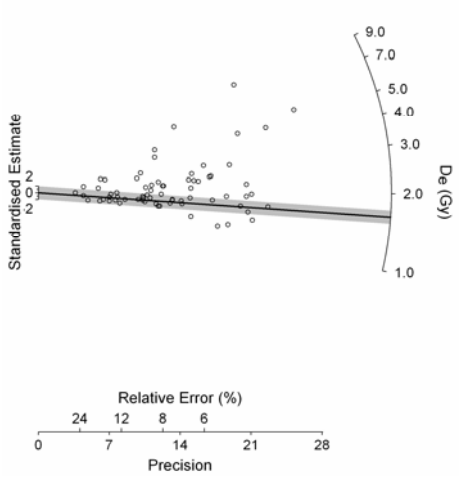

75KL0334

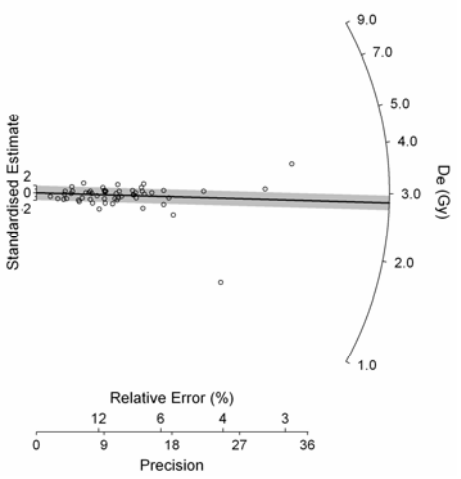

75KL0335

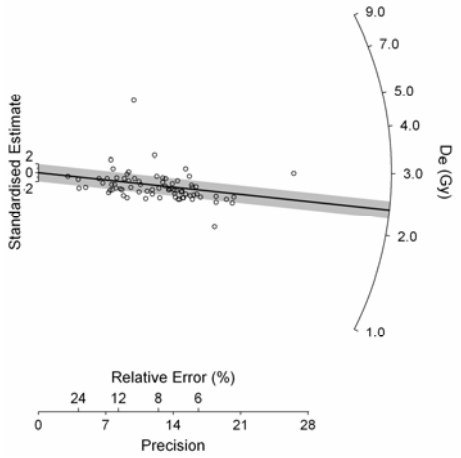

75KL0336

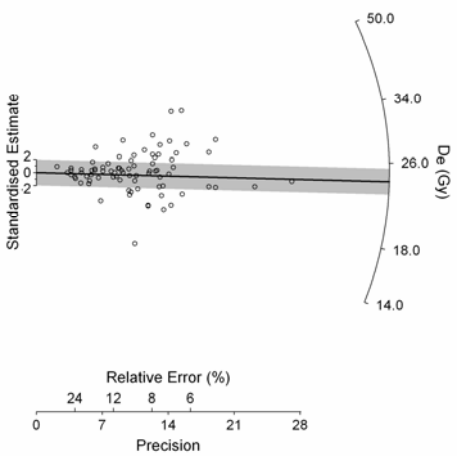

75KL0337

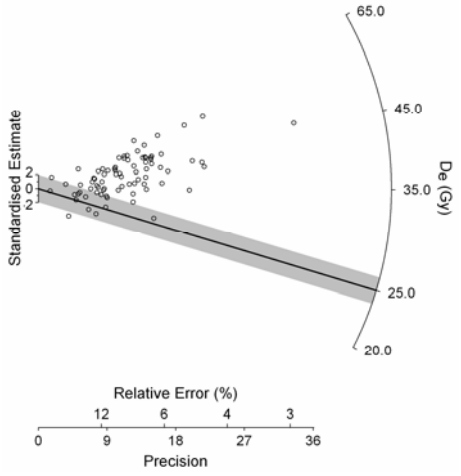

75KL0338

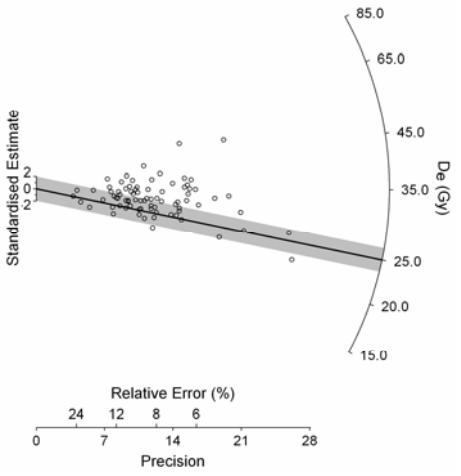

75KL0339

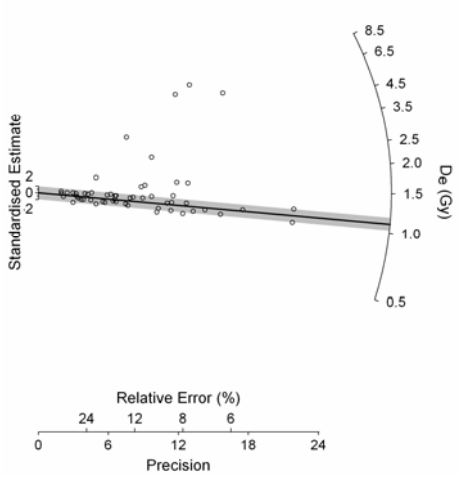

75KL0340

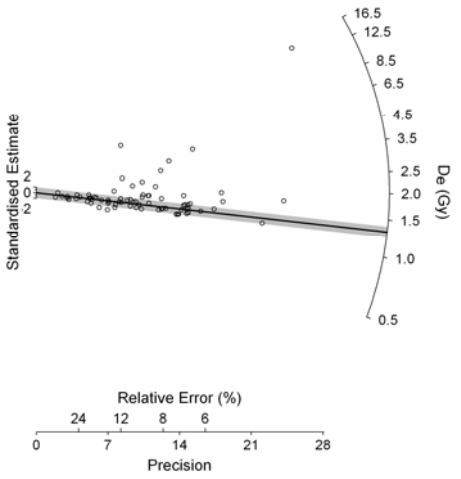

75KL0341

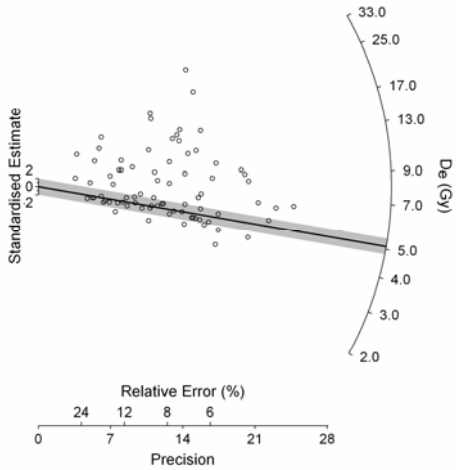

75KL0342

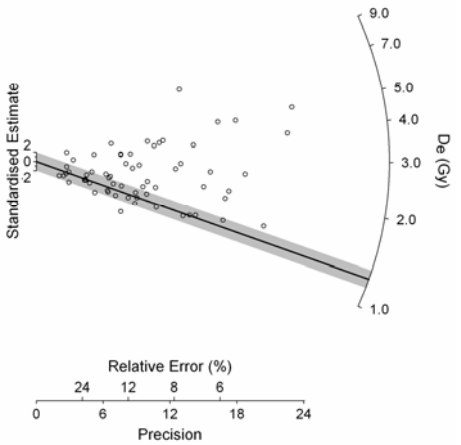

BIBLIOGRAPHY

Adamiec, G. and Aitken, M.J. (1998). Dose-rate conversion factors: update. *Ancient TL* **16**, 37-49.

Aitken, M.J. (1985). "Thermoluminescence Dating". London, Academic Press.

Aitken, M.J. (1990). Pairs precision required in alpha counting. *Ancient TL* **8**, 12-14.

Aitken, M.J. (1998). "An Introduction to Optical Dating". Oxford, Oxford University Press.

Aitken, M.J. and Xie, J. (1990). Moisture correction for annual gamma dose. *Ancient TL* **8**, 6-9.

Allen, J.R.L. (1978). Studies in fluviatile sedimentation: an exploratory quantitative model for the architecture of avulsion-controlled alluvial suites. *Sedimentary Geology* **21**, 129-147.

Argyilan, E.P., Forman, S.L., Johnston, J.W. and Wilcox, D.A. (2005). Optically stimulated luminescence dating of late Holocene raised strandplain sequences adjacent to Lakes Michigan and Superior, Upper Peninsula, Michigan, USA. *Quaternary Research* **63**, 122-135.

Armitage, S.J. (2003). "Testing and application of luminescence techniques using sediment from the southeast African coast". Unpublished PhD thesis, University of Wales, Aberystwyth.

Armitage, S.J., Duller, G.A.T. and Wintle, A.G. (2000). Quartz from southern Africa: sensitivity changes as a result of thermal pretreatment. *Radiation Measurements* **32**, 571-577.

Bailey, R.M. (2000). Circumventing possible inaccuracies of the single aliquot regeneration method for the optical dating of quartz. *Radiation Measurements* **32**, 833-840.

Bailey, R.M. (2000). The interpretation of quartz optically stimulated luminescence equivalent dose versus time plots. *Radiation Measurements* **32**, 129-140.

Bailey, R.M. (2003a). Paper I: The use of measurement-time dependant single-aliquot equivalent-dose estimates from quartz in the identification of incomplete signal resetting. *Radiation Measurements* **37**, 673-683.

Bailey, R.M. (2003b). Paper II: The interpretation of measurement-time-dependant single-aliquot equivalent-dose estimates using predictions from a simple empirical model. *Radiation Measurements* **37**, 685-691.

Bailey, R.M., Singarayer, J.S., Ward, S. and Stokes, S. (2003). Identification of partial resetting using D_e as a function of illumination time. *Radiation Measurements* **37**, 511-518.

Bailey, R.M., Smith, B.W. and Rhodes, E.J. (1997). Partial bleaching and the decay form characteristics of quartz OSL. *Radiation Measurements* **27**, 123-136.

Bailey, S.D., Wintle, A.G., Duller, G.A.T. and Bristow, C.S. (2001). Sand deposition during the last millennium at Aberffraw, Anglesey, North Wales as determined by OSL dating of quartz. *Quaternary Science Reviews* **20**, 701-704.

Banerjee, D., Page, K. and Lepper, K. (2002). Optical dating of palaeochannel deposits in the Riverine Plain, southeastern Australia: testing the reliability of existing thermoluminescence dates. *Radiation Protection Dosimetry* **101**, 327-332.

Barbouti, A.I. and Rustin, B.C. (1983). A study of the absolute intensity of muons at sea level and under various thicknesses of absorber. *Journal of Physics G: Nuclear Physics Dosimetry* **9**, 1577-1595.

Bateman, M.D., Frederick, C.D., Jaiswal, M.J. and Singhvi, A.K. (2003). Investigations into the potential effects of pedoturbation on luminescence dating. *Quaternary Science Reviews* **22**, 1169-1176.

Bell, W.T. (1979). Attenuation factors for the absorbed radiation dose in quartz inclusions for thermoluminescence dating. *Ancient TL* **8**, 2-13.

Berger, G.W. and Luternauer, J.L. (1987). Preliminary field work for thermoluminescence dating studies at the Fraser River delta. British Columbia. *Geological Survey of Canada Paper* **87/1A**, 901-904.

Bøtter-Jensen, L. (1997). Luminescence techniques: instrumentation and methods. *Radiation Measurements* **27**, 749-768.

Bøtter-Jensen, L. and Duller, G.A.T. (1992). A new system for measuring OSL from quartz samples. *Nuclear Tracks and Radiation Measurements* **20**, 549-553.

Bøtter-Jensen, L. and Mejdahl, V. (1988). Assessment of beta dose-rate using a GM multicounter system. Nuclear Tracks and *Radiation Measurements* **14**, 187-191.

Bøtter-Jensen, L., Andersen, C.E., Duller, G.A.T. and Murray, A.S. (2003a). Developments in radiation, stimulation and observation facilities in luminescence measurements. *Radiation Measurements* **37**, 535-541.

Bøtter-Jensen, L., Bulur, E., Duller, G.A.T. and Murray, A.S. (2000). Advances in luminescence instrument systems. *Radiation Measurements* **32**, 523-528.

Bøtter-Jensen, L., Bulur, E., Murray, A.S. and Poolton, N.R.J. (2002). Enhancements in luminescence measurement techniques. *Radiation Protection Dosimetry* **101**, 119-124.

Bøtter-Jensen, L., Duller, G.A.T., Murray, A.S. and Banerjee, D. (1999). Blue light emitting diodes for optical stimulation of quartz in retrospective dosimetry and dating. *Radiation Protection Dosimetry* **84**, 335-340.

Bøtter-Jensen, L., Jungner, H. and Mejdahl, V. (1993). Recent developments of OSL techniques for dating quartz and feldspar. *Radiation Protection Dosimetry* **47**, 643-648.

Bøtter-Jensen, L., McKeever, S.W.S. and Wintle, A.G. (2003b). "Optically Stimulated Luminescence Dosimetry". Amsterdam, Elsevier Science B.V.

Brakenridge, G.R. (1985). Rate estimates for lateral bedrock erosion based on radiocarbon ages, Duck River, Tennessee. *Geology* **13**, 111-114.

Bridge, J.S. (2003). "Rivers and floodplains: forms, processes, and sedimentary record". Oxford, Blackwell.

Bridge, J.S. and Leeder, M.R. (1979). A simulation model of alluvial stratigraphy. *Sedimentology* **26**, 617-644.

Brook, G.A., Srivastava, P. and Marais, E. (2006). Characteristics and OSL minimum ages of relict fluvial deposits near Sossus Vlei, Tsauchab River, Namibia, and a regional climate record for the last 30 ka. *Journal of Quaternary Science* **21**, 347-362.

Brooks, G.R. (2003). Holocene lateral channel migration and incision of the Red River, Manitoba, Canada. *Geomorphology* **54**, 197-215.

Bryant, M., Falk, P. and Paola, C. (1995). Experimental study of avulsion frequency and rate of deposition. *Geology* **23**, 365-368.

Bulur, E. (1996). An alternative technique for optically stimulated luminescence (OSL) experiment. *Radiation Measurements* **26**, 701-709.

Bulur, E. (2000). A simple transformation for converting CW-OSL curves to LM-OSL curves. *Radiation Measurements* **32**, 141-145.

Bulur, E., Bøtter-Jensen, L. and Murray, A.S. (2000). Optically stimulated luminescence from quartz measured using the linear modulation technique. *Radiation Measurements* **32**, 407-411.

Bulur, E., Duller, G.A.T., Solong, S., Bøtter-Jensen, L. and Murray, A.S. (2002). LM-OSL from single grains of quartz: a preliminary study. *Radiation Measurements* **35**, 79-85.

Burbidge, C. (2003). "Luminescence investigations and dating of anthropogenic palaeosols from South Mainland Shetland". Unpublished PhD thesis, University of Wales, Aberystwyth.

Burke, K. (1996). The African Plate. *South African Journal of Geology* **99**, 341-409.

Capon, S.J. and Brock, M.A. (2006). Flooding, soil seed bank dynamics and vegetation resilience of a hydrologically variable desert floodplain. *Freshwater Biology* **51**, 206-223.

Chen, G., Li, S.-H. and Murray, A.S. (2000). Study of the 110°C TL peak sensitivity in optical dating of quartz. *Radiation Measurements* **32**, 641-645.

Choi, J.H., Duller, G.A.T. and Wintle, A.G. (2006). Analysis of quartz OSL curves. *Ancient TL* **24**, 9-20.

Choi, J.H., Murray, A.S., Cheong, C.S., Hong, D.G. and Chang, H.W. (2003a). The resolution of stratigraphic inconsistency in the luminescence ages of marine terrace sediments from Korea. *Quaternary Science Reviews* **22**, 1201-1206.

Choi, J.H., Murray, A.S., Jain, M., Cheong, C.S. and Chang, H.W. (2003b). Luminescence dating of well-sorted marine terrace sediments on the southeastern coast of Korea. *Quaternary Science Reviews* **22**, 407-421.

Chu, S.Y.F., Ekstrom, L.P. and Firestone, R.B. (1999). WWW Table of Radioactive Isotopes, database version 1999-02-28 from URL.

Clarke, M.L. (1996). IRSL dating of sands: bleaching characteristics at deposition inferred from the use of single aliquots. *Radiation Measurements* **26**, 611-620.

Clarke, M.L., Rendell, H.M. and Wintle, A.G. (1999). Quality assurance in luminescence dating. *Geomorphology* **29**, 173-185.

Colls, A.E., Stokes, S., Blum, M.D. and Straffin, E. (2001). Age limits on the late Quaternary evolution of the upper Loire River. *Quaternary Science Reviews* **20**, 743-750.

Crickmay, C.H. (1960). Lateral activity in a river of northwestern Canada. Journal of *Geology* **68**, 377-391.

Davidson, G.R., Carnley, M., Lange, T., Galicki, S.J. and Douglas, A. (2004). Changes in sediment accumulation rate in an oxbow lake following late 19th century clearing of land for agricultural use: a ^{210}Pb, ^{137}Cs, and ^{14}C study in Mississippi, USA. Radiocarbon **46**, 755-764.

de Wit, M.C.J. (1999). Post-Gondwana drainage and the development of diamond placers in western South Africa. *Economic Geology* **94**, 721-740.

Deacon, J. and Lancaster, N. (1988). "Late Quaternary Palaeoenvironments of Southern Africa". Oxford, Clarendon Press.

Deil, U. (2005). A review on habitats, plant traits and vegetation of ephemeral wetlands - a global perspective. *Phytocoenologia* **35**, 533-705.

Dietrich, W.E., Day, G. and Parker, G. (1999). The Fly River, Papau New Guinea: inferences about river dynamics, floodplain sedimentation and fate of

sediment. In "Varieties of fluvial form". A. J. Miller and A. Gupta. Chichester, John Wiley and Sons: 345-376.

Ditlefsen, C. (1992). Bleaching of K-feldspars in turbid water suspensions; a comparison of photo- and thermoluminescence signals. *Quaternary Science Reviews* **11**, 33-38.

Duller, G.A.T. (1991). Equivalent dose determination using single aliquots. Nuclear Tracks and *Radiation Measurements* **18**, 371-378.

Duller, G.A.T. (1994). Luminescence dating of poorly bleached sediments from Scotland. *Quaternary Geochronology (QSR)* **13**, 521-524.

Duller, G.A.T. (1996). Recent developments in luminescence dating of Quaternary sediments. *Progress in Physical Geography* **20**, 127-145.

Duller, G.A.T. (2003). Distinguishing quartz and feldspar in single grain luminescence measurements. *Radiation Measurements* **37**, 161-165.

Duller, G.A.T. (2004). Luminescence dating of Quaternary sediments: recent advances. *Journal of Quaternary Science* **19**, 183-192.

Duller, G.A.T. (in press). Single grain optical dating of glacigenic deposits. *Quaternary Geochronology*.

Duller, G.A.T. and Augustinus, P.C. (in press). Reassessment of the record of linear dune activity in Tasmania using optical dating. *Quaternary Science Reviews.*

Duller, G.A.T. and Bøtter-Jensen, L. (1996). Comparison of optically stimulated luminescence signals from quartz using different stimulation wavelengths. *Radiation Measurements* **26**, 603-609.

Duller, G.A.T. and Murray, A.S. (2000). Luminescence dating of sediments using individual mineral grains. *Geologos* **5**, 88-106.

Duller, G.A.T., Bøtter-Jensen, L. and Murray, A.S. (2000). Optical dating of single sand-sized grains of quartz: sources of variability. *Radiation Measurements* **32**, 453-457.

Duller, G.A.T., Bøtter-Jensen, L., Kohsiek, P. and Murray, A.S. (1999a). A high-sensitivity optically stimulated luminescence scanning system for measurement of single sand-sized grains. *Radiation Protection Dosimetry* **84**, 325-330.

Duller, G.A.T., Bøtter-Jensen, L., Murray, A.S. and Truscott, A.J. (1999b). Single grain laser luminescence (SGLL) measurements using a novel automated reader. *Nuclear Instruments and Methods: B* **155**, 506-514.

Eitel, B., Kaderiet, A., Blümel, W.D., Hüser, K. and Kromer, B. (2005). The Amspoort Stilts, northern Namib desert (Namibia): formation, age and palaeoclimatic evidence of river-end deposits. *Geomorphology* **64**, 299-314.

Eitel, B., Kaderiet, A., Blümel, W.-D., Hüser, K., Lomax, J. and Hilgers, A. (2006). Environmental changes at the eastern Namib Desert margin before and after the Last Glacial Maximum: New evidence from fluvial deposits in the upper Hoanib River catchment, northwest Namibia. *Palaeogeography, Palaeoclimatology, Palaeoecology* **234**, 201-222.

Ethridge, F.G., Skelly, R.L. and Bristow, C.S. (1999). Avulsion and crevassing in the sandy, braided Niobrara River: complex response to base-level rise and aggradation. In "Fluvial Sedimentology VI. International Association of Sedimentologists Special Publication 28". N. D. Smith and J. Rogers. Oxford, Blackwell Science: 179-191.

Feathers, J.K. and Migliorini, E. (2001). Luminescence dating at Katanda - a reassessment. *Quaternary Science Reviews* **20**, 961-966.

Fisk, H.N. (1944). "Geological investigation of the alluvial valley of the Lower Mississippi". Vicksburg, MS, Mississippi River Commission.

Fitzpatrick, F.A., Knox, J.C. and Whitman, H.E. (1999). "Effects of historical land-cover changes on flooding and sedimentation, North Fish Creek, Wisconsin". USGS Water-Resources Investigations Report 99-4083.

Folz, E., Bodu, P., Bonte, P., Joron, J.L., Mercier, N. and Reyss, J.L. (2001). OSL dating of fluvial quartz from Le Closeau, a Late Paleolithic site near Paris - comparison with ^{14}C chronology. *Quaternary Science Reviews* **20**, 927-933.

Friedkin, J.F. (1945). "A laboratory study of the meandering of alluvial rivers". Vicksburg, Mississippi, US Waterways Experiment Station.

Fuchs, M. and Lang, A. (2001). OSL dating of coarse-grain fluvial quartz using single-aliquot protocols on sediments from NE Peloponnese, Greece. *Quaternary Science Reviews* **20**, 783-787.

Fuchs, M. and Wagner, G.A. (2003). Recognition of insufficient bleaching by small aliquots of quartz for reconstruction soil erosion in Greece. *Quaternary Science Reviews* **22**, 1161-1167.

Furbish, D.J. (1988). River-bend curvature and migration: How are they related? *Geology* **16**, 752-755.

Furbish, D.J. (1991). Spatial autoregressive structure in meander evolution. *Geological Society of America Bulletin* **103**, 1576-1589.

Galbraith, R.F. (1990). The radial plot: graphical assessment of spread in ages. *Nuclear Tracks and Radiation Measurements* **17**, 207-214.

Galbraith, R.F. (1998). The trouble with "probability density" plots of fission track ages. *Radiation Measurements* **29**, 125-131.

Galbraith, R.F. and Green, P.F. (1990). Estimating the component ages in a finite mixture. *Nuclear Tracks and Radiation Measurements* **17**, 197-206.

Galbraith, R.F. and Laslett, G. (1993). Statistical models for mixed fission track ages. *Radiation Measurements* **21**, 459-470.

Galbraith, R.F., Roberts, R.G. and Yoshida, H. (2005). Error variation in OSL palaeodose estimates from single aliquots of quartz: a factorial experiment. *Radiation Measurements* **39**, 289-307.

Galbraith, R.F., Roberts, R.G., Laslett, G.M., Yoshida, H. and Olley, J.M. (1999). Optical dating of single and multiple grains of quartz from Jinmium rock shelter, northern Australia: Part I, Experimental design and statistical models. *Archaeometry* **41**, 339-364.

Galloway, R.B. (1993). Stimulation of luminescence using green light emitting diodes. *Radiation Protection Dosimetry* **47**, 67-682.

Galloway, R.B. (1994). On the stimulation of luminescence with green light emitting diodes. *Radiation Measurements* **23**, 547-550.

Galloway, R.B. (1996). Equivalent dose determination using only one sample: alternative analysis of data obtained from infrared stimulation of feldspars. *Radiation Measurements* **26**, 103-106.

Galloway, R.B., Hong, D.G. and Napier, H.J. (1997). A substantially improved green-light-emitting diode system for luminescence stimulation. *Measurement Science Technology* **8**, 267-271.

Gibling, M.R., Nanson, G.C., and Maroulis, J.C. (1998). Anastomosing river sedimentation in the Channel Country of central Queensland. *Sedimentology* **45**, 595-619.

Gilchrist, A.R. and Summerfield, M.A. (1990). Differential denudation and flexural isostasy in formation of rifted-margin upwarps. *Nature* **346**, 739-742.

Gilvear, D., Winterbottom, S. and Sichingabula, H. (2000). Character of channel planform change and meander development: Luangwa River, Zambia. *Earth Surface Processes and Landforms* **25**, 421-436.

Godfrey-Smith, D.I. (1994). Thermal effects in the optically stimulated luminescence of quartz and mixed feldspars from sediments. *Journal of Physics D: Applied Physics* **27**, 1737-1746.

Godfrey-Smith, D.I., Huntley, D.J. and Chen, W.-H. (1988). Optical dating studies of quartz and feldspar sediment extracts. *Journal of Luminescence* **14**, 373-380.

Hall, M. (1976). Dendroclimatology, Rainfall and Human Adaptation in the Later Iron Age of Natal and Zululand. *Annals of Natal Museum* **22**, 693-703.

Heine, K. (2004). Little Ice Age climatic fluctuations in the Namib Desert, Namibia, and adjacent areas: Evidence of exceptionally large floods from slack water deposits and desert soil sequences. In "Palaeoecology of Quaternary Drylands". W. Smykatz-Kloss and P. Felix-Henningsen. Berlin, Springer.

Heine, K. and Heine, J.T. (2002). A paleohydrological interpretation of the Homeb Silts, Kuiseb River, central Namib Desert (Namibia) and paleoclimatic implications. *Catena* **48**, 107-130.

Hickin, E.J. (1974). The development of meanders in natural river-channels. *American Journal of Science* **274**, 414-442.

Hickin, E.J. and Nanson, G.C. (1975). The character of channel migration on the Beatton River, Northeast British Columbia, Canada. *Geological Society of America Bulletin* **86**, 487-494.

Hickin, E.J. and Nanson, G.C. (1984). Lateral migration rates of river bends. *Journal of Hydraulic Engineering* **110**, 1557-1567.

Hjulström, F. (1935). Studies of the morphological activity of rivers as illustrated by the River Fyris. *Bulletin of the Geological Institute University of Uppsala* **24**, 224-257.

Holmes, P.J., Boardman, J., Parson, A.J. and Marker, M.E. (2003). Geomorphological palaeoenvironments of the Sneeuberg Range, Great Karoo, South Africa. *Journal of Quaternary Science* **18**, 801-813.

Holmgren, K., Karlen, W. and Shaw, P.A. (1995). Paleoclimatic Significance of the Stable Isotopic Composition and Petrology of a Late Pleistocene Stalagmite from Botswana. *Quaternary Research* **43**, 320-328.

Holmgren, K., Karlen, W., Lauritzen, S.E., Lee-Thorpe, J.A., Partridge, T.C., Piketh, S., Repinski, P., Stevenson, C., Svanered, O. and Tyson, P.D. (1999). A 3000-year high-resolution stalagmite-based record of palaeoclimate for northeastern South Africa. *The Holocene* **9**, 295-309.

Holmgren, K., Lee-Thorpe, J.A., Cooper, G.R.J., Lundblad, K., Patridge, T.C., Scott, L., Sithaldeen, R., Talma, A.S. and Tyson, P.D. (2003). Persistent millennial-scale climatic variability over the past 25,000 years in Southern Africa. *Quaternary Science Reviews* **22**, 2311-2326.

Hooke, J.M. (1987). Changes in meander morphology. In "International *Geomorphology* 1986 Part I". V. Gardiner. Chichester, John Wiley and Sons Ltd.

Hooke, J.M. (1995). River channel adjustment to meander cutoffs on the River Bollin and River Dane, northwest England. *Geomorphology* **14**, 235-253.

Hooke, J.M. (1997). Styles of channel change. In "Applied fluvial *Geomorphology* for river engineering and management". C. R. Thorne, R. D. Hey and M. D. Newson. Chichester, John Wiley and Sons Ltd: 237-268.

Hudson, P.F. and Kesel, R.H. (2000). Channel migration and meander-bend curvature in the lower Mississippi River prior to major human modification. *Geology* **28**, 531-534.

Huntley, D.J., Godfrey-Smith, D.I. and Thewalt, M.L.W. (1985). Optical dating of sediments. *Nature* **313**, 105-107.

Hütt, G. and Jungner, H. (1992). Optical and TL dating on glaciofluvial sediments. *Quaternary Science Reviews* **11**, 161-163.

Ivanovich, M. and Harmon, R.S. (1992). "Uranium-series disequilibrium: Applications to earth, marine, and environmental sciences". Oxford, Clarendon Press.

Ivanovich, M. and Murray, A. (1992). Spectroscopic methods. In "Uranium-series disequilibrium: Applications to earth, marine and environmental Sciences". M. Ivanovich and R. S. Harmon. Oxford, Clarendon Press: 127-173.

Jackson II, R.G. (1976). Depositional model of point bars in the Lower Wabash River. *Journal of Sedimentary Petrology* **46**, 579-594.

Jacobs, Z. (2004). "Development of luminescence techniques for dating Middle Stone Age sites in South Africa". Unpublished PhD thesis, University of Wales, Aberystwyth.

Jacobs, Z., Duller, G.A.T. and Wintle, A.G. (2003a). Optical dating of dune sand from Blombos Cave, South Africa: II-single grain data. *Journal of Human Evolution* **44**, 613-625.

Jacobs, Z., Duller, G.A.T. and Wintle, A.G. (2006). Interpretation of single grain D_e distributions and calculation of D_e. *Radiation Measurements* **41**, 264-277.

Jacobs, Z., Wintle, A.G. and Duller, G.A.T. (2003b). Optical dating of dune sand from Blombos Cave, South Africa: I-multiple grain data. *Journal of Human Evolution* **44**, 599-612.

Jain, M., Murray, A.S. and Bøtter-Jensen, L. (2003). Characterisation of blue-light stimulated luminescence components in different quartz samples: implications for dose measurement. *Radiation Measurements* **37**, 441-449.

Jain, M., Murray, A.S. and Bøtter-Jensen, L. (2004). Optically stimulated luminescence dating: How significant is incomplete light exposure in fluvial environments? *Quaternaire* **15**, 143-157.

Jones, L.S. and Harper, J. (1998). Channel avulsions and related processes, and large-scale sedimentation patterns since 1875, Rio Grande, San Luis Valley, Colorado. *Geological Society of America Bulletin* **110**, 411-421.

Jones, L.S. and Schumm, S.A. (1999). Causes of avulsion: an overview. In "Fluvial Sedimentology VI. International Association of Sedimentologists Special Publication 28". N. D. Smith and J. Rogers. Oxford, Blackwell Science: 171-178.

Kale, V.S., Singhvi, A.K., Mishra, P.K. and Banerjee, D. (2000). Sedimentary records and luminescence chronology of Late Holocene palaeofloods in the Luni River, Thar Desert, northwest India. *Catena* **40**, 337-358.

Kar, A., Singhvi, A.K., Rajaguru, S.N., Juyal, N., Thomas, J.V., Banerjee, D. and Dhir, R.P. (2001). Reconstruction of the late Quaternary environment of the lower Luni plains, Thar Desert, India. *Journal of Quaternary Science* **16**, 61-68.

Knighton, D. (1998). "Fluvial forms and processes: a new perspective". Chichester, John Wiley and Sons.

Krbetschek, M.R., Rieser, U., Zöller, L. and Heinicke, J. (1994). Radioactive disequilibria in palaeodosimetric dating of sediments. *Radiation Measurements* **23**, 485-489.

Kuhns, C.K., Agersnap Larsen, N. and McKeever, S.W.S. (2000). Characteristics of LM-OSL from several different types of quartz. *Radiation Measurements* **32**, 413-418.

Lamothe, M. and Auclair, M. (1999). A solution to anomalous fading and age shortfalls in optical dating of feldspar minerals. *Earth and Planetary Science Letters* **171**, 319-323.

Leeder, M.R. (1978). A quantitative stratigraphic model for alluvium, with special reference to channel deposit density and interconnectedness. In "Fluvial Sedimentology". A. D. Miall. Calgary, Canadian Society of Petroleum Geologists. Memoir 5: 587-596.

Lee-Thorpe, J.A., Holmgren, K., Lauritzen, S.E., Linge, H., Moberg, A., Partridge, T.C., Stevenson, C. and Tyson, P.D. (2001). Rapid climate shifts in the southern African interior throughout the mid to late Holocene. *Geophysical Research Letters* **28**, 4507-4510.

Leigh, D.S., Srivastava, P. and Brook, G.A. (2004). Late Pleistocene braided rivers of the Atlantic Coastal Plain, USA. *Quaternary Science Reviews* **23**, 65-84.

Lepper, K. and McKeever, S.W.S. (2002). An objective methodology for dose distribution analysis. *Radiation Protection Dosimetry* **101**, 349-352.

Lepper, K., Agersnap Larsen, N. and McKeever, S.W.S. (2000). Equivalent dose distribution analysis of Holocene eolian and fluvial quartz sands from Central Oklahoma. *Radiation Measurements* **32**, 603-608.

Lewis, C.A. and Illgner, P.M. (1998). Fluvial conditions during the Holocene as evidenced by alluvial sediments from above Howison's Poort, near Grahamstown, South Africa. *Transactions of the Royal Society of South Africa* **53**, 53-67.

Lewis, G.W. and Lewin, J. (1983). Alluvial cutoffs in Wales and the Borderlands. Modern and ancient fluvial systems. In "International Association of Sedimentologists Special Publication 6". J. D. Collinson and J. Lewin. Oxford, Blackwell Science: 145-154.

Li, B. and Li, S.-H. (2006). Comparison of D_e estimates using the fast component and the medium component of quartz OSL. *Radiation Measurements* **41**, 125-136.

Lian, O.B. and Brooks, G.R. (2004). Optical dating studies of mud-dominated alluvium and buried hearth-like features from Red River Valley, southern Manitoba, Canada. *The Holocene* **14**, 570-578.

Liritzis, I., Galloway, R.B. and Hong, D.G. (1997). Single aliquot dating of ceramics by green light stimulation of luminescence from quartz. *Nuclear Instruments and Methods in Physics Research B* **132**, 457-467.

Lowe, J.J. and Walker, M.J.C. (1997). "Reconstructing Quaternary Environments". Harlow, Pearson Education Limited.

Mackey, S.D. and Bridge, J.S. (1995). Three-dimensional model of alluvial stratigraphy: theory and application. *Journal of Sedimentary Research* **B65**, 7-31.

Makaske, B. (2001). Anastomosing rivers: a review of their classification, origin and sedimentary products. *Earth-Science Reviews* **53**, 149-196.

Makaske, B., Smith, D.G. and Berendsen, H.J.A. (2002). Avulsions, channel evolution and floodplain sedimentation rates of the anastomosing upper Columbia River, British Columbia, Canada. *Sedimentology* **49**, 1049-1071.

Markey, B.G., Bøtter-Jensen, L. and Duller, G.A.T. (1997). A new flexible system for measuring thermally and optically stimulated luminescence. *Radiation Measurements* **27**, 83-89.

Marren, P.M., McCarthy, T.S., Tooth, S., Brandt, D., Stacey, G.G., Leong, A. and Spottiswoode, B. (in press). A comparison of mud- and sand-dominated meanders in a downstream coarsening reach of the mixed bedrock-alluvial Klip River, eastern Free State, South Africa. *Sedimentary Geology*.

Martinson, D.G., Pisias, N.G., Hays, J.D., Imbrie, J., Moore, T.C. and Shackleton, N.J. (1987). Age dating and the orbital theory of the ice ages: development of a high resolution 0-300,000 year chronostratigraphy. *Quaternary Research* **27**, 1-29.

McCarthy, T.S. and Hancox, P.J. (2000). Wetlands. In "The Cenozoic of Southern Africa". T. C. Partridge and R. R. Maud. Oxford, Oxford University Press: 218-235.

McCarthy, T.S. and Tooth, S. (2004). Incised meanders along the mixed bedrock-alluvial Orange River, Northern Cape Province, South Africa. *Zeitschrift für Geomorphologie* **48**, 273-292.

McGowan, J.H. and Garder, L.E. (1970). Physiographic features and stratification types of coarse-grained point bars: modern and ancient examples. *Sedimentology* **14,** 77-111.

Mejdahl, V. (1979). Thermoluminescence dating: beta-dose attenuation in quartz grains. *Archaeometry* **21**, 61-72.

Mejdahl, V. (1987). Internal radioactivity in quartz and feldspar grains. *Ancient TL* **5**, 10-17.

Mejdahl, V. and Bøtter-Jensen, L. (1994). Luminescence dating of archaeological materials using a new technique based on single aliquot measurements. *Quaternary Geochronology (QSR)* **13**, 551-554.

Morozova, G. and Smith, N.D. (1999). Holocene avulsion history of the lower Saskatchewan fluvial system, Cumberland Marshes, Saskatchewan-Manitoba, Canada. In "International Association of Sedimentologists Special Publication 28". N. D. Smith and J. Rogers. Oxford, Blackwell Science: 231-249.

Murray, A.S. (1981). "Environmental radioactivity studies relevant to thermoluminescence dating". Unpublished PhD thesis, University of Oxford.

Murray, A.S. (1996). Developments in optically stimulated luminescence and photo-transferred thermoluminescence dating of young sediments: application to a 2000 year sequence of flood deposits. *Geochemica et Cosmochimicha Acta* **60**, 565-576.

Murray, A.S. and Olley, J.M. (2002). Precision and accuracy in the optically stimulated luminescence dating of sedimentary quartz: a status review. *Geochronometria* **21**, 1-16.

Murray, A.S. and Roberts, R.G. (1997). Determining the burial time of single grains of quartz using optically stimulated luminescence. *Earth and Planetary Science Letters* **152**, 163-180.

Murray, A.S. and Roberts, R.G. (1998). Measurement of the equivalent dose in quartz using a regenerative-dose single-aliquot protocol. *Radiation Measurements* **29**, 503-515.

Murray, A.S. and Wintle, A.G. (1998). Factors controlling the shape of the OSL decay curve in quartz. *Radiation Measurements* **29**, 65-79.

Murray, A.S. and Wintle, A.G. (2000). Luminescence dating of quartz using an improved single-aliquot regenerative-dose protocol. *Radiation Measurements* **32**, 57-73.

Murray, A.S. and Wintle, A.G. (2003). The single aliquot regenerative dose protocol: potential for improvements in reliability. *Radiation Measurements* **37**, 377-381.

Murray, A.S., Marten, R., Johnston, A. and Martin, P. (1987). Analysis for naturally occurring radionuclides at environmental concentrations by gamma spectrometry. *Journal of Radioanalytical and Nuclear Chemistry, Articles* **115**, 263-288.

Murray, A.S., Olley, J.M. and Caitcheon, G.G. (1995). Measurement of equivalent doses in quartz from contemporary water-lain sediments using optically stimulated luminescence. *Quaternary Geochronology (QSR)* **14**, 365-371.

Murray, A.S., Roberts, R.G. and Wintle, A.G. (1997). Equivalent dose measurement using a single aliquot of quartz. *Radiation Measurements* **27**, 171-184.

Nanson, G.C. (1980). A regional trend to meander migration. *Journal of Geology* **88**, 100-108.

Nanson, G.C. (1981). New evidence of scroll-bar formation on the Beatton River. *Sedimentology* **28**, 889-891.

Nanson, G.C. and Croke, J.C. (1992). A genetic classification of floodplains. *Geomorphology* **4**, 459-486.

Nanson, G.C. and Hickin, E.J. (1983). Channel migration and incision on the Beatton River. *Journal of Hydraulic Engineering* **109**, 327-337.

Nanson, G.C. and Hickin, E.J. (1986). A statistical analysis of bank erosion and channel migration in western Canada. *Geological Society of America Bulletin* **97**, 497-504.

Nanson, G.C., and Knighton, A.D. (1996). Anabranching rivers: their cause, character and classification. *Earth Surface Processes and Landforms* **21**, 217-239.

Nelson, B.W. (1970). Hydrography, sediment dispersal and recent historical development of the Po River delta, Italy. In "Deltaic sedimentation, modern and ancient. SEPM Special Publication 15". J. P. Morgan and R. H. Shaver. Tulsa, Oklahoma Society of Economic Paleontologists and Mineralogists: 152-184.

Nilsson, G. and Martvall, S. (1972). The Ore River and its meanders. *Uppsala University, Department of Physical Geography* **19**: 154pp.

Nyakale, M. and Scott, L. (2002). Interpretation of late Holocene pollen in channel fills in the eastern Free State, South Africa, in terms of local conditions and sediment reworking. *South African Journal of Botany* **68**, 464-468.

Ollerhead, J., Huntley, D.J. and Berger, G.W. (1994). Luminescence dating of sediments from Buctouche Spit, New Brunswick. *Canadian Journal of Earth Sciences* **31**, 365-371.

Olley, J., Murray, A. and Roberts, R.G. (1996). The effects of disequilibria in the uranium and thorium decay chains on burial dose rates in fluvial sediments. *Quaternary Geochronology (QSR)* **15**, 751-760.

Olley, J.M., Caitcheon, G. and Murray, A.S. (1998). The distribution of apparent dose as determined by optically stimulated luminescence in small aliquots of fluvial quartz: implications for dating young sediments. *Quaternary Geochronology (QSR)* **17**, 1033-1040.

Olley, J.M., Caitcheon, G.G. and Roberts, R.G. (1999). The origin of dose distributions in fluvial sediments, and the prospect of dating single grains from fluvial deposits using optically stimulated luminescence. *Radiation Measurements* **30**, 207-217.

Olley, J.M., De Deckker, P., Roberts, R.G., Fifield, L.K., Yoshida, H. and Hancock, G. (2004a). Optical dating of deep-sea sediments using single grains of quartz: a comparison with radiocarbon. *Sedimentary Geology* **169**, 175-189.

Olley, J.M., Pietsch, T. and Roberts, R.G. (2004b). Optical dating of Holocene sediments from a variety of geomorphic settings using single grains of quartz. *Geomorphology* **60**, 337-358.

Olley, J.M., Roberts, R.G. and Murray, A.S. (1997). Disequilibria in the Uranium decay series in sedimentary deposits at Allen's Cave, Nullarbor Plain, Australia: implications for dose rate determinations. *Radiation Measurements* **27**, 433-443.

Osmond, J.K. and Cowart, J.B. (1982). Groundwater. In "Uranium Series Disequilibrium: Applications to Environmental Problems". M. Ivanovich and R. S. Harmon. Oxford, Clarendon Press.

Partridge, T.C. (1997). Cainozoic environmental change in southern Africa, with special emphasis on the last 200 000 years. *Progress in Physical Geography* **21**, 3-22.

Partridge, T.C. and Maud, R.R. (1987). Geomorphic evolution of southern Africa since the Mesozoic. *South African Journal of Geology* **90**, 179-208.

Partridge, T.C., Demenocal, P.B., Lorentz, S.A., Paiker, M.J. and Vogel, J.C. (1997). Orbital forcing of climate over South Africa: a 200,000-year rainfall record from the Pretoria Saltpan. *Quaternary Science Reviews* **16**, 1125-1133.

Prescott, J.R. and Hutton, J.T. (1988). Cosmic ray and gamma ray dosimetry for TL and ESR. Nuclear Tracks and *Radiation Measurements* **14**, 223-227.

Prescott, J.R. and Hutton, J.T. (1994). Cosmic ray contributions to dose rates for luminescence and ESR dating: large depths and long-term time variations. *Radiation Measurements* **23**, 497-500.

Press, F. and Siever, R. (1998). "Understanding Earth". New York, Freeman.

Qian, M. (1990). Fluvial processes in the lower Yellow River after levee breaching at Tongwaxiang in 1855. *International Journal of Sedimentary Research* **5**, 1-13.

Rendell, H.M. and Townsend, P.D. (1988). Thermoluminescence dating of a 10m loess profile in Pakistan. *Quaternary Science Reviews* **7**, 251-255.

Rendell, H.M., Webster, S.E. and Sheffer, N.L. (1994). Underwater bleaching of signals from sediment grains: new experimental data. *Quaternary Geochronology (QSR)* **13**, 433-435.

Repinski, P., Holmgren, K., Lauritzen, S.E. and Lee-Thorpe, J.A. (1999). A late Holocene climate record from a stalagmite, Cold Air Cave, Northern Province, South Africa. *Palaeogeography, Palaeoclimatology, Palaeoecology* **150**, 269-277.

Rhodes, E.J. and Pownall, L. (1994). Zeroing of the OSL signal in quartz from young glaciofluvial sediments. *Radiation Measurements* **23**, 581-585.

Richards, K.S. (1982). “Rivers: form and process in alluvial channels”. Methuen, London.

Rittenour, T.M., Goble, R.J. and Blum, M.D. (2003). An optical age chronology of Late Pleistocene fluvial deposits in the northern lower Mississippi valley. *Quaternary Science Reviews* **22,** 1105-1110.

Rittenour, T.M., Goble, R.J. and Blum, M.D. (2005). Development of an OSL chronology for Late Pleistocene channel belts in the lower Mississippi valley, USA. *Quaternary Science Reviews* **24**, 2539-2554.

Roberts, H.M. and Duller, G.A.T. (2004). Standardised growth curves for optical dating of sediment using multiple-grain aliquots. *Radiation Measurements* **38**, 241-252.

Roberts, R.G., Galbraith, R.F., Olley, J.M., Yoshida, H. and Laslett, G.M. (1999). Optical dating of single and multiple grains of quartz from Jinmium rock shelter, northern Australia: Part II, results and implications. *Archaeometry* **42**, 365-395.

Rowland, J.C., Lepper, K., Dietrich, W.E., Wilson, C.J. and Sheldon, R. (2005). Tie channel sedimentation rates, oxbow formation age and channel migration rate from optically stimulated luminescence (OSL) analysis of floodplain deposits. *Earth Surface Processes and Landforms* **30**, 1161-1179.

Rust, U. (1999). River-end deposits along the Hoanib River, northern Namib: archives of Late Holocene climatic variation on a subregional scale. *South African Journal of Science* **95**, 205-208.

Schumm, S.A. (2005). "River variability and complexity". Cambridge, University Press.

Scott, L. (1982). A Late Quaternary Pollen Record from the Transvaal Bushveld, South Africa. *Quaternary Research* **17**, 339-370.

Scott, L. (1989). Late Quaternary vegetation history and climate change in the eastern Orange Free State, South Africa. *South African Journal of Botany* **55**, 107-116.

Scott, L. (1993). Palynological evidence for late Quaternary warming episodes in Southern Africa. *Palaeogeography, Palaeoclimatology, Palaeoecology* **101**, 229-235.

Scott, L. and Nyakale, M. (2002). Pollen indicators of Holocene palaeoenvironments at Florisbad spring in the central Free State, South Africa. *The Holocene* **12**, 497-503.

Scott, L. and Vogel, J.C. (1983). Late Quaternary Pollen Profile from the Transvaal Highveld, South Africa. *South African Journal of Science* **79**, 266-272.

Shankman, D. (1991). Botanical evidence for the age of oxbow lakes: a test of Harper's hypothesis. *Southeastern Geographer* **31**, 67-74.

Singarayer, J.S. and Bailey, R.M. (2003). Further investigations of the quartz optically stimulated luminescence components using linear modulation. *Radiation Measurements* **37**, 451-458.

Singarayer, J.S. and Bailey, R.M. (2004). Component-resolved bleaching spectra of quartz optically stimulated luminescence: preliminary results and implications for dating. *Radiation Measurements* **38**, 111-118.

Singarayer, J.S., Bailey, R.M., Ward, S. and Stokes, S. (2005). Assessing the completeness of optical resetting of quartz OSL in the natural environment. *Radiation Measurements* **40**, 13-25.

Slingerland, R. and Smith, N.D. (1998). Necessary conditions for meandering-river avulsion. *Geology* **26**, 435-438.

Slingerland, R. and Smith, N.D. (2004). River avulsions and their deposits. *Annual Review of Earth and Planetary Science* **32**, 257-285.

Smith, A.M. (1992). Holocene palaeoclimatic trends from palaeoflood analysis. *Palaeogeography, Palaeoclimatology, Palaeoecology* **97**, 235-240.

Smith, B.W. and Rhodes, E.J. (1994). Charge movements in quartz and their relevance to optical dating. *Radiation Measurements* **23**, 329-333.

Smith, J.M., Lee-Thorpe, J.A. and Sealy, J.C. (2002). Stable carbon and oxygen isotopic evidence for late Pleistocene to middle Holocene climatic fluctuations in the interior of southern Africa. *Journal of Quaternary Science* **17**, 683-695.

Smith, R.M.H., Eriksson, P.G. and Botha, W.J. (1993). A review of the stratigraphy and sedimentary environments of the Karoo-aged basins of Southern Africa. *Journal of African Earth Sciences* **16**, 143-169.

Spooner, N.A. (1994a). The anomalous fading of infrared-stimulated luminescence from feldspars. *Radiation Measurements* **23**, 625-632.

Spooner, N.A. (1994b). On the optical dating signal from quartz. *Radiation Measurements* **23**, 593-600.

Srivastava, P., Brook, G.A., Marais, E., Morthekai, P. and Singhvi, A.K. (2006). Depositional environment and OSL chronology of the Homeb silt deposits, Kuiseb River, Namibia. *Quaternary Research* **65**, 478-491.

Srivastava, P., Juyal, N., Singhvi, A.K., Wasson, R.J. and Bateman, M.D. (2001). Luminescence chronology of river adjustment and incision of Quaternary sediments in the alluvial plain of the Sabarmati River, north Gujarat, India. *Geomorphology* **36**, 217-229.

Srivastava, P., Sharma, M. and Singhvi, A.K. (2003). Luminescence chronology of incision and channel pattern change in the River Ganga, India. *Geomorphology* **51**, 259-268.

Stevenson, C., Lee-Thorpe, J.A. and Holmgren, K. (1999). A 3000 year isotopic record from a stalagmite in Cold Air Cave, Makapan Valley, Northern Province. *South African Journal of Science* **95**, 46-48.

Stokes, S. (1992). Optical dating of young (modern) sediments using quartz: results from a selection of depositional environments. *Quaternary Science Reviews* **11**, 153-159.

Stokes, S. (1994). The timing of OSL sensitivity changes in a natural quartz. *Radiation Measurements* **23**, 601-605.

Stokes, S., Bray, H.E. and Blum, M.D. (2001). Optical resetting in large drainage basins: tests of zeroing assumptions using single-aliquot procedures. *Quaternary Science Reviews* **20**, 879-885.

Stokes, S., Colls, A.E.L., Fattahi, M. and Rich, J. (2000). Investigations of the performance of quartz single aliquot D_e determination procedures. *Radiation Measurements* **32**, 585-594.

Stolum, H.H. (1996). River meandering as a self-organisation process. *Science* **271**, 1710-1713.

Stouthamer, E. and Berendsen, H.J.A. (2001). Avulsion frequency, avulsion duration, and the interavulsion period of Holocene channel belts in the Rhine-Meuse delta, The Netherlands. *Journal of Sedimentary Research* **71**, 589-598.

Sundborg, A. (1956). The River Klarälven: a study of fluvial processes. *Geografiska Annaler* **38**, 127-316.

Talma, A.S. and Vogel, J.C. (1992). Late Quaternary Paleotemperatures Derived from a Speleothem from Cango Caves, Cape Province, South Africa. *Quaternary Research* **37**, 203-213.

Thackeray, J.F. (1996). Ring width variation in a specimen of South African Podocarpus, circa 1350-1937 AD. *Palaeoecology of Africa* **24**, 233-240.

Thackeray, J.F. and Potze, S. (2000). A sectioned yellowwood tree trunk housed at the Transvaal Museum, Pretoria. *Annals of the Transvaal Museum* **37**, 131-137.

Thomas, D.S.G. and Shaw, P.A. (2002). Late Quaternary environmental change in central southern Africa: new data, synthesis, issues and prospects. *Quaternary Science Reviews* **21**, 783-797.

Thomas, P.J., Jain, M., Juyal, N. and Singhvi, A.K. (2005). Comparison of single-grain and small-aliquot OSL dose estimates in <3000 years old river sediments from South India. *Radiation Measurements* **39**, 457-469.

Thomsen, K.J., Jain, M., Bøtter-Jensen, L., Murray, A.S. and Jungner, H. (2003). Variation with depth of dose distributions in single grains of quartz extracted from an irradiated concrete block. *Radiation Measurements* **37**, 315-321.

Thomsen, K.J., Murray, A.S., and Bøtter-Jensen, L. (2005). Sources of variability in OSL dose measurements using single grains of quartz. *Radiation Measurements* **39**, 47-61.

Tinkler, K.J., and Wohl, E.E. (1998). A primer on bedrock channels. In “Rivers over rock: fluvial processes in bedrock channels. Geophysical Monograph Series”. Tinkler, K.J., and Wohl, E.E. American Geophysical Union, Washington, DC.

Tooth, S. and McCarthy, T.S. (2004). Controls on the transition from meandering to straight channels in the wetlands of the Okavango Delta, Botswana. *Earth Surface Processes and Landforms* **29**, 1627-1649.

Tooth, S. and Nanson, G.C. (2004). Forms and processes of two highly contrasting rivers in arid central Australia, and the implications for channel-pattern discrimination and prediction. *Geological Society of America Bulletin* **116**, 802-816.

Tooth, S., Brandt, D., Hancox, P.J. and McCarthy, T.S. (2004). Geological controls on alluvial river behaviour: a comparative study of three rivers on the South African Highveld. *Journal of African Earth Sciences* **38**, 79-97.

Tooth, S., McCarthy, T.S., Brandt, D., Hancox, P.J. and Morris, R. (2002). Geological controls on the formation of alluvial meanders and floodplain wetlands: the example of the Klip River, Eastern Free State, South Africa. *Earth Surface Processes and Landforms* **27**, 797-815.

Tooth, S., Rodnight, H., Duller, G.A.T., McCarthy, T.S., Marren, P.M. and Brandt, D. (submitted). Chronology and controls of avulsion along a mixed bedrock-alluvial river. *Geological Society of America Bulletin*.

Törnqvist, T.E. (1994). Middle and late Holocene avulsion history of the River Rhine (Rhine-Meuse delta, Netherlands). *Geology* **22**, 711-714.

Törnqvist, T.E. and Bridge, J.S. (2002). Spatial variation of overbank aggradation rate and its influence on avulsion frequency. *Sedimentology* **49**, 891-905.

Tower, W.S. (1904). The development of cutoff meanders. *Bulletin of the American Geological Society of New York* **36**, 589-599.

Truscott, A.J., Duller, G.A.T., Bøtter-Jensen, L., Murray, A.S. and Wintle, A.G. (2000). Reproducibility of optically stimulated luminescence measurements from single grains of Al_2O_3:C and annealed quartz. *Radiation Measurements* **32**, 447-451.

Tsukamoto, S., Rink, W.J. and Watanuki, T. (2003). OSL of tephric loess and volcanic quartz in Japan and an alternative procedure for estimating D_e from a fast OSL component. *Radiation Measurements* **37**, 459-465.

Tyson, P.D. (1987). "Climatic change and variability in southern Africa". Cape Town, Oxford University Press.

Tyson, P.D. (1999). Late-Quaternary and Holocene palaeoclimates of southern Africa: a synthesis. *South African Journal of Geology* **102**, 335-349.

Tyson, P.D. and Lindesay, J.A. (1992). The climate of the last 2000 years in southern Africa. *The Holocene* **2**, 271-278.

Tyson, P.D. and Preston-Whyte, R.A. (2000). "The Weather and Climate of Southern Africa". Cape Town, Oxford University Press Southern Africa.

Tyson, P.D., Dyer, T.G.J. and Mametse, M.N. (1975). Secular changes in South African rainfall: 1880-1972. *Quarterly Journal of the Royal Meteorological Society* **101**, 817-833.

Tyson, P.D., Karlen, W., Holmgren, K. and Heiss, G.A. (2000). The Little Ice Age and medieval warming in South Africa. *South African Journal of Science* **96**, 121-126.

Tyson, P.D., Odada, E.O. and Partridge, T.C. (2001). Late Quaternary environmental change in southern Africa. *South African Journal of Science* **97**, 139-150.

Vogel, J.C. and Rust, U. (1990). Ein in der Kleinen Eiszeit begrabener Wald in der norlichen Namib. *Berliner Geographische Studien* **30**, 15-34.

Wallinga, J. (2002). Optically stimulated luminescence dating of fluvial deposits: a review. *Boreas* **31**, 303-322.

Wallinga, J., Murray, A.S., Duller, G.A.T. and Tornqvist, T.E. (2001). Testing optically stimulated luminescence dating of sand-sized quartz and feldspar from fluvial deposits. *Earth and Planetary Science Letters* **193**, 617-630.

Ward, S., Stokes, S., Bailey, R., Singarayer, J., Goudie, A. and Bray, H. (2003). Optical dating of quartz from young samples and the effects of pre-heat temperature. *Radiation Measurements* **37**, 401-407.

Winkley, B.R. (1982). Response of the Lower Mississippi to river training and realignment. In "Gravel bed rivers". R. D. Hey, J. C. Bathurst and C. R. Thorne. Chichester, Wiley: 659-680.

Wintle, A.G. and Huntley, D.J. (1982). Thermoluminescence dating of sediments. *Quaternary Science Reviews* **1**, 31-53.

Wintle, A.G. and Murray, A.S. (1999). Luminescence sensitivity changes in quartz. *Radiation Measurements* **30**, 107-118.

Wintle, A.G. and Murray, A.S. (2006). A review of quartz optically stimulated luminescence characteristics and their relevance in single-aliquot regeneration dating procedures. *Radiation Measurements* **41**, 369-391.

Yoshida, H., Roberts, R.G., Olley, J.M., Laslett, G.M. and Galbraith, R.F. (2000). Extending the age range of optical dating using single 'supergrains' of quartz. *Radiation Measurements* **32**, 439-446.

Zawada, P.K. (2000). Slackwater Sediments and Paleofloods. In "The Cenozoic of Southern Africa". T. C. Partridge and R. R. Maud. Oxford, Oxford University Press: 198-206.

Zhang, J.F., Zhou, L.P. and Yue, S.Y. (2003). Dating fluvial sediments by optically stimulated luminescence: selection of equivalent doses for age calculation. *Quaternary Science Reviews* **22**, 1123-1129.

Zimmerman, D.W. (1971). Thermoluminescence dating using fine grains from pottery. *Archaeometry* **13**, 29-52.